JOHANNES KEPLER
UNIVERSITY LINZ

Author
DI Jakob Hofinger

Submission at
Linz Institute for Organic Solar Cells (LIOS) / Institute of Physical Chemistry

Supervisor and first evaluator
a. Univ. Prof. Dr. Markus Scharber

Second Evaluator
Univ.-Prof Dr. Gregor Trimmel

April 2022

Novel Alternative Acceptor Materials for Organic Solar Cells

Doctoral Thesis

to obtain the academic degree of

Doktor der technischen Wissenschaften

in the Doctoral Program

Technische Wissenschaften

JOHANNES KEPLER UNIVERSITY LINZ
Altenbergerstraße 69
4040 Linz, Austria
www.jku.at
DVR 0093696

Statutory Declaration

I hereby declare under oath that the submitted Doctoral Thesis has been written solely by me without any third-party assistance, information other than provided sources or aids have not been used and those used have been fully documented. Sources for literal, paraphrased and cited quotes have been accurately credited.

Linz, 13.04.2022

Place, date

Signature

Abstract

The increasing demand for energy, driven by technological progress and the rapid growth of the worldwide population, strongly suggests looking for renewable alternatives to commonly used fossil energy sources. Inevitably, at some point these non-renewable energy reserves will be depleted and by then at the latest our transition to a clean and renewable energy source should be completed. On top of this, the adverse environmental effects accompanied with the combustion of fossil fuels are thought to be the main driver of anthropogenic global warming and suggest changing to an abundant and sustainable energy source sooner rather than later. A wise approach to secure the world's current and future energy demand is to exploit the largest source of clean, abundant, and free energy in our (astronomically) close proximity – the sun. Photovoltaics convert solar energy directly into electricity and offer a practical and sustainable solution to the challenge of meeting the increasing global energy demand. One emerging class of photovoltaic technologies, which has attracted a lot of academic as well as industrial research interest is the field of organic photovoltaics. Compared to common inorganic photovoltaic devices (e.g. Si, GaAs), solar cells based on organic semiconductors offer the unique advantages of large-scale and low-cost solution processing, bandgap tunability, a short energy payback time, and the possibility to fabricate semi-transparent and/or light-weight, flexible devices.

The aim of this thesis is the investigation of novel, as well as state-of-the-art small molecule materials for the application as acceptor compounds in organic solar cells. For decades the dominating acceptor materials for organic photovoltaics were based on soluble fullerene derivatives, which are characterized by excellent electronic but only moderate optical properties. The recent development of high-performance non-fullerene acceptor materials has completely changed this narrative. Their superior optical properties helped to revitalize the field of organic photovoltaics and caused power conversion efficiencies to skyrocket. A second critical advantage of non-fullerene acceptors is the enhanced synthetic flexibility, which allows for fine-tuning of e.g. energy level alignments in selected donor:acceptor combinations, giving rise to solar cells with reduced open-circuit voltage losses and record efficiencies currently closing in on the 20 % threshold. The rapid success of non-fullerene-based solar cells in the last 5 years has caused the fundamental understanding of these new acceptors to lag behind. As a contribution to the collective endeavor of the organic photovoltaics

community in furthering the knowledge of device physics and working mechanisms of these new class of solar cell materials, a detailed investigation of the - at the time - record-breaking donor:acceptor combination D18 and Y6 (power conversion efficiencies >18 %) is presented. The main focus of the D18:Y6 study is on understanding the voltage losses in high-performance non-fullerene-acceptor-based solar cells, as improving the knowledge in this area is critical in promoting their recent success. The voltage losses of D18:Y6 devices are compared to fullerene devices consisting of D18 and $PC_{71}BM$ to highlight the differences between non-fullerene and fullerene acceptors.

The second main achievement presented in this thesis is the characterization and development of efficient organic solar cells based on a novel perylene-based non-fullerene acceptor referred to as PMI-FF-PMI. Using a set of screening methods, the material based on a perylene monoimide (PMI) triad structure in the form of PMI-linker-PMI, was chosen as the most promising candidate out of 17 other, structurally related, perylene-based non-fullerene acceptors. The PMI-FF-PMI acceptor was combined with the high-performance donor polymer D18 to fabricate efficient organic solar cells, characterized by an extremely high open-circuit voltage of 1.41 V, which to the best of our knowledge is the highest reported value for solution-processed organic solar cells so far. With an effective bandgap of 2.02 eV, the D18:PMI-FF-PMI blend can be categorized as a wide-bandgap organic solar cell and is an attractive candidate for application as a wide-bandgap sub-cell in all-organic triple-junction solar cell devices. The comparison of D18:PMI-FF-PMI solar cells with state-of-the-art D18:Y6 devices revealed potential areas of optimization (e.g. photovoltaic external quantum efficiency and short-circuit current density) of this newly developed donor:acceptor combination and provides valuable insights for the design of new and improved non-fullerene acceptors based on this class of materials.

Efforts in improving the performance of D18:PMI-FF-PMI solar cells have led to the development of a new electron transport layer for organic solar cells, capable of significantly reducing the work function of common electrode materials. Thus, the new interlayer based on a mixture of the polymers PEIE and PFN-Br is suited to contact organic materials with high “lowest unoccupied molecular orbital (LUMO)” energy levels and can be used as an alternative to reactive low work function metal interlayers such as calcium.

Kurzfassung

Der steigende globale Energiebedarf, verursacht durch den technologischen Fortschritt und den drastischen Anstieg der Weltbevölkerung, gibt Anlass zur Entwicklung von erneuerbaren Energie-Technologien als Alternative zu den derzeit dominierenden fossilen Energieträgern. Spätestens zu dem Zeitpunkt, an dem diese begrenzt verfügbaren und nicht erneuerbaren Energiereserven aufgebraucht sind, sollte die Menschheit den Umstieg auf nachhaltige und erneuerbare Energiequellen abgeschlossen haben. Die Vielzahl an ökologisch problematischen Nebeneffekten, die die Verbrennung von fossilen Brennstoffen mit sich bringt, ist dabei noch nicht berücksichtigt. Umweltschädliche Verbrennungsnebenprodukte (Treibhausgase) gelten als Hauptgrund für den anthropogenen Klimawandel und legen nahe, dass der Umstieg auf erneuerbare Energieträger eher früher als später vollzogen werden sollte. Ein ratsamer Ansatz um den aktuellen und den zukünftigen Energiebedarf der Menschheit zu decken ist es, die größte Quelle an sauberer, unbegrenzter und erneuerbarer Energie in unserer (astronomisch betrachtet) unmittelbaren Umgebung zu nutzen – die Sonne. Photovoltaik nutzt die Energie der Sonne und konvertiert sie effizient und auf direktem Weg in elektrische Energie. Dadurch stellen Technologien, die auf dem photovoltaischen Prinzip beruhen, eine nachhaltige und attraktive Möglichkeit dar um die Sonnenenergie zu nutzen und den steigenden globalen Energiebedarf zu decken. Eine aufstrebende, neue Solarzellentechnologie, welche bereits beträchtliches Interesse der akademischen und industriellen Forschung geweckt hat, ist das Forschungsgebiet der organischen Solarzellen. Im Vergleich zu herkömmlichen anorganischen Solarzellen (z.B. Si, GaAs) besitzen organische Solarzellen einzigartige Vorteile wie zum Beispiel kostengünstige und skalierbare Lösungsprozessierbarkeit, variable Bandlücken, geringe Energierückgewinnungszeit und die Möglichkeit semi-transparente und/oder Solarzellen mit geringem Gewicht herzustellen.

Über zwei Jahrzehnte hinweg waren lösungsprozessierbare Fullerenederivate das dominierende Akzeptormaterial für organische Solarzellen. Diese Klasse an Akzeptoren zeichnet sich durch exzellente elektronische, jedoch aber nur moderate optische Eigenschaften aus, welche schlussendlich die maximal erreichbare Effizienz limitieren. Aktuelle Entwicklungen von

hocheffizienten Nicht-Fulleren-Akzeptoren haben es geschafft, die Dominanz der Fullerenbasierten Akzeptoren zu brechen. Die überlegenen optischen Eigenschaften dieser Materialien führten zu einer dramatischen Verbesserung der Effizienz von organischen Solarzellen und trugen maßgeblich zum aktuellen Aufschwung der organischen Solarzellenforschung bei. Ein weiterer vorteilhafter Aspekt dieser neuen Akzeptor Materialien ist die erhöhte synthetische Flexibilität, welche ein präzises Feintuning von den Materialeigenschaften von Donor und Akzeptor ermöglicht. Dadurch kann beispielsweise der Klemmenspannungsverlust von organischen Solarzellen reduziert werden, wodurch in naher Zukunft Effizienzen von über 20 % erreicht werden könnten. Die rapide Entwicklung von Nicht-Fulleren-Akzeptor-basierten Solarzellen in den letzten 5 Jahren hat dazu geführt, dass das grundlegende Verständnis dieser neuartigen Akzeptoren zurückblieb. Um das allgemeine Verständnis über die physikalischen Prozesse und Mechanismen dieser neuen Akzeptorklasse besser zu verstehen, wurde die Rekordmaterialkombination D18 und Y6 (Leistungsumwandlungseffizienz > 18 %) detailliert analysiert. Das Hauptaugenmerk der Untersuchung von D18:Y6 Solarzellen liegt auf der Analyse der Klemmenspannungsverlusten von hocheffizienten nicht-Fulleren-Akzeptorbasierten Solarzellen im Vergleich zu analogen Bauteilen, die auf auf klassischen Fulleren Akzeptoren (D18:$PC_{71}BM$) basieren.

Weiters wurden Solarzellen basierend auf neuartigen Perylen-Nicht-Fulleren-Akzeptoren charakterisiert und weiterentwickelt. Aufgrund verschiedener Screening Methoden wurde das Material PMI-FF-PMI basierend auf einer Perylenmonoimide Triadenstruktur (PMI-linker-PMI) als erfolgversprechender Anwärter für die Anwendung in organischen Solarzellen ausgewählt. Organische Solarzellen basierend auf dem hocheffizienten Donor Polymer D18 und dem neuartigen PMI-FF-PMI Akzeptor lieferten besonders hohe Klemmenspannungen über 1.41 V. Dies stellt einen Rekordwert für lösungsprozessierte organische Solarzellen dar. Mit einer optischen Bandlücke von 2.02 eV ist das D18:PMI-FF-PMI System außerdem interessant für den Einsatz in triple-junction Solarzellen. Durch den Vergleich mit state-of-the-art D18:Y6 Solarzellen konnte der Photostromgenerierung in D18:PMI-FF-PMI Bauteilen das größtes Optimierungspotential zugeordnet werden. Dadurch wurden wertvolle Erkenntnisse für das Design von neuen und verbesserten Nicht-Fulleren-Akzeptoren gewonnen, die auf dieser Klasse von Perylen-Akzeptoren beruhen.

Versuche zur Verbesserung der Performance von D18:PMI-FF-PMI Solarzellen haben zur Entwicklung einer neuen Elektrontransportschicht geführt, welche die Arbeitsfunktion von typischen Elektrodenmaterialien deutlich reduziert. Basierend auf einer Mischung aus den Polymeren PEIE und PFN-Br, macht es diese Zwischenschicht möglich organische Materialien mit hohem „lowest unoccupied molecular obital (LUMO)“ Energielevel zu kontaktieren. Damit stellt sie eine geeignete Alternative dar, um reaktive Metallzwischenschichten mit niedriger Arbeitsfunktion (z.B. Calcium) zu ersetzen.

Acknowledgments

First and foremost, I would like to express my very great appreciation to my supervisor Assoc. Prof. DI Dr. Markus Clark Scharber for offering me the possibility to complete my PhD in the interesting field of organic photovoltaics. Without his excellent guidance, encouragement, and support, this thesis would not have been possible. I am especially thankful for all the time we spent on the countless, insightful scientific, and non-scientific discussions over the last years. Additionally, I would like to thank the head of the LIOS institute o. Univ.-Prof. Mag. Dr. DDr. h.c. Niyazi Serdar Sariciftci for the opportunity to work in his well-equipped research facility, but more importantly for the opportunity to work as a part of a great team - the world-famous LIOS family. Moreover, special thanks go to my current and former office colleagues and friends, Felix Mayr, Katarina Gugujonovic, Dominik Wielend, Christoph Putz, and Hathaichanok Seelajaroen who made the last years really enjoyable and a truly memorable time. Whether we tinkered together on the PDS setup, we learned together the intricacies of OPV fabrication, or you were always there to discuss controversial experimental results, I would like to sincerely thank every one of you. Since the risk of omitting someone is too high, I would like to collectively thank all the members of the LIOS team: from the administrative office to the chemical and technical support, the mechanical workshop, the research colleagues, and students. Thank you for the exceptional working environment, for your willingness to help each other out, and for all the remarkable memories and experiences I have gathered in the last years. In addition, my gratitude extend beyond our institute walls, especially to our project partners from the TU Graz, the group of Prof. Gregor Trimmel. A special thanks for the constructive and successful collaboration goes to the synthesis experts Gregor Trimmel, Thomas Rath, Matiss Reinfelds, Stefan Weber, and Peter Fürk. Financial support by the Austrian "Climate and Energy Fund" within the program Energy Emission Austria (Project: ALTAFOS, FFG No. 865072) and by the Austrian Academy of Science under the Chemical Monthly Fellowship (MOCHEM) is gratefully acknowledged. Last but definitely not least I would like to acknowledge my family and friends for their unconditional support and encouragement during my whole life. Especially I would like to thank my partner Hannah for always having my back and for her ability to always cheer me up no matter what the circumstances are. Without all of you, it would not have been possible to complete this important step in my academic career.

Aim of the Thesis

Over the last decades photovoltaic devices, consisting of conjugated polymers (donors) and solution-processable fullerene derivatives (acceptors), emerged as the leading organic photovoltaics (OPV) technology and reached power conversion efficiencies (PCEs) of 10-12 %. Regardless, fullerene acceptors exhibit several disadvantageous characteristics such as an expensive synthesis and unfavorable optical properties. In polymer-fullerene solar cells, several different recombination processes are active resulting in moderate open-circuit voltages (V_{OC}) and an overall limited power conversion efficiency. The recent development of highly efficient non-fullerene acceptors (NFAs) seems to overcome these limitations and marks the beginning of a new OPV era with solar cell efficiencies surpassing 18 %. As a consequence of the rapid efficiency improvements of NFA-based solar cells, the fundamental understanding of these new acceptors is lagging behind. For the long-term commercial success of OPV, it is crucial to identify the relevant mechanisms and properties of current high-performance NFA-based solar cells. A better understanding could lead to new design strategies for future NFA materials with further improved photovoltaic properties and preferably less synthetic complexity.

In this thesis a combination of state-of-the-art commercially available OPV materials, as well as novel perylene-based non-fullerene acceptors are investigated and characterized in detail to get new insights into the working mechanism of this new material class. To accomplish this task, different optical, electronic, electrochemical, and photovoltaic characterization techniques are used.

The objectives of this PhD thesis can be summarized as follows:

- To advance the current understanding of the success of novel high-performance NFAs
  - Comparing the performance of state-of-the-art fullerene and non-fullerene-based solar cells.
  - Identifying the key properties and important mechanisms responsible for the superior performance of NFA-based organic solar cells (OSCs).

  - Investigating and comparing the open-circuit voltage losses of fullerene- and NFA-based solar cells as the open-circuit voltage loss is thought to be one of the main factors limiting OSC device performance.
  - Using the acquired knowledge to formulate design strategies for the development of new NFA materials

- Development and characterization of novel NFAs
  - Identifying the most promising synthesized acceptor materials for OPV applications using electrochemical, optical, and photovoltaic screening methods.
  - Device characterization and optimization of organic solar cells based on most promising non-fullerene acceptor materials.
  - Explore the basic properties and working principles of newly synthesized and commercially available, high-performance NFA materials.
  - Use a commercially available, high-performance NFA-based solar cell as a benchmark system to quantify the performance of newly developed acceptor materials.
  - Formulate optimization strategies for the synthesized NFA materials to optimize their performance.

Structure of the Thesis

Chapter 1 gives a theoretical background on solar energy conversion and the development, the working principle, and current research challenges of OPV. In addition to promoting the use of photovoltaics, Chapter 1 outlines the different approaches to solar energy conversion and their fundamental limits. Moreover, the historical development, unique advantages, and current shortcomings of OPV technology are briefly discussed.

Chapter 2 contains a detailed summary of the main characterization techniques, evaluation methods, and materials used in this thesis. The used experimental setups and their working principles are summarized and categorized into electrochemical, optical, and photovoltaic characterization techniques. A special focus is put on the methods used to analyze the charge transfer state energy/optical bandgap and the open-circuit voltage loss of organic solar cells. These methods have been used as the main tools to investigate the voltage losses of the organic solar cells studied in this thesis. Moreover, Chapter 2 gives a summary of the used (commercially available) materials and details about the device fabrication.

Chapter 3 presents the results from our recent publication "Understanding the low voltage losses in high-performance non-fullerene acceptor-based organic solar cells". To gain further inside into the working mechanisms of the novel, high-performance non-fullerene acceptors, the -at the time- record-breaking D/A blend D18:Y6 was thoroughly investigated in terms of optical properties, photovoltaic performance, and observed voltage losses. The NFA-based solar cells were compared to their fullerene counterparts (D18:$PC_{71}BM$) in order to identify the mechanisms for the enhanced performance of this new class of highly-efficient NFAs. Based on the experimental results, material optimization strategies to further reduce the open-circuit voltage losses of OPV devices are discussed.

Chapter 4 gives an overview of the studied non-fullerene acceptors synthesized by the group of Prof. Trimmel (Institute for Chemistry and Technology of Materials, TU Graz, Austria). The novel perylene-based acceptors are categorized into a group of perylenediimide (PDI) acceptors and three groups of perylenemonoimide (PMI) acceptors. The chapter describes the performed screening process of these materials and rationalizes the choice of the most promising acceptor candidate (*i.e.* PMI-FF-PMI) for OPV applications.

Chapter 5 covers the results from our recent publication "Wide-bandgap organic solar cells with a novel perylene-based non-fullerene acceptor enabling open-circuit voltages beyond 1.4 V". The in Chapter 4 selected novel wide-bandgap acceptor PMI-FF-PMI was used in combination with the high-performance donor D18 to fabricate efficient organic bulk heterojunction solar cells with an extraordinary high open-circuit voltage beyond 1.4 V. To evaluate the performance of the newly-developed acceptor, the photovoltaic parameters, optical properties, and voltage losses of D18:PMI-FF-PMI solar cells are compared to state-of-the-art organic solar cells based on fullerene ($PC_{71}BM$) and non-fullerene (Y6) acceptors.

Chapter 6 includes the optimization of the D18:PMI-FF-PMI device geometry. The calcium ETL of devices in the "standard" architecture was replaced with a new solution-processed ETL blend using the polymers PEIE and PFN-Br. The new interlayer significantly improved the photovoltaic external quantum efficiency of D18:PMI-FF-PMI devices by 10 % resulting in an increase in PCE from around 5 % to slightly above 6 %.

Chapter 7 aims to summarize the main findings of this thesis and tries to give an outlook on remaining research challenges and potential future studies based on the presented OPV materials.

Remark: *It should be noted that for the sake of uniformity, throughout this thesis, the numbering of figures, tables, and equations of Chapters 3 and 5 deviates from the numbering in the published manuscripts. Moreover, the sections introduction and methods of the two referenced papers are slightly modified to avoid repeating information given in the in-depth introductory and experimental chapters of this thesis.*

Publications

List of papers included in this thesis

- J. Hofinger, C. Putz, F. Mayr, K. Gugujonovic, D. Wielend, and M. C. Scharber, Understanding the low voltage losses in high-performance non-fullerene acceptor-based organic solar cells, ***Mater. Adv.***, 2021, **2**, 4291–4302 DOI: 10.1039/d1ma00293g.

  Contribution report

  J. Hofinger is the main author and was responsible for the device fabrication and optimization. Moreover, J. Hofinger has conducted all the presented electrochemical, optical, and photovoltaic measurements. Electrochemical measurements and analysis were done under the supervision of D. Wielend. External quantum efficiency measurements were done together with M. C. Scharber. J. Hofinger performed the data analysis and wrote the first draft of the manuscript. All the co-authors helped to finalize the manuscript. During the entire process J. Hofinger was supervised and guided by M. C. Scharber.

- J. Hofinger, S. Weber, F. Mayr, A. Jodlbauer, M. Reinfelds, T. Rath, G. Trimmel, M. C. Scharber, Wide-bandgap organic solar cells with a novel perylene-based non-fullerene acceptor enabling open-circuit voltages beyond 1.4 V, ***J. Mater. Chem. A***, 2022, **10**, 2888-2906 DOI: 10.1039/d1ta09752k

  Contribution report

  J. Hofinger is the main author and was responsible for the device fabrication and optimization. The synthesis of the perylene-acceptor and chemical analysis was done by S. Weber and M. Reinfelds, supervised by G. Trimmel. J. Hofinger has conducted all the presented electrochemical, optical, photovoltaic measurements, with the exception of:

  - *Light-dependent J-V and saturation current measurements were done by T. Rath.*
  - *Fabrication and characterization of solar cells in the "inverted" structure were done by A. Jodlbauer.*

- *Time correlated single photon counting measurements were done by F. Mayr*
- *PLQY measurements were done by M. C. Scharber*

J. Hofinger was responsible for the data analysis and wrote the first draft of the manuscript. All the co-authors helped to finalize the manuscript. During the entire process J. Hofinger was supervised and guided by T. Rath, G. Trimmel, and M. C. Scharber.

Publications not included in this thesis

- S. Weber, J. Hofinger, T. Rath, M. Reinfelds, D. Pfeifer, S. M. Borisov, P. Fürk, H. Amenitsch, M. C. Scharber, and G. Trimmel, Comparison of fluorene, silafluorene, and carbazole as linkers in perylene monoimide based non-fullerene acceptors, ***Mater. Adv.***, 2020, **1**, 2095–2106 DOI: 10.1039/d0ma00470g.
- F. Mayr, E. Leeb, K. Matura, D. Ziss, O. Brüggemann, N. S. Sariciftci, J. Hofinger, Y. Salinas, M. C. Scharber, Stable and highly fluorescent perovskite nanoparticles prepared via water-assisted precipitation, *in preparation*
- B. Schweda, M. Reinfelds, J. Hofinger, G. Bäumel, T. Rath, P. Kaschnitz, R. C. Fischer, M. Flock, H. Amenitsch, M. C. Scharber, and G. Trimmel, Phenylene-Bridged Perylene Monoimides as Acceptors for Organic Solar Cells – A Study on the Structure-Properties Relationship, ***Chem. Eur. J.***, 2022, DOI: 10.1002/chem.202200276
- P. Fürk, J. Hofinger, M. Reinfelds, T. Rath, H. Amenitsch, M. C. Scharber, and G. Trimmel, Glycol bearing perylene monoimide based non-fullerene acceptors with increased dielectric permittivity, *in preparation*

Contents

Abstract ii

Acknowledgments vi

Aim of the Thesis vii

Structure of the Thesis ix

Publications xi

Contents xii

1 Introduction 1
- 1.1 Energy Crisis & Climate Change . . . 1
- 1.2 Solar Energy Conversion . . . 4
  - 1.2.1 Photothermal Energy Conversion . . . 4
  - 1.2.2 Photovoltaic Energy Conversion . . . 8
- 1.3 Development of (Organic) Photovoltaics . . . 19
- 1.4 Potential Analysis of OPV . . . 22
- 1.5 OPV Working Principle . . . 25
- 1.6 Optimization of OPV . . . 30
  - 1.6.1 Charge Transfer Loss . . . 30
  - 1.6.2 Non-radiative Voltage Loss . . . 32
- 1.7 Device Structure . . . 34

2 Experimental Section 36
- 2.1 Characterization Techniques . . . 36
  - 2.1.1 Electrochemistry . . . 36
  - 2.1.2 Optical Spectroscopy . . . 40
  - 2.1.3 Photovoltaic Characterization . . . 51
- 2.2 Methods . . . 56
  - 2.2.1 Determination of the Optical Bandgap & CT-State Energy . . . 56
  - 2.2.2 Voltage Loss Analysis . . . 59
- 2.3 Materials & Device Fabrication . . . 65
  - 2.3.1 Electrodes . . . 66
  - 2.3.2 Hole & Electron Transport Layers . . . 66

2.3.3 Absorber Materials . . . 68
2.3.4 List of Used Materials . . . 71

3 Understanding the low voltage losses in high-performance non-fullerene acceptor-based organic solar cells 72
3.1 Abstract . . . 73
3.2 Introduction . . . 73
3.3 Experimental Note . . . 74
3.4 Results & Discussion . . . 76
3.4.1 CT-state & Voltage Loss Analysis . . . 81
3.4.2 Efficiency Limit & Optimization Potential . . . 85
3.5 Summary & Conclusion . . . 87
3.6 Acknowledgments . . . 88
3.7 Supplementary Information . . . 88

4 Material Screening 94
4.1 ALTAFOS Materials . . . 94
4.1.1 PDI Acceptors . . . 96
4.1.2 PMI-linker-PMI Acceptors . . . 96
4.1.3 Screening Process . . . 97

5 Wide-bandgap organic solar cells with a novel perylene-based non-fullerene acceptor enabling open-circuit voltages beyond 1.4 V. 102
5.1 Abstract . . . 103
5.2 Introduction . . . 103
5.3 Experimental Notes . . . 107
5.4 Results . . . 108
5.5 Discussion . . . 118
5.5.1 Charge Generation Efficiency in D18:PMI-FF-PMI Blends . . . 118
5.5.2 CT State & Voltage Loss Analysis . . . 122
5.5.3 ELQY *vs.* Non-Radiative Voltage Loss . . . 124
5.5.4 Application in Triple Junction Devices & Optimization Potential . . . 126
5.6 Summary & Conclusion . . . 127
5.7 Acknowledgments . . . 129
5.8 Supplementary Information . . . 129

6 Optimization of D18:PMI-FF-PMI 145
6.1 Introduction . . . 145
6.2 Experimental Notes . . . 147
6.3 Results & Discussion . . . 148
6.3.1 Optimization of D18:PMI-FF-PMI Solar Cells . . . 148
6.3.2 Universality of the PEIE:PFN-Br Interlayer Approach . . . 150
6.4 Summary & Conclusion . . . 152

7 Summary & Outlook 153

Bibliography 155

Nomenclature 173

Chapter 1

Introduction

1.1 Energy Crisis & Climate Change

In 2019 the global primary energy consumption was quantified as approximately 18 TWy (1 TWy = 8760 TWh) according to the BP statistical review of world energy.[1] A recent report by the U.S. Energy Information Administration predicts that the world's energy demand is expected to almost double by the year 2050.[2] Among other issues, this dramatic increase in energy demand is known as the Terawatt (TW) Challenge, first formulated by Nobel Prize laureate Richard E. Smalley more than 15 years ago.[3] Smalley highlighted the importance to develop a largely renewable-energy landscape until 2050, which is able to supply 30-60 TW average power.[4] Fast forward to the present day, the world's energy mix is still dominated by fossil-based energy sources as shown in Figure 1.1. Fossil energy in the form of coal, oil, and natural gas accounted for more than 80 % of the world's total energy supply in 2018. The strong dependence on fossil energy reserves gives rise to several problems which can be considered as some of the biggest challenges of our civilization in the current century. Fossil fuels are a non-renewable, finite resource and as a consequence, sooner or later this energy source will be depleted. At the latest by this time, mankind should have developed an alternative technology to secure future energy needs. Taking into account the adverse environmental effects accompanied with the combustion of fossil fuels, such as greenhouse gasses or air pollutants strongly suggest changing to an abundant and sustainable energy source sooner rather than later. Combustion byproducts such as carbon dioxide (CO_2) enhance the greenhouse effect in our atmosphere, leading to an increase in the average global temperature. According to the United Nations Framework Convention on Climate Change (UNFCCC) and the Paris climate agreement, it is critical to limit the global average temperature rise to 1.5-2 °C with respect to pre-industrial levels to prevent dangerous human interference with the climate system.[5] Despite the Paris climate agreement, the amount of CO_2 in our atmosphere is steadily increasing and humans around the globe are starting to

experience dramatic effects of the change in temperatures such as rising of sea levels, polar ice cap melting, severe draughts, wildfires, storms, and floods. In addition to the discussed environmental effects, fossil fuel-based transport and coal-fired power plants are one of the major sources of ambient air pollution. According to the World Health Organization (WHO), 9 out of 10 people breathe air that exceeds WHO guidelines causing about seven million premature deaths every year.[6]

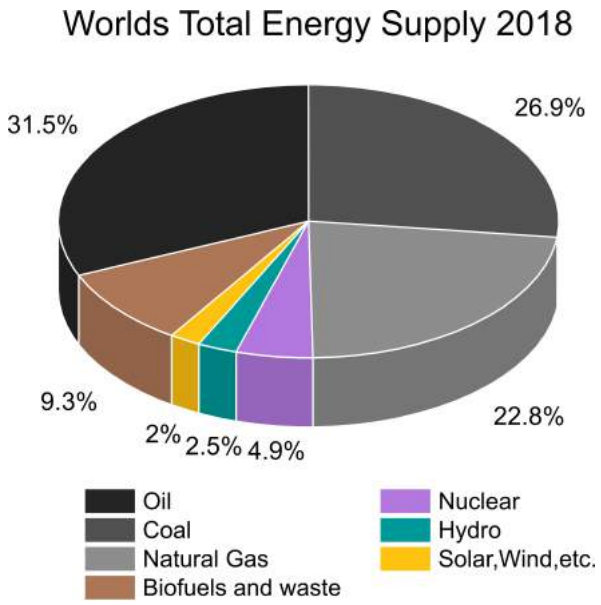

Figure 1.1: Worlds total energy supply by source in 2018. Data taken from International Energy Agency (IEA) [7].

The world's rising energy demand, the limited availability of fossil-based energy sources and their adverse environmental and health effects strongly suggest changing to an abundant and sustainable energy source. In quest of an appropriate source of energy in our solar system, the obvious choice is the sun with its 5778 K hot surface, emitting energy at a rate of 3.8×10^{14} TW in form of electromagnetic radiation. Only a small fraction of this radiation is intercepted by the earth, which regardless, is constantly delivering an enormous power of 120000 TW to earth. In fact, almost all commonly exploited energy sources shown in Figure 1.2, except nuclear and geothermal energy, are indirectly solar-powered. Fossil fuels like crude oil, coal, and natural gas are originating from anaerobe decayed plants, algae, and microorganisms that lived millions of years ago and gained their energy from sunlight via photosynthesis. The potential energy of water, which has been evaporated from the oceans by the power of the sun and has rained down in regions with high altitudes, can be used by hydroelectric dams to create electricity. Wind energy is a result of the sun heating the surface of the earth unevenly, resulting in local pressure differences in the atmosphere. Those pressure differences give rise to the diffusion of air molecules, whose kinetic energy can be transformed into electricity using a wind turbine. In all discussed cases, solar energy is transferred into electricity via irreversible, multi-step processes. Taking wind energy as an example, in order to extract

electric energy from a wind turbine, the energy of the solar radiation is first transformed into heat via absorption processes on the earth's surface, followed by the conversion into kinetic energy of air molecules due to diffusion processes, which finally can be converted into electricity. The indirect usage of solar energy results in energy dissipation upon every real-world, non-ideal energy conversion process. The accumulated entropic losses associated with every irreversible conversion process highlight the big advantage of a technology allowing the direct conversion of solar radiation into useful electrical energy. By considering only sunlight falling on land masses and assuming 65 % losses by atmosphere and clouds, Perez and Perez derived an estimation for the usable energy potential of solar energy of 23000 TWy/y.[8] As graphically illustrated in Figure 1.2, direct utilization of solar energy unambiguously dwarfs the technical potentials (*i.e.* achievable energy generation given system performance, topographic, environmental, and land-use constraints) of all the other renewable energy sources. In fact, even the global energy reserves of all fossil energy sources combined, only account for a small fraction of the energy provided by the sun every year. Thus, it is fair to say that solar radiation offers almost unlimited potential for energy harvesting and is the only renewable energy source that can provide more than enough energy to meet the world's long-term energy demand. Developing strategies and technologies to utilize the energy from solar radiation is of paramount importance to secure future energy requirements and at the same time eliminate the adverse environmental effects accompanied by fossil fuel energy sources.

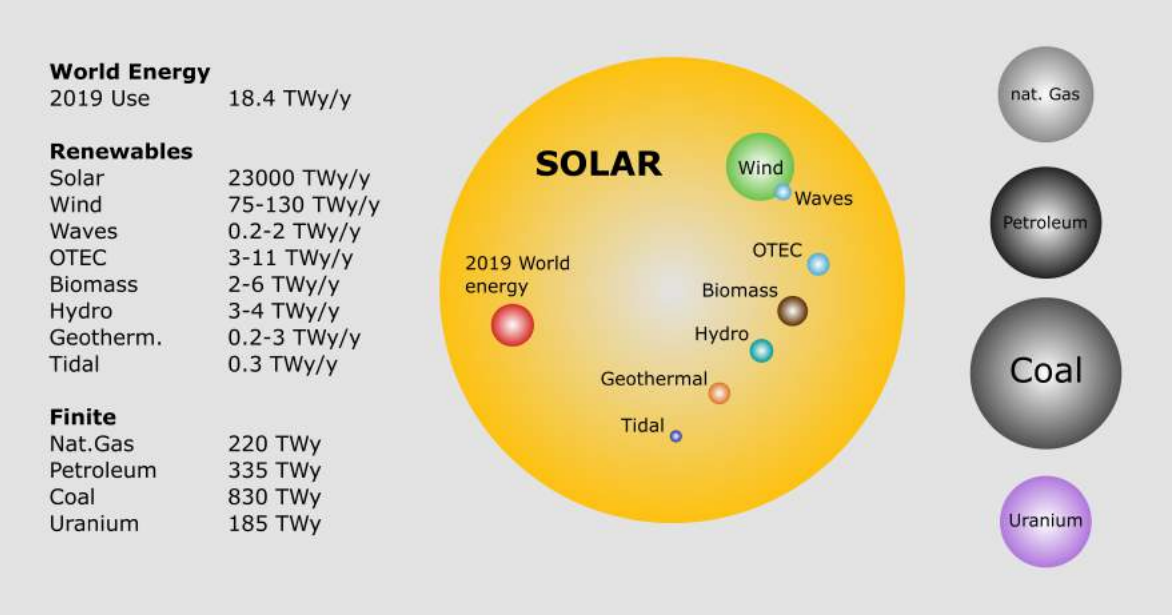

Figure 1.2: Graphical illustration of finite planetary energy reserves in TWy and the estimated technical potential of renewable energy sources in TWy/y. The volume of each sphere represents the respective amount of energy recoverable from depicted finite and renewable sources. OTEC=Ocean Thermal Energy Conversion. This figure is redrawn from Reference [8]. The data from Reference [1] was used to estimate the global primary energy consumption in 2019.

1.2 Solar Energy Conversion

As discussed in Section 1.1, the efficient conversion of the sheer unlimited energy provided by the sun is crucial to cover future energy needs. The following sections discuss the fundamental limits of solar energy conversion to quantify the room for improvement of any solar energy converting technology.

1.2.1 Photothermal Energy Conversion

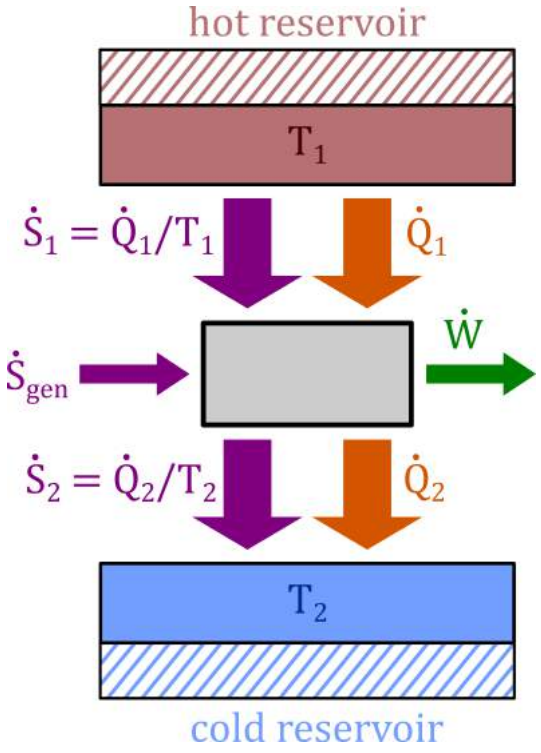

Figure 1.3: Schematic illustration of heat and entropy fluxes between a hot and cold reservoir exploited by a Carnot engine.

Let us first assume an idealized situation of a hot and a cold reservoir of infinite capacity with temperatures T_1 and T_2. This temperature difference can be exploited to extract work from heat flow using a thermodynamic engine as depicted in Figure 1.3. The input and output energy fluxes (transferred heat) are depicted in orange and the respective entropy fluxes are depicted in purple. $\dot{S}_{\text{gen}}$ takes into account that additional entropy might be generated in the energy conversion process. $\dot{W}$ denotes the amount of energy converted into useful work (green arrow).

The efficiency η of the conversion process is given by the ratio of the generated work $\dot{W}$ and the input energy flux $\dot{Q}_1$.

$$\eta = \frac{\dot{W}}{\dot{Q}_1} \tag{1.1}$$

Balancing the energy fluxes (1st law of thermodynamics) and considering Equation 1.1 leads to Equations 1.2 and 1.3,respectively.

$$\dot{Q}_1 = \dot{Q}_2 + \dot{W} \tag{1.2}$$

$$\eta = \frac{\dot{Q}_1 - \dot{Q}_2}{\dot{Q}_1} = 1 - \frac{\dot{Q}_2}{\dot{Q}_1} \tag{1.3}$$

Balancing the entropy fluxes (2nd law of thermodynamics) allows to express the term $\dot{Q}_2/\dot{Q}_1$ as

$$\begin{aligned} \dot{S}_1 + \dot{S}_{\text{gen}} &= \dot{S}_2 \\ \frac{\dot{Q}_1}{T_1} + \dot{S}_{\text{gen}} &= \frac{\dot{Q}_2}{T_2} \\ \frac{T_2}{T_1} + \frac{T_2 \dot{S}_{\text{gen}}}{\dot{Q}_1} &= \frac{\dot{Q}_2}{\dot{Q}_1} \end{aligned} \tag{1.4}$$

Inserting Equation 1.4 in Equation 1.3 allows to determine the ultimate efficiency for the energy conversion process.

$$\begin{aligned} \eta &= 1 - \frac{T_2}{T_1} - \frac{T_2 \dot{S}_{\text{gen}}}{\dot{Q}_1} \\ \eta_{\text{C}} &= 1 - \frac{T_2}{T_1} \end{aligned} \tag{1.5}$$

It can be easily seen that the efficiency is maximized if the conversion is reversible and additional entropy generating processes are avoided ($\dot{S}_{\text{gen}} = 0$). In this case, the efficiency is exclusively determined by the temperatures of reservoirs 1 and 2. This famous formula is known as the Carnot efficiency and represents the ultimate efficiency limit for an engine operating between a hot and a cold reservoir. Consequently, the ultimate efficiency limit for solar energy conversion is 94.8 %, assuming T_1 equals the temperature of the sun (T_1 = 5778 K) and T_2 equals room temperature on earth (T_2 = 300 K).

The Carnot limit implicitly assumes a perfect thermal contact between the two heat reservoirs and the Carnot engine. Obviously, the enormous distance between sun and earth and the lack of a heat transporting medium (in the Carnot limit with no thermal resistance) contradict the idealized assumptions of the Carnot model. The so-called Blackbody (BB) limit represents a more realistic model, where the converter is described as a blackbody absorber coupled to a Carnot engine, as depicted in Figure 1.4. Moreover, the sun is more accurately described as a

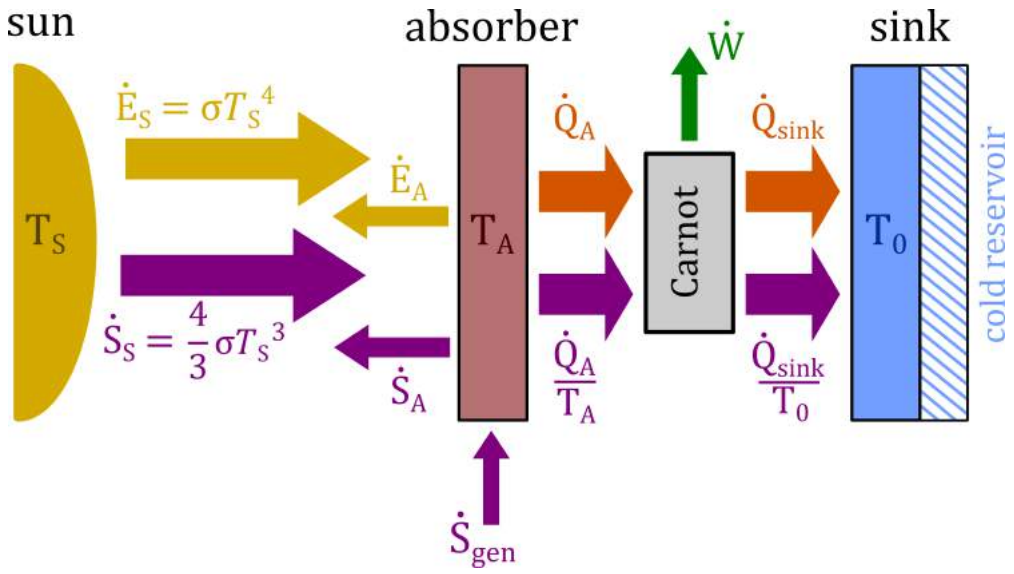

Figure 1.4: Schematic illustration of the photothermal energy conversion process. A blackbody absorber is used to convert the solar radiation into heat. A Carnot engine is used to convert the heat flux between absorber and sink into useful work $\dot{W}$.

blackbody, which emits energy in form of radiation. The relation between the radiated energy flux of a blackbody and its temperature is given by the Stefan Boltzmann law in Equation 1.6 with the Stefan-Boltzmann constant $\sigma = 5.67 \times 10^{-8}\,\mathrm{W\,m^{-2}\,K^{-4}}$.

$$\dot{E} = \sigma T^4, \tag{1.6}$$

while the associated entropy flux is given by

$$\dot{S} = \frac{4}{3}\sigma T^3 \tag{1.7}$$

In Figure 1.4, the subscripts S and A denote the energy and entropy from the sun and absorber, respectively. The energy conversion in this model can be divided into two steps:

First, the absorber is exposed to the energy flux $\dot{E}_S$ and entropy flux $\dot{S}_S$ from the sun. As a blackbody with a finite temperature T_A, the absorber itself emits corresponding energy and entropy fluxes $\dot{E}_A$ and $\dot{S}_A$. Second, if the absorber has a temperature $T_A > T_0$ we can use a Carnot engine to convert the heat flux between the absorber and the sink into entropy free work (e.g. electrical energy) with an efficiency according to Equation 1.5.

$$\dot{W} = \eta_C\,\dot{Q}_A \tag{1.8}$$

$\dot{Q}_A$ can be simply derived by balancing the absorbed and emitted energy fluxes.

$$\dot{Q}_A = \dot{E}_S - \dot{E}_A = \sigma\left(T_S^4 - T_A^4\right) \tag{1.9}$$

The overall conversion efficiency η can then be calculated by comparing the energy input from the sun $\dot{E}_S$ to the extracted work $\dot{W}$.

$$\begin{aligned}\eta &= \frac{\dot{W}}{\dot{E}_S} = \frac{\eta_C \dot{Q}_A}{\dot{E}_S} = \frac{\eta_C \sigma \left(T_S^4 - T_A^4\right)}{\sigma T_S^4} \\ &= \left(1 - \frac{T_A^4}{T_S^4}\right) \eta_C \\ &= \left(1 - \frac{T_A^4}{T_S^4}\right) \left(1 - \frac{T_0}{T_A}\right) \end{aligned} \tag{1.10}$$

The temperature T_A of the absorber can be in the range between T_S and T_0. At T_A=T_S the absorbed and emitted energy and entropy fluxes are balanced, *i.e.* the sun and the absorber are in thermal equilibrium ($\dot{Q}_A$=0). If heat energy in form of $\dot{Q}_A$ is extracted from the absorber, the temperature T_A is reduced below T_S. In the other extreme case at T_A=T_0, there is a maximum heat transfer but the work is extracted with a Carnot efficiency of zero. Analyzing Equation 1.10 shows that the maximum efficiency can be obtained for an absorber temperature T_A of 2.478 K resulting in an efficiency value of 84.9 % (assuming T_S=5778 K and T_0=300 K). Figure 1.5 illustrates the maximum efficiency curves in the Carnot and Blackbody limit, respectively.

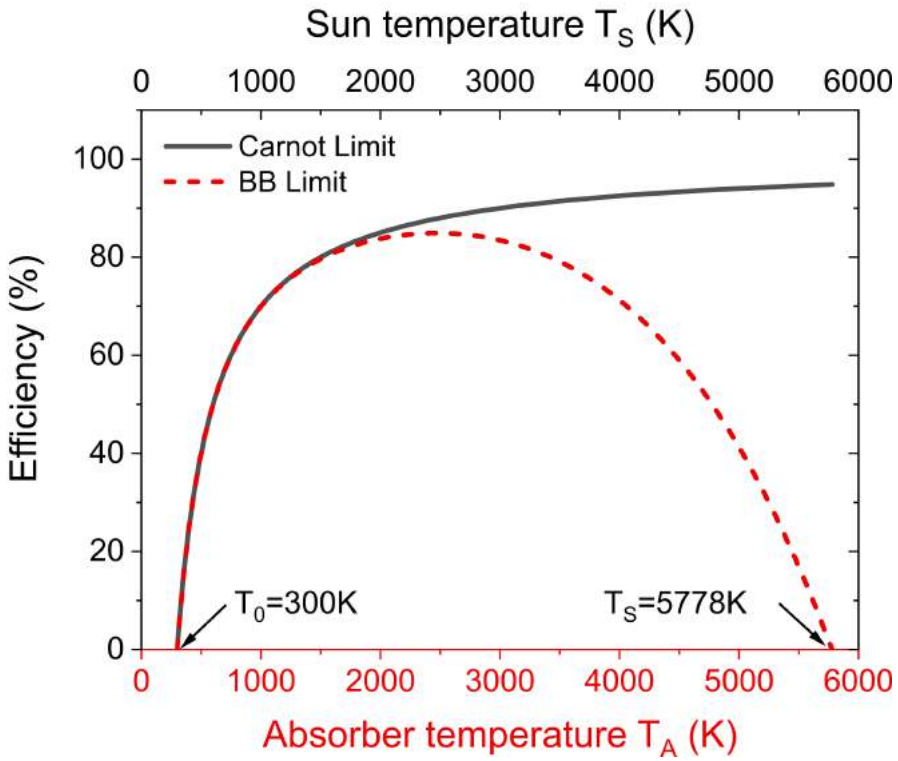

Figure 1.5: Maximum efficiency curves in the Carnot limit with T_0=300 K and varying T_S and in the Blackbody limit with T_0=300 K, T_S=5778 K, and varying T_A.

It should be noted that by using the radiative energy flux $\dot{E}_S = \sigma T_S^4$ as energy input, we implicitly have assumed a maximum concentration of the sunlight. Without concentration, only a fraction of the solar emission reaches the absorber, which can be described by a geometrical factor f

$$f = \frac{\Omega_{sun}}{\pi} = \frac{1}{C}, \tag{1.11}$$

where Ω_{sun} is the solid angle subtended by the sun seen from the earth. Using the suns radius and the average distance between the sun and the earth Ω_{sun} can be derived as $\sim 6.8 \times 10^{-5}$ sr. The reciprocal value of f can be interpreted as the concentration factor C. Without concentration, the efficiency of photothermal energy conversion calculated with Equation 1.10 is significantly reduced to values below 15 %.

1.2.2 Photovoltaic Energy Conversion

In addition to blackbody absorbers, another class of materials is widely and successfully used to harness the energy provided by solar radiation. These materials are characterized by a forbidden gap between their energy bands and are called semiconductors. In contrast to photothermal converters, the photovoltaic effect in semiconductors allows efficient conversion of radiative solar energy into entropy-free, chemical energy even at ambient temperatures.

Radiative to Chemical Energy Conversion

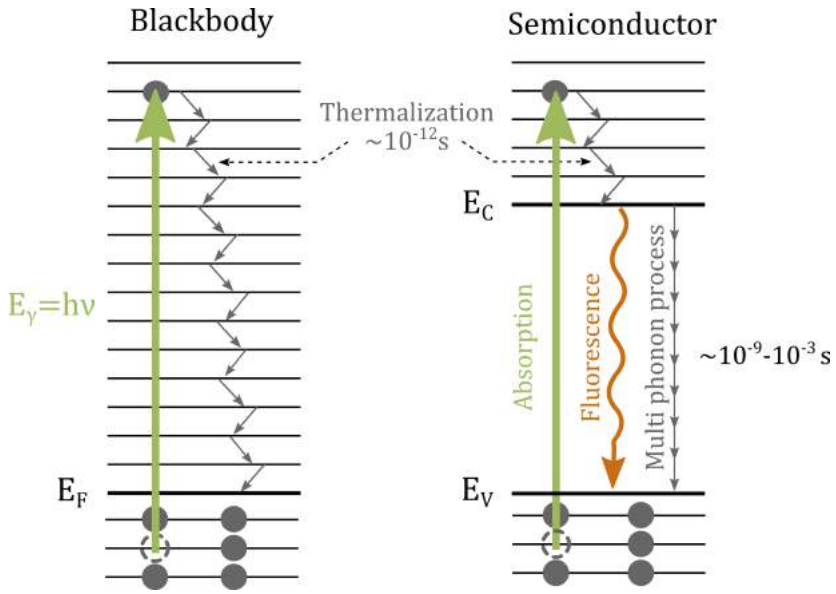

Figure 1.6: Illustration of the photoexcitation and deactivation processes in blackbody absorbers and semiconductors.

A blackbody, as discussed in Section 1.2.1, is characterized by a continuous density of electron states, where electrons can be excited into higher energy states by the absorption of incoming photons. Regardless of the photon energy, the excited electrons can lose their energy within ps timescale due to rapid thermalization, as illustrated in Figure 1.6. In this process, the energy is dissipated incrementally to the lattice in the form of phonons leading to an increase in temperature. On the contrary, in semiconductors, only the photons with an energy larger than the bandgap are able to excite an electron from the valence into the conduction band. Photons with energy below the bandgap are either transmitted or reflected. The density of states in the conduction band is comparable to the one of a blackbody. Thus, excess photon energy larger than the bandgap is efficiently dissipated to the lattice and electrons will rapidly thermalize to the edge of the conduction band. Due to the lack of electron states in the bandgap, the energy from an electron located at the edge of the conduction band has to be released in a single step in order to return to a state in the valence band (*i.e.* recombination of the e-h pair). The energy can be released via a multi phonon process, where the energy equivalent to E_g is distributed to multiple phonons each carrying a fraction of the energy, or via the emission of a single photon with an energy $h\nu = E_g$. Both processes (intra-band transitions) are significantly slower than the thermalization process (inter-band transition). Hence, the lifetime of electrons in the conduction band and holes in the valence band is in the range of 10^{-9} – 10^{-3} s. Only these relatively long lifetimes open up the possibility to efficiently extract the photogenerated charge carriers and enable the conversion of chemical energy (stored in the e-h pairs) into electrical energy as it will be further discussed in Section 1.2.2.

However, first, it is necessary to discuss the physics behind the conversion process of radiation energy into the chemical energy stored in e-h pairs. This conversion process can be illustrated by considering the following "chemical reaction" occurring inside an illuminated semiconductor.

$$\gamma \rightleftharpoons \mathrm{e} + \mathrm{h} \tag{1.12}$$

The reaction describes the absorption / emission of a photon γ and the creation / recombination of an e-h pair. A semiconductor in the dark and with the temperature T_C is considered in thermal and chemical equilibrium with the incoming blackbody radiation from the environment with temperature T_0 if T_C=T_0 and μ_γ=μ_{eh}=0. At thermochemical equilibrium, the intrinsic electron (n_i) and hole (p_i) distributions of a semiconductor are given by the product of the density of electron states D_e and the Fermi distribution function f_e, as shown in Equations 1.13 and 1.14. E_C and E_V represent the energies at the edge of the conduction and valence band, as depicted in Figure 1.6. The density of states and the Fermi distribution for electrons are presented in Equations 1.15 and 1.16, with $m^*_{e/p}$ as the respective effective mass of the electron or hole, h as the Planck constant, E_e as electron energy, E_F as the Fermi energy,

and k_B as the Boltzmann constant. For $E_F < E_C - 3k_BT$, the "+1" term in the denominator of $f_e(E_e)$ can be neglected and allows deriving Equations 1.17 and 1.18.

$$n_i = \int_{E_C}^{\infty} D_e(E_e)\, f_e(E_e)\, dE_e \tag{1.13}$$

$$p_i = \int_{-\infty}^{E_V} D_e(E_e) \left[1 - f_e(E_e)\right] dE_e \tag{1.14}$$

$$D_e(E_e) = 4\pi \left(\frac{2m_e^*}{h^2}\right)^{3/2} (E_e - E_C)^{1/2} \tag{1.15}$$

$$f_e(E_e) = \frac{1}{\exp\left(\frac{E_e - E_F}{k_BT}\right) + 1} \tag{1.16}$$

$$n_i = N_C \exp\left(-\frac{E_C - E_F}{k_BT}\right) \quad with \quad N_C = 2\left(\frac{2\pi\, m_e^*\, k_BT}{h^2}\right)^{3/2} \tag{1.17}$$

$$p_i = N_V \exp\left(-\frac{E_F - E_V}{k_BT}\right) \quad with \quad N_V = 2\left(\frac{2\pi\, m_p^*\, k_BT}{h^2}\right)^{3/2} \tag{1.18}$$

$$n_i p_i = N_C N_V \exp\left(-\frac{E_g}{k_BT}\right) \tag{1.19}$$

N_C and N_V are the effective densities of states of the conduction and valence bands describing the number of electron states per unit volume.

Upon illumination, additional e-h pairs are created and the densities of electrons and holes will differ from their equilibrium (*i.e.* intrinsic) values. Equation 1.17 shows that an increase of the electron density $n > n_i$ requires a decrease of the E_C - E_F term in the exponent. Thus, the Fermi level is expected to increase. Analogously, the increased hole density $p > p_i$ requires the Fermi level to decrease (see Equation 1.18). These contrary requirements can only be fulfilled by a splitting of the Fermi levels in an electron and a hole quasi-Fermi levels E_F^n and E_F^p, giving rise to a chemical potential μ_{eh}. Considering the quasi-Fermi level splitting in an illuminated semiconductor the density of electrons n in the conduction band and density of holes p in the valence band can be calculated using modified versions of Equations 1.17 and 1.18, where E_F is replaced with E_F^n and E_F^p:

$$n = N_C \exp\left(-\frac{E_C - E_F^n}{k_BT}\right) \tag{1.20}$$

$$p = N_V \exp\left(-\frac{E_F^p - E_V}{k_BT}\right) \tag{1.21}$$

The above relationship can be used to derive the quasi-Fermi levels E_F^n and E_F^p as shown in Equations 1.22 and 1.23, which in the next step allows the calculation of the chemical potential μ_{eh} in an illuminated semiconductor.

$$E_F^n = E_C - k_B T \ln\left(\frac{N_C}{n}\right) \tag{1.22}$$

$$E_F^p = E_V + k_B T \ln\left(\frac{N_V}{p}\right) \tag{1.23}$$

$$\mu_{eh} = E_F^n - E_F^p = E_g - k_B T \ln\left(\frac{N_C N_V}{np}\right) \tag{1.24}$$

Thus, in an illuminated semiconductor the radiative energy is internally converted into chemical energy. Moreover, the chemical potential of the e-h pairs is free of entropy and can theoretically be converted into electrical energy without loss.

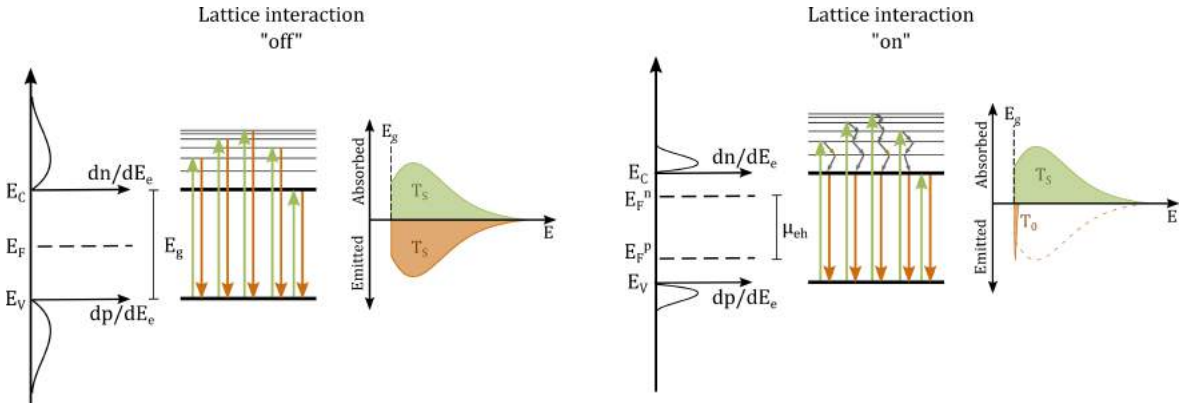

Figure 1.7: Graphical illustration of the thought experiment by Würfel.[9] Left: Situation before the charge carriers interact with the lattice. Absorbed and emitted spectrum are identical Right: Situation when the charge carriers interact with the lattice. The semiconductor is emitting light at ambient temperature T_0 according to the generalized Planck equation.

A thought experiment by Würfel allows estimating the efficiency of this conversion process by considering the generation and thermalization of e-h pairs step by step.[9] A schematic illustration of the thought experiment is shown in Figure 1.7. Under maximum concentration the total photon flux emitted from the sun with energies larger than E_g will be absorbed in the semiconductor. As a first step, the interaction of photogenerated charge carriers and lattice is assumed to be "switched off". This would prevent the thermalization process of charge carriers above E_g and conserve their initial energy. In other words, the energy distribution of the electron-hole pairs is identical to the energy distribution of the absorbed photons. As the temperature of the electron-hole pairs is defined by their energy distribution, they are in thermal ($T_{eh} = T_S$) and chemical equilibrium ($\mu_\gamma = \mu_{eh} = 0$) with the incoming solar radiation.

As a consequence of $\mu_{eh}(T_S) = 0$ the right side of Equation 1.24 has to be zero as well. Under these conditions Equation 1.24 can be written as:

$$\frac{E_g}{k_B T_S} = \ln\left(\frac{N_C N_V}{np}\right) \tag{1.25}$$

In a second step, the interaction of lattice and charge carriers is "turned on". Electrons will rapidly cool down to the lattice temperature T_0 resulting in the creation of entropy in the form of phonons. According to Equation 1.24 the chemical potential $\mu_{eh}(T_0)$ at lattice temperature T_0 is given by:

$$\mu_{eh}(T_0) = E_F^n - E_F^p = E_g - k_B T_0 \ln\left(\frac{N_C N_V}{np}\right) \tag{1.26}$$

It should be noted that due to the thermalization, *i.e.* the respective change in the energy distribution of electron-hole pairs, the thermal and chemical equilibrium is lost ($T_0 \neq T_S, \mu_{eh}(T_0) > 0 = \mu_\gamma$). However, the concentration of electrons and holes inside of the semiconductor remains constant and the logarithm term in Equation 1.26 can be expressed with Equation 1.25.

$$\mu_{eh}(T_0) = E_g - k_B T_0 \left(\frac{E_g}{k_B T_S}\right) = E_g \left(1 - \frac{T_0}{T_S}\right) \tag{1.27}$$

$$\eta_{h\nu\to\mu}(\nu) = \frac{\mu_{eh}(T_0)}{h\nu} \tag{1.28}$$

Equation 1.27 describes the chemical energy per electron-hole pair produced by the cooling process. Comparing the chemical energy to the energy of the incoming solar radiation allows calculating the conversion efficiency from radiation energy to chemical energy $\eta_{h\nu\to\mu}(\nu)$. If the semiconductor is illuminated with monochromatic radiation with the energy $h\nu = E_g$, Equation 1.28 reduces to the Carnot efficiency. Thus, under these conditions, the semiconductor represents an ideal converter for the transformation of radiation energy into chemical energy. On the other hand, the energy difference $h\nu$ - E_g for radiation with $h\nu > E_g$ is lost due to thermalization and reduces the average conversion efficiency for radiation with a broad energy spectrum (*i.e.* solar radiation).

If only radiative recombination is allowed, the number of absorbed and emitted photons in the semiconductor is identical because every absorbed photon creates an electron-hole pair and every recombination process creates a photon. As discussed above the emitted spectrum is different from the absorbed spectrum due to thermalization losses and thus less energy is emitted than absorbed. However, the emission of high-energy photons with a nonzero chemical potential (*i.e.* luminescence) in a semiconductor reduces the entropy generation compared to a blackbody absorber at the same temperature. In fact, this is the reason why

high-efficiency values can be obtained for semiconductor-based converters (e.g. solar cells) at ambient temperatures, which is beneficial for many applications and can be considered as one of the main advantages of photovoltaic over photothermal conversion technologies.

Chemical to Electrical Energy

In the previous section, we have seen that semiconductors can convert radiative energy into chemical energy. This stored chemical energy can be used to initiate further chemical reactions as in the photosynthesis process in plants. In a photovoltaic device, an additional step is required to transform chemical energy into electrical energy, which can then be extracted in an outer circuit to perform electrical work. In other words, we want to extract an electron-hole pair current J_{eh}, where each electron-hole pair carries the chemical energy μ_{eh}. In a typical (inorganic) pn-junction solar cell the photogenerated electron-hole pairs are not stable due to their weak coulombic attraction (high relative permittivity ϵ_{r}). Thus, at room temperature, the exciton is separated into an electron and a hole, which can be considered as quasi-free charge carriers. Ideally the p- and n-type sides of the semiconductor have metal electrodes that form an ohmic contact to the valence and conduction band, respectively. Such devices are commonly known as diodes. To avoid recombination at the electrodes, the contacts should be selective, preventing the holes from reaching the anode and electrons from reaching the cathode. Additionally, a driving force is needed to extract the free electrons and holes from the device. Electrons and holes are charged particles. Thus either chemical ($\nabla\mu_{\mathrm{eh}}$) or electrical potential gradients ($\nabla\Phi$) can act as driving forces and give rise to diffusion and drift currents, respectively.

Applying a voltage V between the metal electrodes allows modifying the electrochemical potential of the electron-hole pairs η_{eh}.

$$\begin{aligned}\eta_{\mathrm{e}}(x) &= -e\phi(x) + \mu_{\mathrm{e}}(x) = E_{\mathrm{F}}^{n}(x)\\ \eta_{\mathrm{h}}(x) &= e\phi(x) + \mu_{\mathrm{h}}(x) = -E_{\mathrm{F}}^{p}(x)\\ \eta_{\mathrm{eh}}(x) &= \mu_{\mathrm{eh}}(x) = E_{\mathrm{F}}^{n}(x) - E_{\mathrm{F}}^{p}(x) = qV\end{aligned} \tag{1.29}$$

In Section 1.2.2, no current was extracted or injected from or into the device ($I_{\mathrm{eh}} = 0$). Illumination of the semiconductor led to a maximum value of η_{eh} at open-circuit conditions. As discussed, at open circuit conditions all the absorbed photons are being re-emitted and no

energy is extracted from the solar cell. Using Equations 1.20 and 1.21 allows to express the product of electron and hole densities as:

$$np = \overbrace{N_C N_V \exp\left(-\frac{E_C - E_V}{k_B T}\right)}^{n_i p_i} \exp\left(\overbrace{\frac{E_F^n - E_F^p}{k_B T}}^{qV}\right)$$

$$np = n_i p_i \exp\left(\frac{qV}{k_B T}\right) \tag{1.30}$$

$$\eta_{eh} = E_F^n - E_F^p = qV = k_B T \ln\left(\frac{np}{n_i p_i}\right) \tag{1.31}$$

As seen from Equation 1.30 the densities of photogenerated electrons and holes (np) are being reduced upon negative biasing due to the extraction of electron-hole pairs from the semiconductor. As a consequence, the electrochemical potential is reduced as well, as described by Equation 1.31. If at a certain negative bias all photogenerated charge carriers are extracted from the device, η_{eh} approaches zero as $np = n_i p_i$. This condition, where the voltage across the pn-junction is zero, is commonly referred to as short-circuit condition. Once again no energy is extracted from the solar cell as the electrochemical potential of the extracted charge carriers is zero. Thus, there exists a combination of electrochemical potential and the number of extracted charge carriers, which gives rise to a maximum of extracted power. Hence, this point is called maximum power point.

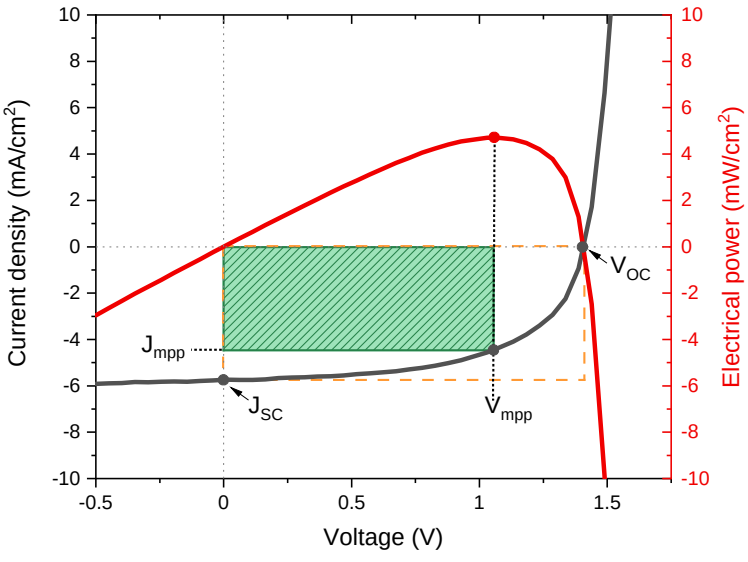

Figure 1.8: A typical J-V-curve of a solar cell under solar illumination (black, solid line). The electrical power is depicted in red. The maximum power point in combination with the open-circuit voltage and the short circuit current can be used to calculate the electrical fill factor (FF). The fill factor can be illustrated graphically as the areal ratio of the green shaded rectangular and the rectangular formed by V_{OC} times J_{SC} (depicted in orange).

The relationship between extracted charge carrier current and electrochemical potential per e-h pair is an important parameter for any photovoltaic device. Thus, the measurement of the so-called *J-V*-response of a solar cell represents a fundamental photovoltaic characterization technique. In a typical *J-V* measurement the solar cell is biased between a certain voltage range (V) and the extracted current density of charge carriers (J) is measured. As discussed above a *J-V*-curve is characterized by several characteristic points, highlighted in Figure 1.8. The open-circuit voltage (V_{OC}) represents the maximum chemical potential of e-h pairs under a fixed illumination, as no charge carriers are extracted from the solar cell and $J = 0\ \mathrm{mA\,cm^{-2}}$. Similarly, the short circuit current density J_{SC} represents the point where all photogenerated charge carriers are extracted from the device and the chemical potential is reduced to zero. At both points on the *J-V*-curve, no net power is generated as the electrical power is a product of current and voltage (red curve in Figure 1.8). The maximum power point can be derived by finding the maximum of the electrical power curve.

$$\frac{d\big(J(V) \times V\big)}{dV} = 0 \tag{1.32}$$

In addition, the electrical fill factor of a solar cell is defined using the following relationship:

$$\mathrm{FF} = \frac{V_{mpp}\, J_{mpp}}{V_{OC}\, J_{SC}} \tag{1.33}$$

The fill factor is often described as the "squareness" of the *J-V* curve. Graphically, the FF can be interpreted as the areal ratio of the green rectangular given by $V_{mpp} \times J_{mpp}$ to the dashed orange rectangular given by $V_{OC} \times J_{SC}$, as illustrated in Figure 1.8. The power conversion efficiency PCE of the solar cell is then calculated using

$$\mathrm{PCE} = \frac{P_{el}}{P_{sun}} = \frac{V_{mpp}\, J_{mpp}}{P_{sun}} = \frac{V_{OC}\, J_{SC}\, \mathrm{FF}}{P_{AM1.5G}}, \tag{1.34}$$

where the electrical power output P_{el} is divided by the input power of the solar radiation. By convention, the solar spectrum is approximated by the AM1.5 global spectrum normalized to a power of $P_{AM1.5G} = 100\ \mathrm{mW\,cm^{-2}}$.

Shockley-Queisser Limit

The fundamental efficiency limit of a solar cell operated at ambient temperature T_0 and without concentration was derived by Shockley and Queisser based on detailed balance arguments.[10] The SQ limit is based on the following assumptions:

- Concentration of one sun
- Sun and cell are blackbodies with T_S=6000 K and T_C=300 K

- Step function-like absorptance $A(E) = \begin{cases} 0 & \text{for } E < E_g \\ 1 & \text{for } E > E_g \end{cases}$
- Each absorbed photon generates exactly one e-h pair
- Infinite mobilities *i.e.* perfect charge collection
- The only recombination mechanism is radiative recombination

The paper by Shockley and Queisser uses the fact that in thermal equilibrium and in the dark, the generation rate of e-h pairs is governed by the absorption of ambient blackbody radiation with a temperature of 300 K. In the described equilibrium state the generation of e-h pairs has to be balanced with the rate of radiative recombination. The absorbed and emitted photon fluxes $\Phi_{\gamma,\text{abs}}$ and $\Phi_{\gamma,\text{emit}}$ can be expressed using the generalized Planck equation (*cf.* Equation 1.35) and the absorptance $A(E)$.

$$\Phi_\gamma(E, T, \mu_{\text{eh}}, \Omega) = \int_0^\infty \frac{2\Omega}{h^3c^2} \frac{E^2}{\exp\left(\frac{E-\mu_{\text{eh}}}{k_B T}\right) - 1} dE \tag{1.35}$$

$$\Phi_{\gamma,\text{abs}}(E, T, \mu_{\text{eh}}, \Omega) = \int_0^\infty A(E) \, \frac{2\Omega}{h^3c^2} \frac{E^2}{\exp\left(\frac{E-\mu_{\text{eh}}}{k_B T}\right) - 1} dE \tag{1.36}$$

The steplike absorptance $A(E)$ can be mathematically described with the Heaviside function, which simply changes the integral boundaries of Equation 1.36 to $\int_{E_g}^\infty dE$. Using Kirchhoff's law of thermal radiation to establish a relationship between absorptivity and emissivity allows an analogous definition of $\Phi_{\gamma,\text{emit}}(E, T, \mu_{\text{eh}}, \Omega)$.

At thermal equilibrium between the solar cell and its surroundings, the net current flow in the dark can be calculated using Equation 1.37.

$$J_0(\mu_{\text{eh}}, E_g) = q\Big(\Phi_{\gamma,\text{abs}}(E_g, T_0, 0, \Omega_{\text{BB}}) - \Phi_{\gamma,\text{emit}}(E_g, T_0, \mu_{\text{eh}}, \Omega_{\text{BB}})\Big) \tag{1.37}$$

Typical semiconductors used for photovoltaic applications have bandgaps between 1-2 eV. For $E_g > 0.5\,\text{eV}$ the "-1 term" in the denominator of the Planck equation can be neglected. Using this so-called Boltzmann approximation, and setting $\mu_{\text{eh}} = E_F^n - E_F^p = qV$ allows to simplify Equation 1.37.

$$J_0(V, E_g) = q\left(\Phi_{\gamma,\text{abs}}(E_g, T_0, 0, \Omega_{\text{BB}}) - \Phi_{\gamma,\text{emit}}(E_g, T_0, 0, \Omega_{\text{BB}}) \exp\left(\frac{qV}{k_B T_0}\right)\right) \tag{1.38}$$

If the solar cell is in thermochemical equilibrium with its surroundings the net current flow $J_0(V, E_g)$ and the chemical potential μ_{eh} are both zero and Equation 1.38 leads to:

$$\Phi_{\gamma,abs}(E_g, T_0, 0, \Omega_{BB}) = \Phi_{\gamma,emit}(E_g, T_0, 0, \Omega_{BB}) \tag{1.39}$$

Inserting Equation 1.39 in 1.38 and replacing q with the elementary charge (q = -e), leads to the current $J_0(V, E_g)$ of a solar cell device in the dark and in thermal equilibrium with its surroundings.

$$J_0(V, E_g) = e\left(\Phi_{\gamma,abs}(E_g, T_0, 0, \Omega_{BB})\left(\exp\left(\frac{qV}{k_B T_0}\right) - 1\right)\right) \tag{1.40}$$

Under solar illumination the balance of photon fluxes in Equation 1.37 has to be extended, taking into account the absorbed photon flux emitted from the sun.

$$J(V, E_g) = q\left(\Phi_{\gamma,abs}(E_g, T_S, 0, \Omega_{sun}) + \Phi_{\gamma,abs}(E_g, T_0, 0, \Omega_{BB}) - \Phi_{\gamma,emit}(E_g, T_0, V, \Omega_{BB})\right) \tag{1.41}$$

Similarly to Equation 1.40 the total current of a solar cell under illumination is given by:

$$J(V, E_g) = e\left(\Phi_{\gamma,abs}(E_g, T_0, 0, \Omega_{BB})\left(\exp\left(\frac{qV}{k_B T_0}\right) - 1\right) - \Phi_{\gamma,abs}(E_g, T_S, 0, \Omega_{sun})\right) \tag{1.42}$$

It should be noted that the first term of Equation 1.42 resembles the Shockley-Diode Equation in the dark, characterized by an exponential dependence on the applied voltage across the diode. The second term is independent of the voltage and represents the photocurrent caused by the absorption of sunlight, which shifts the dark *J-V* curve downward in the 4th quadrant as depicted in Figure 1.8.

Shockley and Queisser derived their upper-efficiency limit under the assumptions that the 300 K blackbody radiation is originating from a hemisphere above a flat solar cell and that the solar cell emits back in the same solid angle (= perfectly reflecting back-electrodes) Ω_{BB} is equal to π. In addition, they treated the sun as a blackbody emitter with a temperature of 6000 K and $\Omega_{sun} = 6.8 \times 10^{-5}$ sr.

$$\begin{aligned} J(V, E_g) = {} & q\,\frac{2\Omega_{sun}}{h^3c^2}\int_{E_g}^{\infty}\frac{E^2}{\exp\left(\frac{E}{k_B T_S}\right) - 1}dE \\ & - q\,\frac{2\pi}{h^3c^2}\left[\exp\left(\frac{qV}{k_B T_0}\right) - 1\right]\int_{E_g}^{\infty}\frac{E^2}{\exp\left(\frac{E}{k_B T_0}\right) - 1}dE \end{aligned} \tag{1.43}$$

As described previously, the electrical energy extracted from the solar cell is given by $V \times J(V, E_g)$ and the power conversion efficiency can be calculated using:

$$\eta(E_g, V) = \frac{V \times J(V, E_g)}{P_{sun}} \quad with \quad P_{sun} = \frac{2\Omega_{sun}}{h^3 c^2} \int_0^\infty \frac{E^3}{\exp\left(\frac{E}{k_B T_S}\right) - 1} dE \tag{1.44}$$

The efficiency with respect to the bandgap of the semiconductor can be numerically evaluated and is plotted in Figure 1.9. Shockley and Queisser derived a maximum efficiency value of ~30 % for a bandgap of 1.3 eV.[10] Under maximum concentration ($\Omega_{sun} = \Omega_{BB} = \pi$) the efficiency limit increases to ~44 %.[11] For a solar cell on earth (considering atmospheric effects) the maximum efficiency can be derived by replacing the blackbody spectrum of the solar radiation with the conventionally chosen AM1.5G spectrum. Under these conditions, the red curve in Figure 1.9 exhibits two distinct maxima with an efficiency of 33.4 % and 33.6 % at optimal bandgap energies of 1.13 eV and 1.34 eV, respectively.

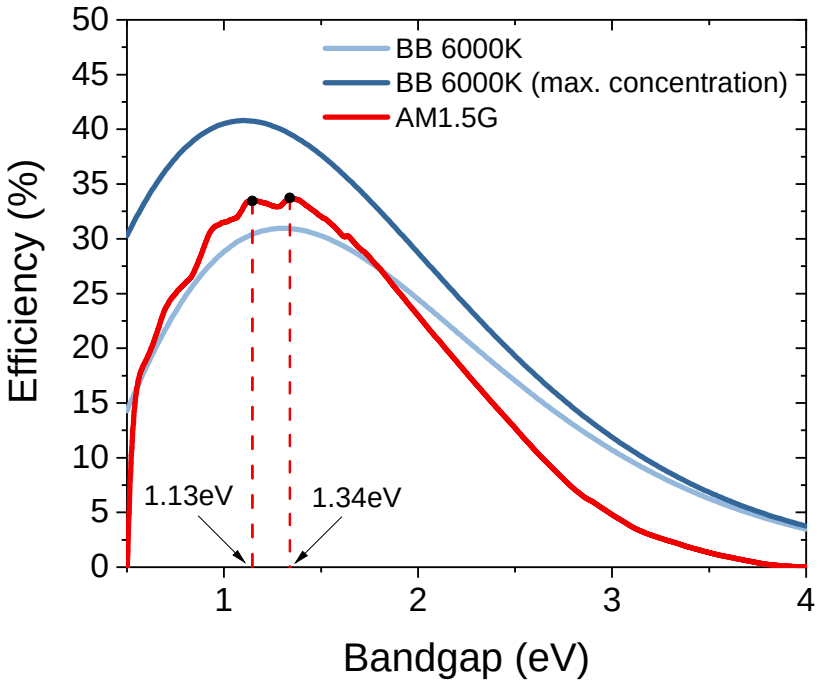

Figure 1.9: Maximum theoretical efficiency plots calculated using Equation 1.44. Using 6000 K blackbody radiation as illumination source leads to the dark and light blue efficiency curves for non-concentrated and fully concentrated conditions, respectively. The red curve is calculated using the AM1.5G spectrum.

1.3 Development of (Organic) Photovoltaics

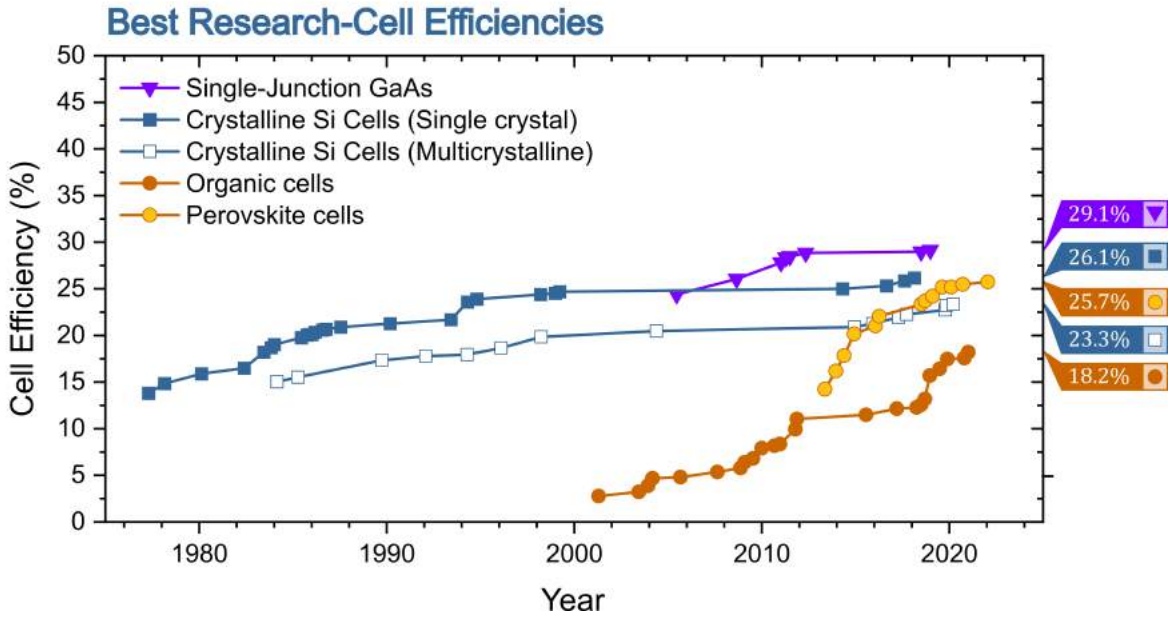

Figure 1.10: Historic research cell efficiency development of selected PV technologies. The data was taken from the NREL efficiency chart.[12]

Owing to their great potential for converting solar energy into electricity at ambient temperatures, the development of efficient semiconductor-based PV technologies has been a focal point of academic and industrial research since the discovery of the photovoltaic effect by Becquerel in 1839.[13] Consequently, the first photovoltaic device prototypes have already been demonstrated back in the late 1800s by Fritts.[14] An important milestone in PV history was the development of a silicon pn-junction solar cell at Bell Laboratories with an efficiency of around 4%.[15] This breakthrough can be considered as the advent of silicon-based photovoltaics. Over the next 6 decades, fueled by persistent research and development efforts and incentives during the oil crisis in the 1970s, silicon became the dominating material for photovoltaic technology. Nowadays, Si-wafer-based PV is dominating the solar market accounting for more than 95 % of the sold solar modules.[16]

The continuous research on Si-based solar cells has led to a steady increase in device performance and an impressive reduction in cost. According to a report by Haegel *et al.*, global average PV module selling prices have decreased by more than two orders of magnitude in a 40-year period and have already reached values below 0.25 US$ W^{-1}.[17] In many parts of the world PV already is or will soon become cost-competitive with conventional electricity generation technologies. This milestone is also reflected in the rapid increase of global installed solar photovoltaic capacity. By the end of 2018, the PV capacity exceeded 500 GW and is expected to reach TW-level capacity by 2022-23.[17]

The main disadvantage of silicon-based PV technology is the energy-intensive silicon purification process, necessary for the fabrication of high-quality wafers. Consequently, Si-based PV modules are characterized by moderate energy payback times of approximately 1-1.5 years.[18] Moreover, the energy mix in Si-wafer-producing countries being dominated by fossil fuels combined with the energy-intensive fabrication process harms the CO_2 balance of Si-solar cells and equates to non-negligible CO_2 emissions of 50 g/kWh.[16,19]

According to Mazzio *et al.*[20], further drawbacks of Si-based PV technologies are:

- Production limitation due to direct competition for materials with the microelectronics industry
- High material cost due to absorber layers with thicknesses around 200 µm.
- Vacuum processing required for production
- High installation costs ($\propto$ weight of solar cells >10 kg m^{-2})

Back in the early 2000s typical energy payback times of Si modules were approximately 4-5 years and the electricity produced by PV was roughly 10 times more expensive than energy from fossil fuels.[21] Thus, in addition to efforts in increasing the efficiencies and reducing the costs of Si-based PV, chemists, physicists, and material scientists had focused on the development of alternative, economically competitive PV technologies. One class of those emerging PV materials with the potential to drastically reduce the costs of PV-generated electricity were organic molecules. Following the discovery of (semi-)conducting polymers by Nobel Prize laureates Heeger, MacDiarmid, and Shirakawa in the 1970s (Nobel Prize in chemistry in 2000), these materials started to attract research attention and formed the foundation of the research field of organic electronics.

Organic semiconductors predominantly consist of hydrocarbon molecules or polymers, which are characterized by a conjugated backbone of alternating C-C single and double bonds. This distinct configuration results in an sp^2-hybridization of the 2*s* and two of the three 2*p* orbitals. The three, in-plane, $2sp^2$ hybrid orbitals of the carbon atom can form strong σ-bonds with hydrogen or neighboring carbons, which are responsible for the stability of the molecule. The remaining $2p_z$ orbitals are aligned perpendicular to the carbon-hydrogen plane and form a so-called π-conjugated system, which allows a certain degree of delocalization of the π electrons over the entire molecule, similar to electrons in the conduction or valence bands of crystalline inorganic semiconductors.

The first organic solar cells consisted of organic dye molecules sandwiched between two metal contacts forming a metal-organic junction. Power conversion efficiencies of these devices initially were as low as 10^{-5} % but could rapidly be increased to around 0.1 %.[22] The development of hetero-junction organic solar cells by Tang in 1986 can be considered as the next important milestone of OPV history.[23] These cells comprised of a bilayer of two organic

materials (donor: copper phthalocyanine, acceptor: perylene tetracarboxylic derivative) enabling efficiencies of around 1 %. In the following, the successful concept of organic D/A heterojunction solar cells attracted a lot of research attention and led to the development of first, co-evaporated and later, solution-processed bulk-heterojunction solar cells (BHJ). The interpenetrating network of donor and acceptor domains in BHJ solar cells led to a further increase in device performance due to an increased D/A surface area compared to bilayer solar cells.

In 1992, the first organic solar cells based on BHJ polymer:fullerene blends were demonstrated by laboratories in Santa Barbara and Osaka initiating the era of fullerene-based solar cells.[24–27] For the next 20 years fullerene-derivatives were the unequivocally dominating acceptor materials owing to their excellent electron-accepting and electron transport properties. As shown in Figure 1.10 the efficiencies of OSCs increased steadily until a plateau of approximately 10-12 % was reached.[28,29] The ultimately limited performance of fullerene-based solar cells can be mainly attributed to the weak optical absorption and the wide (indirect) bandgap of fullerenes. Material design efforts were mainly focused on optimizing the donor polymers due to their sheer endless synthetic possibilities to fine-tune material properties. Hence, the lack of synthetic flexibility of fullerene-based acceptors can be identified as an additional drawback.

To overcome those limitations, considerable efforts were expended in the 2000s to find alternative acceptor materials. In the early stages of these so-called non-fullerene acceptors (NFAs), the reported power conversion efficiencies were low (1-3 %) and could not compete with the established fullerene acceptors. However, learning from these pioneering works and from the success of fullerene acceptors led to the development of more “3D-like” NFA molecules, often characterized by a “twist” in the backbone to reduce the excessive stacking behavior of small molecules acceptors. This design strategy significantly improved NFA efficiencies up to around 10 %, on par with the best fullerene systems.[30–32] In 2015 Lin *et al*. reported the fused-ring (indacenodithieno[3,2-b]thiophene core) acceptor-donor-acceptor (A-D-A) molecule ITIC with strong near-infrared (NIR) absorption and high electron mobility.[33] The initially reported power conversion efficiency (PCE) of 6.8 % for ITIC-based solar cells was still inferior to its fullerene counterparts. However, optimization of the donor polymer soon enabled efficiencies beyond 11 %, marking the first time where non-fullerene acceptors outperformed the established fullerene acceptors.[34] Due to the continuous development of new non-fullerene acceptors with improved NIR-light-harvesting properties and readily-tunable electronic energy levels, the PCEs of NFA-based solar cells have increased substantially over the last five years up to efficiencies of 15-18 %.[35–42] At the beginning of 2020, Liu *et al*. reported a record-breaking PCE of 18.2 % (17.6 % certified) for the donor polymer D18 blended with the high-performance NFA Y6.[43]

1.4 Potential Analysis of OPV

This section provides an overview of the main advantages and limitations of OPV technology and motivates the consistent research interest at present day and in the future.

As discussed in Section 1.3, the main motivation to develop OPV as an alternative to Si-based PV, was the elaborate and energy-consuming fabrication process of high-quality Si wafers. As touched upon before, due to significant improvements in the cost-effectiveness of Si solar cells, the main claim of OPV, as a cheaper alternative for the production of green electricity, may no longer be valid. However, if the vast increase in OPV efficiencies over the last 3 years can be maintained and if the reported efficiency values of almost 20 % for solar cells in the lab can be transferred to commercially available products, a long-term establishment of OPV in the PV market is still within the realm of possibility. A recent estimation suggests that OSC costs could come down to $\sim$8 US\$ m^{-2} assuming a module efficiency of 15 %. This would make electric energy generated by OPV the cheapest source of electricity beating even silicon-based PV by a factor of 5 in terms of US\$ W^{-1}.[16]

The great advantage of OPV with regards to cost-effectiveness is their low temperature and solution processability. These properties enable the possibility of an efficient roll-to-roll manufacturing or large area printing of organic solar cells. These large-throughput techniques theoretically allow to fabricate OPV at a rate many times faster than conventional silicon solar cells. Organic semiconductors mainly consist of abundant materials like carbon, hydrogen, oxygen, or nitrogen. Moreover, they typically possess high absorption coefficients, which allow efficient light absorption even in absorber films with thicknesses as thin as 100 nm. Thus, for organic solar cells, the amount of absorber material is significantly less than in silicon devices, where absorber layers are in the range of 200 µm. This economical usage of absorber material is another aspect that adds up to the overall cost-effectiveness of OPV. It remains to be seen if the advancement of the OPV technology at some point in the future will challenge the established wafer-based PV technologies for rooftop and PV power station applications.

Due to the diverse and unique material properties of organic semiconductors, OPV does not necessarily have to replace the successful Si-based PV technology. Instead, the field of OPV should focus on complementing the Si technology in highly specialized applications where the use of opaque, rigid, heavy, bulky, and fragile Si-based solar cells is disadvantageous. In fact, organic materials are in general characterized by the exact opposite properties. The form and shape of solution-processed OSCs using inkjet or screen printing techniques are highly customizable. Due to the thin absorber layers, the physical properties and appearance are mainly determined by the employed substrate. The substrate can thus be tailored to fit the demands of highly specialized applications. Plastic foils (e.g. PET) can be used as substrates for applications where flexible solar cells are required e.g. wearable energy sources,

retraceable solar sails, power applications of Internet of Things (IoT), or soft robots. The usage of ultrathin plastic foils additionally allows the fabrication of extremely lightweight devices, which are beneficial for applications with weight restrictions e.g. in the electrification of the automotive or aviation industry or load-capacity-limited rooftop applications. It has been shown that ultrathin OPV devices (together with ultrathin perovskite devices) generate the highest power per weight ($\sim 10\,W/g$) of all common PV technologies.[44] Another appealing property of OPV is the possibility to fabricate semi-transparent devices. In contrast to most other PV technologies, the great tunability of the absorption properties of OPV materials allows to control the intensity and spectral distribution of absorbed and transmitted light. This makes them ideal candidates in the field of building-integrated PV, where they can be used to replace common tinted glass windows with so-called "solar windows". This technology could be relevant for skyscrapers, where the rooftop area is small and the typically glass-covered side walls represent a large unexploited area. Another promising application is the use of semitransparent OPV on top of greenhouses. The absorption of the organic solar cells could be optimized to allow high transmission of light in the spectral region which is utilized by plants, while other parts of the solar spectrum are absorbed and converted into electricity.

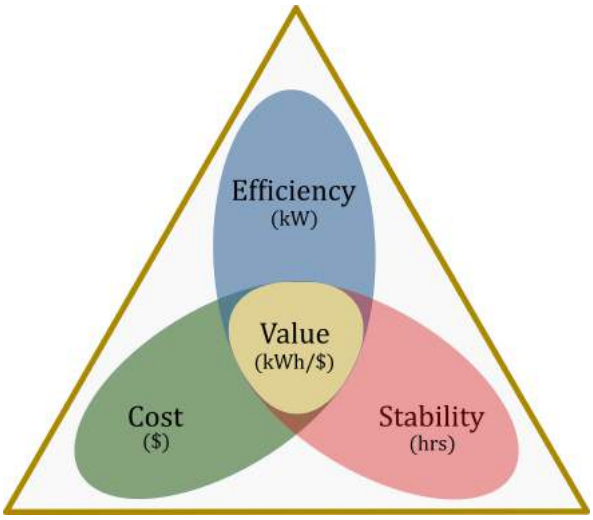

Figure 1.11: The "golden triangle" highlights the importance of efficiency, cost and stability of any PV technology

Despite their unique properties and the great variety of fields of application, the commercial availability of OPV remains limited. According to Meng *et al.*, the "golden triangle" comprising the efficiency, stability (or lifetime), and cost of a PV technology (see Figure 1.11) is commonly considered to gauge its technical feasibility for commercialization.[45] Considering all three aspects underlines the dominance of Si PV technology with greater module efficiencies (>20 %) and lifetimes (>25 years) compared to OPV. Moreover, the recent cost-reduction in c-Si production additionally narrows the margin of cost-benefit from OPV. Therefore it should be emphasized that the current extensive research effort in increasing the PCE can

only be the first step towards commercialization of OPV as from an economic point of view the device stability and cost are equally important. Recently Moser *et al.* have discussed the main challenges to the success of commercial OPV products, where they analyzed the current limitations of common high-performance D/A blends.[46] In addition to shifting the collective research focus from PCE to device stability, the authors emphasize the need to reduce the synthetic complexity of current highly efficient materials to increase the industrial scale-up potential of OPV.

Nevertheless, as with other thin-film technologies, OPV is suffering from the fact that efficiency is becoming an increasingly important driver to reduce the cost of large-area PV systems.[47] According to a recent study module efficiencies of around 20 %, lifetimes of more than 20 years, and lower production/installation costs than silicon are needed to compete with crystalline silicon in the mainstream "power" PV market (*i.e.* outdoor solar parks).[16] As stated previously the successful implementation of OPV in niche markets like building-integrated PV or consumer applications that profit from the flexibility, might reduce those requirements and pose the most likely scenario for OPV to be commercialized.

Consequently, in addition to efforts in increasing the stability and reducing the costs, further research aiming to optimize the power conversion efficiencies can be identified as one of the main challenges for the commercial success of OPV. Thus, in the following, the performance of a state-of-the-art OPV device is compared to other selected PV technologies on a laboratory cell level. Despite its limited use compared to silicon, GaAs was chosen as a benchmark representative of inorganic PV technologies due to its unrivaled performance. In addition, perovskite-based PV was chosen as a highly efficient representative of another class of emerging PV technologies. Organic solar cells based on the donor polymer D18 and acceptor Y6 were selected as a state-of-the-art representative of non-fullerene-based OPV. The optical bandgap, photovoltaic parameters, and open-circuit voltage losses of these solar cells are summarized in Table 1.1.

In order to readily compare the performance of solar cells with different bandgaps E_g, the photovoltaic parameters are additionally presented normalized to their parameters in the Shockley-Queisser limit. Normalization with respect to the SQ limit eliminates the influence of different spectral absorption profiles of the solar cells and represents a good figure of merit to quantify how a solar cell performs with respect to its ultimate efficiency limit. As presented in Table 1.1, the current record-breaking GaAs solar cell reaches 88 % of its maximum achievable power conversion efficiency due to impressive values around 95 % for all three photovoltaic parameters (V_{OC}, $J_{SC,}$ and FF). Similarly, consistent high values > 90 % are found for the 25.6 % efficient perovskite solar cell maintaining more than 80 % of its power conversion efficiency with respect to the SQ limit. In addition, Table 1.1 shows that the J_{SC} and FF values in % of SQ for D18:Y6 solar cells are not far off from those of their GaAs and perovskite counterparts. However, the typically low V_{OC} of organic solar cells (77 % of SQ

value) can be identified as the main factor limiting the overall device performance to around 50 % of its detailed balance limit. This trend can also be seen from the open-circuit voltage loss column in Table 1.1. The total voltage loss of a solar cell is defined as the difference between the bandgap (E_g) and the measured open-circuit voltage (V_{OC}) under AM1.5G illumination as given by $\Delta V_{OC}^{total} = E_g/q - V_{OC}$. The GaAs cell is characterized by a voltage loss increase of 18 % compared to its minimum value in the SQ limit. On the contrary, the experimentally observed voltage loss of the D18:Y6 blend is twice as large as compared to its minimum SQ value.

Table 1.1: Comparison of the bandgaps, photovoltaic parameters, and open-circuit voltage losses of selected organic, inorganic, and perovskite solar cells. J_{SC} and FF represent the short-circuit current density and the fill factor, respectively.

Material	E_g (eV)	V_{OC} (V)	J_{SC} (mA cm^{-2})	FF (%)	PCE (%)	ΔV_{OC}^{total} (V)	Source
GaAs	1.43	1.12	29.78	86.7	29.1	0.31	[48, 49]
% of SQ	-	96%	94%	97%	88%	118%	
Perovskite	1.53	1.19	26.35	81.7	25.6	0.34	[50]
% of SQ	-	94%	94%	90%	81%	127%	
D18:Y6	1.38	0.86	27.7	76.6	18.22	0.52	[51]
% of SQ	-	77%	82%	86%	54%	200%	

To conclude, the comparison with other highly efficient PV technologies reveals the room for improvements of current OPV devices. Especially, the large open-circuit voltage loss of organic solar cells has to be decreased in order to close the performance gap to perovskite or crystalline inorganic solar cells. In order to understand the origin of the enhanced voltage losses in OPV, we have to take a closer look at the working principle of organic solar cells.

1.5 OPV Working Principle

The basic requirement of any efficient photovoltaic device is the effective absorption of light. Clearly, any photon which does not get absorbed (e.g. reflected or transmitted) cannot be converted into electrical energy and represents a loss process. The capability of a material to absorb light can be described by the absorption coefficient α. Organic semiconductors exhibit high absorption coefficients around 10^5 cm^{-1}, which are significantly higher than the one of silicon (=indirect semiconductor). Thus, an organic thin-film as thin as 100 nm is typically capable of absorbing the majority of the incident sunlight above its optical bandgap.

The free charge generation in inorganic semiconductor-based pn-junctions is based on the formation of weakly bound excitons upon the absorption of photons with energies $E = h\nu > E_g$. At room temperature the low binding energies of these excitons can be easily overcome by thermal activation. Thus, under typical operation conditions, the weakly bound excitons essentially dissociate immediately into free charge carriers, which can then be collected at the anode and the cathode by employing chemical potential and/or electric potential gradients. In general, the binding energy of the excitions depend on their Coulomb attraction, which can be described by the potential $\phi(r)$ as shown in Equation 1.45.

$$\phi(r) = \frac{e^2}{4\pi\epsilon_r\epsilon_0 r} \tag{1.45}$$

Hereby, e represents the elementary charge, ϵ_r and ϵ_0 the relative and vacuum permittivity, and r the average distance between electron and hole. The reason for the weakly bound excitons in inorganic semiconductors are the typically high relative permittivity values (e.g. ϵ_r=12 in silicon) and the delocalized nature of the excited state (= increased electron-hole separation distance r). Organic materials on the other hand have much lower dielectric constants (ϵ_r∼2-4). As a consequence, the screening of the Coulomb attraction is significantly reduced and results in tightly bound electron-hole pairs. The binding energy of these so-called Frenkel or local excitons (LE) exceeds the available thermal energy at room temperature and prevents a barrierless dissociation into free charges. If the exciton cannot be separated into free charges within its lifetime, it will decay back into its ground state. The absorbed photon energy is thus either dissipated as heat (non-radiative recombination) or emitted radiatively.

The lack of free charge generation in organic semiconductors helps to understand the low efficiencies of the first homojunction (=metal-organic-metal) OSCs, discussed in the previous section. As first demonstrated by Tang, an efficient exciton dissociation in OPVs can be realized by the presence of a two-compound system, consisting of an electron-donating material with a large ionization potential and an electron-accepting material with a high electron affinity.[23] The ionization potential represents the energy necessary to remove an electron from the highest occupied molecular orbital (HOMO) to the vacuum. The electron affinity describes the ability of a material to accept an electron and is often approximated as the lowest unoccupied molecular orbital (LUMO) energy level of the molecule relative to vacuum. It is generally agreed that the first step of free charge generation involves an electron transfer from the donor to the acceptor or *vice versa* a hole transfer from the acceptor to the donor. As a first approximation, the energy offsets between HOMOs and LUMOs of donor and acceptor can be identified as the driving force for hole and electron transfer, respectively. Therefore, the precise control of the energy levels of donor and acceptor is of paramount importance for the success of OPV donor:acceptor systems.

Furthermore, the necessity for a charge transfer between donor and acceptor highlights the critical role of the D/A interface in organic solar cells. In OPV blends the diffusion length of the photogenerated excitons is typically limited to 5-20 nm.[52] Thus, only excitons generated in close proximity of a D/A interface have the chance to form a CT-state. Consequently, the D/A blend morphology in OSCs has to be carefully optimized to form small enough domains enabling efficient exciton diffusion to the interface. At the same time, as it will be discussed below, a morphology consisting of too small and disconnected donor or acceptor domains can have adverse effects on the electron and hole transport properties of the film. The large interfacial area and the (theoretical) possibility to fine-tune the morphology of the blend unveil the main advantages of the BHJ device structure compared to a bilayer device geometry.

As stated above, the formation of a CT-state is only the first step in the free charge generation process. Generally, the CT-state can be described as an electron-hole pair, where the hole is located on the donor and the electron is located on the acceptor. Therefore, the electron and hole remain in close proximity and form a coulombically tightly bound exciton according to Equation 1.45. It has been shown that the calculated binding energies of CT excitons are in the same range as the binding energy for excitons in the pure organic materials proposing equally limited dissociation efficiencies. These findings fundamentally contradict the experimentally observed high dissociation efficiencies reported for various D/A blends. This dilemma has been a matter of controversial discussion and is still not yet fully understood. A possible explanation is that the values derived from Equation 1.45 might severely overestimate the binding energies. Especially the macroscopic treatment of a uniform relative dielectric constant of the entire film might oversimplify the, assumably more complex, local dielectric environment at the D/A interface. Alternative explanation attempts involve the dissociation via so-called hot CT states or the role of disorder in the CT dissociation process. For a detailed overview of the CT dissociation theories (and the working principle of OSCs in general), the interested reader is referred to Chapter 3 of the excellent book of W.Tress.[53]

Alternatively, to the electron-hole pair picture, the CT state can be viewed as the excited state of the CT-complex, which is formed by the interaction of valence states (π,π^*orbitals) of adjacent donor and acceptor molecules. Accordingly, the CT state can be represented in an excited state diagram shown in Figure 1.12. The formation of the CT complex can be compared to the well-known formation of dimers or excimers of certain molecules. The interaction of two identical molecules can lead to additional optical transitions which can be experimentally observed in the absorption or fluorescence behavior. Thus, if allowed, radiative transitions between the ground and CT state should be experimentally observable. Indeed, highly sensitive absorption (e.g. highly sensitive EQE_{PV} or photothermal deflection spectroscopy measurements) or electroluminescence measurements have confirmed CT absorption/emission features for numerous D/A blends. The discussed dissociation process has to occur within the lifetime of the CT state. Otherwise, the CT state will decay into the

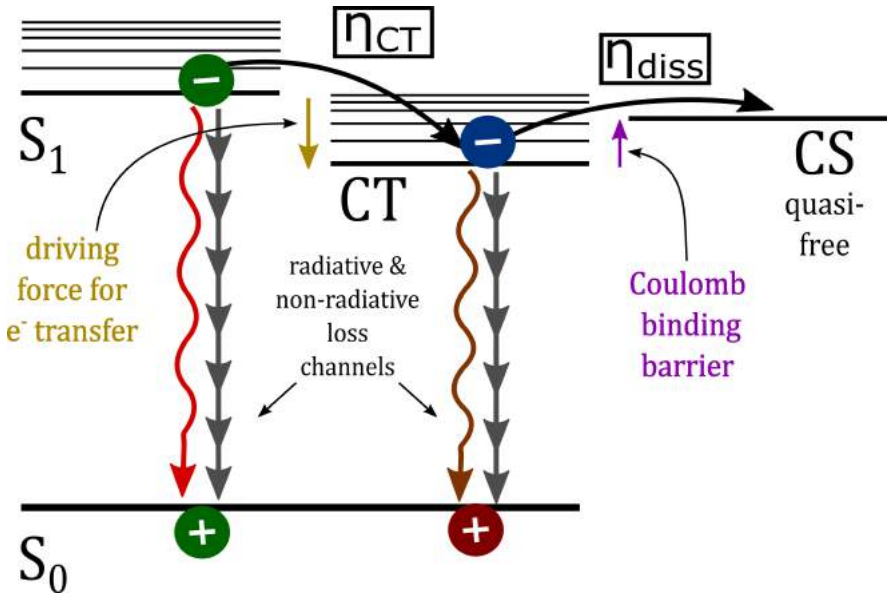

Figure 1.12: Illustration of the CT state in the excited state diagram.

ground state before free charges can be generated. This loss process, related to the strength of the CT exciton binding energy, is termed geminate recombination. Once the coulombic attraction of the exciton has been overcome, electron and hole can be described as free charges, which can be transported within the respective donor or acceptor domains driven by electric fields and/or diffusion gradients. Due to the interpenetrating domain morphology in BHJ solar cells, there is a chance that a free hole and a free electron cross paths before they can be extracted at the contacts. An encounter of two free, oppositely charged carriers can result in a re-formation of a bound CT exciton. If the exciton does not re-dissociate within its lifetime, the electron and the hole will recombine (*i.e.* the CT-state will decay back into the ground state) giving rise to an additional loss channel known as non-geminate recombination. Once the separated free charges reach the electrodes they can be extracted. A key criterion for contacts with a high charge extraction efficiency is to ensure a selective extraction of either electrons or holes. If the "wrong" charge carrier reaches the contact it will immediately recombine with charges in the contact material reducing the maximum extractable photocurrent.

To conclude, the energy conversion process in OPV from incident photons to extracted charge carriers is a sophisticated multistep process. Each of the discussed steps is summarized in the following:

- Absorption of photons (η_{abs})
- Exciton diffusion to D/A interface (η_{diff})
- CT state formation (η_{CT})
- CT dissociation into free charge carriers (η_{diss})

- Charge transport to contacts (η_{trans})
- Extraction at contacts (η_{extr})

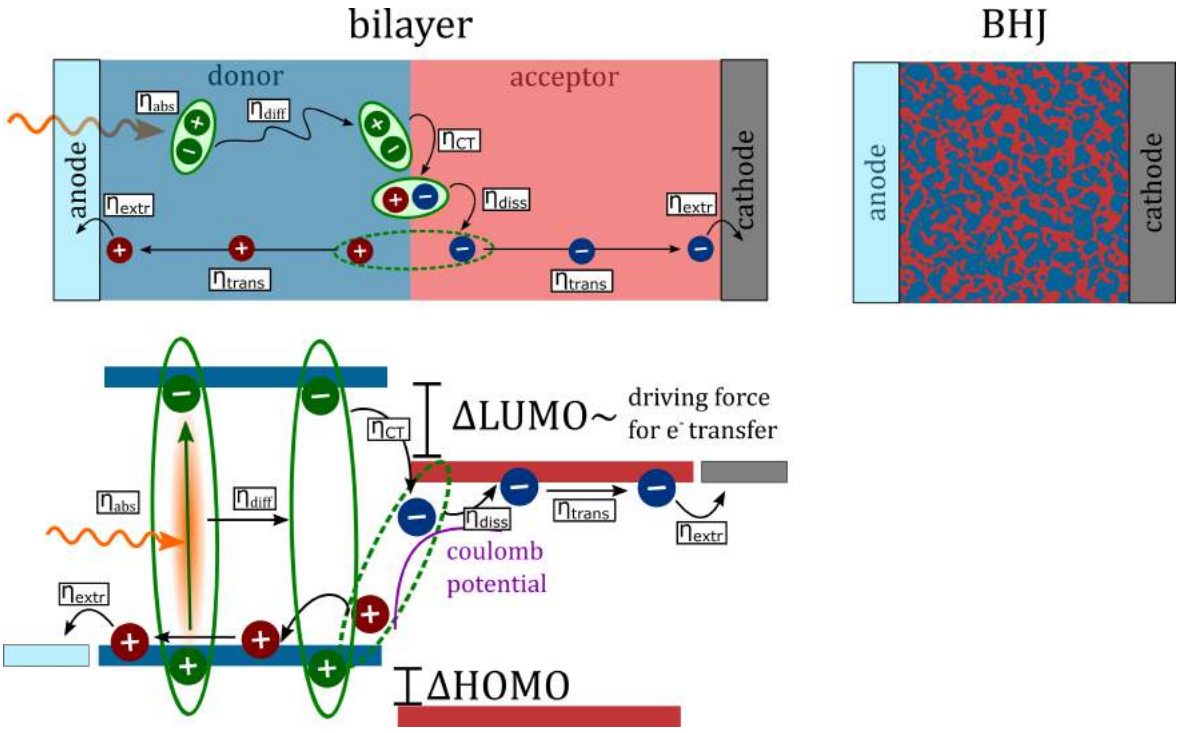

Figure 1.13: Schematic illustration of the working principle of organic solar cells.

As defined in the brackets and illustrated in Figure 1.13, each process can be assigned a certain efficiency η. Combining the efficiencies of all individual processes allows formulating an overall incident photon to current efficiency (IPCE) commonly (and throughout this thesis) referred to as photovoltaic external quantum efficiency (EQE_{PV}).

$$\text{EQE}_{\text{PV}} = \eta_{\text{abs}}\,\eta_{\text{diff}}\,\eta_{\text{CT}}\,\eta_{\text{diss}}\,\eta_{\text{trans}}\,\eta_{\text{extr}} \tag{1.46}$$

$$\text{EQE}_{\text{PV}} = \eta_{\text{abs}}\,\text{IQE}_{\text{PV}} \tag{1.47}$$

Thus, the EQE_{PV} can be considered as the ratio of incident photons to extracted charge carriers. As shown in Equation 1.47, the photovoltaic internal quantum efficiency (IQE_{PV}) can be defined by specifically considering the absorption efficiency η_{abs}. Consequently, the IQE_{PV} represents the ratio of absorbed photons to extracted charge carriers. The EQE_{PV} is typically measured at short circuit conditions. Hence, it allows to (1) quantify the maximum amount of charge carriers that can be extracted at I_{SC} conditions and (2) estimate the number of charge carriers that are lost in the conversion process. To maximize the PCE not only the number of extracted e-h pairs (*i.e.* the current J) is relevant. The chemical potential difference per extracted e-h pair (*i.e.* the voltage V) is equally important, as the electrical power is defined as $P_{\text{el}} = J \times V$.

As rationalized in Section 1.4, the severe reduction of the chemical potential compared to its maximum value in the SQ limit can be identified as the main factor limiting the power conversion efficiency of OPV devices. The reason for the enhanced open-circuit voltage losses in OSCs and strategies to significantly reduce them will be covered in the next section.

1.6 Optimization of OPV

1.6.1 Charge Transfer Loss

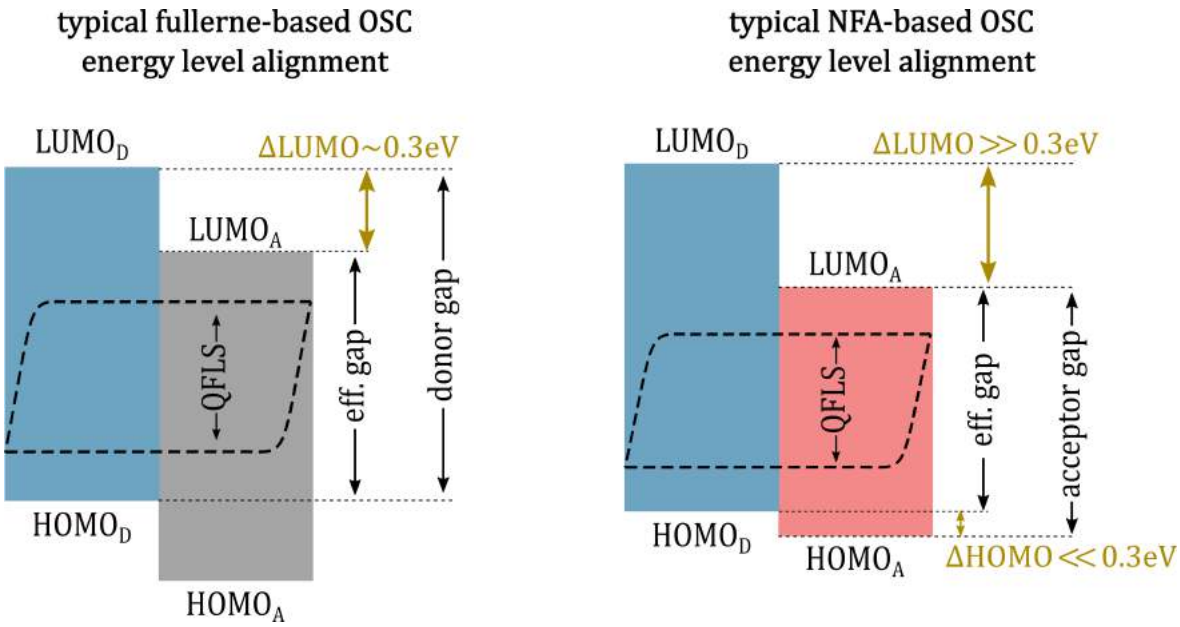

Figure 1.14: Schematic sketch of the energetic offsets in typical fullerene and high-performance non-fullerene acceptors.

As discussed in the previous section, the fundamental concept of organic heterojunction solar cells relies on efficient exciton splitting at the D/A interface. An energetic offset between the HOMOs or LUMOs of donor and acceptor were postulated as driving forces for an efficient charge transfer and dissociation process. At the same time, the combination of D/A molecules and the formation of a CT state reduces the effective bandgap of the D/A blend and consequently the maximum quasi-Fermi level splitting as shown in Figure 1.14. This inverse relationship leads to one of the main difficulties in optimizing OPV devices. On the one hand, large energy offsets are beneficial for efficient charge transfer and high photocurrents. On the other hand, they reduce the maximum quasi-Fermi level splitting of the device. A minimum energetic offset in the range of 0.3 eV has been empirically derived as a prerequisite for efficient dissociation of local excitons into free charges.[54] Hence, an associated voltage loss of ∼0.3 eV was commonly believed to be a fundamental requirement for efficient OSCs. Encouragingly, with the recent development of efficient small-bandgap NFAs, novel D/A

combinations have demonstrated the ability to efficiently generate free charge carriers even with small or negligible energetic offsets.[55–58] This new class of efficient donor:NFA systems allows to overcome the driving force *vs.* voltage loss dilemma and promises a new generation of organic solar cells with high EQE_{PV} (efficient charge generation) and high V_{OC} (low energetic offset losses). This superior behavior triggers the critical question of how free charge generation occurs in these systems. In general, the driving force for charge generation has remained a disputed topic in the literature. Researchers have suggested the need for energetic offsets,[59,60] hot charges[61,62], delocalization[63,64], low reorganization energies[65], electric fields,[66,67] energetic cascades and disorder,[68,69] and entropy,[70,71] as possible driving forces for charge generation. Recently, the concept of electrostatic potential (ESP) was introduced to explain the phenomenon of efficient charge generation despite low energetic offsets.[72] Wang *et al.* have proposed that intermolecular electrostatic fields, induced by different ESP values of donor and acceptor molecules facilitate charge separation in NFA-based OPVs.[73] Karuthedath *et al.* have shown that the strong quadrupole moment of NFA acceptors near the interface can cause band bending as shown in Figure 1.14.[74] This band bending destabilizes the interfacial CT state and allows for "barrierless" CT dissociation. On the other hand, the band bending reduces the energetic offset and thus lessens the driving force for CT state formation. Considering both of these constraints, Karuthedath *et al.* found a critical energy offset of 0.5 eV as a requirement for high IQE_{PV} values. It should be noted that this requirement is contradicting the reports of highly successful D/A systems with close to zero energetic offsets, most likely caused by the difficulties in reliably accessing the energy levels of donor and acceptor molecules in the BHJ-blend.

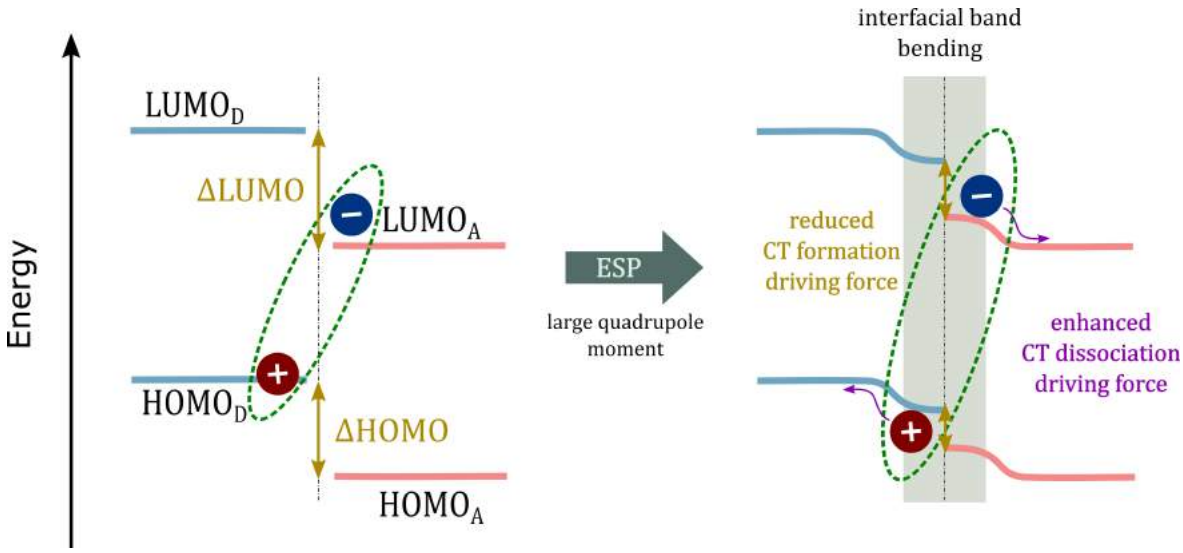

Figure 1.15: Graphical illustration of the interfacial band bending effect caused by strong local electrostatic potentials as proposed by Karuthedath *et al.* [74]. This Figure has been redrawn from Reference [74].

1.6.2 Non-radiative Voltage Loss

Reducing the charge transfer driving force does not necessarily lead to a small voltage loss as it is not the only voltage loss mechanism in OSCs. From Equation 1.31 it is obvious that any additional mechanism reducing the number of photogenerated electrons and holes (np) in the device will ultimately lead to a decreased quasi-Fermi level splitting. Hence, any additional recombination processes besides the inevitable radiative recombination, postulated by the detailed balance theory, can significantly alter the observed V_{OC}. In fact, the deactivation via non-radiative pathways *i.e.* multi-phonon processes in OSCs is typically far more likely than radiative recombination and accounts for the largest part of the experimentally observed voltage loss. The voltage loss due to non-radiative recombination is therefore strongly connected to the ratio of radiative and non-radiative recombination events. According to Rau[75], the non-radiative voltage loss is directly proportional to the logarithm of the external radiative efficiency (ERE) of a solar cell as shown in Equation 1.48.

$$\Delta V_{OC}^{non-rad} \propto \ln(\text{ERE}) \tag{1.48}$$

The ERE is defined as the fraction of the total dark current recombination in the device that results in radiative emission from the device. An in-depth derivation of this relationship will be presented in Section 2.2.2. The origin of the enhanced non-radiative recombination, or synonymous, the low radiative efficiency in OSCs has been subject to controversial discussions. Based on a two-state model, exclusively involving transitions between the electronic charge transfer (CT) and ground state (GS), Benduhn *et al.* reported a direct correlation between the height of the CT state energy and the observed non-radiative voltage losses for various donor:fullerene cells.[76] The reported decrease of non-radiative voltage losses with increasing CT state energy is commonly referred to as the energy-gap law and can be explained by a decrease in vibrational wavefunction overlap between CT and GS state.

Encouragingly, several highly efficient NFA-based solar cells with strong NIR absorption and low CT state energies have recently been reported, with relatively low $\Delta V_{OC}^{non-rad}$ losses of around 0.2 V. The strong deviation from the energy gap law highlights the need for an improved model to describe the non-radiative recombination in OPV devices. Chen *et al.* have reported a unified description of non-radiative voltage losses in OSCs based on a three-state model, which specifically incorporates the interaction (hybridization) between LE and CT states.[77] In addition, their model accounts for the thermal population of LE and CT states and can be used to determine the radiative and non-radiative recombination rates of OPV devices. With the extended three-state model they are able to explain the energy-gap law dependence found in fullerene-based blends, as well as the deviation from the energy-gap law in state-of-the-art NFA-based blends. The three-state model highlights the importance of the $\Delta E_{\text{LE-CT}}$ offset and the electronic coupling between LE and CT state ($t_{\text{LE-CT}}$). Moreover, they show that for low $\Delta E_{\text{LE-CT}}$ offset systems the ERE approaches the ERE of the pristine low bandgap

component, which is ultimately determining the minimum non-radiative voltage loss for any D/A blend. This result suggests focusing the synthetic efforts in the design of novel, highly emissive NFAs with a low energy offset $\Delta E_{\text{LE-CT}}$ and strong electronic coupling $t_{\text{LE-CT.}}$ Promisingly, organic materials in principle have the potential for high radiative efficiencies, as frequently displayed in fluorescence dyes or OLED applications.

The increased PCE with increased radiative efficiency of NFA-based solar cells compared to their fullerene-based counterparts is in good agreement with Equation 1.48, which highlights the fact that research efforts have to be focused on improving the radiative efficiency of solar cell devices to reduce non-radiative voltage losses. This leads to the famous requirement that a good solar cell with low voltage loss has to be a good light-emitting diode (LED). In fact, the ERE can be identified as a critical parameter in the optimization of any PV technology. Indeed, focusing on improving the ERE has turned out to be a successful strategy in improving the power conversion efficiencies of other PV technologies. Figure 1.16 depicts the chronological increase in PCE of GaAs and perovskite solar cells with respect to their ERE. Despite, being fundamentally different technologies and being developed in different time spans the increase in device performance with an increase in radiative efficiency follows the same trend. In addition, Figure 1.16 includes two organic solar cells, which will be further analyzed in Chapter 3. D18:PC_{71}BM and D18:Y6 were chosen as representatives of state-of-the-art fullerene- and non-fullerene-based organic solar cells. The ERE of D18:Y6 is considerably improved compared to its fullerene-based counterpart, but it is still more than a factor of 100 lower compared to the best perovskite and GaAs devices.

Finding a way to increase the ERE of organic solar cells will be of paramount importance to maximize their efficiencies and close the performance gap to their inorganic counterparts. As depicted, the development of non-fullerene acceptors was a step in the right direction. However, gaining a better understanding of the radiative and non-radiative recombination processes in NFAs, leading to the development of novel D/A systems with high radiative efficiencies will be critical to maintain the recent success.

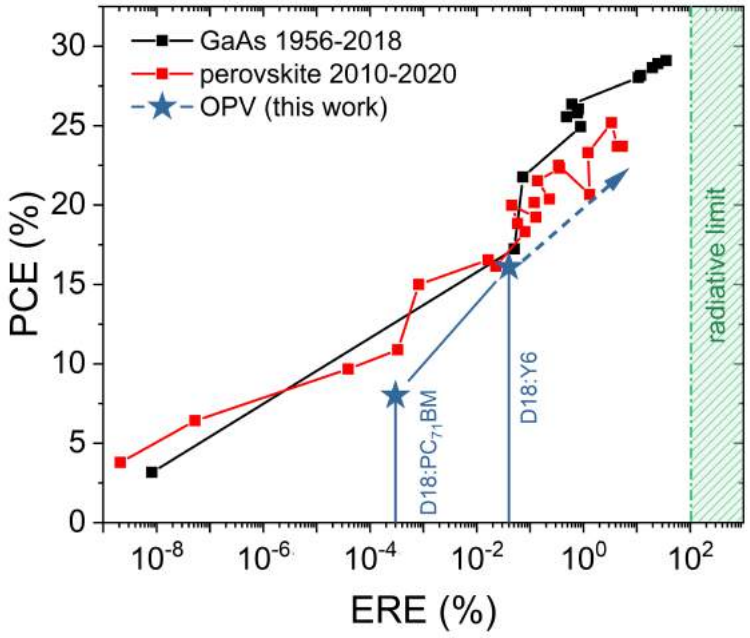

Figure 1.16: Fundamental relationship between the ERE and the maximum PCE of GaAs and perovskite solar cells. The data has been taken from Reference [78] and [79] In addition, the ERE values of the in Chapter 3 discussed organic solar cells based on D18:Y6 and D18:$PC_{71}BM$ are presented.

1.7 Device Structure

Typical solution-processed OSCs are formed by a stack of several layers as depicted in Figure 1.17. A hole transport (HTL) and electron transport (ETL) are commonly used to sandwich the absorber layer and to realize a so-called p-i-n ("conventional") or n-i-p ("inverted") device structure. Various reports have shown a beneficial effect on the device performance upon the educated choice of HTL and ETL materials.[80–82] A semi-transparent bottom electrode and a metal top electrode are typically used to collect the photo-generated charge carriers.

As discussed in Section 1.2.2, the requirement of selective contacts to extract the photogenerated electrons and holes at different sides of the semiconductor is a key criterion for an efficient solar cell design. Thus, the insertion of hole and electron transport interlayers between the absorber layer and the electrodes is of utmost importance for the charge collection efficiency and can significantly improve the overall device performance. Ideally, the electrode materials form an ohmic contact with the organic semiconductors and allow a selective, barrier-less extraction of the photogenerated, free charge carriers. To realize selectivity, the interlayers should efficiently transport the majority charge carriers (e^- for ETL; h^+ for HTL) and prevent the minority charge carriers (h^+ for ETL; e^- for HTL) from reaching the electrode interface. Moreover, the ETL and HTL materials are used to modify the metal or ITO work

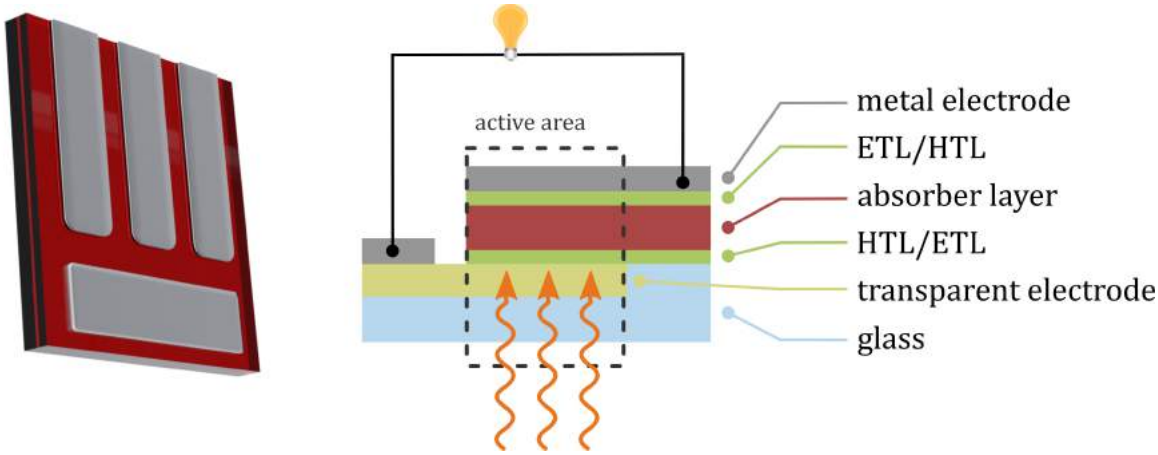

Figure 1.17: Device structure of a typical OSCs.

function. Alignment of the electrode work function with the respective HOMO level of the donor or LUMO level of the acceptor is crucial to form an ohmic contact between the electrode and the organic semiconductor. An ohmic contact is necessary to avoid charge extraction/injection barriers, which can significantly alter the device performance.

As discussed in detail in Section 1.5, the D/A interface plays a critical role in the charge generation process in OSCs. Consequently, the nanomorphology of D/A domains in the blend film has a strong influence on the device performance. In typical solution-processed BHJ OSCs, the donor and acceptor molecules are mixed and dissolved in a common solvent and deposited in a single processing step. The nanomorphology is affected by various factors such as D/A crystallinity, solubility, miscibility, as well as the choice of solvent, solvent additive, substrate, processing temperature, post-annealing, or deposition technique. In the optimization process of a newly developed OPV blend, all these parameters have to be tuned to achieve an intimate mixing of D/A domains (*i.e.* ensuring domain sizes smaller than the exciton diffusion length), while keeping them large enough to ensure an efficient charge transport in the pristine donor or acceptor domains to the respective contacts.

The used materials and the fabrication process of the organic solar cells presented in this thesis will be discussed in Section 2.3. In addition, chapter-specific experimental details are provided in the experimental notes of Chapters 3 - 6.

Chapter 2

Experimental Section

2.1 Characterization Techniques

2.1.1 Electrochemistry

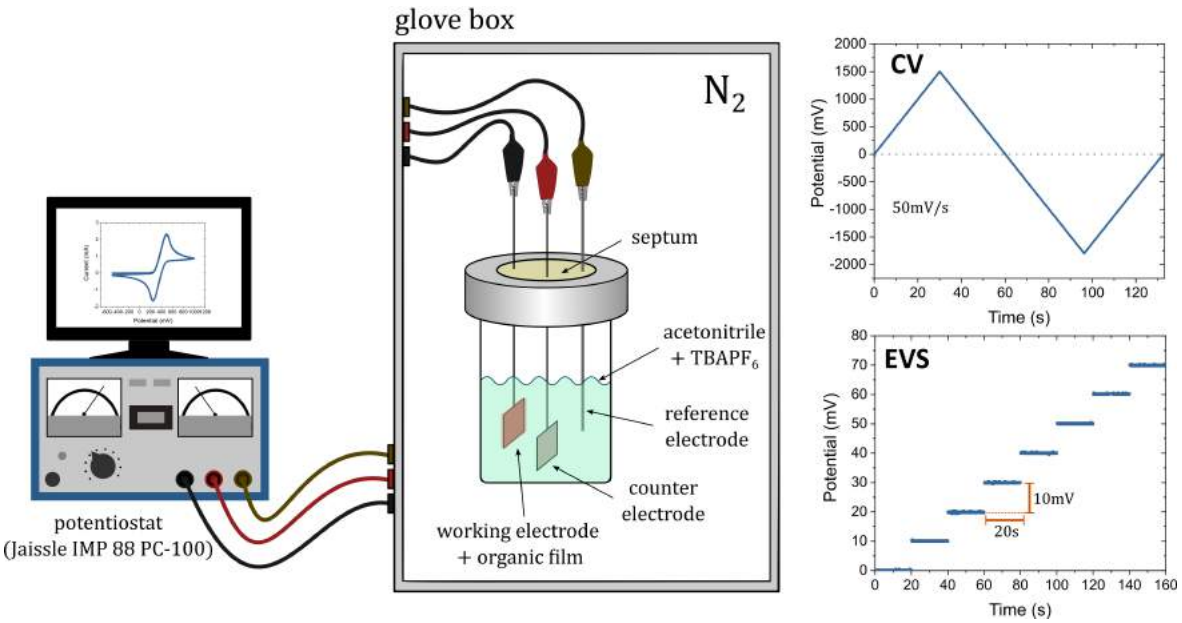

Figure 2.1: Left: Schematic sketch of the experimental setup and the electrochemical cell. Right: Illustration of the applied bias during CV and EVS measurements.

Electrochemical voltage spectroscopy (EVS) and cyclic voltammetry (CV) measurements were performed to estimate the HOMO and LUMO energy levels of the investigated organic materials. Both measurements were performed using the same experimental setup. As depicted in Figure 2.1, an electrochemical cell with three electrodes was used in combination with a

Jaissle Potentiostat-Galvanostat IMP 88 PC-100. An Ag/AgCl wire served as a quasi-reference electrode (RE) and two Pt-plates served as working (WE) and counter electrodes (CE). The investigated organic materials were deposited onto the working electrode via drop-casting from chloroform solution under an N_2 atmosphere. All measurements were performed in a nitrogen-filled glovebox using 0.1 M tetrabutylammonium hexafluorophosphate ($TBAPF_6$) in acetonitrile (MeCN) as the electrolyte solution.

During CV measurements the potentiostat controls the potential difference between WE and RE and measures the current flow between WE and CE. As shown in Figure 2.1, the applied potential is linearly swept from zero to the minimum set point, from the minimum to the maximum setpoint and back to zero (or *vice versa*). At each potential step, the current between WE and CE is recorded. For all the CV measurements in this thesis, the scan speed was set to 50 mVs^{-1}.

In contrast to the linear potential sweep in CV, EVS measurements are characterized by a stepwise increase or decrease of the applied potential as shown in Figure 2.1. The system is kept at a constant potential for a certain time, long enough to reach quasi-equilibrium conditions. For all the EVS measurements in this thesis, the voltage was stepwise varied by 10 mV and the potential was kept constant for t_{meas}=20 s. The current at each potential step is measured every tenth of a second (Δt = 0.1 s, N=200 measurements per voltage step). The amount of charge (ΔQ) passing through the system at each voltage step is obtained by integrating the current $I(t)$ following Equation 2.1.

$$\Delta Q = \int_0^{t_{meas}} I(t)\, dt \cong \sum_{i=1}^{N=200} I_i(t)\Delta t \tag{2.1}$$

In the absence of an electrochemical reaction, no net current is observed, leading to a constant baseline of ΔQ. The oxidation and reduction onsets of the materials are usually determined where ΔQ starts to deviate from the baseline. In general, the observed currents in EVS are much lower compared to CV measurements and allow evaluating the reduction or oxidation onsets with higher sensitivity. Moreover, typical dynamic influences of standard CV measurements (e.g. scan speed) are reduced due to the slow, incremental variation of the applied potential. Therefore, in this thesis primarily the EVS measurements were used to determine the energy levels of the investigated materials. However, for the sake of reliability, every OPV material was characterized using both measurement techniques following the presented.

Measurement procedure

- Step I: Clean electrodes (Ag/AgCl: rinse with acetone + blow with N_2, Pt: flame-annealing)

- Step II: Drop cast organic thin film on WE under N_2 atmosphere
- Step III: Assemble EC cell and add MeCN+$TBAPF_6$ electrolyte
- Step IV: Measure EVS in the reductive regime (negative applied bias)
- Step V: Measure CV (start towards negative applied bias)
- Step VI: Add ferrocene and measure CV (-500 mV to 1000 mV *vs.* Ag/AgCl 2x)
- Step VII: Repeat Steps I-VI for the oxidative regime

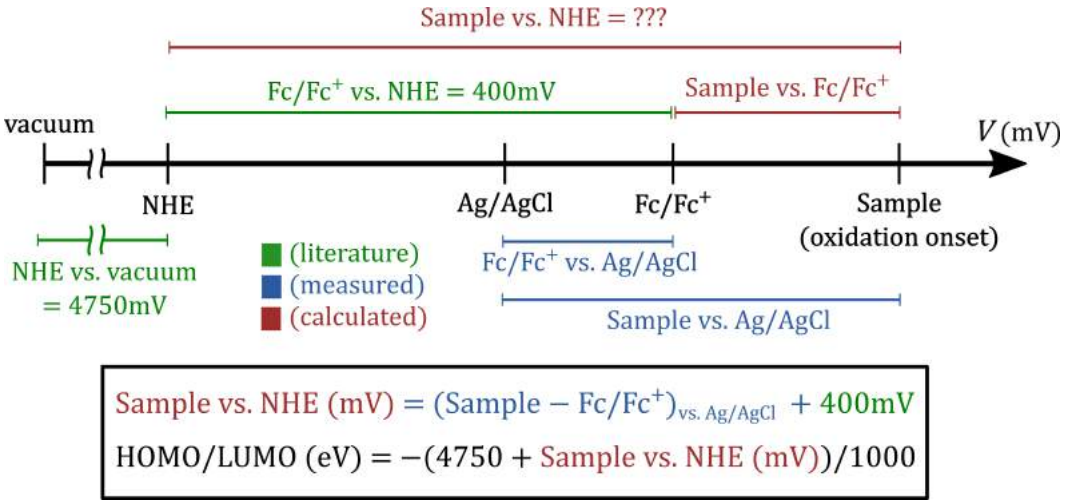

Figure 2.2: Exemplary calculation of the HOMO energy levels from the electrochemical oxidation onset of the sample. The measured potentials of the sample and the Fc/Fc^+ redox couple *vs.* Ag/AgCl reference electrode (depicted in blue) can be used to calculate the sample potential *vs.* Fc/Fc^+ . The HOMO level can then be calculated using the literature values for Fc/Fc^+ *vs.* NHE (400 mV) and NHE *vs.* vacuum (4750 mV).

As stated in the measurement procedure, the reduction and oxidation behavior of the organic materials were investigated subsequently and on freshly prepared WEs to avoid hysteresis effects caused by incomplete re-reduction or re-oxidation. Similarly, only the CV data where the material is reduced or oxidized for the first time is used to determine the energy levels. As emphasized in Step V, the CV potential is initially swept towards negative values to determine the LUMO level from the first reduction peak. *Vice versa*, the HOMO level is always determined from CV measurements where the potential is initially swept towards positive values. As stated in Step VI of the measurement procedure, every measurement was externally calibrated by dissolving ferrocene in the electrolyte solution and measuring the half-wave potential of the ferrocene/ferrocenium (Fc/Fc^+) redox couple. The measured Fc/Fc^+ half-wave potential was used to plot the measured data (sample *vs.* Ag/AgCl) in reference to the normal hydrogen electrode (NHE). An oxidation potential for Fc/Fc^+ vs. NHE of 400 mV was used and the Fermi level of NHE *vs.* vacuum was taken as -4.75 eV.[83,84]

The performed conversion of the measured potentials into potentials *vs.* NHE and the subsequent determination of the energy levels are summarized in Figure 2.2.

Evaluation procedure

In order to derive the HOMO and LUMO energy levels of the investigated materials, an exact determination of the oxidation and reduction onsets from electrochemical measurements is required. Contradicting reports for HOMO and LUMO levels of organic materials suggest that commonly used electrochemical techniques suffer from large measurement and evaluation errors.[85,86] Depending on the used method, HOMO and LUMO levels may vary significantly, often leading to deviations in the magnitude of several tenths of eV. The difficulty in defining the reduction and oxidation onsets is considered the main source for the evaluation error in electrochemical measurements. For CV analysis a so-called tangent evaluation method is commonly used, where a tangent is fitted to the slope of the CV peak and the baseline, respectively. The intersection point is considered as the onset of the electrochemical reaction. Another possibility often used to evaluate EVS data, is to define the first deviation from the baseline as the reduction/oxidation onset. Throughout this thesis, the oxidation and reduction onsets of the organic materials were determined using both evaluation methods. The baseline deviation is considered as a lower limit and the crossing point of the two tangents is considered as an upper limit of the evaluation error which is still justified by the measured data.

Figure 2.3a shows the exemplary evaluation of a typical EVS measurement (D18). The results of the two evaluation techniques are highlighted by the orange triangle (1^{st} deviation method) and diamond symbols (tangent method). In addition, the construction of a typical energy level box plot from the determined reaction onsets is illustrated, where the "1^{st} deviation method" values were used to plot the box diagram and the "tangent evaluation" values are represented by the whiskers. As a general trend, it was observed that regardless of the measurement technique or evaluation method the HOMO level of donor and acceptor materials can be determined with good accuracy. The determination of the LUMO levels on the other hand shows a strong variation between the measurement techniques and the evaluation methods. Especially the LUMO of the donor polymers were hard to identify, which is further discussed in Note S5.2. Due to reliable measurements of the HOMO energy levels and the optical bandgap (E_{opt}) throughout this thesis, the LUMO levels were estimated by adding E_{opt} to the HOMO level evaluated from EVS via the "first deviation method" as illustrated in Figure 2.3b and Equation 2.2.

$$\mathrm{LUMO_{opt}} = \mathrm{HOMO_{EVS,1^{st}dev.}} + E_{opt} \tag{2.2}$$

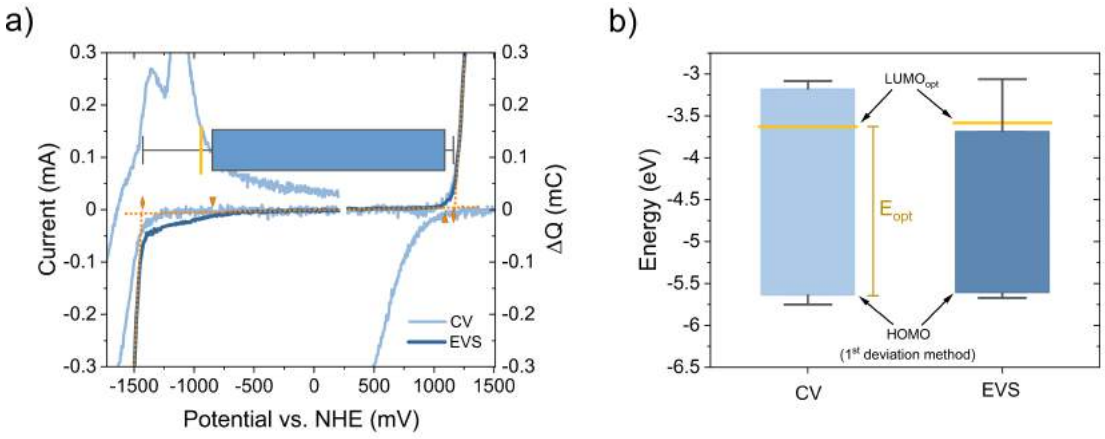

Figure 2.3: Exemplary evaluation of a typical EVS measurement. a) EVS (dark blue) and CV (light blue) measurements of D18. The orange triangles and diamonds represent the determined reaction onset from the 1st deviation and tangent method, respectively. As illustrated the determined onsets are used to calculate the typical boxplots for HOMO and LUMO levels. b) Comparison of the energy levels determined from EVS and CV measurements. The $LUMO_{opt}$ level is highlighted in yellow.

2.1.2 Optical Spectroscopy

UV-vis-NIR Absorbance & Transmission

A Lambda 1050 double-beam UV-vis-NIR spectrometer from PerkinElmer was used to determine the optical transmission T and absorbance A of the organic thin films on glass. The setup is schematically depicted in Figure 2.4. A combination of a tungsten-halogen and a deuterium lamp is used to cover a broad range of excitation wavelengths. Two holographic grating monochromators are used to precisely control the excitation wavelength. The common beam is split up in a sample and reference beam to correct for e.g. substrate absorption. The spectrometer is furthermore equipped with a photomultiplier tube (UV-Vis regime <850nm), an InGaAs, and a PbS detector (NIR and IR, respectively). The optical absorbance (A) was calculated using the negative decadic logarithm of the transmission:

$$A = -\log_{10}(T) \tag{2.3}$$

A specular reflectance module as shown in Figure 2.4 was used to measure the reflectance R under an incidence angle of 6°. The measurements were performed relative to an aluminum mirror which, in a first approximation, acts as an ideal reference with a reflectance value of $R = 1$. A Si wafer with known reflectance was used to calibrate the setup to account for the

non-ideal reflectance behavior of the Al mirror. Typically, the corrected reflectance values were used to calculate the absorption coefficient using

$$\alpha = \frac{1}{d} \ln\left(\frac{1-R}{T}\right), \tag{2.4}$$

where d is the film thickness measured with a DekTakXT stylus profilometer (Bruker).

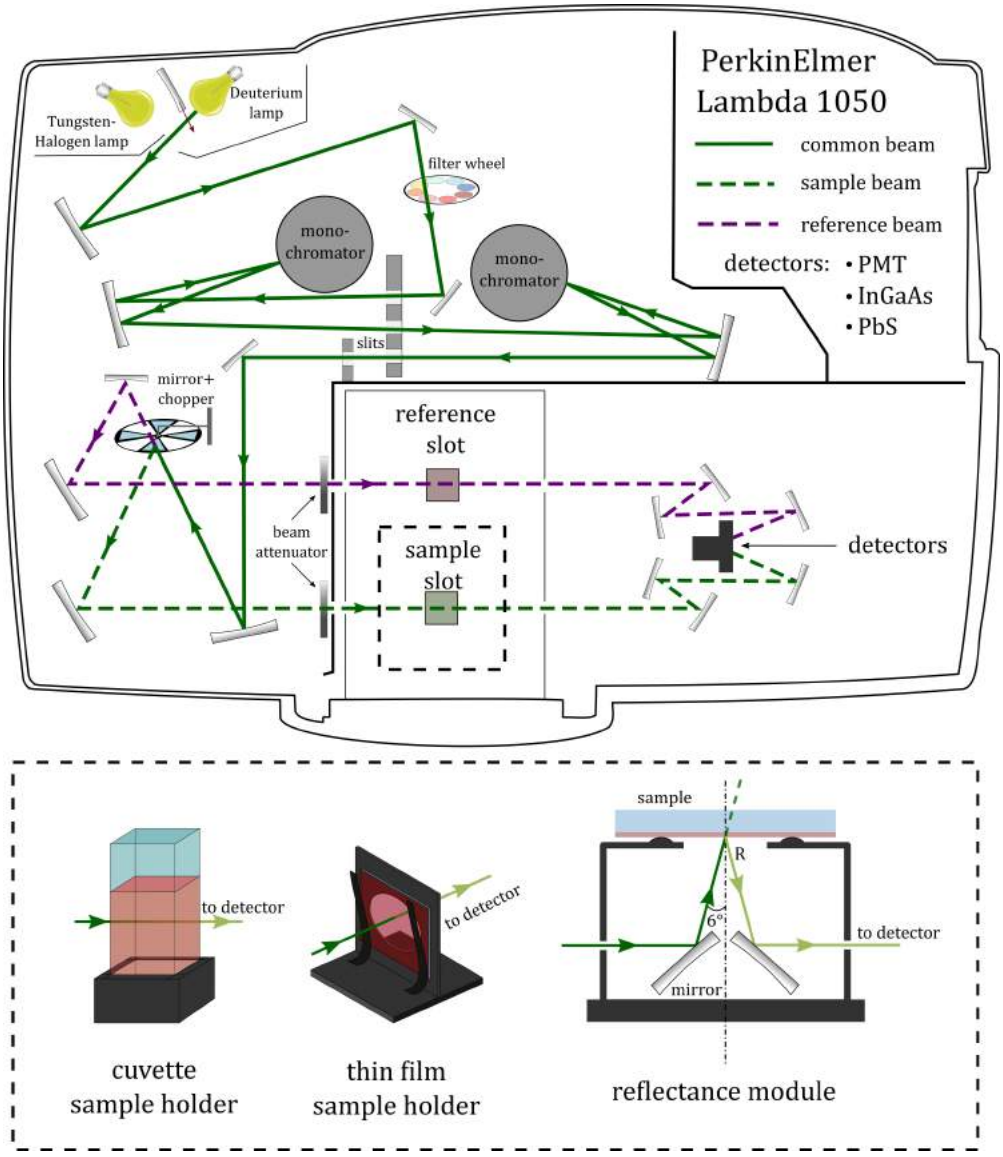

Figure 2.4: Sketch of the UV-vis-NIR spectrometer and the accessories to measure solutions, thin films and the reflectance of thin film.

Excitation & Emission spectra

Excitation and emission spectra of donor and acceptor thin films were measured with a PTI QuantaMaster 40 fluorescence spectrometer. As shown in Figure 2.5, a xenon arc lamp is used as an excitation light source. Two Czerny-Turner monochromators are used to ensure monochromatic excitation of the sample. Furthermore, the use of an additive double monochromator setup significantly enhances the stray light rejection. Similarly, two monochromators in combination with a photomultiplier tube are used to analyze the emission signal. As depicted, a beam splitter is used to direct a small part of the excitation light onto the calibrated reference diode detector. The reference photodiode allows to correct the excitation light for the spectral emission shape and any temporal fluctuations of the xenon arc lamp. The detected emission signal has to be corrected for the spectral response of optics, gratings, and the detector. Thus, the measured signal was corrected using a factory calibration file based on measurements with a known light source (e.g. NIST-traceable standard).

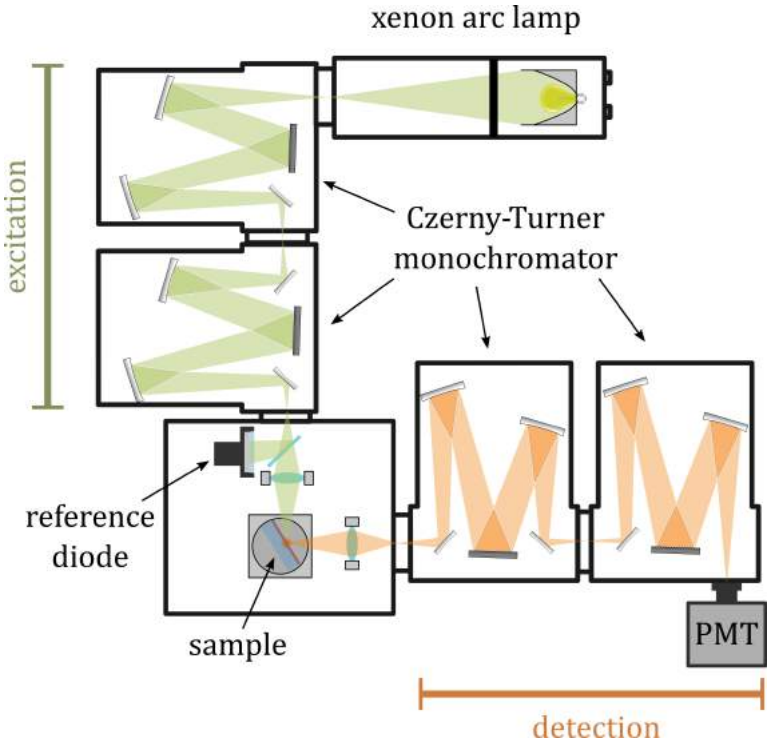

Figure 2.5: Sketch of the PTI QuantaMaster 40 fluorescence spectrometer used to record excitation and emission scans.

Photo- & Electroluminescence

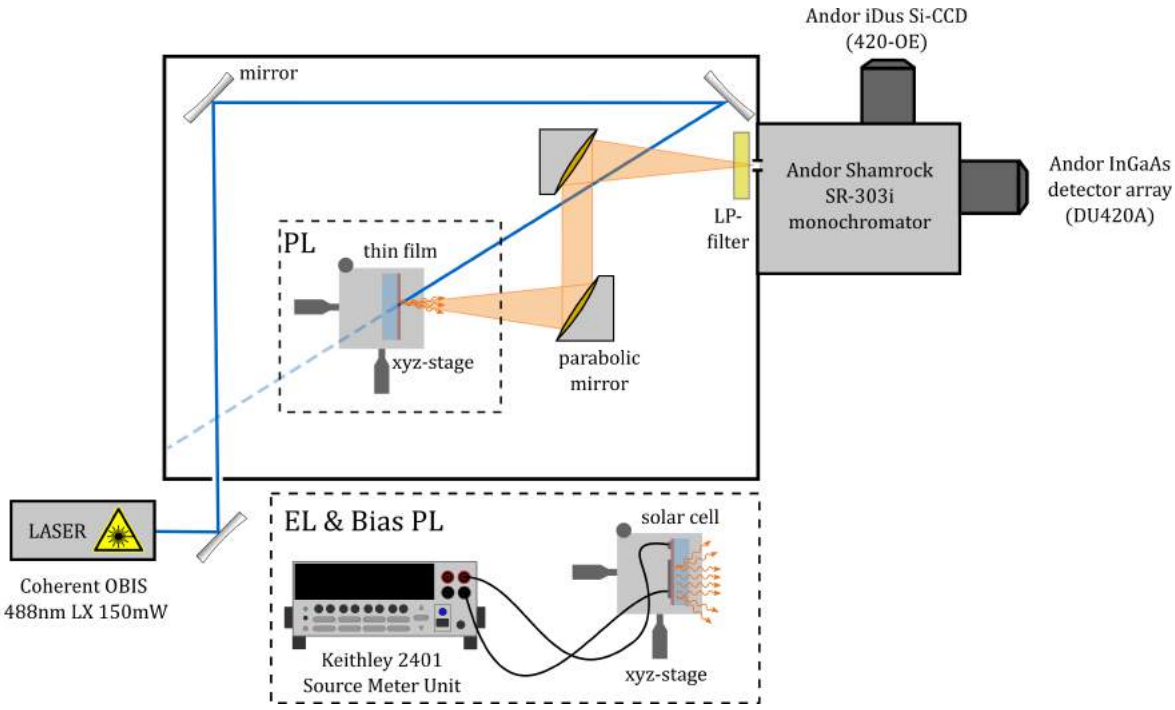

Figure 2.6: Sketch of the experimental setup used to record EL, PL and bias-PL spectra.

The setup depicted in Figure 2.6 was used to measure: (1) (bias dependent) PL and EL spectra of organic solar cells and (2) PL spectra of organic thin films on glass. The setup is built within a light-tight box to reduce stray light. The samples were mounted onto an XYZ-translation stage, which allows positioning the active area of the solar cell in the center of the first parabolic mirror. In combination with a second parabolic mirror, the emission of the solar cell or thin-film is focused onto the entrance slit of the Andor Shamrock SR-303i monochromator. The monochromator is equipped with two Peltier-cooled detectors: (1) Andor iDus Si CCD (420-OE) and (2) Andor InGaAs detector array (DU420A). In order to minimize the dark counts, the two detectors were operated at a temperature of -60 °C. A long-pass filter in front of the entrance slit of the monochromator was used to block excitation stray light from the laser and emission contributions from second-order diffraction. As indicated by the dashed boxes in Figure 2.6, a Coherent OBIS 488 nm LX 150mW laser was used as an excitation source during PL experiments, while a Keithley 2401 SMU was used to bias the OSC during EL and bias-dependent PL measurements. A calibrated tungsten halogen source (Ocean Optics HL-2000) was used to determine the overall spectral response of the monochromator/detector system.

Electroluminescence Quantum Yield

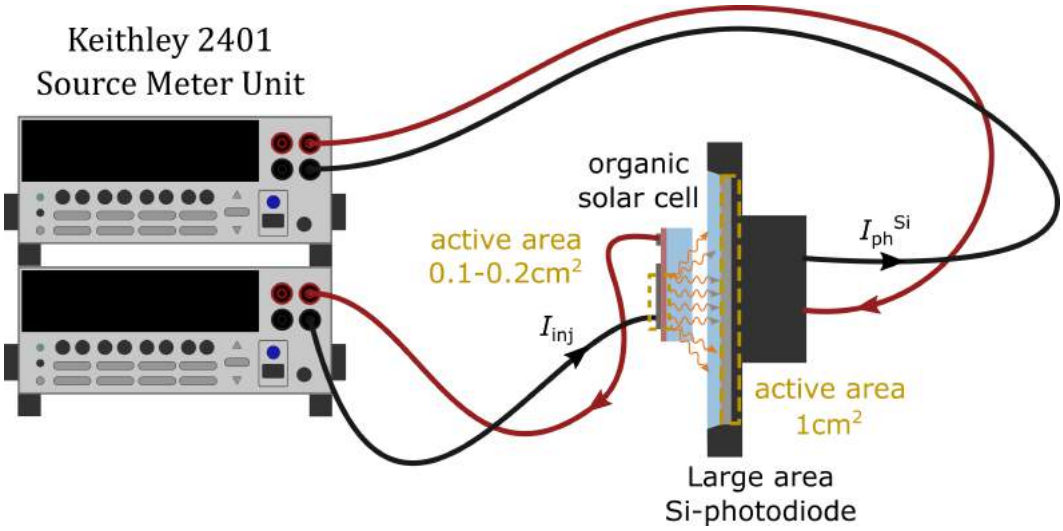

Figure 2.7: Experimental arrangement to measure the ELQY of organic solar cells.

Measurements to estimate the ELQY were performed using a calibrated, large area Si photodiode (Hamamatsu S2281). The organic solar cell (0.173 cm^2) was positioned in the center and directly in front of the large area Si photodiode (1 cm^2) as depicted in Figure 2.7. A Keithley 2401 SMU was used to operate the solar cell as a LED, while another Keithley 2401 SMU was used to measure the photocurrent of the Si photodiode (I_{ph}^{Si}). Using I_{ph}^{Si} and the spectral responsivity of the calibrated Si photodiode (R^{Si} [AW^{-1}]) allows determining the incident light power (P_0) on the Si device following Equation 2.5.

$$P_0[W] = \frac{I_{ph}^{Si}}{R^{Si}} \tag{2.5}$$

When operated in a dark environment, the only significant contribution to I_{ph}^{Si} stems from the photons, emitted from the OSC during EL. Moreover, it is assumed that all the light emitted from the solar cell is collected by the large area Si diode. Under these assumptions, integration of the spectral photon flux of the solar cell ($\Phi_{SC}(\lambda)$ [#photons s^{-1} nm^{-1}]) times the energy per photon ($E_{h\nu} = hc/\lambda$) allows calculating P_0 as depicted Equation 2.6

$$P_0[W] = \int \frac{hc}{\lambda} \Phi_{SC}(\lambda)\, d\lambda \tag{2.6}$$

where h is the Planck constant, c is the speed of light, and λ is the wavelength. From standard EL measurements (see Section 2.1.2) the spectral shape of the EL emission from OSCs is known in counts per nm. The relative spectral photon flux ($\Phi_{SC}^{rel}(\lambda)$) [a.u. nm^{-1}]) can be

derived by normalizing the measured EL spectrum. As shown in Equation 2.7, the absolute spectral photon flux $\Phi_{SC}(\lambda)$ can be expressed as $\Phi_{SC}^{rel}(\lambda))$ times a scaling factor ξ:

$$\Phi_{SC}(\lambda) = \Phi_{SC}^{rel}(\lambda) \times \xi \tag{2.7}$$

Combining Equations 2.6 and 2.7 leads to Equation 2.8:

$$P_0[W] = \xi \int \frac{hc}{\lambda} \Phi_{SC}^{rel}(\lambda)\, d\lambda \tag{2.8}$$

It should be noted that the scaling factor ξ is independent of the wavelength and can be placed in front of the integral. Inserting Equation 2.5 in Equation 2.8 leads to Equation 2.9, which can be used to determine the appropriate scaling factor ξ, necessary to match the total absorbed light power P_0 at the Si photodiode.

$$\xi = \frac{I_{ph}^{Si}}{R^{Si}} \times \left(\int \frac{hc}{\lambda} \Phi_{SC}^{rel}(\lambda)\, d\lambda \right)^{-1} \tag{2.9}$$

This allows the determination of the spectral photon flux $\Phi_{SC}(\lambda)$ from the measured Si photocurrent and the normalized EL spectrum of the OSC. The total number of emitted photons/s can be easily obtained by the integration of $\Phi_{SC}(\lambda)$ over all wavelengths, while the number of injected electrons/s is given by dividing the measured injection current (I_{inj} by the elementary charge q. Thus, the ELQY can be calculated using Equation 2.10

$$\text{ELQY} = \frac{\int \Phi_{SC}(\lambda)\, d\lambda}{\frac{1}{q} I_{inj}} = \frac{[\#\text{photons/s}]}{[\#\text{electrons/s}]} \tag{2.10}$$

ELQY Corrections:

The described procedure only considers photons that can escape the device and are detected at the Si photodiode. The layered device geometry of OSCs consisting of a stack of materials with different refractive indices prevents a significant part of the emitted photons to exit the device due to internal total reflection and light-guiding effects. If the light is emitted from a point-like source in the organic absorber layer, only a fraction of the emitted light with an incidence angle below the critical angle of total reflection can escape the device (escape cone). The critical angle (φ_c) can be determined from Snell's law at an interface between two media with refractive index n_1 and n_2 ($\varphi_c = \sin^{-1}(n_2/n_1)$). Throughout this thesis, the ELQY was corrected for the main outcoupling loss, which is caused by total reflection at the glass-air interface where the change of the refractive index is well defined. Here, the total reflection at the ITO, ETL, or organic absorber layers is not included in the corrections. A graphical illustration on how to calculate the infinitesimal surface area of the escape cone (dA) is shown in Figure 2.8a. Integration of dA allows calculating the callote-shaped surface area (shaded in green) as presented in Equation 2.11. The ratio of the callote-shaped surface

area to the surface area of a hemisphere ($2\pi r^2$) allows estimating the fraction of the light which can escape the solar cell as shown in Equation 2.12.

$$A = \int_0^{2\pi} d\theta \int_0^{\varphi_c} r^2 \sin(\varphi)\, d\varphi$$
$$A = 2\pi r^2 \left(1 - \cos(\varphi_c)\right) \tag{2.11}$$

$$P_{\text{escape}} = P_{\text{source}} \times \left[1 - \cos\left(\sin^{-1}\left(\frac{n_2}{n_1}\right)\right)\right] \tag{2.12}$$

Calculating the escape cone based on the refractive indices of air (n_1 = 1.00) and glass (n_2 = 1.51) and assuming a fully reflective back surface (metal electrode) leads to a correction factor of 4.0058. Thus, all the presented ELQY measurements were obtained by multiplying the experimentally derived ELQY values by a factor of 4.

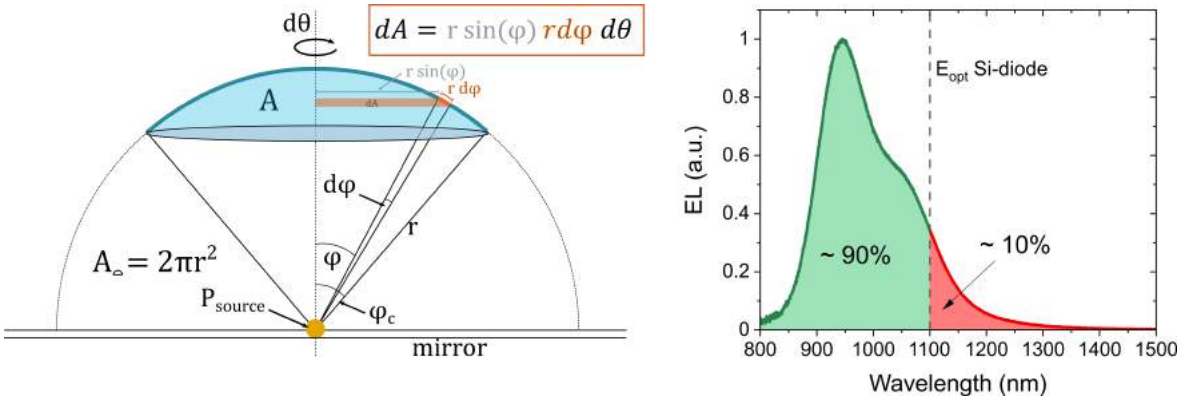

Figure 2.8: Left: Sketch of the escape cone calculation. Right: Exemplary emission spectrum with a significant contribution beyond 1100 nm.

A second correction was applied to all the devices with significant NIR emission beyond 1100 nm. As depicted in Figure 2.8, roughly 10 % of the EL of Y6-based devices extends beyond 1100 nm. In the spectral region below the Si bandgap, the radiation does not contribute to the measured photocurrent. Thus, the bandgap of silicon was set as an upper boundary for the integration in Equation 2.9.

Photoluminescence Quantum Yield

The absolute photoluminescence quantum yield was measured using a Hamamatsu C9920-03 Absolute PLQY Spectrometer equipped with an integrating sphere. A sketch of the setup is presented in Figure 2.9. The excitation wavelength is selected from the output of a xenon lamp (C9920) by a monochromator (A10080-01). The excitation light is coupled into the

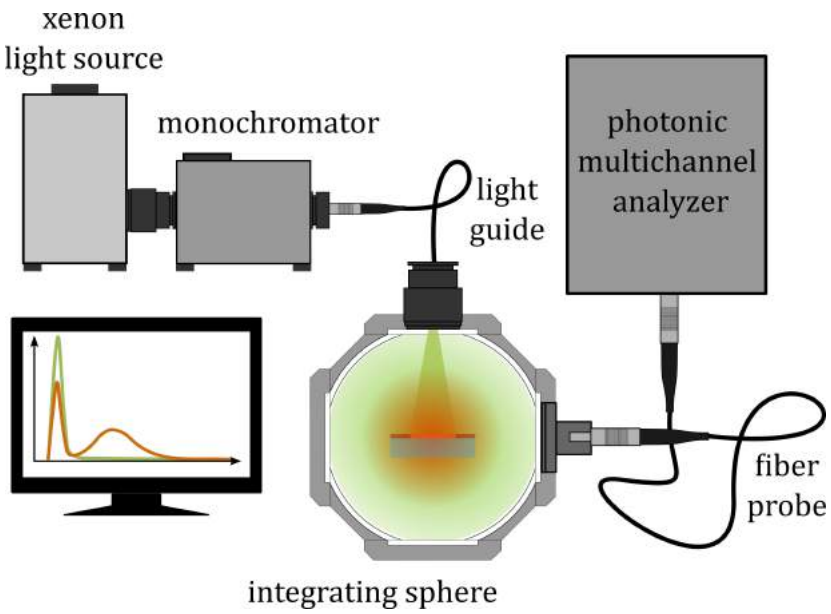

Figure 2.9: Sketch of the integrating sphere setup used for measuring the PLQY of organic materials.

integrating sphere via a light guide (A10079-01). The emission is coupled into a photonic multichannel analyzer (PMA-12) via a fiber probe. The PLQYs of the organic thin films were determined from a two-measurement procedure (2MM method) as described in Reference [87]. First, a reference measurement with an empty integrating sphere is performed. In the empty sphere measurement, the detected signal is exclusively caused by scattered excitation light. As a next step, the sample of interest is placed in the integrating sphere and the measurement is repeated with the same parameters. If the sample is inserted into the sphere, the detected excitation peak is reduced due to absorption of the sample. Moreover, if the sample is fluorescent, additional peaks corresponding to the emission spectrum of the sample are visible in the second measurement as shown schematically in Figure 2.9 (orange curve).

Calculation of the PLQY:

The measured spectra are multiplied by the current wavelength value at each wavelength step to obtain a quantity proportional to the photon flux. Integration of the modified spectra allows to quantify the relative number of photons in the excitation peak S and photoluminescence peak P. In the following, subscript 1 is used for the empty sphere measurement and subscript 2 represents the measurement with the sample mounted inside of the sphere.

The empty sphere measurement acts as a baseline and the determined peak area S_1 is used to quantify the number of detected photons if no sample is present inside of the sphere. In the second measurement (with the sample), an incoming photon has only a limited amount of possible pathways once it enters the integrating sphere, as schematically depicted in Figure 2.10b. The variable f describes the probability that the incident photon directly hits the sample. The variable A can be interpreted as the absorptance (probability of absorption) of

the sample and μ represents the probability that the photon is absorbed after one or more scattering events in the sphere (not directly). Considering all the possible photon pathways depicted in Figure 2.10b allows formulating the following set of equations:[87]

$$S_1 = S_1 \tag{2.13}$$

$$S_2 = \Big[f\,(1-A)\,(1-\mu) + (1-f)\,(1-\mu) \Big] S_1 \tag{2.14}$$

$$P_1 = 0 \tag{2.15}$$

$$P_2 = \Big[fA + (1-f)\,\mu + f\,(1-A)\,\mu \Big] \eta_{\mathrm{PL}} S_1 \tag{2.16}$$

S_1 is obtained by integrating the excitation light peak in the empty sphere measurement and P_1 is assumed to be zero (no PL emission if the sphere is empty). The three terms in the square brackets of Equation 2.16 represent all the cases where a photon is absorbed (Figure 2.10b orange boxes). For every absorbed photon (independent of the path) the sample emits a photon with an efficiency η_{PL} corresponding to its PLQY. Similarly, Equation 2.14 sums up all the pathways where the excitation light is not absorbed and can reach the detector (Figure 2.9b green boxes).

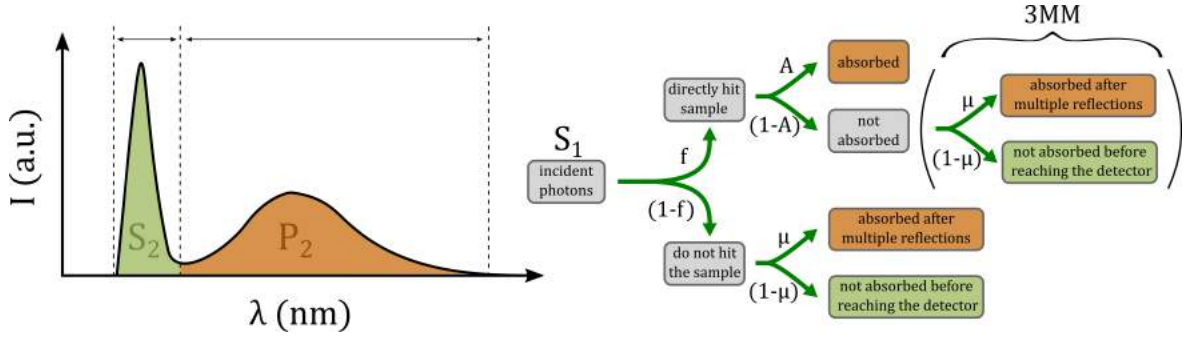

Figure 2.10: Graphical illustration how to derive the individual terms of Equations 2.14 and 2.16.

According to Reference [87] an additional measurement with the sample inside of the sphere but with no direct excitation of the sample is necessary to determine the absolute PLQY from Equations 2.13-2.16 (3MM method). Alternatively, it is possible to determine the PLQY from only two measurements (as discussed above), if the term $f(1-A)(1-\mu)$ in Equation 2.14 is reduced to $f(1-A)$ and the term $f(1-A)\mu$ in Equation 2.16 is neglected. This approximation assumes that photons which directly hit the sample are either absorbed or not absorbed and neglects the possibility of absorption at a later stage after one or multiple scattering events (see bracket with label 3MM in Figure 2.10b). Faulkner *et al.* demonstrated that despite the theoretical and practical difference between the two methods, the derived values tend to be in excellent agreement.[87] Thus, in this thesis the 2MM method was exclusively used to determine the PLQYs.

The PLQY for the 2MM method can be calculated by reformulating Equation 2.16 and neglecting the $f(1-A)\mu$ term:

$$\eta_{\mathrm{PL}} = \frac{P_2}{\Big[fA + (1-f)\mu\Big] S_1} \tag{2.17}$$

The denominator in Equation 2.17 represents all the absorbed photons and is thus identical to the term $S_1 - S_2$ (# of initial excitation photons − # of detected excitation photons = # of absorbed photons). This allows the calculation of the PLQY using the measured peak areas S_1, S_2, and P_2 according to:

$$\eta_{\mathrm{PL}} = \frac{P_2}{S_1 - S_2} \tag{2.18}$$

Time Correlated Single Photon Counting

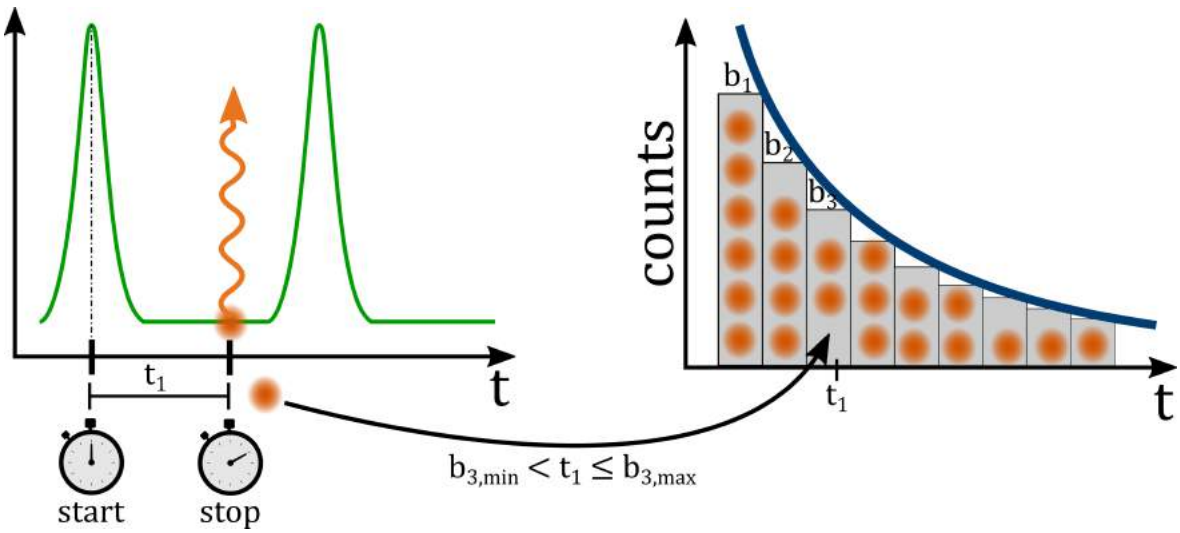

Figure 2.11: TCSPC measurement principle.

The PL decay behavior following an excitation event can be studied to gain information about excited state properties of the sample (e.g. quenching, electron/hole transfer, energy transfer, ...). An established tool to study the average exciton lifetime is the highly sensitive technique called time-correlated single-photon counting (TCSPC). During TCSPC measurements the time delays of single emission events with respect to an excitation pulse are monitored. As shown in Figure 2.11, the emission of an excitation laser pulse starts the time measurement and as soon as a photon is recorded by the detector, the time measurement is stopped. The measured time difference between the start and stop signal corresponds to the lifetime of this single emission event t_1. Reiteration of this process allows storing the measured lifetimes in a histogram with the delay time as x-axis as shown in Figure 2.11. In principle, a laser

pulse repetition rate in the MHz regime repeats the measurement more than a million times per second. The high number of individual lifetime measurements justifies the statistical determination of the PL decay behavior. Typically, the TCSPC data is presented in PL decay curves, which correspond to the envelope function of the recorded histogram. Throughout this thesis, the delay time, where the intensity of the decay curve is reduced to $1/e$ of its initial value, was used to estimate the PL lifetime.

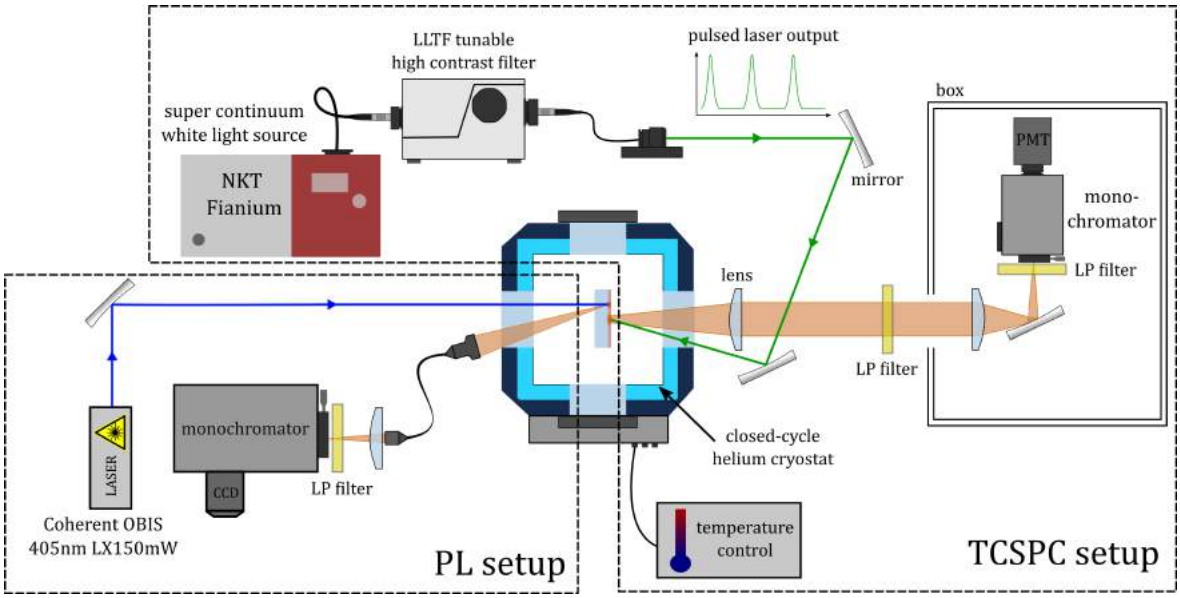

Figure 2.12: Sketch of the TCSPC experimental setup.

The TCSPC setup is depicted in Figure 2.12. As shown, the sample is mounted inside a closed-cycle helium cryostat (Oxford OptistatDry). A supercontinuum laser (NKT Photonics SuperK FIANIUM FIU-15) equipped with a pulse picker and a wavelength selection unit (Photonetc LLTF CONTRAST VIS) was used to excite the sample. The pulse duration of the supercontinuum laser is $\sim$5 ps and the measurements were typically performed with a pulse repetition rate of 4.88 MHz. The setup for time-correlated single-photon counting detection is built inside a box to reduce stray light and consists of a DeltaNu DNS-300 monochromator, a Becker&Hickl, SPC 150, PMC-100-1 cooled photomultiplier.

As presented in Figure 2.12, an additional PL setup allows measuring steady-state PL spectra without repositioning of the sample. A Coherent OBIS 405nm laser was used to excite the sample from the backside window of the cryostat. A combination of collimators, lenses, and an optical fiber was used to guide the emitted light to the input slit of a Andor Shamrock monochromator equipped with an Andor iStar iCCD detector. Furthermore, the closed-cycle helium cryostat allows controlling the temperature during steady-state or time-dependent PL measurements in a temperature range of 4 K - RT.

2.1.3 Photovoltaic Characterization

Current-Voltage Response

Current density voltage (*J-V*) measurements of the solar cell devices were performed using a LOT-QD solar simulator (LS0821) and a Keithley 2401 SMU. The setup is schematically shown in Figure 2.13. The light intensity was calibrated using a reference Si diode and set to 100 mW cm^{-2} (AM1.5G). The *J-V*-response of the solar cell under AM1.5G illumination and in the dark was recorded using a custom-built LabVIEW software.

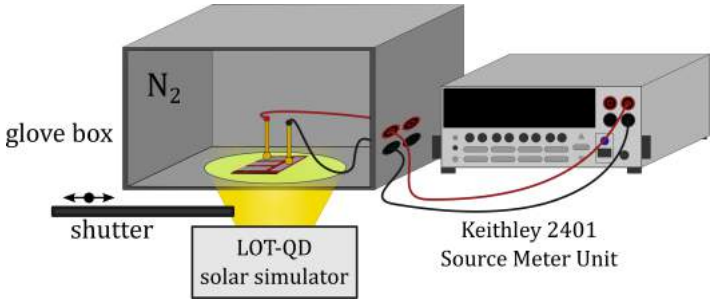

Figure 2.13: Schematic sketch of the *J-V* measurement setup.

Photovoltaic External Quantum Efficiency

The photovoltaic external quantum efficiencies (EQE_{PV}) of the organic solar cells were measured with two custom-built experimental setups. Depending on the wavelength regime of interest the appropriate setup was chosen. The first setup is optimized for EQE_{PV} measurements at wavelengths <1000 nm (EQEs1) while the second setup allows for highly-sensitive EQE_{PV} measurements up to wavelengths of 1800 nm (EQEs2). As shown in Figure 2.14, the first EQE_{PV} setup consists of a xenon lamp, a monochromator (Oriel Cornerstone), a Jaissle 1002 potentiostat, and a lock-in amplifier (SR830, Stanford Research Systems). The light from the xenon lamp was modulated by a mechanical chopper and coupled into the monochromator. A mechanical filter wheel equipped with long pass (LP) filters was used to avoid higher-order contributions and guarantees monochromatic illumination of the device. The potentiostat was used in a two-electrode configuration and acts as a current to voltage converter with variable gain ranging from 10 to 10^8 VA^{-1}. The combination of phase-sensitive lock-in detection (chopping frequency = 173 Hz) and variable preamplification enables highly sensitive EQE_{PV} measurements over several orders of magnitude. A calibrated silicon diode (Hamamatsu S2281) was used as a reference to correct for the xenon lamp spectrum.

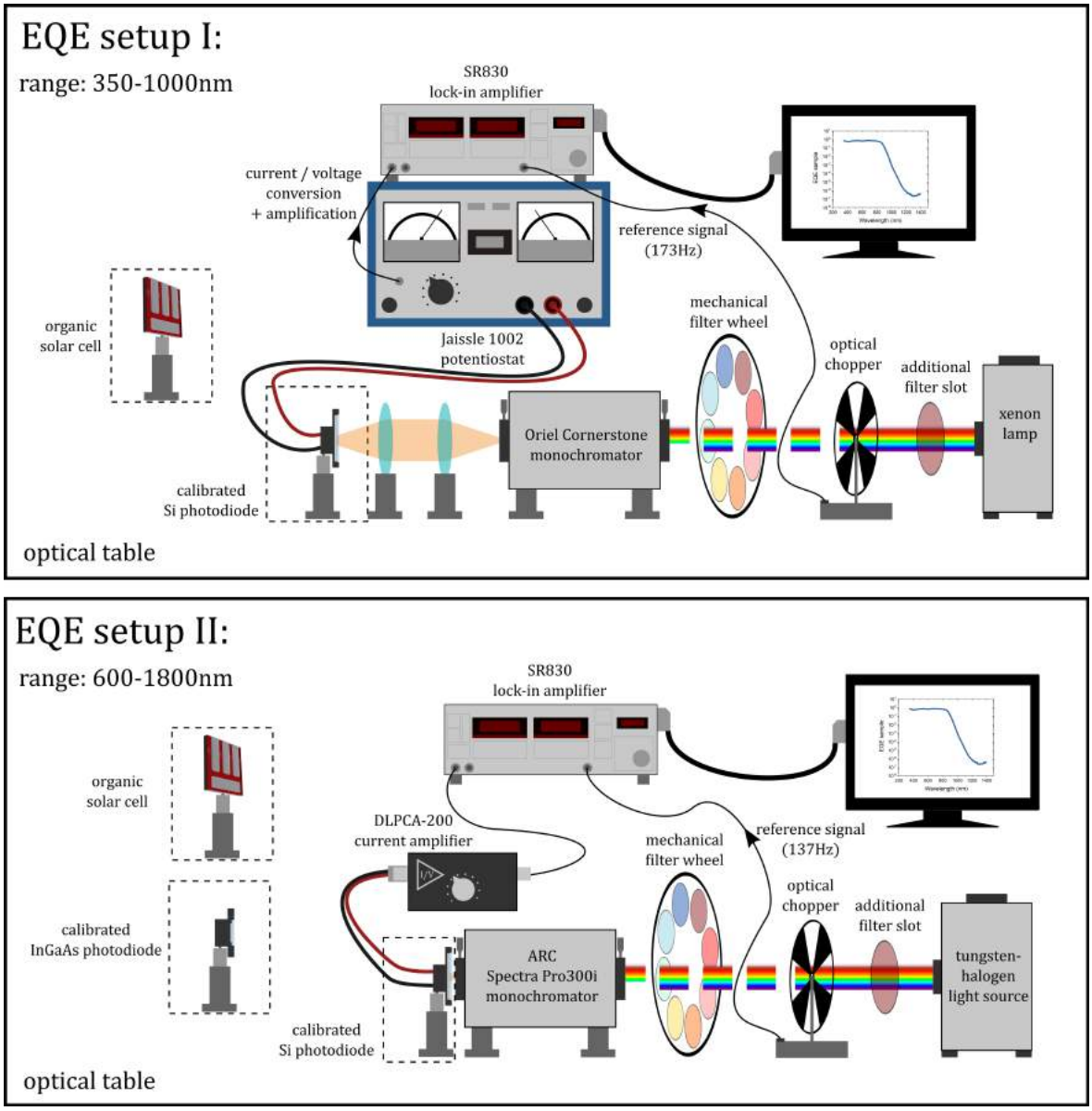

Figure 2.14: Graphical illustration of the two different EQE_{PV} setups.

To extend the measurement range up to 1800 nm, a similar setup (see Figure 2.14) but equipped with a different light source was used (Tungsten-Halogen light source TS-428S, Princeton Instruments). In this setup, a SpectraPro-300i monochromator from ARC was used. Furthermore, a DLPCA-200 Variable Gain Low Noise Current Amplifier from Femto was used as a preamplifier instead of the potentiostat. The rest of the setup is similar to the previously described EQE setup (EQEs1), featuring an optical chopper (chopping frequency = 137 Hz), a mechanical filter wheel, and an SR830 lock-in amplifier. In addition to the calibrated silicon diode (Hamamatsu S2281), a calibrated InGaAs diode (Hamamatsu G12180) was used as a reference in the spectral region above 1100 nm.

It should be noted that despite its name, the EQE_{PV} setup does not measure the EQE_{PV} directly. Instead, the spectral photocurrent ($I_{SC}(\lambda)$) of the OSCs is measured, which allows a straightforward calculation of the EQE_{PV}. At each wavelength step (monochromatic illumination), the photocurrent of the solar cell is given by

$$I_{SC}(\lambda) = q\,EQE_{PV}(\lambda)\Phi_{lamp}(\lambda) \tag{2.19}$$

Thus, if the photon flux per wavelength from the light source $\Phi_{lamp}(\lambda)$ is known, the spectral $EQE_{PV}(\lambda)$ of the solar cell can be calculated by rearranging Equation 2.19. $\Phi_{lamp}(\lambda)$ can be derived from a reference measurement with a calibrated photodiode where the $EQE_{PV}(\lambda)$ is known.

$$I_{SC}^{Ref}(\lambda) = q\,EQE_{PV}^{Ref}(\lambda)\Phi_{lamp}(\lambda) \tag{2.20}$$

This allows calculating the EQE_{PV} at a specific wavelength according to

$$EQE_{PV}(\lambda) = I_{SC}(\lambda)\frac{EQE_{PV}^{Ref}(\lambda)}{I_{SC}^{Ref}(\lambda)}, \tag{2.21}$$

where $I_{SC}(\lambda)$ and $I_{SC}^{Ref}(\lambda)$ are the spectral photocurrent measurements of the OSC and reference photodiode, respectively. $EQE_{PV}^{Ref}(\lambda)$ is the known EQE_{PV} spectrum of the calibrated reference photodiode.

Measurement procedure:

- Step I: Wait until the light source has reached a constant output (∼15-30 min)
- Step II: Measurement of Si reference diode
- Step III: Measurement of OSC
- Step IV: Measurement of OSC below the bandgap
  - Set excitation wavelength far below the bandgap
  - Increase the preamplification (x10^2)
  - Continuously increase wavelength until the signal is close to overload (= starting wavelength)
  - Add additional LP filter below starting wavelength to reduce stray light
- Step V: Measurement of Si reference diode
- Step VI: Measurement of Si reference diode + LP filter with standard preamplification
- Step VII: Use the measured data to calculate EQEs

The standard EQE_{PV} and the EQE_{PV} spectrum with higher preamplification are then joined to form a combined EQE_{PV} spectrum with an increased sensitivity range, as shown in Figure 2.15a. For materials with strong NIR absorption, where the sub-bandgap behavior extends beyond 1000 nm, additional measurements with the EQEs2 setup were performed. The measurement procedure was similar as previously described. However, the EQEs2 setup typically allowed a higher preamplification. Therefore, StepIV was repeated with an increased preamplification by a factor of 10^3. Overall, a total of 4 EQE spectra were combined to achieve highly sensitive EQE measurements as shown in Figure 2.15b.

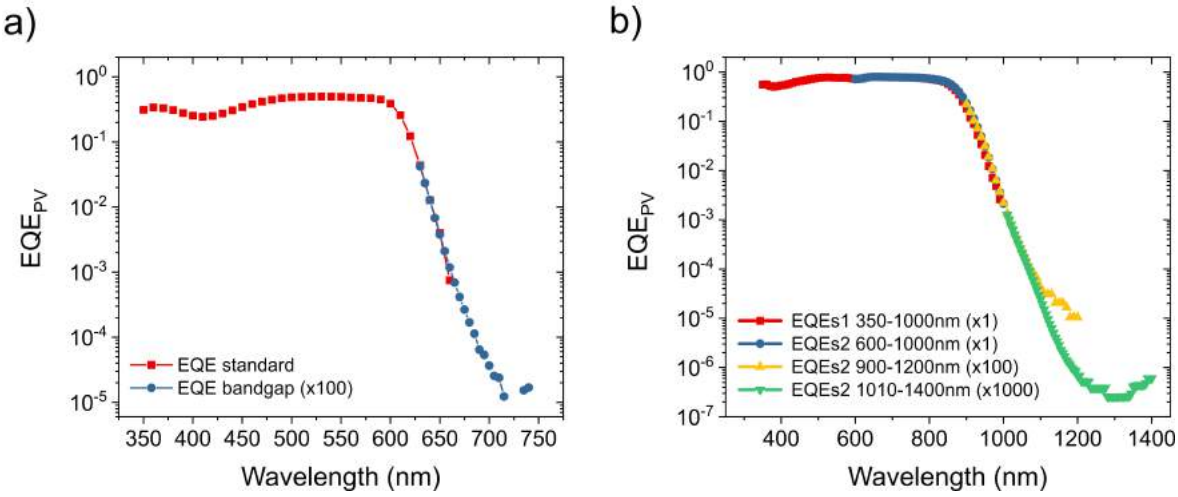

Figure 2.15: Example how full EQE_{PV} spectra are obtained from individual measurements.

Photovoltaic Internal Quantum Efficiency

The internal quantum efficiency (IQE_{PV}) describes the ratio of extracted electrons per absorbed photons and is thus closely related to the previously discussed EQE_{PV} (= extracted electrons per incident photons). The exact number of photons that are absorbed in the solar cell is difficult to determine experimentally. In this thesis, a lower estimate of the IQE_{PV} was derived from EQE_{PV} measurement with a slightly off-axis illumination alignment as shown in Figure 2.16. As depicted, the solar cell is tilted by an angle of 13°, which allows measuring the reflected light intensity. A calibrated Si photodiode was used to calculate the reflected photon flux (Φ_r) using Equation 2.20. In a second measurement, the spectral photocurrent of the OSC is measured. Finally, the initial photon flux Φ_{lamp} is determined using a calibrated Si photodiode. This leads to the reflection corrected version of Equation 2.19:

$$I_{SC}(\lambda) = q\,\mathrm{IQE_{PV}}(\lambda)\Big[\Phi_{lamp}(\lambda) - \Phi_r(\lambda)\Big] \tag{2.22}$$

From this point, the IQE_{PV} is calculated analogously to the described determination of the EQE_{PV} as discussed in the previous section.

It should be emphasized that in this simple model the incident photons are assumed to be either absorbed in the active layer of the solar cell or reflected towards (and detected by) the large area Si photodiode. Moreover, the metal top electrode is assumed to be a perfect mirror with a reflectance of 1.

Therefore the following processes are not considered by the simple model:

- Non-ideal reflection at the metal electrode
- Parasitic absorption in glass, ITO, ETL, HTL, metal electrode
- Scattering
- Light-guiding effects
- PL emission of the solar cell

For an optimized OSC device, the error caused by the listed processes is assumed to be relatively small, and the derived IQE_{PV} values can be used as lower estimates of the actual IQE_{PV} spectra.

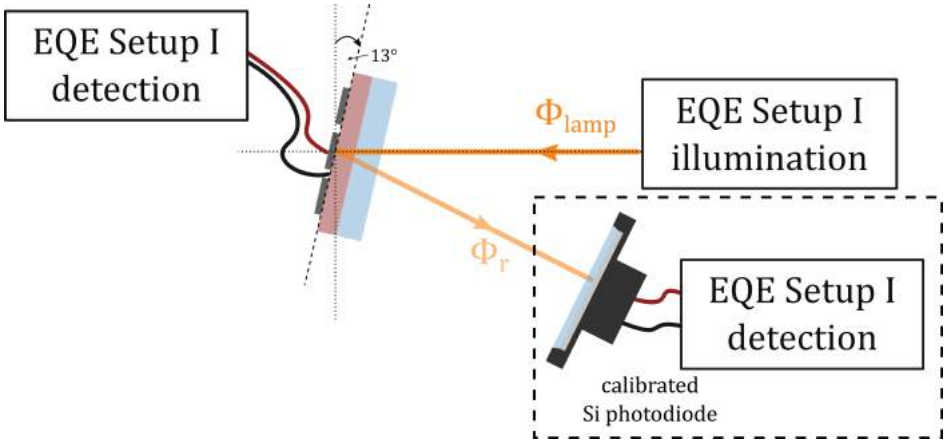

Figure 2.16: Experimental arrangement to measure the IQE_{PV} of organic solar cells using the EQE_{PV} setup described previously.

2.2 Methods

2.2.1 Determination of the Optical Bandgap & CT-State Energy

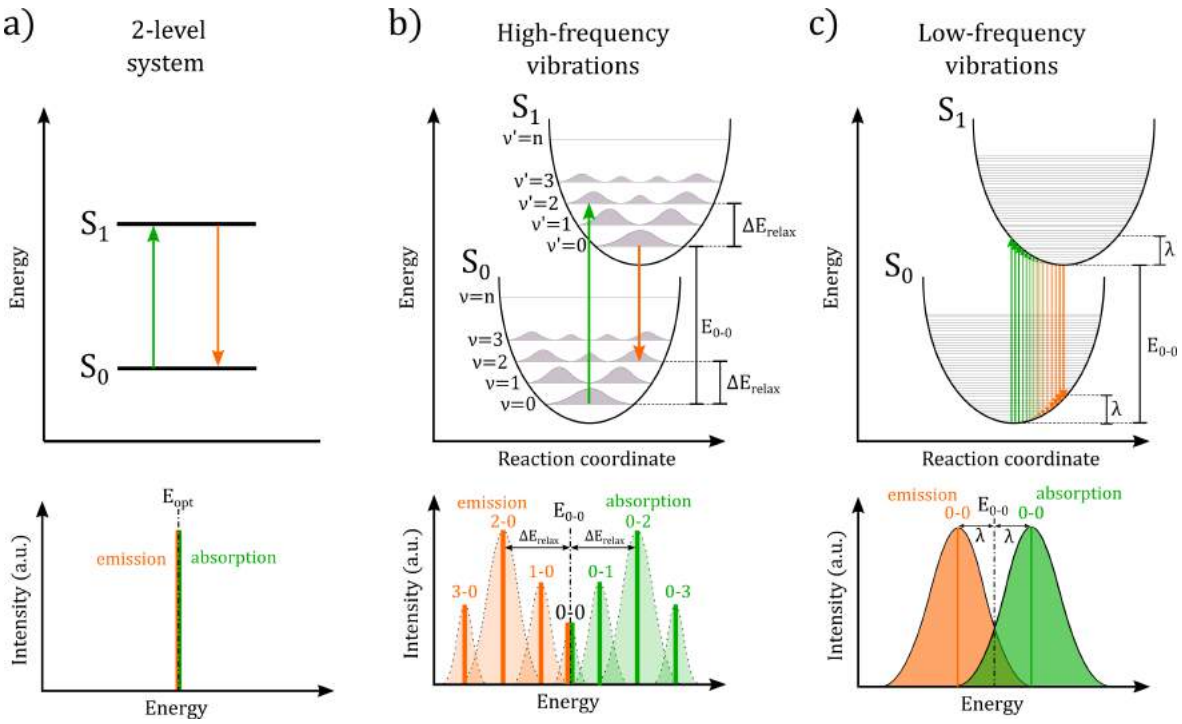

Figure 2.17: Optical transistions in a two level system. a) idealized b) with high-frequency vibrations c) with low-frequency vibrations.

As highlighted in Section 1.4 the high open-circuit voltage loss of organic solar cells can be identified as one of the main factors responsible for the lower power conversion efficiencies compared to inorganic or perovskite PV devices. The total open circuit voltage loss is commonly defined as the difference between the bandgap E_g $/q$ and the V_{OC} of the device. Throughout this manuscript, the bandgap E_g is estimated using the optically determined bandgap value E_{opt}. Therefore, a precise determination of the optical bandgap is of paramount importance for a reproducible and comparable voltage loss analysis of the organic solar cells.

A common method to determine E_{opt} of organic materials is by fitting a linear curve to the exponential decay of the absorption spectrum plotted on a logarithmic scale. The intersection with the abscissa axis or with the tangent of the absorption tail is then identified as the optical bandgap. Relying on this method is subjective and irreproducible.[88] Moreover, this method is prone to errors caused by light scattering (often present in spin-coated thin films) and often severely underestimates the optical bandgap compared to other determination methods.

A variety of alternative methods to determine the optical bandgap more accurately were summarized by Wang and co-workers.[88]

In this thesis, a method developed by Vandewal *et al.* was used to determine the optical bandgaps of the presented OPV materials.[89] In reference[89], the authors first discuss an idealized case for a solar cell with steplike absorption. In this trivial case, E_{opt} can be straightforwardly derived from the absorption spectrum, indicated by the lowest absorbed photon energy (see Figure 2.17a). The absorption spectrum of a solar cell based on real organic materials typically deviates strongly from this ideal behavior due to static and dynamic disorder, CT, and defect states. Absorption and emission spectra of organic materials are characterized by broad absorption and emission peaks. The spectral broadening can be caused by strong electron-phonon coupling and molecular vibrations. These molecular vibrations can be categorized into high- and low-frequency vibrations. As depicted in Figure 2.17b, high-frequency vibrations (e.g. ring breathing modes) lead to discrete absorption and emission peaks and represent optical transitions from discrete vibrational energy levels of ground and excited state. The spacing of these high-frequency modes is much larger than the available thermal energy at room temperature. Therefore, electrons only can populate the lowest energy vibrational level ν=0. Absorption events can promote an electron into one of the vibrational energy levels ν' of the excited state. Due to rapid thermalization (non-radiative relaxation processes), emission only occurs from the lowest vibrational energy level ν'=0 into one of the vibrational energy levels ν of the ground state. Thus, the $E_{0\text{-}0}$ transition energy between the relaxed ground and excited state represents the lowest absorption and highest emission energy. Taking into account low-frequency vibrations, with an energy spacing less than the thermal energy, leads to non-discrete and broad absorption and emission spectra, as shown in Figure 2.17c. The thermal population of vibronic energy levels in the ground and excited-state lead to optical transitions with absorption energies lower and emission energies higher than $E_{0\text{-}0}$. According to Vandewal *et al.*, these low-frequency vibrations can be treated as harmonic oscillators resulting in mirror image Gaussian absorption and emission line-shapes:[89]

$$\frac{1}{E}A(E) \propto \exp\left(\frac{(E - E_{0-0} - \lambda)^2}{4\lambda k_{\mathrm{B}}T}\right) \tag{2.23}$$

$$\frac{1}{E^3}N(E) \propto \exp\left(\frac{(E - E_{0-0} + \lambda)^2}{4\lambda k_{\mathrm{B}}T}\right) \tag{2.24}$$

Hereby, E represents the energy, k_{B} is the Boltzmann constant, T is the temperature and λ is the reorganization energy. It has been shown that the absorption *A(E)* and $\mathrm{EQE_{PV}}$ spectrum for organic solar cells are interchangeable due to rather constant internal quantum efficiencies ($\mathrm{IQE_{PV}}$) in the low-energy region.[90] Similarly, the emission *N(E)* can be identified with EL or PL spectra of the organic materials. Thus, the reduced absorption and emission spectra can be obtained from readily accessible $\mathrm{EQE_{PV}}$ and EL data. As depicted in Equations 2.23 and

2.24 the reduced absorption and emission spectra can be calculated by dividing the measured EQE_{PV} and EL spectra by E and E^3, respectively. It should be noted that even the comparably low EQE_{PV} values of devices based on either pristine donor or acceptor materials allowed to perform the discussed analysis. As an example, the reduced EQE_{PV} and EL spectra of a pristine D18 device are shown in Figure 2.18a. In the absence of an acceptor, absorption and emission are exclusively stemming from the D18 local exciton (LE) state. Equations 2.23 and 2.24 were used to fit the low energy absorption and high energy emission peaks and are depicted as grey dotted parabolas. The used fit parameters are presented in the boxes in the bottom right corner of the graphs. In this case, the derived fitting parameter $E_{0\text{-}0}$ can be identified as the optical bandgap of the pristine material.

For solar cells with a prominent CT state absorption and emission, the equations above can be used to fit the low energy CT absorption and high energy CT emission behavior as shown for D18:$PC_{71}BM$ in Figure 2.18b. In this case, the crossing point $E_{0\text{-}0}$ can be identified as the CT state energy E_{CT}. Thus, the discussed method has been widely used in the field of OPV to determine the E_{CT} of D/A blends. However, with the development of non-fullerene acceptors, the method often cannot provide exact CT state energy values due to the typically weakly pronounced CT absorption and emission features of D/NFA blends. A more detailed discussion is presented in Chapter 5.

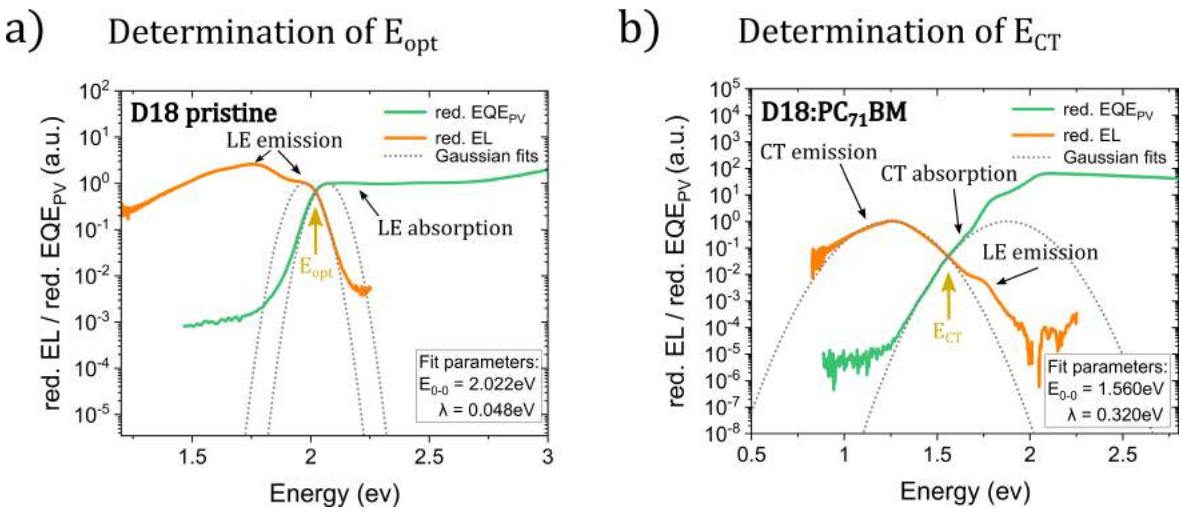

Figure 2.18: Experimental determination of a) E_{opt} and b) E_{CT} using the method by Vandewal.

For the sake of completeness, it should be mentioned that the method discussed by Vandewal *et al.* was only used to derive the optical bandgap of the materials used in the OSCs presented in Chapters 3 and 5. For the material screening (see Chapter 4) a much simpler and less time-intensive method was used. As described in Reference [88] the crossing point of normalized absorption and emission spectra can be used as a first estimate of E_{opt}. Due to the excellent emission properties of the investigated materials, the normalized excitation and

emission spectra were used to estimate E_{opt} of the organic thin films. The use of the excitation rather than the absorbance spectrum eliminates errors caused by light scattering and is thus recommended if highly emissive samples are investigated. The E_{opt} values derived from this method were used to calculate the $LUMO_{opt}$ level of the organic donor and acceptor materials presented in Chapter 4.

2.2.2 Voltage Loss Analysis

Theory

As proposed by Hirst and Ekins-Daukes the open-circuit voltage reduction of an ideal solar cell can be attributed to three contributions.[91] Similar to the assumptions by Shockley and Queisser, "ideal" refers to a solar cell featuring a step like EQE_{PV} spectrum and radiative recombination as the only deactivation mechanism. Once again the derivation assumes a balance of incoming and outgoing photon fluxes as discussed for the derivation of the SQ limit. Under solar illumination the absorption contribution from the T_0=300 K blackbody radiation $\Phi_{\gamma,abs}(E_g, T_0, 0, \Omega_{BB})$ can be neglected for of typical PV materials with bandgaps E_g in the range between 1-2 eV. This leads to a simplified version of Equation 1.42:

$$J(V, E_g) = \Phi_{\gamma,abs}(E_g, T_0, 0, \Omega_{BB}) \exp\left(\frac{qV}{k_B T_0}\right) - \Phi_{\gamma,abs}(E_g, T_S, 0, \Omega_{sun}) \tag{2.25}$$

Per definition $J(V, E_g) = 0$ at open-circuit voltage conditions. Hence, Equation 2.25 can be used to express V_{OC} as:

$$V_{OC} = k_B T_0 \ln\left(\frac{\Phi_{\gamma,abs}(E_g, T_S, 0, \Omega_{sun})}{\Phi_{\gamma,abs}(E_g, T_0, 0, \Omega_{BB})}\right) \tag{2.26}$$

Since Equation 2.26 describes the open-circuit voltage of an ideal solar cell in the SQ limit, the determined V_{OC} value can be interpreted as an upper limit for any real device and is denoted as V_{OC}^{SQ}.

$$V_{OC}^{SQ} = k_B T_0 \ln\left(\frac{\Omega_{abs}}{\Omega_{emit}} \times \frac{\int_{E_g}^{\infty} E^2 \exp\left(\frac{-E}{k_B T_S}\right) dE}{\int_{E_g}^{\infty} E^2 \exp\left(\frac{-E}{k_B T_0}\right) dE}\right) \tag{2.27}$$

$$= k_B T_0 \ln\left(\frac{\Omega_{abs}}{\Omega_{emit}} \times \frac{\gamma(E_g, T_S) \exp\left(\frac{-E_g}{k_B T_S}\right) dE}{\gamma(E_g, T_0) \exp\left(\frac{-E_g}{k_B T_0}\right) dE}\right) \tag{2.28}$$

$$with \quad \gamma(E_g, T) = \frac{2k_B T}{h^3 c^2}(E^2 + 2k_B T E + 2k_B^2 T^2)$$

$$V_{OC}^{SQ} = E_g \left(1 - \frac{T_0}{T_S}\right) - k_B T_0 \ln\left(\frac{\Omega_{emit}}{\Omega_{abs}}\right) + k_B T_0 \ln\left(\frac{\gamma(E_g, T_S)}{\gamma(E_g, T_0)}\right) \tag{2.29}$$

The first term of Equation 2.29 resembles the efficiency formula of a Carnot engine and thus describes the open-circuit voltage loss reduction caused by the temperature difference of the sun (T_S) and the solar cell (T_0). According to Hirst and Ekins-Daukes, the second term is referred to as Boltzmann term, as it resembles Boltzmann's equation representing entropy generation with increased occupancy of available states $\Delta S = k_B \ln\left(\frac{\Omega_{emit}}{\Omega_{abs}}\right)$. The energy flow associated with that entropy generation is given by $T\Delta S$ similar to the second term in Equation 2.29. The third term increases the V_{OC} due to the thermalization process of photons with $h\nu > E_g$, where heat is transferred from the carrier distribution to the lattice. This process reduces the internal energy U of the charge carrier distribution. At the same time, this cooling reduces the entropy of the carrier distribution and partly compensates for the reduction of U leading to a slightly higher free energy per e-h pair. The total entropy of the system (carrier distribution + phonons) still increases in accordance with the second law of thermodynamics.

It should be noted that in the initial assumptions of Shockley and Queisser, cited in Section 1.2.2, the three conditions of a steplike absorption profile, each photon generating one e-h pair and a perfect charge collection can be unified with the assumption of an ideal steplike EQE_{PV}. Therefore, it is possible to replace the absorptance $A(E)$ with the EQE_{PV} spectrum of the solar cell in the definition of $\Phi_{\gamma,abs}$ (see Equation 1.36). In accordance with Equation 2.26, the V_{OC} of a solar cell with an arbitrary EQE_{PV} spectrum can be expressed using Equation 2.30. It should be noted that radiative recombination is still the only recombination mechanism. Therefore, the determined V_{OC} is considered as the radiative limit value of the solar cell V_{OC}^{rad}.

$$V_{OC}^{rad} = k_B T_0 \ln\left(\frac{\int_0^\infty EQE_{PV}(E)\ \Phi_{\gamma,abs}(E_g, T_S, 0, \Omega_{sun})\, dE}{\int_0^\infty \overline{EQE}_{PV}(E)\ \Phi_{\gamma,abs}(E_g, T_0, 0, \Omega_{BB})\, dE}\right) \tag{2.30}$$

In Equation 2.30 $\overline{EQE}_{PV}(E)$ denotes the angularly weighted value of the EQE_{PV}.

Finally, additional non-radiative recombination processes have to be considered in order to describe the experimentally observed V_{OC} values of non-ideal solar cells. The so-called external radiative efficiency (ERE) is defined as the fraction of the total dark current recombination in the device that results in radiative emission from the device. The denominator of Equation

2.30 represents the emission flux of the solar cell and is consequently reduced by the ERE since only a fraction of all the recombination events results in the emission of a photon.

$$V_{\mathrm{OC}} = k_{\mathrm{B}} T_0 \ln\left(\frac{\int_0^\infty \mathrm{EQE_{PV}}(E)\ \Phi_{\gamma,\mathrm{abs}}(E_{\mathrm{g}}, T_{\mathrm{S}}, 0, \Omega_{\mathrm{sun}})\, dE}{\int_0^\infty \mathrm{ERE} \times \overline{\mathrm{EQE}}_{\mathrm{PV}}(E)\ \Phi_{\gamma,\mathrm{abs}}(E_{\mathrm{g}}, T_0, 0, \Omega_{\mathrm{BB}})\, dE}\right) \tag{2.31}$$

$$= k_{\mathrm{B}} T_0 \ln\left(\frac{\int_0^\infty \mathrm{EQE_{PV}}(E)\ \Phi_{\gamma,\mathrm{abs}}(E_{\mathrm{g}}, T_{\mathrm{S}}, 0, \Omega_{\mathrm{sun}})\, dE}{\int_0^\infty \overline{\mathrm{EQE}}_{\mathrm{PV}}(E)\ \Phi_{\gamma,\mathrm{abs}}(E_{\mathrm{g}}, T_0, 0, \Omega_{\mathrm{BB}})\, dE}\right) - k_{\mathrm{B}} T_0 \ln(\mathrm{ERE}) \tag{2.32}$$

The derived quantities $V_{\mathrm{OC}}^{\mathrm{SQ}}$ and $V_{\mathrm{OC}}^{\mathrm{rad}}$ allow us to analyze the individual loss contributions to the total voltage loss $\Delta V_{\mathrm{OC}}^{\mathrm{total}}$ as it will be discussed in the next section.

Practical Use

In the previous section, we have discussed the theoretical foundation of the voltage loss analysis. Here the focus is set on its application to analyze the voltage loss of the organic solar cells presented in this thesis. To do so, a few assumptions and approximations have to be made.

First, it should be noted that the absorption of the earth's atmosphere was neglected in the derivation of the incoming solar radiation by Shockley and Queisser. The atmospheric effect can be easily considered by replacing the solar blackbody spectrum with the conventionally chosen AM1.5G spectrum. Moreover, the ERE is replaced by the closely related and experimentally easier accessible ELQY. $\mathrm{EQE_{PV}}(E)$ spectra are typically measured for near perpendicular illumination, which mimics the absorption of solar radiation. This is not necessarily the case for the absorbed blackbody radiation from the environment or the emitted radiation of the solar cell. Thus, $\overline{\mathrm{EQE}}_{\mathrm{PV}}(E)$ represents the appropriately weighted $\mathrm{EQE_{PV}}$ value over all angles of incident light. For high-quality cells, this will not differ greatly from the near-perpendicular value and is replaced by the measured $\mathrm{EQE_{PV}}$ spectrum throughout this thesis. As described in Section 2.2.1, the optically measured bandgap E_{opt} was used to estimate the bandgap E_{g} of the solar cell. A comparison of the theoretical and experimentally used values is presented in Table 2.1. In addition, the abbreviated expression $\Phi_{\gamma}^{\mathrm{BB300K}}(E)$ is used from now on to represent the blackbody radiation with temperature T_0 = 300 K, chemical potential μ_{eh}=0 and solid angle $\Omega_{\mathrm{BB}} = \pi$.

Table 2.1: Comparison of the physical variables used in the theoretical description of the voltage loss analysis (*cf.* Section 2.2.2) to the experimentally determined or practically used variables.

	Theory variable	Practically used variable
Bandgap	E_g	$E_{\text{opt}}{}^a$
Solar radiation	$\Phi_\gamma(E, T_S, 0, \Omega_{\text{sun}})$	$\Phi_\gamma^{\text{AM1.5G}}(E)$
Blackbody radiation	$\Phi_\gamma(E, T_0, 0, \Omega_{\text{BB}})$	$\Phi_\gamma^{\text{BB300K}}(E)^b$
Fraction of radiative recombination	ERE	ELQY
Angularly weighted EQE_{PV}	$\overline{\text{EQE}}_{\text{PV}}(E)$	$\text{EQE}_{\text{PV}}(E)$

[a] Optical bandgap deterimned following the method described in Section 2.2.1
[b] with $T_0 = 300\,\text{K}$, $\mu_{\text{eh}} = 0$, $\Omega_{\text{BB}} = \pi$

The assumptions in Table 2.1, in combination with Equation 2.31 lead to the following formula initially suggested by Rau:[75]

$$V_{\text{OC}} = \frac{k_B T}{q} \ln\left(\frac{1}{\text{ELQY}} \frac{J_{\text{ph}}}{J_0} + 1\right) \tag{2.33}$$

$$with \quad J_{\text{ph}} = q \int \text{EQE}_{\text{PV}}(E)\ \Phi_\gamma^{\text{AM1.5G}}(E)\, dE \tag{2.34}$$

$$and \quad J_0 = q \int \text{EQE}_{\text{PV}}(E)\ \Phi_\gamma^{\text{BB300K}}(E)\, dE \tag{2.35}$$

In Equations 2.34 and 2.35, J_{ph} denotes the photocurrent and J_0 the dark saturation current. Analogous to the analysis in Section 2.2.2, $V_{\text{OC}}^{\text{SQ}}$, $V_{\text{OC}}^{\text{rad}}$ and V_{OC} can be calculated using the respective assumptions for EQE_{PV} and ELQY, illustrated in Figure 2.19. From an experimental point of view, special emphasis has to be put on the integrand of Equation 2.35, which is used to determine J_0. Due to the exponential increase of the blackbody spectrum ($\Phi_\gamma^{\text{BB300K}}$) towards lower energies, J_0 is dominated by the low-energy tail of the EQE_{PV} spectrum (*cf.* right panel in Figure 2.19). Therefore, high-sensitivity EQE_{PV} measurements over several orders of magnitudes are necessary to perform a reliable estimation of the V_{OC} in the radiative limit.

Considering the derived quantities $V_{\text{OC}}^{\text{SQ}}$ and $V_{\text{OC}}^{\text{rad}}$ allow us to analyze the total voltage losses in organic solar cells. As illustrated in Figure 2.19, $\Delta V_{\text{OC}}^{\text{total}}$ can be expressed in terms of three voltage loss contributions. The individual losses are defined in Equation 2.36:[92]

$$\begin{aligned}
\Delta V_{\text{OC}}^{\text{total}} &= \frac{E_{\text{opt}}}{q} - V_{\text{OC}} \\
&= \underbrace{\left(\frac{E_{\text{opt}}}{q} - V_{\text{OC}}^{\text{SQ}}\right)}_{} + \underbrace{\left(V_{\text{OC}}^{\text{SQ}} - V_{\text{OC}}^{\text{rad}}\right)}_{} + \underbrace{\left(V_{\text{OC}}^{\text{rad}} - V_{\text{OC}}\right)}_{} \\
&= \quad \Delta V_{\text{OC}}^{\text{rad,SQ}} \quad + \quad \Delta V_{\text{OC}}^{\text{rad,b.g.}} \quad + \quad \Delta V_{\text{OC}}^{\text{non-rad}}
\end{aligned} \tag{2.36}$$

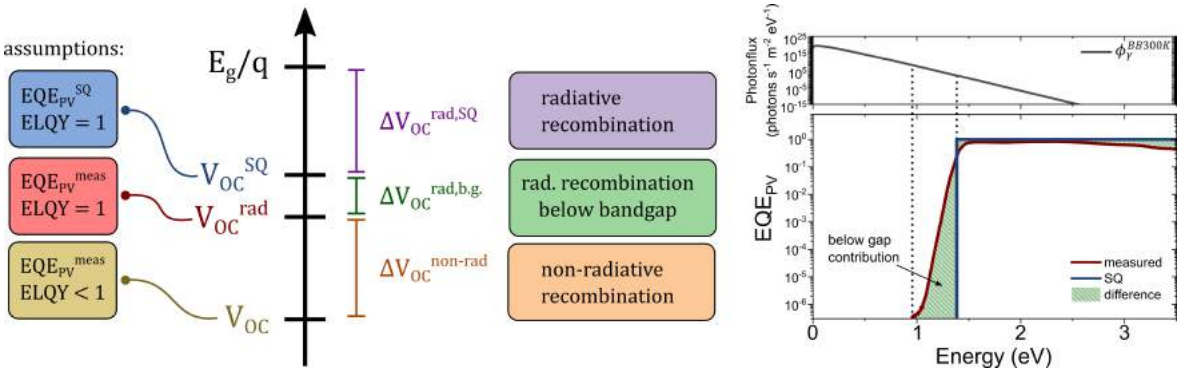

Figure 2.19: Right: Graphical illustration of the derived/measured voltages and the associated voltage loss terms. Left: Difference between an ideal (step-like) EQE_{PV} and a typical measured EQE_{PV} spectrum of an OSC. The inset on the top depicts the exponential increase of the 300 K blackbody spectrum toward lower energies and emphasizes the importance of the below bandgap EQE_{PV} contributions of OSCs (shaded in green).

As discussed in Section 2.2.2, the first loss term ($\Delta V_{OC}^{rad,SQ}$) is a direct consequence of the detailed balance principle described by Shockley and Queisser.[10] Therefore, any solar cell with a distinct bandgap will exhibit an unavoidable voltage loss due to the radiative recombination of charge carriers. Hirst and Ekins-Daukes showed that the loss is solely defined by E_{gap} of the absorber, the temperature difference between sun and earth and the solid angle of absorbed and emitted radiation (see Equation 2.29). $\Delta V_{OC}^{rad,SQ}$ is typically in the range of 0.25-0.3 V.[73] The loss could be further reduced by changing the operating temperature of the cell T_0 or by manipulating Ω_{abs} and Ω_{emit} by improving the light management in the device or by using concentrators.[91] The definition of V_{OC}^{SQ} and V_{OC}^{rad} illustrates that the second loss term ($\Delta V_{OC}^{rad,b.g.}$) is a consequence of the difference between an ideal step-like EQE_{PV}^{SQ} and the experimentally observed EQE_{PV}. For OPV devices, the measured EQE_{PV} often differs substantially from the steep absorption edges found in inorganic direct semiconductors or perovskite solar cells, due to CT-state absorptions or trap states caused by impurities or molecular aggregates. $\Delta V_{OC}^{rad,b.g.}$ can thus be identified as a combination of the radiative recombination losses below the optical bandgap and the difference between J_{SC}^{SQ} and the experimentally observed J_{SC} of the device. The contribution of the latter is rather small and will be neglected in the following.[93] The third term ($\Delta V_{OC}^{non-rad}$) takes into account that not every electron-hole pair recombines radiatively (as assumed by V_{OC}^{rad}) and thus accounts for the open-circuit voltage loss due to non-radiative recombination. Experiments on solar cell devices suggest that non-radiative recombination is far more likely than radiative recombination and accounts for the largest part of the observed voltage loss. With Equation 2.33 the non-radiative voltage loss can be related to the ELQY and be expressed as

$$\Delta V_{OC}^{non-rad} = -\frac{k_B T}{q} \ln(\text{ELQY}) \tag{2.37}$$

Therefore, improving the ELQY of a solar cell directly results in a reduction of the non-radiative voltage loss. A tenfold increase of the ELQY is equivalent to a voltage loss reduction of approximately 0.06 V.

Limitations

The presented voltage loss analysis strongly relies on the optoelectronic reciprocity relations between light-emitting and photovoltaic properties of a solar cell, which link the excess emission flux $\delta\Phi_{\mathrm{em}}$ of a solar cell in forward bias to its photovoltaic quantum efficiency $\mathrm{EQE}_{\mathrm{PV}}(E)$ as shown in Equation 2.38. Building on Equation 2.38 a second reciprocity relation connecting the V_{OC} of a solar cell with its ELQY can be derived as shown in Equation 2.33:

$$\delta\Phi_{\mathrm{em}} = \mathrm{EQE}_{\mathrm{PV}}(E)\ \Phi_{\gamma}^{\mathrm{BB300K}}(E)\left[\exp\left(\frac{qV}{k_{\mathrm{B}}T}\right) - 1\right] \tag{2.38}$$

The expression in Equation 2.38 is closely related to the dark current of a solar cell (*cf.* Equation 1.40). This relationship was used in Equation 2.25 to balance the emitted and absorbed photon fluxes of a solar cell. In Equation 2.25 we implicitly assumed the applicability of the superposition principle, which allows treating the total current in a solar cell as the superposition of the *J-V* characteristics of the solar cell in the dark, shifted by the short circuit current density under illumination. In the presented voltage loss analysis the detailed balance approach for thermal equilibrium conditions is extrapolated to non-equilibrium conditions (semiconductor exposed to solar radiation or charge extraction/injection) and is only valid if the superposition principle is fulfilled. Lindholm *et al.* have shown that the superposition principle is applicable if the continuity equations for electrons and holes are both linear in the respective minority charge carrier concentration.[94] Additionally, they have shown that for Si solar cells these requirements are only fulfilled in the quasi-neutral regions of the pn-junction. In the space charge region, the electric field (dependent on the hole and electron concentrations) introduces nonlinearity into the current density expressions. Furthermore, recombination in the space charge region requires a hole and an electron to meet and is therefore dependent on the product of excess electron and hole concentrations. Thus, the continuity equations for holes and electrons are both nonlinear and superposition does not apply to the junction space charge region. Hence, in systems where the superposition principle breaks down the exploited reciprocity relations in Equations 2.37 and 2.38 will not be strictly valid anymore.

In addition, as discussed by Kirchartz *et al.*, the two reciprocity relations rely on the validity of the Donolato theorem.[95] The theorem is valid if the electrical injection from a junction into a semiconductor can be quantitively related to the charge carrier extraction from the illuminated semiconductor to the junction.[96] In other words, the Donolato theorem specifies that the spatial profile of injected minority carriers is identical to the spatial collection probability

of photogenerated minority carriers in the semiconductor. Similar to the superposition principle, the Donolato theorem can be only derived for the field-free region of a Si pn-junction (e.g. p-base) where the recombination is linearly dependent on the minority carrier concentration. OSCs and thin-film solar cells in general are typically characterized by a large space charge region extending over the entire absorber. As discussed above, in such systems, the applicability of the reciprocity relations will not be strictly valid anymore due to the violation of the superposition principle and the Donolato theorem. Kirchartz *et al.* studied the effect of nonlinear recombination, space charge, and low mobilities on the validity of the Donolato theorem and the two discussed optoelectronic reciprocity relations in organic solar cells.[95] By simulating the spatially averaged collection and injection efficiencies they found that the reciprocity relation shown in Equation 2.37 is affected considerably only at relatively low mobilities and FFs. Thus, the authors suggest the applicability of Equation 2.37 for high-performance organic solar cells. In addition, they state that if nonlinear recombination is combined with space-charge effects, *i.e.*, due to asymmetric mobilities, then the shape of the EL spectrum is no longer directly related to the shape of the solar cell quantum efficiency. However, space-charge effects can be minimized by reducing cell thickness and they find that in particular for typical active layer thicknesses around 100 nm the method should be hardly affected by violations of the Donolato theorem.

Accordingly, various reports have demonstrated the excellent conformity of measured and calculated ELQYs for different OSCs.[51,90,97–99] However, it should be emphasized that the voltage loss analysis and the reciprocity relations are derived for conditions that are not strictly valid for typical OSCs due to violations of the superposition principle and the Donolato theorem. Thus, the derived values should be considered as estimations of the actual voltage losses, which can lead to significant errors, depending on the impact of the violation. It has been shown that the reciprocity relations hold for devices with high and balanced mobilities and/or thin absorber layers (<100 nm). In practice, *J-V* measurements in the dark and under illumination allow us to estimate the violation of the superposition principle by determining their crossing point.[100] For an ideal device where the superposition principle is fulfilled both curves approach asymptotically but do not cross. The closer the crossing point is to the V_{OC} of the solar cell the more severe is the violation of the superposition principle. Moreover, the applicability of the reciprocity relations can be checked if the experimentally observed spectrum (e.g. EQE_{PV}) can be reproduced using the reciprocity relation (e.g. EL/Φ_{BB}).

2.3 Materials & Device Fabrication

As discussed in Section 1.7, typical device geometries of OSCs consist of a stack of several layers. This section gives a general overview of the electrode, ETL, HTL, and absorber

materials used in this thesis. All used materials are summarized in Table 2.2 at the end of this section.

2.3.1 Electrodes

As the name implies, optoelectronic devices such as solar cells or LEDs rely on the interaction (absorption/emission) with light. Thus, transparent conductive materials are indispensable in allowing light to enter or exit the device. Transparent conductive oxides (TCOs) like indium tin oxide (ITO), fluorine-doped tin oxide (FTO), or aluminum-doped zinc oxide (AZO) are commonly deployed in optoelectronic applications. Organic materials such as graphene, carbon nanotube networks, or transparent conducting polymers (e.g. PEDOT:PSS) provide an alternative to TCOs. Moreover, metal grids or ultrathin metal films are often used to obtain transparent electrodes for semi-transparent devices. In this thesis, the presented organic solar cells were exclusively fabricated on glass substrates with a 100 nm thick ITO film as the bottom electrode and with a 100 nm thick metal film as the top electrode. The metal electrodes were thermally evaporated on top of the absorber layer/HTL/ETL of the cells using a shadow mask. For the OSCs in this thesis aluminum (Al) and silver (Ag) were used as metal top contacts.

2.3.2 Hole & Electron Transport Layers

In this thesis, several electron and hole transport layers were used. The precursor preparation and typical fabrication conditions are discussed in the next section. As touched upon previously, the choice of the appropriate hole and electron transport layers between the absorber layer and the electrodes is essential to achieve optimal device performance.

Electron Transport Layers

A common strategy to achieve an ohmic contact between the metal top electrode and the LUMO of most fullerene, as well as non-fullerene acceptors, is to insert a thin, low-work function metal layer to decrease the high work function (WF) values of commonly used electrode materials (e.g. Al or Ag). Unless otherwise stated, a roughly 10-20 nm thick, thermally evaporated calcium layer with a low work function of 2.9 eV[101] was used as ETL in this thesis to form selective electron extracting contacts. The thin calcium layer was exclusively used in combination with evaporated Al electrodes. The evaporation of the ETL and the electrode were performed consecutively and without breaking the vacuum

($< 5 \times 10^{-5}$ mbar). Alternatively, conductive conjugated polymers, metal oxides, or non-conjugated polymers are widely used as ETLs in OSCs.[80] The alternative ETL materials used in this thesis are discussed in the following.

The typically large structural differences between fullerene and non-fullerene acceptors (e.g. shape, size, anisotropy) can affect the working mechanism and effectiveness of established ETLs developed for fullerene-based solar cells. Thus, the advent of non-fullerene acceptors has promoted an increased development of novel ETL materials.[80] N-type perylene diimide-based ETLs (e.g. PDIN, PDINO) have shown excellent compatibility with state-of-the-art non-fullerene acceptors based on the Y-series. The chemical structure of N,N′-Bis[3-(dimethylamino)propyl]perylene-3,4,9,10-tetracarboxylic diimide (PDIN) is presented in Figure 2.20. PDIN was purchased from 1-material Inc. and was dissolved in a mix of methanol and glacial acetic acid with a volume ratio of 1000:3 to obtain a solution with a concentration of 2 mg/mL. The addition of acetic acid significantly increases the solubility of PDIN in methanol due to the protonation of the side-chain amino groups. The solution was spincoated on top of the active layer using a spin speed of 5000 rpm for 30 s. The optimized film thickness was too thin to perform reliable measurements with the profilometer. The estimated thickness is below 10 nm.

An alternative, widely used solution-processed ETL material is the polyfluorene derivative PFN-Br. The chemical structure of poly(9,9-bis(3'-(N,N-dimethyl)-N-ethylammoinium-propyl-2,7-fluorene)-alt-2,7-(9,9-dioctylfluorene))dibromide is depicted in Figure 2.20. PFN-Br was purchased from 1-material Inc. and was used as received. It was dissolved in methanol with a concentration of 0.5 mg/mL. After continuous stirring at RT for ∼12 h, PFN-Br was fully dissolved and a clear solution was obtained. Spincoating at 2000 rpm for 30 s led to a optimized thickness of ∼10 nm.

A non-conjugated polymer, which has been successfully used to decrease the work function of electrode materials is polyethyleneimine (PEI). In this thesis, the PEI derivative polyethyleneimine-ethoxylated (80 %) (PEIE) was used. The material is dissolved in water with a concentration of 37 %w/w. Methanol was used as a solvent to prepare a 5 mg/mL PEIE master solution in MeOH with small residues of water (∼0.83 %v/v).

Widely used solution-processed ETLs for OSCs in the inverted device geometry are zinc oxide (ZnO) thin films, which among other techniques can be obtained from a low-temperature sol-gel method.[102,103] A ZnO precursor solution was prepared by dissolving 0.5 g zinc acetate dihydrate in 5 mL 2-methoxyethanol and 148 µL ethanolamine. The precursor was vigorously stirred at room temperature for at least 12 h to form a clear and homogenous solution. Moreover, the solution was stirred in air to promote the hydrolysis reaction described in Reference [104]. Before spin-coating, the precursor solution was filtered with a PVDF syringe filter with a pore size of 0.45 µm. The spincoating recipe comprised of a ramp up periode with 1500 rpm for 2 s followed by the main 4000 rpm, 20 s step.

Hole Transport Layers

In contrast to ETLs, HTLs were mainly unaffected by the development of non-fullerene acceptors, since the same or similar donor polymers have been used in combination with both acceptor families. Thus, two established HTL materials were used throughout this thesis depending on the desired device geometry (conventional or inverted). The transparent conductive polymer poly(3,4–ethylenedioxythiophene):polystyrene sulphonate (PEDOT:PSS) is widely used in organic optoelectronic or flexible electronic applications. Its chemical structure is presented in Figure 2.20. For this thesis, the aqueous PEDOT:PSS dispersion Clevios™ P VP Al 4083 from Heraeus was used as a hole transport layer on top of ITO coated glass substrates for solar cell devices in the conventional geometry. The dispersion was filtered with a 0.45 µm PES filter before use. PEDOT:PSS was spin-coated at ambient conditions and room temperature for 45 s/3000 rpm/1500 rpm s^{-1}. After the spin-coating process, the PEDOT:PSS films were annealed at 150 °C for 10 minutes to evaporate residual water in the PEDOT:PSS film. The optimal film thickness of PEDOT:PSS lies between 30 and 50 nm. For solar cells in the inverted device geometry a thin (∼10 nm), thermally evaporated molybdenum oxide (MoO_{3-X}) film was used as HTL. The high work function transition metal oxide MoO_{3-X} forms a good electrical contact with the HOMO energy levels of common donor polymers. In this thesis, MoO_{3-X} was exclusively used in combination with a silver top electrode. Both materials were sequentially evaporated in a one-step evaporation process using a shadow mask. The evaporation was performed at pressures below 5×10^{-5} mbar and without breaking the vacuum.

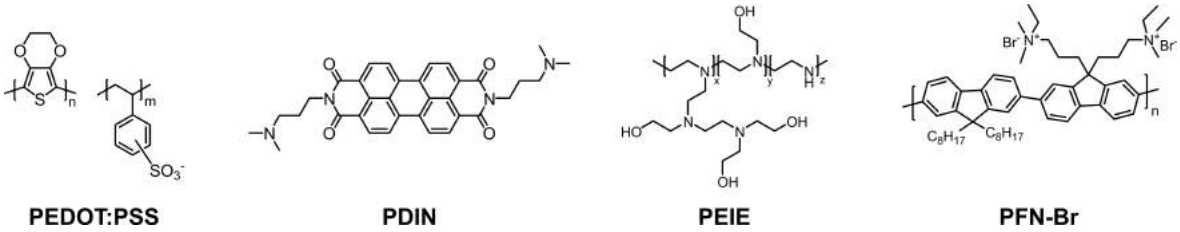

Figure 2.20: Chemical structure of the polymer or small molecule HTLs and ETLs used throughout this thesis.

2.3.3 Absorber Materials

This section gives an overview of all the commercially available donor and acceptor materials that were used in this thesis. As listed in Table 2.2 all the OPV materials were purchased from 1-material Inc. except for $PC_{71}BM$, which was obtained from Solenne BV. All materials were used as received and without further purification. The non-commercial, novel NFA materials of Prof. Trimmel's group will be discussed separately in Chapter 4. It should be emphasized

that solar cells based on the donor polymer D18 and the acceptors Y6 and $PC_{71}BM$ were the main focal point of Chapter 3 and are therefore discussed in greater detail.

D18

The wide bandgap donor polymer D18 was first reported by Liu *et al.* and is characterized by an extremely deep HOMO level and excellent hole mobilities.[42,43] As presented in Figure 2.21, D18 is a D-A copolymer based on an electron-donating BDT monomer (4,8-bis(5-(2-ethylhexyl)-4-fluorothiophen-2-yl)benzo[1,2-b:4,5-b']dithiophene) and an electron-withdrawing DTBT monomer (dithieno[3',2':3,4;2'',3'':5,6]benzo[1,2-c][1,2,5]thiadiazole) linked with 2-(2-butyloctyl)thiophene π-bridges in the backbone. At the beginning of 2020, the combination of D18 and Y6 marked the first time OSCs exceeded the 18 % efficiency mark.

Y6

Y6 and its derivatives represent the emerging class of A-DA'D-A type fused-ring electron acceptors characterized by strong NIR absorption, high electron affinity, and excellent tunability of their optoelectronic properties. The rise of these high-performance acceptors has accelerated OPV development and has repeatedly enabled efficiencies beyond 18 %. The narrow bandgap, poster molecule Y6 employs a ladder-type multi-fused ring with an electron-deficient core as a central unit and was first reported by Yuan and co-workers.[41] As shown in Figure 2.21, its highly symmetrical core can be considered as an electron-deficient benzothiadiazole center, fused with two identical electron-rich thienothienopyrrole units (BTP). The fused-ring core of Y6 is capped with two identical electron-withdrawing end groups based on 2-(3-oxo-2,3-dihydroinden-1-ylidene)malononitrile (INCN).

$PC_{71}BM$

Before the development of efficient NFAs, fullerene derivatives were the unrivaled acceptor materials for organic solar cells due to their strong electron affinity and excellent electron transport properties. The soluble C_{60} derivative, [6,6]-phenyl-C_{61}-butyric acid methyl ester ($PC_{61}BM$)[105] developed into one of the most popular acceptor materials and was used in combination with various donor polymers.[106] In addition to the beneficial electrical properties of $PC_{61}BM$, its unsymmetrical counterpart $PC_{71}BM$ shows an enhanced absorption in the visible region and is therefore the most desirable choice for highly efficient fullerene-based OSCs.[107] Hence, throughout this thesis, solar cells based on the acceptor material $PC_{71}BM$ were chosen as representatives for the class of fullerene-based organic solar cells.

Alternative Donors and Acceptors

The other commercial donors and acceptors shown in Figure 2.21 appear sparingly throughout this thesis and are therefore only shown for the sake of completeness. For more information on these materials, the reader is referred to references[55,108–112].

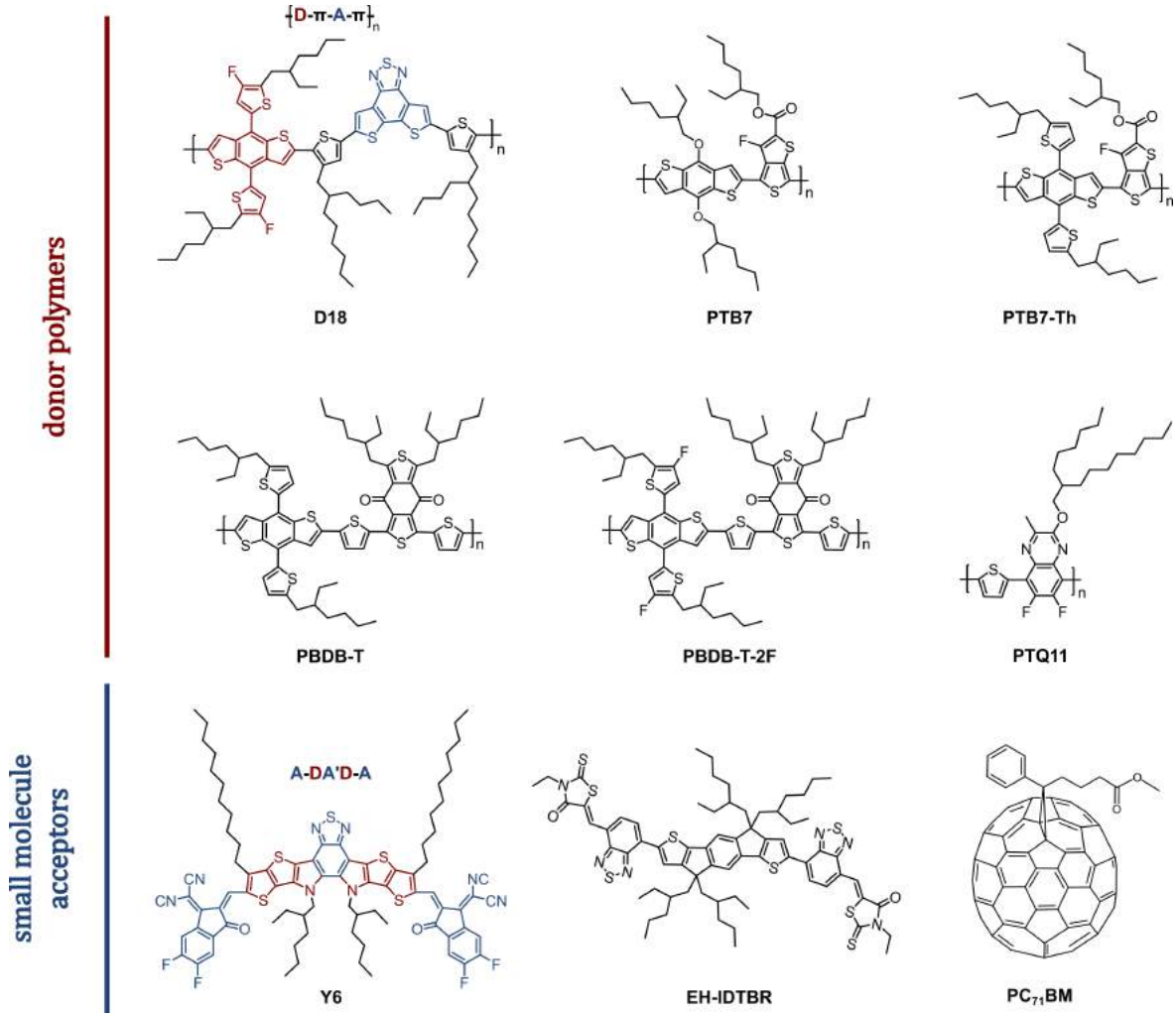

Figure 2.21: Chemical structure of investigated OPV materials.

2.3.4 List of Used Materials

Table 2.2: Summary of all the commercial materials and solvents used in this thesis.

PV Materials	Formula	CAS	Vendor	Grade
D18	see Fig. 2.21	2433725-54-1	1-material	-
PTB7	see Fig. 2.21	1266549-31-8	1-material	-
PTB7-Th	see Fig. 2.21	1469791-66-9	1-material	-
PBDB-T	see Fig. 2.21	1802013-83-7	1-material	-
PBDBT-2F	see Fig. 2.21	1802013-84-8	1-material	-
PTQ11	see Fig. 2.21	-	1-material	-
Y6	see Fig. 2.21	2304444-49-1	1-material	>99%
EH-IDTBR	see Fig. 2.21	2102510-60-9	1-material	-
PC71BM	see Fig. 2.21	609771-63-3	Solenne BV	-

Solvents	Formula	CAS	Vendor	Grade
Chloroform	$CHCl_3$	67-66-3	Sigma Aldrich	>99%
Chlorobenzene	C_6H_6Cl	108-90-7	Sigma Aldrich	99.8%
Methanol	CH_3OH	67-56-1	VWR	-
Acetic Acid	$C_2H_4O_2$	64-19-7	Merck	-
2-Methoxyethanol	$C_3H_8O_2$	109-86-4	Sigma Aldrich	99.8%
Ethanolamine	C_2H_7NO	141-43-5	Sigma Aldrich	99.5%

Interlayer materials	Formula	CAS	Vendor	Grade
PEIE, 80 % ethoxylated (37 wt.% solution in H_2O)	see Fig. 2.20	26658-46-8	Sigma Aldrich	-
PFN-Br	see Fig. 2.20	889672-99-5	1-material	-
PDIN	see Fig. 2.20	117901-97-0	1-material	>99%
Zinc acetate dihydrate	$ZnC_4H_8O_4{\cdot}H_2O$	5970-45-6	Fluka	>99%
Calcium	Ca	7440-70-2	Sigma Aldrich	99.99%
Molybdenum oxide	MoO_3	1313-27-5	Alfa Aesar	99.9995%
PEDOT:PSS (Clevios™ P VP Al4083)	see Fig. 2.20	155090-83-8	Heraeus	-

Electrode materials	Formula	CAS	Vendor	Grade
Silver pellets	Ag	7440-22-4	-	-
Aluminum wire	Al	7429-90-5	Chempur	99.999%

Electrochemistry	Formula	CAS	Vendor	Grade
Acetonitrile	CH_3CN	75-05-8	VWR	>99.9%
Tetrabutylammonium hexafluorophosphate ($TBAFP_6$)	$C_{16}H_{36}F_6NP$	3109-63-5	Sigma Aldrich	99.0%
Ferrocene (Fc)	$C_{10}H_{10}Fe$	102-54-5	Sigma Aldrich	98%

Chapter 3

Understanding the low voltage losses in high-performance non-fullerene acceptor-based organic solar cells

J. Hofinger, C. Putz, F. Mayr, K. Gugujonovic, D. Wielend and M. C. Scharber

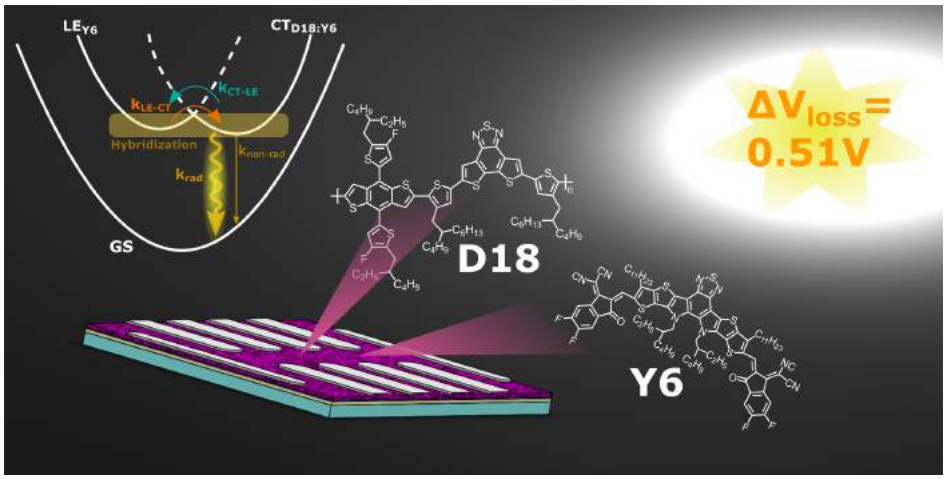

The results of this chapter have been published in:

Materials Advances, 2021, **2**, 4291-4302
DOI: https://doi.org/10.1039/D1MA00293G

3.1 Abstract

Despite the rapid increase in power conversion efficiency (PCE) of non-fullerene acceptor (NFA) based solar cells in recent years, organic photovoltaic (OPV) devices exhibit considerably larger voltage losses compared to their highly-efficient inorganic counterparts (e.g. Si or GaAs). Further material optimizations and strategies to reduce the voltage losses in OPV systems are required to close the gap to inorganic PV technologies and allow for efficiencies surpassing 20 %. The main focus of this study is on understanding the voltage losses in high-performance NFA-based solar cells, as furthering the knowledge in this area is critical in promoting their recent success. In this article, the open-circuit voltage losses observed in high-performance D18:Y6 organic solar cells with a PCE of 16 % are investigated in detail. The voltage losses of D18:Y6 devices are compared to fullerene devices consisting of D18 and $PC_{71}BM$ in order to highlight the differences between non-fullerene and fullerene acceptors. A low open-circuit voltage loss of 0.51 V has been found for Y6-based devices suggesting a 0.29 V lower voltage loss compared to $PC_{71}BM$-based devices (0.8 V). The observed differences can be explained by the high-lying charge-transfer state energy in Y6-based solar cells and the strong emissivity of the pristine acceptor. Both properties seem to be prerequisites for efficient OPV systems with low voltage losses. Based on the experimental results, we suggest two design strategies to further improve the performance of OPV systems.

3.2 Introduction

As discussed in Chapter 1, the efficiencies of photovoltaic devices based on organic semiconductors[113–115], typically consisting of a conjugated polymer (donor) blended with a solution-processable fullerene derivative (acceptor), increased steadily until a plateau of approximately 12 % was reached.[28,29] The limited performance can be mainly attributed to the weak optical absorption and the wide (indirect) bandgap of fullerenes. The recent development of efficient non-fullerene acceptors (NFAs) featuring strong optical absorption marked the beginning of a new OPV era.[30] In 2015 Lin *et al.* reported the fused-ring (indacenodithieno[3,2-b]thiophene core) acceptor-donor-acceptor (A-D-A) molecule ITIC with strong near-infrared (NIR) absorption and high electron mobility.[33] The reported power conversion efficiency (PCE) of 6.8 % for the ITIC-based solar cell was still inferior to its fullerene counterparts. Due to the development of new non-fullerene acceptors with improved NIR-light-harvesting properties and readily-tunable electronic energy levels, the PCEs of NFA-based solar cells have increased substantially over the last five years up to efficiencies of 15-18 %.[35–42] At the beginning of 2020, Liu *et al.* reported a record-breaking PCE of 18.2 % (17.6 % certified) for the donor polymer D18 blended with the high-performance NFA Y6.[43]

As a consequence of the rapid success of NFA-based solar cells, the fundamental understanding of these new acceptors is lagging behind. For the design of new NFAs, it is crucial to identify the relevant mechanisms and properties, which enable the high performance of current NFA-based solar cells. The described voltage analysis (see Section 2.2.2), based on the readily accessible EQE_{PV} spectrum of the solar cell, provides a reliable tool to gain insights into the loss processes, which are an important aspect that separates NFA-based from fullerene-based devices. Herein, we aim to thoroughly investigate the photovoltaic performance and optical properties of the current record-breaking polymer:NFA system D18:Y6 reported by Liu *et al*.[43]. The study by Liu *et al*. is mainly focused on device optimization and gives a detailed analysis of the influence of processing conditions on the photovoltaic parameters of D18:Y6 solar cells. To the best of our knowledge, a thorough analysis of the observed voltage losses for a better understanding of the material combination D18:Y6 has not been reported yet and is the motivation for this work.

In order to investigate the properties that elevate D18:Y6 devices from other systems, high-performance D18:Y6 solar cells were fabricated and compared to their fullerene counterparts based on D18:$PC_{71}BM$. For both systems, current density - voltage (*J-V*) curves and the corresponding photovoltaic parameters under AM1.5G illumination and in the dark are shown in this work. Moreover, highly-sensitive EQE_{PV} measurements, as well as photo- and electroluminescence measurements of blend and pristine devices are presented. Based on these results, the described V_{OC} loss analysis was performed to quantify the differences in radiative and non-radiative recombination for D18:Y6 and D18:$PC_{71}BM$ solar cells. The non-radiative losses were validated with ELQY measurements, and the solar cell performance of both devices was evaluated by comparison to their maximal achievable performance defined by the SQ limit. Based on the results, two design strategies are formulated to further improve the V_{OC} of NFA-based solar cells, aiming towards efficiencies surpassing the 20 % mark.

3.3 Experimental Note

This section provides additional experimental details relevant for this chapter, which have not been discussed in the general experimental section in Chapter 2.

Addendum Materials & device preparation

The materials used for D18:Y6 solar cell preparation (D18, Y6, and PDIN) were purchased from 1-materials, while the $PC_{71}BM$ was purchased from Solenne BV. Pre-patterned ITO glass was thoroughly cleaned by wiping it with toluene followed by subsequent ultrasonication in Hellmanex (2 %v/v solution in deionized water, approx. 50 °C), 2x Milli-Q water, acetone, and isopropanol for 15 min each. After blow-drying with N_2, the cleaned substrates were

plasma treated for 5 min (O_2, 100 W). Next, 0.45 µm filtered PEDOT:PSS (Clevios Al4083) was spin-coated onto the substrates for 45 s with 3000 rpm in ambient conditions resulting in films with a thickness of 30-40 nm. The thickness was determined with a DekTak profilometer. The active layer solutions D18:Y6 and D18:$PC_{71}BM$ were prepared in chloroform with a D/A ratio of 1:1.6. The concentration of D18:Y6 was 7-11 mg/mL while the concentration of D18:$PC_{71}BM$ was 9 mg/mL. The active layer was spin-coated in a glovebox under a dry nitrogen atmosphere using various spin speeds ranging from 1000-5000 rpm resulting in active layer film thicknesses from 55 nm to 190 nm. As a next step, a thin (<10 nm) PDIN layer was spin-coated on top of the active layer with 5000 rpm for 30 s. The PDIN solution was dissolved in a mix of methanol and acetic acid (100 %) with a volume ratio of 1000:3 and a concentration of 2 mg/mL. As the last step, 100 nm Ag electrodes were thermally evaporated at a pressure < 10^{-6} mbar. A homemade shadow mask was used to define the evaporated electrodes resulting in an active device area of 0.173 cm^2. All cells were encapsulated in the glovebox using a UV-curable epoxy sealant. The UV-exposure time was approximately 5 minutes.

Addendum: EQE_{PV}

All the EQE_{PV} spectra presented in this study are superpositions of several EQE_{PV} measurements using the two experimental setups described in Section 2.1.3. The presented, highly sensitive EQE_{PV} spectra typically consists of 4 individual measurements with different amplification factors and overlapping spectral measurement regions: (1) 350-1000 nm ($\times 10^4$), (2) 600-1000 nm ($\times 10^4$), (3) 900-1200 nm ($\times 10^6$) and (4) 1010-1400 nm ($\times 10^9$). During measurements with high amplification (10^6 - 10^9) either an 800 nm LP or a combination of 800 nm LP and 1000 nm LP-filter were used to reduce stray light and improve the signal/noise ratio of the setup. As shown in Figure S3.5b the individual EQE_{PV} measurements coincide well and their large spectral overlaps allow to reliably combine the individual measurements.

Addendum: Photoluminescence & Electroluminescence

Photoluminescence and electroluminescence measurements of all the devices were acquired using the setup described in Section 2.1.2. For the PL measurements, the devices were excited using an OBIS 488 nm LX150mW solid-state laser with a wavelength of 488 nm. The optical output power was set to 1 mW. A 550 nm LP-filter was used for luminescence spectra recorded with the Si-CCD and a 795 nm LP-filter was used for measurements with the InGaAs detector array. The LP filters in front of the monochromator successfully suppressed the 488 nm laser light and allowed the acquisition of a PL spectrum without the influence of the excitation light or emission contributions from second-order diffraction. Thus, a spectral measurement window from 550-1050 nm and 800-1500 nm was realized for the Si-CCD and the InGaAs

detector array, respectively. Due to the strong NIR emission of Y6, the presented emission spectra are a superposition of the Si-CCD and InGaAs detector array measurements. For EL measurements the injection currents were kept low and typically did not, or just barely exceed the observed photocurrents under AM1.5G illumination.

3.4 Results & Discussion

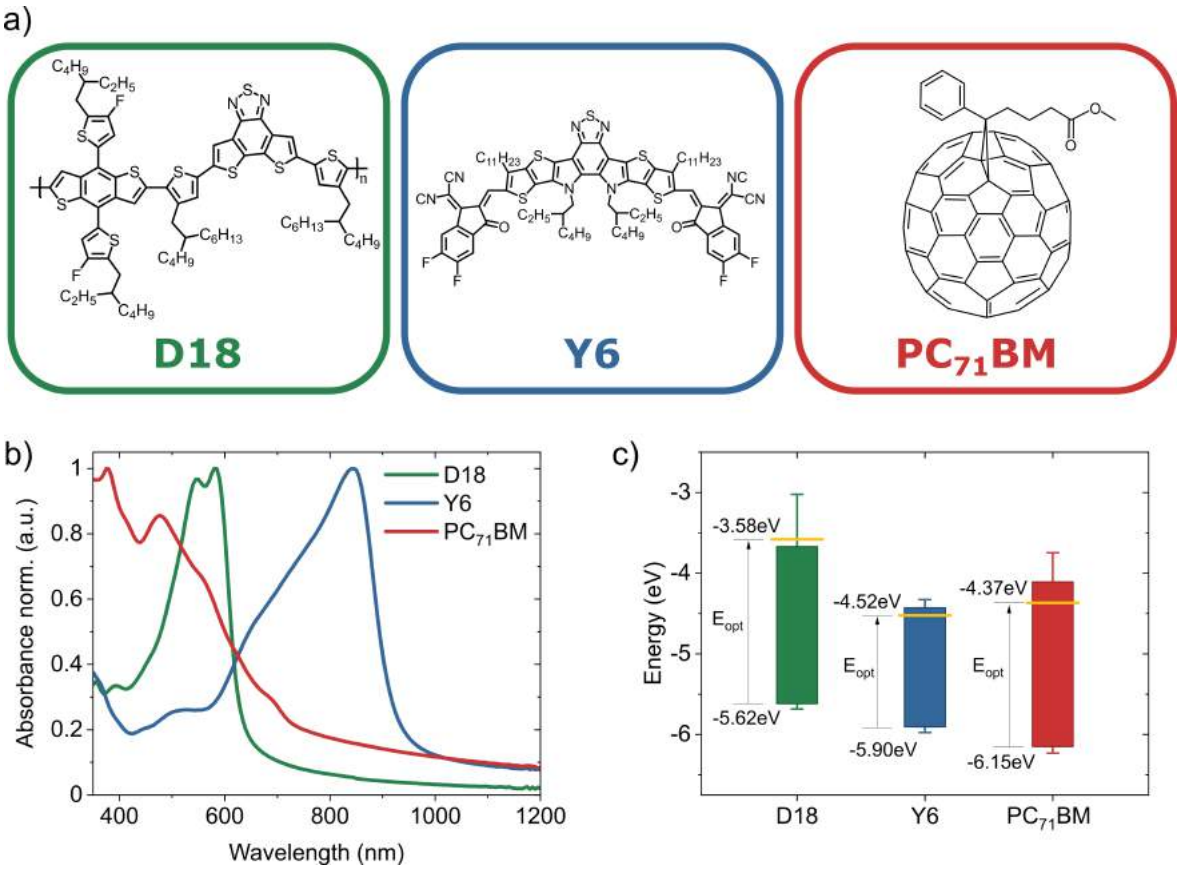

Figure 3.1: Chemical structure, optical and electrochemical characterizations. a) Molecular structure of the used OPV materials. b) UV-vis-NIR absorbance spectra of D18, Y6, and $PC_{71}BM$ thin films on glass. c) Electrochemical estimations of HOMO and LUMO levels of the used OPV materials.

The chemical structures of the investigated OPV materials are presented in Figure 3.1a. The D-A copolymer D18 is a wide bandgap donor with strong absorption in the visible light spectrum, whereas the Y6 non-fullerene acceptor has a complementary narrow bandgap, enabling light gathering in the NIR-region as shown in the absorbance spectra in Figure 3.1b. In contrast, $PC_{71}BM$ (red curve in Figure 3.1b) shows high absorption only in the UV and blue region of the visible light spectrum and exhibits only weak absorption in the range between 600-700 nm, which can be attributed to partly forbidden optical transitions near the band

edge observed in fullerene molecules.[116,117] In addition to the optical absorbance, HOMO and LUMO levels of the molecules were measured electrochemically using electrochemical voltage spectroscopy (EVS). The slow, stepwise variation of the applied potential in EVS measurements allows the system to be close to thermodynamic equilibrium, which reduces dynamic influences such as the scan speed in standard CV measurements. The EVS measurements of the investigated materials are shown in Figure S3.1. HOMO levels of -5.62 eV, -5.90 eV, and -6.15 eV and LUMO levels of -3.58 eV, -4.52 eV, and -4.37 eV have been found for D18, Y6, and $PC_{71}BM$ respectively and are presented in Figure 3.1c. Considering a typical error margin of ± 0.1 eV for electrochemical measurements[85], the electrochemical bandgaps are in good agreement with the optical absorption onsets.

To evaluate the photovoltaic performance of D18:Y6, solar cell devices with the structure of ITO/PEDOT:PSS/D18:Y6/PDIN/Ag were fabricated. The device geometry and chemical structures of PEDOT:PSS and PDIN are presented in Figure S3.2. Different concentrations of the active layer solution and different spin speeds were used to fabricate devices with various thicknesses (see Figure S3.3 & S3.4. In Table S3.1 the photovoltaic parameters of D18:Y6 devices with various thicknesses are presented. PCEs typically varied between 14-16 %. Hence, a cell with an efficiency close to 15.2 % (see Table 3.1) was chosen as a typical representative of the fabricated D18:Y6 solar cells, which has been investigated and characterized in detail. Based on earlier results, an optimized D/A ratio of 1:1.6 was used.[43] To keep processing as simple as possible, no additives, post-annealing, or solvent annealing steps were performed. The best device showed a good photovoltaic efficiency of approximately 16 % with a high open-circuit voltage of 0.87 V, a short-circuit current of 25.2 mA/cm^2 and an electrical fill factor of 73.6 %. Table 3.1 shows that our results are in good agreement with the National Institute of Metrology (NIM) certified photovoltaic parameters reported earlier.[43] The difference in PCE is mainly caused by the reduced FF, which might be related to minor differences in the fabrication process and solar cell geometry. Interestingly, for some devices a, V_{OC} as high as 0.88 V was measured, suggesting that the full PCE potential of the D18:Y6 system might not have been reached yet.

Table 3.1: Measured and earlier reported photovoltaic parameters of D18:Y6 and D18:$PC_{71}BM$ solar cells. Equation 2.34 was used to calculate the short circuit current density ($J_{SC,EQE}$) from the measured EQE_{PV} spectrum. The values of $J_{SC,EQE}$ are presented in parentheses. Average values and standard deviations were calculated from at least 10 cells.

Material	V_{OC} (V)	J_{SC} ($mA\,cm^{-2}$)	$J_{SC,EQE}$ ($mA\,cm^{-2}$)	FF (%)	PCE (%)	Source
D18:Y6 (lit.)	0.84	26.67	-	78.4	17.6	[43]
D18:Y6 (best)	0.87	25.24	24.70	73.6	16.1	This work
D18:Y6 (ave.)	0.87±0.01	24.46±0.92	23.48	70.5±0.63	15.2±0.51	This work
D18:$PC_{71}BM$ (ave.)	0.98±0.01	11.26±0.49	11.15	71.4±1.52	8.0±0.49	This work

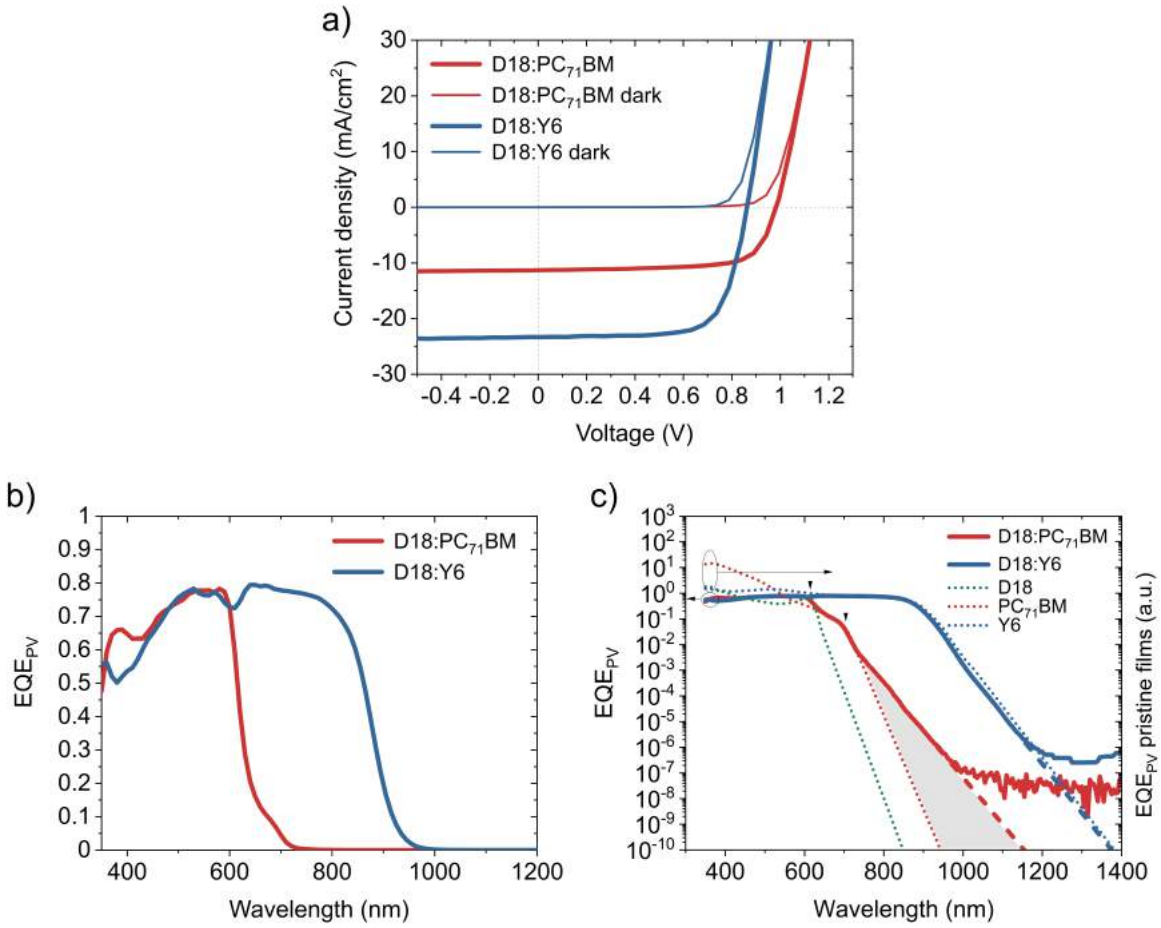

Figure 3.2: Photovoltaic characterization. a) Current density - voltage (*J-V*) curves of typical D18:Y6 and D18:$PC_{71}BM$ solar cells in the dark and under AM1.5G illumination (100 mW cm^{-2}). b) High-sensitivity EQE_{PV} spectra of typical D18:Y6 and D18:$PC_{71}BM$ solar cells on a linear scale. The black circle highlights the EQE contribution of the low absorption of $PC_{71}BM$. c) High-sensitivity EQE_{PV} spectra of typical D18:Y6, and D18:$PC_{71}BM$ solar cells presented on a semi-logarithmic plot (left axis). The dotted curves represent the (linearly extended) EQE_{PV} spectra of pristine D18, Y6, and $PC_{71}BM$ devices in arbitrary units (right axis). The small black triangles indicate the band edge of pristine D18 and $PC_{71}BM$. The grey area under the D18:$PC_{71}BM$ curve (solid red line) illustrates the additional CT-absorption observed in fullerene-based devices.

Following the successful fabrication of high-performance, state-of-the-art solar cells with PCE >15 %, the devices were compared to fullerene-based solar cells with the same device structure (ITO/PEDOT:PSS/D18:$PC_{71}BM$/PDIN/Ag) and D/A ratio (1:1.6). Throughout this report, the results measured for two representative solar cells, one for the Y6-based and one for the $PC_{71}BM$-based devices, are presented and compared in detail. *J-V*-curves were recorded under AM1.5G illumination and in the dark for both devices and are presented in Figure 3.2a, while the corresponding photovoltaic parameters are highlighted in Table 3.1. The fullerene device shows a superior V_{OC}, but at the same time, its J_{SC} is approximately

50 % lower compared to the Y6 device. Both solar cells exhibit a high FF of more than 70 %, indicating efficient charge transport through the device.

High-sensitivity EQE_{PV} measurements were performed for both solar cells and are shown in Figure 3.2b&c on a linear and logarithmic scale, respectively. The EQE_{PV} comparison on the linear scale indicates an almost identical behavior of fullerene and non-fullerene devices in the region of strong light absorption of the donor polymer D18 between 425-600 nm. EQE_{PV} values > 75 % suggest good charge generation and high collection efficiency for both acceptors. Due to the strong absorption of $PC_{71}BM$ below 425 nm, the EQE_{PV} of the fullerene device is larger in comparison to the NFA device in this region. Similarly, the shoulder in the D18:$PC_{71}BM$ EQE_{PV} spectrum at 675 nm can be attributed to the pristine $PC_{71}BM$ absorption (see Figure 3.1b). Furthermore, the EQE_{PV} spectra clearly illustrate the big advantage of the Y6 acceptor, namely its strong absorption in the NIR region, enabling efficient light-harvesting until approximately 920 nm. The semi-logarithmic plot of the high-sensitivity EQE_{PV} measurements reveals the sub-bandgap EQE_{PV} behavior over several orders of magnitude, which plays a critical role in determining the photovoltaic performance of the solar cells. As described in the methods, combining a monochromator, additional long-pass filters, and an external preamplifier with a phase-sensitive lock-in measurement technique allows us to reliably determine the EQE_{PV} of the solar cells over a range of 6-7 orders of magnitude. For both solar cells, the EQE_{PV} values >1000 nm for the fullerene device and >1200 nm for the NFA device are considered as limited by the sensitivity of the measurement. To calculate the dark saturation current J_0 using Equation 2.35, a linear function was fitted to the tail of the EQE_{PV} spectrum (dashed lines in Figure 3.2c) to avoid distortion of the determined J_0 values by measurement noise. For this method, we assume that the main physical behavior of the system is already described by the measured EQE_{PV}, and no physically relevant contributions are hidden below the sensitivity limit of the experimental setup. In addition to the EQE_{PV} spectra of the investigated organic solar cells, Figure 3.2c shows the EQE_{PV} of the pristine materials (dotted curves). An active layer of pure D18, $PC_{71}BM$, or Y6 was used for the pristine devices, while the contacts and interlayers were identical to the ones from fullerene and non-fullerene solar cell devices (ITO/PEDOT:PSS and PDIN/Ag). The EQE_{PV} spectra of the neat materials are presented in arbitrary units and scaled to fit the EQE_{PV} spectra of the blend devices. For the sake of visibility, the linearly extended EQE_{PV} of the pristine devices is depicted in Figure 3.2c. A comparison of the measured and linear extended EQE_{PV} of the pristine devices is presented in Figure S3.5a. The EQE_{PV} spectrum of the D18:$PC_{71}BM$ solar cell exhibits two distinct kinks at approximately 600 and 700 nm highlighted by small black triangles, which correspond to the absorption edges of the pristine materials. Figure 3.2c shows a pronounced deviation of the sub-bandgap EQE_{PV} behavior (> 800 nm) of D18:$PC_{71}BM$ from the EQE_{PV} of the pristine $PC_{71}BM$ device (red dotted curve). The deviation is highlighted by the grey area under the EQE_{PV} spectrum of D18:$PC_{71}BM$. This additional absorption below the bandgap of the pristine materials

is typical for polymer:fullerene solar cells and can be attributed to CT-state absorption. In contrast, no such additional absorption is found for D18:Y6 solar cells, suggesting a high-lying CT state close to the energy levels of the pure Y6 acceptor.

Complementary to the EQE_{PV} measurements, electroluminescence (EL) and photoluminescence (PL) spectra of the pristine and blend devices were recorded and are presented in Figure 3.3a&b. For the non-fullerene devices (Figure 3.3a), there is no observable difference between EL and PL spectra, suggesting that the recombination process upon charge injection or light stimulation involves the same energetic states. Moreover, the close resemblance of the luminescence spectra of the D18:Y6 device and the pristine Y6 device indicates that in highly-efficient D18:Y6 solar cells, the radiative recombination process is dominated by the energy levels of the pure Y6 acceptor. In addition to EL and PL spectra, the emissivity of the solar cell (EM_{EQE}) is shown (yellow line in Figure 3.3a&b). The EM_{EQE} can be calculated as the product of the measured EQE_{PV} spectrum and the black body spectrum at 300 K. Excellent agreement of the calculated EM_{EQE} with the measured EL and PL spectra is found for both Y6-based devices. The PL spectra (light red curves) of both fullerene-containing devices (pristine $PC_{71}BM$ and D18:$PC_{71}BM$) in Figure 3.3b are similar in shape, with the exception of an additional peak at 625 nm for the D18:$PC_{71}BM$ device. During PL measurements the high-energy laser light, which is used to excite the sample (λ=488 nm), predominantly leads to localized excitons on the pure donor or acceptor molecules. Thus, the PL spectrum of the D18:$PC_{71}BM$ blend device resembles the PL emission peaks of pure D18 (625 nm) and $PC_{71}BM$ (715 and 780 nm). The emission spectra of the pristine D18 device are presented in Figure S3.6. In contrast, the EL spectra (red curves) of both fullerene-containing devices vary clearly in position and shape. Direct comparison of the EL maxima of the pure and blend device indicates a significant redshift from 828 nm to 966 nm. In polymer:fullerene solar cells, this behavior can be assigned to the formation of a pronounced CT-state, which is in good agreement with the previously presented EQE_{PV} data. In the top graph in Figure 3.3b, the EM_{EQE} of the pristine $PC_{71}BM$ device resembles the observed PL spectrum. The EL spectrum exhibits peaks at the same spectral positions, but with different relative intensities. PL and EL measurements are used to analyze the light emitted due to radiative recombination of either electrically injected (EL) or optically excited (PL) charge carriers. Optically excited charge carriers usually recombine within the typical exciton diffusion length of the organic materials, while electrically injected charge carriers can recombine anywhere within the organic thin film, depending on the injection properties of the electrodes and the hole and electron mobilities of the materials. Thus, the observed differences in intensity of EL and PL measurements could be caused by interference effects, resulting from different recombination positions within the film. In the bottom graph in Figure 3.3b, the EM_{EQE} of the D18:$PC_{71}BM$ blend resembles the measured EL spectrum of the CT-state, which can be attributed to light emission from the CT state and suggests that the electrically injected charge carriers recombine predominantly via the CT state.

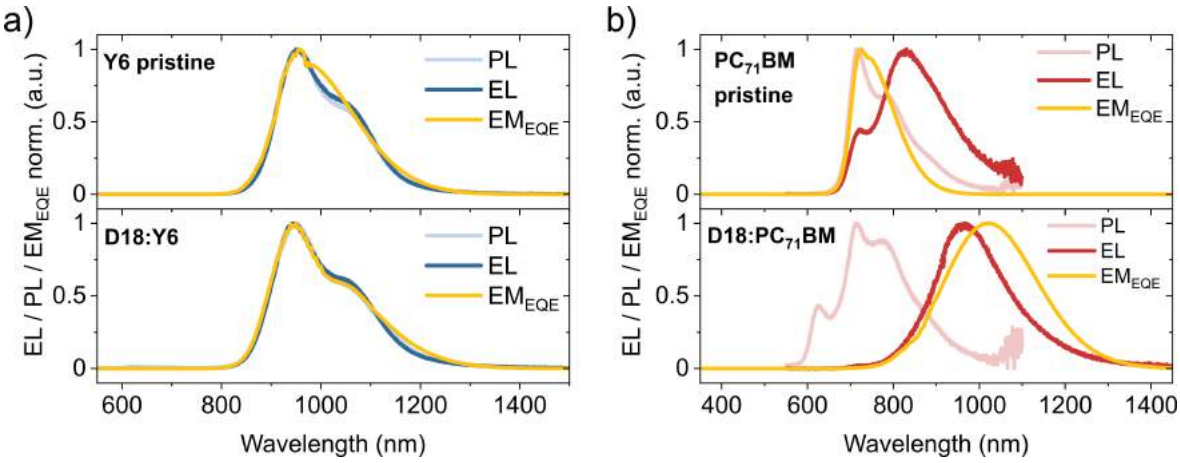

Figure 3.3: Photo- and electroluminescence characterizations. a) EL (blue) and PL (light blue) spectra of non-fullerene-based devices (pristine Y6 and D18:Y6). b) EL (red) and PL (light red) spectra of fullerene-based devices (pristine $PC_{71}BM$ and D18:$PC_{71}BM$). Additionally, the EM_{EQE} spectra (calculated from the EQE_{PV}) for all devices is presented (yellow curves) and compared to the measured EL and PL spectra.

3.4.1 CT-state & Voltage Loss Analysis

As discussed in Section 2.2.1, the measured EQE_{PV} and EL spectra of the pure donor and acceptor materials can be used to identify their optical bandgaps following the procedure developed by Vandewal and co-workers.[89] The reduced high-energy EL and low-energy EQE_{PV} peaks were fitted with Equations 2.23 and 2.24, and the determined fitting parameter $E_{0\text{-}0}$ was used to estimate the optical bandgaps. As presented in Figure S3.7, the bandgap energies of D18, Y6, and $PC_{71}BM$ are 2.02, 1.38, and 1.78 eV, respectively.

The presented EL and EQE_{PV} measurement data suggest a strong influence of the CT-state in the fullerene-based device. Thus, the method by Vandewal *et al*. based on the reduced emission and reduced absorption spectrum was performed to determine the CT-state energy of the D/A blends as described in Section 2.2.1. The reduced EL and reduced EQE_{PV} spectra of the D18:Y6 and D18:$PC_{71}BM$ solar cells are presented in Figure 3.4. According to Equation 2.24, values for $E_{0\text{-}0}$ and λ were determined for the two blends by performing a two-parameter fit in the high-energy region of the reduced EL spectrum using a Levenberg-Marquardt iteration algorithm. The fitting interval is set to match the high-energy tail of the relevant electronic state with the lowest energy. Therefore, the high-energy tail of the CT-state emission of the D18:$PC_{71}BM$ device has to be considered for the fit, as shown in Figure 3.4b. The absence of a pronounced CT-emission of the D18:Y6 device suggests to fit the Gaussian curves to the high-energy tail of the emission spectrum, as presented in Figure 3.4a. The corresponding fit results are shown in the insets in Figure 3.4 and were used to calculate the Gaussian curves (dashed parabolas) using Equations 2.23 and 2.24. The EQE_{PV}

spectra were scaled to fit the calculated Gaussian curves for the reduced absorption. The E_{CT} analysis quantitatively confirms the previously described assumption of a high-lying CT state for the D18:Y6 solar cell, since the derived E_{CT} value of 1.38 eV is essentially identical to the observed optical bandgap of the neat Y6 absorber. Furthermore, the analysis of the fullerene-based solar cell suggests an E_{CT} value of 1.56 eV, which is lower than the optical gap of $PC_{71}BM$ (E_{gap} = 1.78 eV) and is expected to significantly influence the observed optical and photovoltaic parameters of the solar cell.

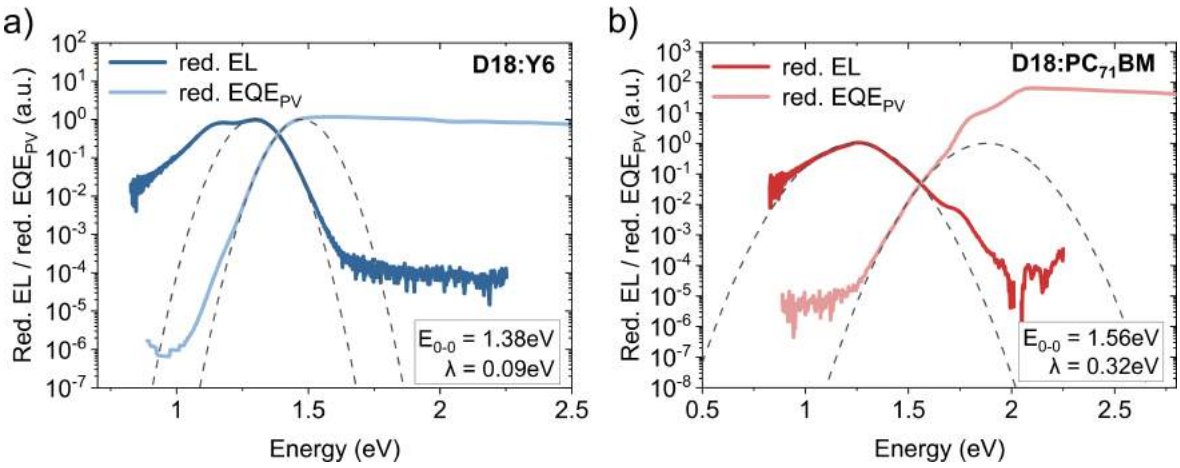

Figure 3.4: Analysis of the CT-state energy. a) Reduced EL and reduced EQE_{PV} spectra of the D18:Y6 device. b) Reduced EL and reduced EQE_{PV} spectra of the D18:$PC_{71}BM$. Equation 2.24 was used to fit the reduced EL spectrum. The fitted parameters for E_{CT} and λ are presented in the small insets. The dashed parabolas were calculated via Equations 2.23 and 2.24 using the derived fit parameters.

A substantial drawback of organic solar cells compared to other photovoltaic technologies is the high voltage loss (ΔV_{OC}^{total}), resulting in moderate V_{OC} values. The total voltage loss is defined as the difference between the optical bandgap (E_{gap}/q) and the measured V_{OC} of the photovoltaic device. In this study, the optical bandgap of the small bandgap absorber is defined as the resulting optical gap of the D/A blend. The measured V_{OC} values presented in Table 3.1 and the obtained optical gaps of pristine Y6 and $PC_{71}BM$ from Figure S3.7 allow us to calculate a total voltage loss of 0.51 and 0.80 V for the Y6-based and fullerene-based device, respectively.

In the following, we will perform a detailed analysis (see Section 2.2.2) to quantify the contributions of the individual loss terms (as shown in Equation 2.36) to the observed total voltage losses and to emphasize the differences between D18:Y6 and D18:$PC_{71}BM$ devices. The highly-sensitive EQE_{PV} measurements presented in Figure 3.2c were used to calculate V_{OC}^{rad} by substituting Equations 2.34 and 2.35 into Equation 2.33 and assuming ELQY=1. The V_{OC}^{SQ} was determined using the same set of equations but replacing the measured EQE_{PV} with an ideal step-function EQE, solely defined by the optical gaps of pure Y6 (E_{gap}=1.38 eV) and

$PC_{71}BM$ (E_{gap}=1.78 eV). The results of the voltage loss analysis based on Equation 2.36 are summarized in Table 3.2 and presented graphically in Figure 3.5a. The data shows that the increased total voltage loss in the fullerene-based device results from an increased $\Delta V_{OC}^{rad,b.g.}$ (0.17 V), as well as an increased $\Delta V_{OC}^{non-rad}$ (0.33 V) compared to the Y6-based device (0.04 and 0.20 V). The comparatively high voltage loss due to radiative recombination below the bandgap in D18:$PC_{71}BM$ solar cells is a result of the pronounced CT-state absorption below the $PC_{71}BM$ bandgap as highlighted in Figure 3.2c (grey area). On the contrary, the absence of a clear CT-state absorption feature in the EQE_{PV} and a steep absorption edge (resembling the one of pure Y6) of the D18:Y6 solar cell translates to a small $\Delta V_{OC}^{rad,b.g.}$ of 0.04 V. It should be emphasized that this result is comparable to the values reported for solar cells based on inorganic semiconductors like c-Si (0.01 V)[118] or GaAs (0.008 V)[97]. The enhanced non-radiative recombination loss in the D18:$PC_{71}BM$ device can be related to the formation of a prominent CT-state. As seen from the EL measurements (Figure 3.3b), the weak CT-state emission dominates the luminescence spectrum, whereas the emission of the D18:Y6 device is almost identical to the EL of the pure Y6 acceptor device. To the best of our knowledge, a $\Delta V_{OC}^{non-rad}$ value of 0.20 V for the D18:Y6 device is one of the lowest ever reported for organic solar cells, closing the gap to c-Si solar cells ($\Delta V_{OC}^{non-rad}$ = 0.18 V).[118]

Table 3.2: Comparison of the voltage losses of D18:Y6 and D18:$PC_{71}BM$ solar cells.

Material	E_{opt}/q (V)	$\Delta V_{OC}^{rad,SQ}$ (V)	V_{OC}^{SQ} (V)	$\Delta V_{OC}^{rad,b.g.}$ (V)	V_{OC}^{rad} (V)	$\Delta V_{OC}^{non\text{-}rad}$ (V)	V_{OC} (V)	ΔV_{OC}^{total} (V)
D18:Y6	1.38	0.27	1.11	0.04	1.07	0.20	0.87	0.51
D18:$PC_{71}BM$	1.78	0.30	1.48	0.17	1.31	0.33	0.98	0.80

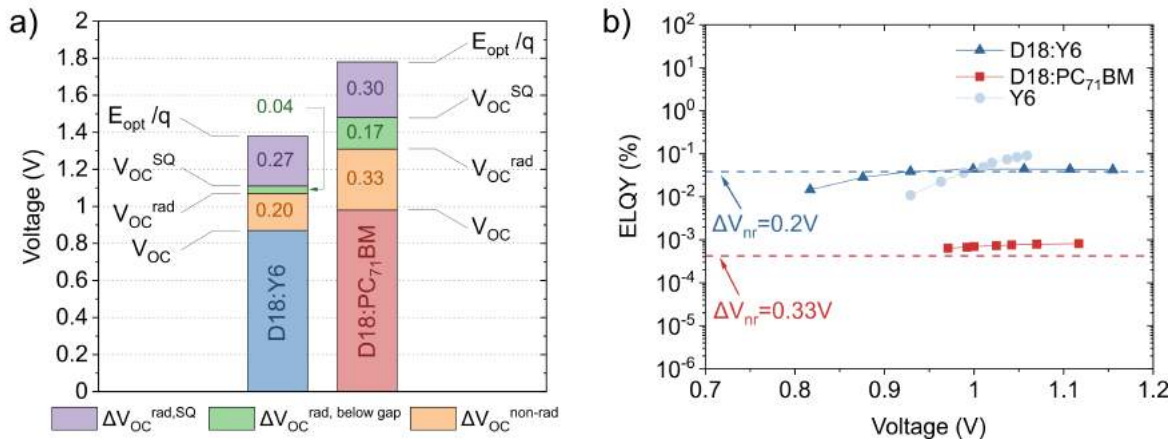

Figure 3.5: Voltage loss diagram and ELQY measurements: a) Illustration of the voltage losses derived for D18:Y6 and D18:$PC_{71}BM$ solar cells. The data is presented in Table 3.2. b) ELQY measurements of D18:$PC_{71}BM$, D18:Y6, and pristine Y6 devices. The dashed lines represent the ELQY values calculated via Equation 2.37, assuming a non-radiative voltage loss of 0.20 V and 0.33 V, respectively.

In order to validate the voltage loss analysis, ELQY measurements of D18:Y6, D18:$PC_{71}BM$, and pristine Y6 were performed. The ELQY values measured at different applied voltages are presented in Figure 3.5b. The non-radiative voltage losses for D18:Y6 and D18:$PC_{71}BM$ were used to calculate the respective ELQY values using Equation 2.37. The calculated ELQY values are indicated by the dashed lines in Figure 3.5b. The good agreement of measured and calculated ELQY data indicates the validity of the performed analysis.

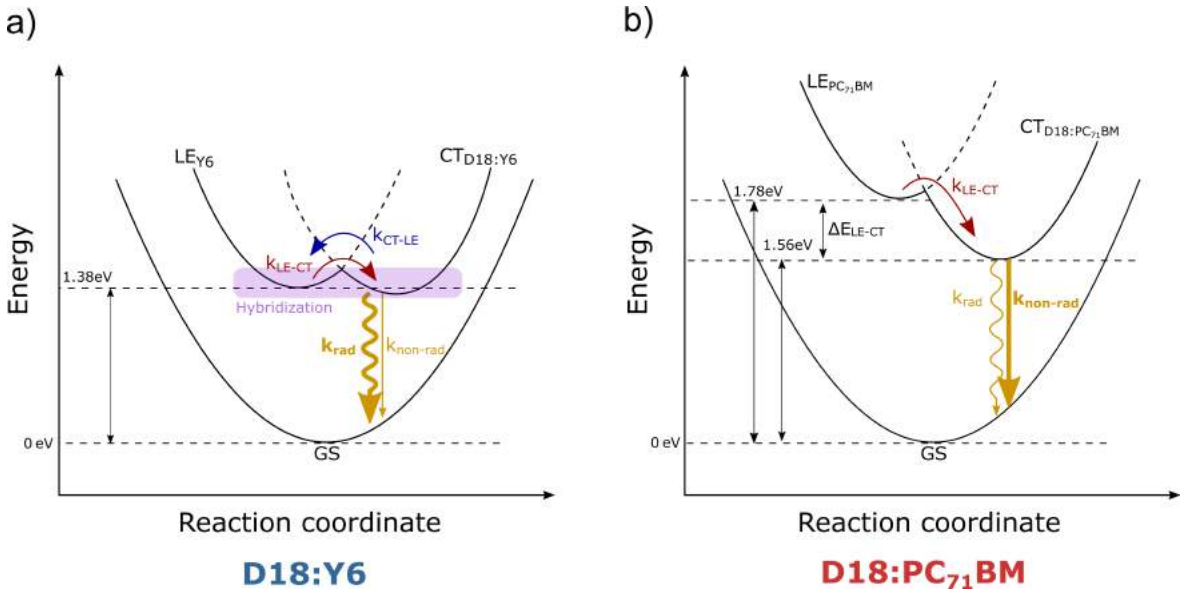

Figure 3.6: Schematic sketch of the three-state model for D18:Y6 and D18:$PC_{71}BM$ solar cells. a) The relevant electronic states of D18:Y6 solar cells according to the three-state model. The high-lying CT state leads to an increased hybridization with the LE-state of the Y6 molecule. Due to the contribution of the high-emissive local exciton (LE) state of Y6 the radiative recombination rate (k_{rad}) is increased. b) The pronounced CT-state in D18:$PC_{71}BM$ solar cells leads to a larger ΔE_{LE-CT} offset and reduces the hybridization. Due to the weakly-emissive LE-state of $PC_{71}BM$ and the reduced hybridization, an increased non-radiative voltage loss is observed.

In addition, the presented results are in excellent agreement with the findings reported by Qian *et al.*[119], which highlight the importance of a high-lying CT state for low non-radiative voltage losses. As a consequence of the high-lying CT state, the widely used two-state Mulliken-Hush model has to be adapted to a three-state model, including the influence of the strongly absorbing local-exciton (LE) state.[77] A sketch of the three-state model for D18:Y6 and D18:$PC_{71}BM$ solar cells is presented in Figure 3.6. According to the three-state model, small energy offsets between the lowest energy LE and CT states (ΔE_{LE-CT}) can result in hybridization between LE and CT states. For small ΔE_{LE-CT} systems, transitions from the CT state back to the LE state are allowed and provide an additional radiative recombination pathway. Due to the typically high-emissive nature of the LE state an increased radiative, and a decreased non-radiative recombination rate are expected, resulting in a relatively large

ELQY (reduced $\Delta V_{OC}^{non-rad}$). In the fullerene-based device, the hybridization is reduced due to an increased $\Delta E_{LE\text{-}CT}$ offset of 0.22 eV. The lowest energy LE state in the D18:$PC_{71}BM$ device is defined by the LE state of the fullerene. The resulting CT-state shows very moderate emissivity due to the low oscillator strength of the partly forbidden optical transitions in fullerene molecules. Therefore, the ELQY is expected to be severely reduced in comparison to the Y6-based solar cell, which is confirmed by the increased non-radiative voltage loss shown in Table 3.2 and the significantly lower ELQY values presented in Figure 3.5.

3.4.2 Efficiency Limit & Optimization Potential

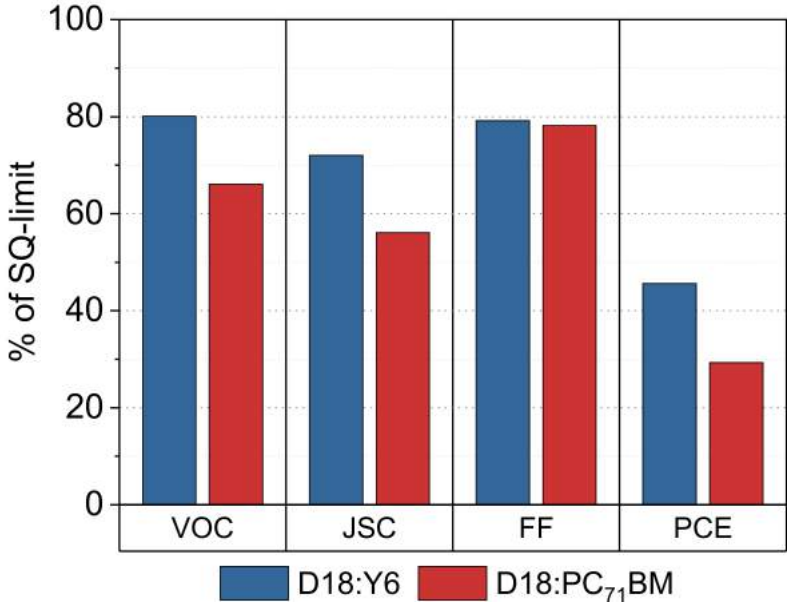

Figure 3.7: Relative photovoltaic performance with respect to the SQ limit. The relative photovoltaic parameters of D18:Y6 and D18:$PC_{71}BM$ in % of their respective values in the SQ limit.

In the following, we try to estimate upper-efficiency limits for D18:Y6 solar cells and discuss potential optimization strategies to further improve the performance of this material combination. The fundamental limit for any solar cell with a defined bandgap is the Shockley Queisser limit.[10] Knowledge of the optical bandgaps of D18:Y6 and D18:$PC_{71}BM$ blends allows the determination of power conversion efficiencies in the SQ limit PCE^{SQ} of 33.1 % and 27.2 %, respectively. To compare the performance of the solar cells regarding their fundamental limit, the measured photovoltaic parameters were normalized by the respective photovoltaic parameters in the SQ limit (see Table S3.2). Figure 3.7 presents the measured photovoltaic parameters (V_{OC}, J_{SC}, FF, PCE) in % of the SQ limit. The reduced voltage loss in Y6-based devices leads to an impressive value of 80 % of its V_{OC}^{SQ}, while the fullerene-based device barely reaches 65 %. Moreover, Figure 3.7 shows that the J_{SC} is comparatively higher

for D18:Y6. The low J_{SC} for D18:$PC_{71}BM$ is a result of the limited optical absorption of the fullerene, which severely limits the EQE_{PV} beyond the absorption of D18. Both devices reach approximately 80 % of their FF^{SQ}. For D18:Y6 solar cells, this leads to a relative PCE of almost 50 % of its SQ limit. The fullerene-containing device is limited to approximately 30 % of its PCE^{SQ}.

While J_{SC} and FF of D18:Y6 solar cells can be improved by optimizing the fabrication process to improve parameters such as film thickness, morphology, domain sizes, light management, etc., the V_{OC} is mainly limited by the previously discussed voltage losses, which are a result of fundamental properties of the investigated materials. Reducing the total voltage loss in OPV will be critical to push organic solar cell efficiencies beyond 20 %. To achieve higher V_{OC}s, further improvements in the synthesis of high-performance donor and acceptor materials are needed. Based on the presented results, two strategies to improve the V_{OC} of D18:Y6 solar cells are suggested in the following.

Several reports have shown high-efficiency OPV material combinations where the measured $HOMO_D$ - $HOMO_A$ offset (Δ_{HOMO}) between donor and acceptor is almost zero.[55–58] Considering the presented HOMO levels for D18 and Y6 suggests a Δ_{HOMO} offset of 0.28 eV. Carefully reducing the Δ_{HOMO} offset (without affecting the bandgaps) results in a larger $HOMO_D$-$LUMO_A$ difference, which could potentially result in a higher V_{OC}. Minor chemical modifications to either reduce the HOMO level of D18 or to increase the LUMO level of Y6 (without changing E_{gap}) could help to increase the V_{OC} of solar cells based on D18 and Y6 derivatives. An optimum balance has to be found since the Δ_{HOMO} offset is considered as the driving force for charge separation. A too low offset could result in a reduced IQE_{PV}. A recent study by Karuthedath *et al*. on several OPV materials showed a strong correlation between the Δ_{HOMO} offset and the observed IQE_{PV}.[74] Their results suggest high IQE_{PV}'s of almost 100 % for D/A blends with a Δ_{HOMO} offset >0.5 eV. Below this value, the IQE_{PV} is reduced rapidly to values lower than 50 %. A minimal Δ_{HOMO} offset of 0.5 eV is contradicting the high-performance systems reported earlier with a Δ_{HOMO} offset close to 0 eV.[55–58] It should be noted that the HOMO levels reported by Karuthedath *et al*. were measured with ultraviolet photoelectron spectroscopy (UPS), while for the reports with $\Delta_{HOMO} \approx 0$ eV, the energy levels were determined using cyclic voltammetry (CV). Various reports point out large discrepancies between HOMO levels derived by UPS and CV[74,120], while others claim excellent conformity[55,56,58]. The correct determination of HOMO and LUMO levels remains controversial but the contradicting reports suggest that both methods are prone to measurement, and most notably, evaluation errors of several tenths of eV. Despite the difficulties accompanied when comparing different methods, the statement that the IQE_{PV} is reduced significantly below a critical Δ_{HOMO} offset holds true. Minor chemical modifications, such as incorporating different heteroatoms or blending of similar components with slightly different energy levels, to gradually shift the energy levels of the acceptor (or donor) would be necessary to find the lowest Δ_{HOMO} offset without reducing the IQE_{PV} of the solar cell.

A second possible strategy to improve the V_{OC} of D18:Y6 solar cells is to further reduce the non-radiative voltage losses. The high-lying CT state in D18:Y6 solar cells and the associated hybridization of the LE and CT state, as discussed above [119], underlines the importance of the LE state of the small bandgap component. As seen from Figure 3.5, the measured ELQY of D18:Y6 is almost identical to the one of Y6. This result raises the question of whether the observed ELQY in the blend is limited by the ELQY of the pure Y6. Thus, modifying the chemical structure of Y6 to increase its ELQY might lead to a higher V_{OC} of D18:Y6 solar cells. Based on the NIM-certified J_{SC} and FF values from Table 3.1, a tenfold increase of the ELQY would boost the PCE of D18:Y6 to 19.3 % (V_{OC}=0.93 V), while a hundredfold increase would break the 20 % efficiency mark by delivering a PCE of 20.5 % (V_{OC}=0.99 V).

3.5 Summary & Conclusion

In summary, optical and electrochemical measurements on the high-performance OPV materials D18, Y6, and $PC_{71}BM$ have been shown. Furthermore, we report the fabrication of high-performance D18:Y6 solar cells with a PCE of 16 % and fullerene-based solar cells (D18:$PC_{71}BM$) with a PCE of 8 %. Two representative devices of the fabricated fullerene- and non-fullerene-based solar cells were analyzed and compared in detail. High-sensitivity EQE_{PV} and luminescence (EL, PL) measurements strongly suggest the formation of a pronounced charge transfer (CT) state in the fullerene-based device. In contrast to this observation, the EQE_{PV} and luminescence spectra of the D18:Y6 device essentially coincide with the spectra of pristine Y6, suggesting a high-lying CT state, which cannot be distinguished from the local exciton (LE) state of pristine Y6. CT-state energy levels of 1.38 eV and 1.56 eV have been found for D18:Y6 and D18:$PC_{71}BM$ devices, respectively. The results from EQE_{PV} and electroluminescence measurements were used to quantify the observed V_{OC} losses of D18:Y6 and D18:$PC_{71}BM$ solar cell devices. The non-fullerene device exhibits a decreased radiative and decreased non-radiative voltage loss compared to the fullerene device. A $\Delta V_{OC}^{rad,b.g.}$ of 0.04 V and a $\Delta V_{OC}^{non-rad}$ of 0.20 V for the D18:Y6 device are among the lowest values ever reported for OPV devices. The CT-absorption below the $PC_{71}BM$ bandgap of the D18:$PC_{71}BM$ device leads to a substantially higher $\Delta V_{OC}^{rad,b.g.}$ of 0.17 V. The weak $PC_{71}BM$ oscillator strength leads to a low emissivity of the formed CT-state, which can be attributed to the high $\Delta V_{OC}^{non-rad}$ of 0.33 V. For both devices, the measured non-radiative voltage losses are in good agreement with the calculated $\Delta V_{OC}^{non-rad}$ values from ELQY measurements. The three-state model was used to describe the observed experimental results successfully.

To conclude, a high-lying CT-state appears to be a prerequisite to achieving low voltage losses. Furthermore, the three-state model and the experimental results highlight the importance of a strongly emissive LE-state of the small bandgap component, which seems to significantly reduce the non-radiative voltage loss in low $\Delta E_{LE\text{-}CT}$ systems. Based on the experimental

results two possible strategies to improve the V_{OC} of D18:Y6 solar cells are proposed. The EVS measurements of D18 and Y6 (Δ_{HOMO}=0.28 eV) support the idea to reduce the Δ_{HOMO} offset between donor and acceptor without affecting the IQE_{PV} of the solar cell. As a result, the increased energetic difference between $HOMO_D$ and $LUMO_A$ could potentially lead to a higher V_{OC}. Another approach to improve the V_{OC} is to reduce the non-radiative voltage losses of D18:Y6 solar cells by enhancing the ELQY. As suggested by the experimental results, this may be achieved by improving the luminescence properties of Y6. The proposed optimization strategies might be of paramount importance to further reduce the observed voltage losses and allow for OPV efficiencies to exceed the 20 % mark.

3.6 Acknowledgments

Financial support by the Austrian "Climate and Energy Fund" within the program Energy Emission Austria (Project: ALTAFOS, FFG No. 865 072) is gratefully acknowledged.

3.7 Supplementary Information

Electrochemistry

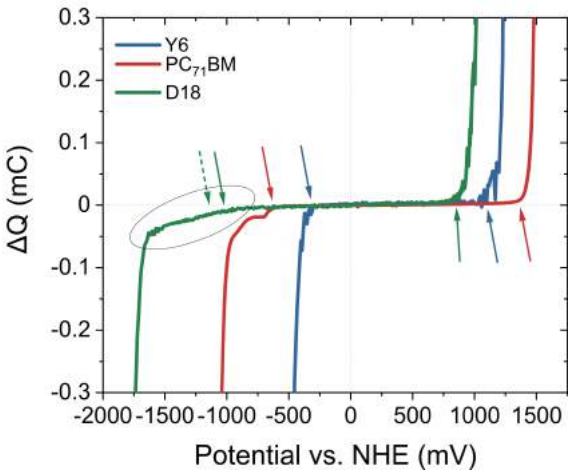

Figure S3.1: Electrochemical characterization. EVS measurements of the used OPV Materials D18, Y6, and $PC_{71}BM$. The arrows indicate the respective onset of reduction or oxidation. The dashed arrow indicates an estimation of the $LUMO_{opt}$ level of D18 calculating $HOMO_{D18}$ + optical gap.

EVS is a good tool to estimate the HOMO and LUMO levels of OPV materials. The measurement is performed close to equilibrium conditions (see Section 2.1.1) and allows to determine the onset of oxidation or reduction more precisely than in cyclic voltammetry measurements. Typical CV measurements are analyzed by fitting tangents to the baseline and the oxidation or reduction peak. This type of analysis is prone to substantial evaluation errors and can be avoided using EVS. Here the onset of the reaction is defined as the first deviation from the baseline. As shown in Figure S3.1 the oxidation onset can be evaluated precisely for all 4 investigated materials. The reduction onset of the acceptors can be identified clearly. It should be emphasized that the indirect nature of the fullerene molecule can also be identified in the EVS spectrum. It seems like a limited reaction starts already at -600 mV *vs.* NHE, while a strong reduction is observed at approximately -900 mV *vs.* NHE. The reduction onset for the D18 polymer is hard to define as indicated by the black ellipse. Thus, the presented LUMO levels of the polymers could exhibit significant errors. Fortunately, the investigated systems consist of large bandgap polymers and low bandgap acceptors with moderate or low Δ_{HOMO} offsets. In any case, the LUMO level of the polymer is expected to be significantly higher than the LUMO of the acceptor. Thus, a precise measurement of the LUMO level of the polymer is not required.

Device Geometry

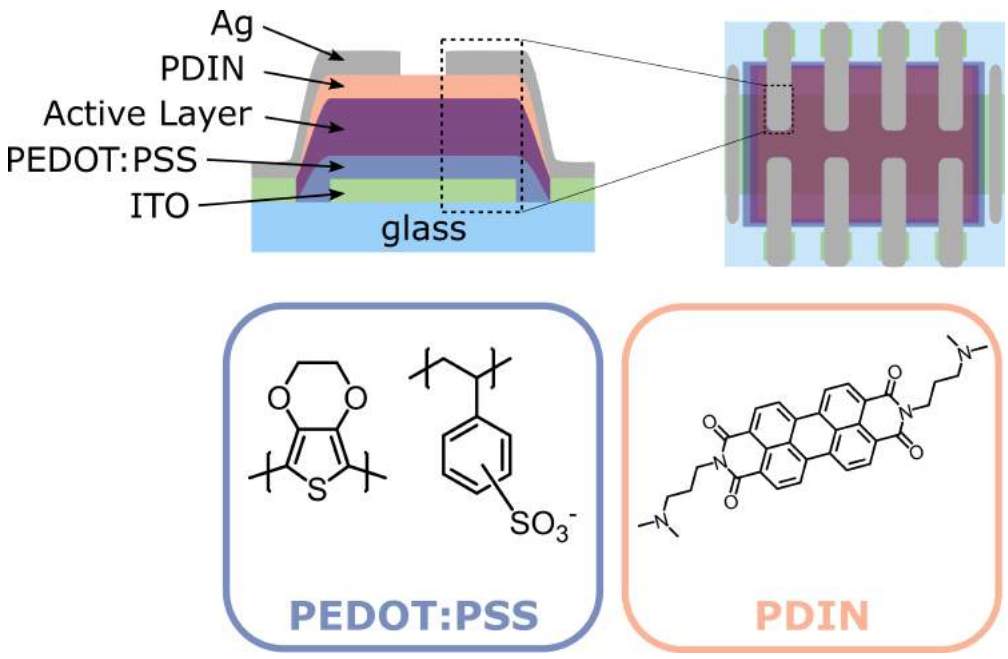

Figure S3.2: Device geometry and chemical structures of PEDOT:PSS and PDIN.

Table S3.1: Photovoltaic parameters of D18:Y6 (1:1.6) solar cells with different thicknesses of the active layer. The presented values are averages over at least 8 cells.

Thickness (nm)	V_{OC} (V)	J_{SC} (mA cm^{-2})	FF (%)	PCE (%)
60	0.87	-18.20	73.8	11.7
68	0.87	-18.78	74.3	12.1
79	0.87	-24.75	74.5	16.0
85	0.87	-23.05	73.9	14.8
87	0.87	-22.19	74.7	14.4
89	0.86	-25.24	73.6	16.0
96	0.86	-23.39	73	14.7
97	0.87	-22.88	73	14.5
100	0.87	-25.12	72.8	15.9
102	0.86	-24.85	72.8	15.6
117	0.86	-25.57	70.8	15.6
119	0.86	-22.46	71.4	13.8
123	0.85	-24.04	67.5	13.8
140	0.86	-22.56	69.4	13.5
192	0.84	-24.19	66.8	13.6

Thickness variation of D18:Y6 solar cells

The various active layer thicknesses of D18:Y6 (1:1.6) solar cells were achieved by different concentrations of the active layer solution (7 mg/mL, 9 mg/mL, 11 mg/mL in chloroform) and spin speeds ranging from 1000-5000 rpm. It should be mentioned that solar cells with almost 200 nm thick active layers showed a high PCE of 13.6 %. Furthermore, the highest FF values were found for the thinnest devices. Figure S3.3 clearly shows that the J_{SC} of devices with 60 nm and 68 nm is slightly reduced. For the thin devices, the active layer was not thick enough to absorb all the incoming photons which leads to a reduced J_{SC}. The result suggests that an active layer thickness of at least 80 nm is required to reach high J_{SC} values. For a better visibility, the EQE_{PV} spectra are presented in arbitrary units. Increasing the thickness strongly affects the shape of the EQE_{PV}. Thin devices exhibit two pronounced peaks which can be identified as the pristine absorption peaks of D18 and Y6. Upon increasing the thickness, the gap between the peaks is reduced until a plateau of an almost constant EQE_{PV} is formed. The observed behavior is assumed to be caused by interference effects resulting from the different layer thicknesses of the solar cells. EL measurements show a similarly strong influence on the active layer thickness. Increasing the active layer thickness gradually increases the shoulder around 1100 nm. Furthermore, the maximum of the EL peaks shifts towards lower

wavelengths for thinner devices. Again, this behavior is assumed to be caused by interference effects.

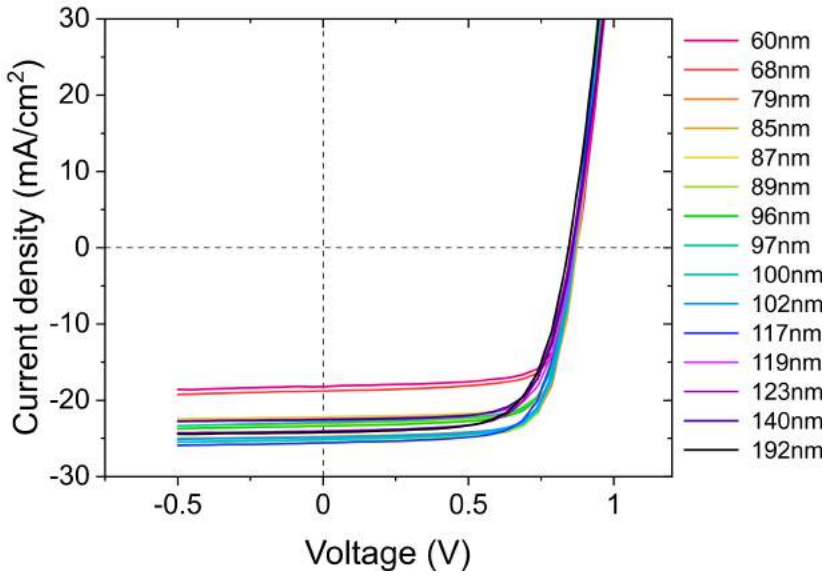

Figure S3.3: *J-V*-curves of D18:Y6 (1:1.6) solar cells with different thicknesses. The presented curves are averages over at least 8 cells. The respective photovoltaic parameters are summarized in Table S3.1

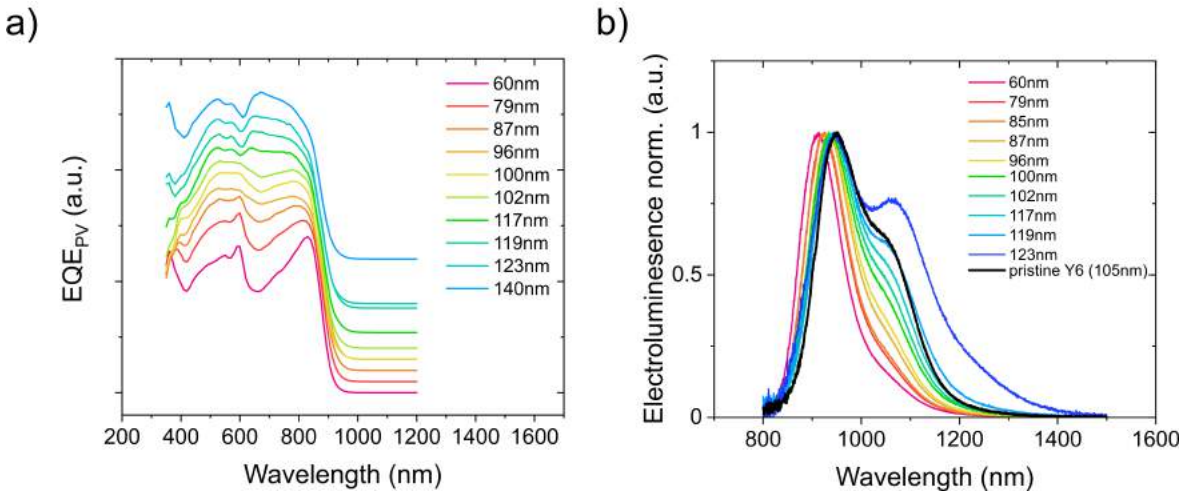

Figure S3.4: EQE_{PV} and EL spectra of D18:Y6 solar cells with various active layer thicknesses.

Additional EQE_{PV} Measurements

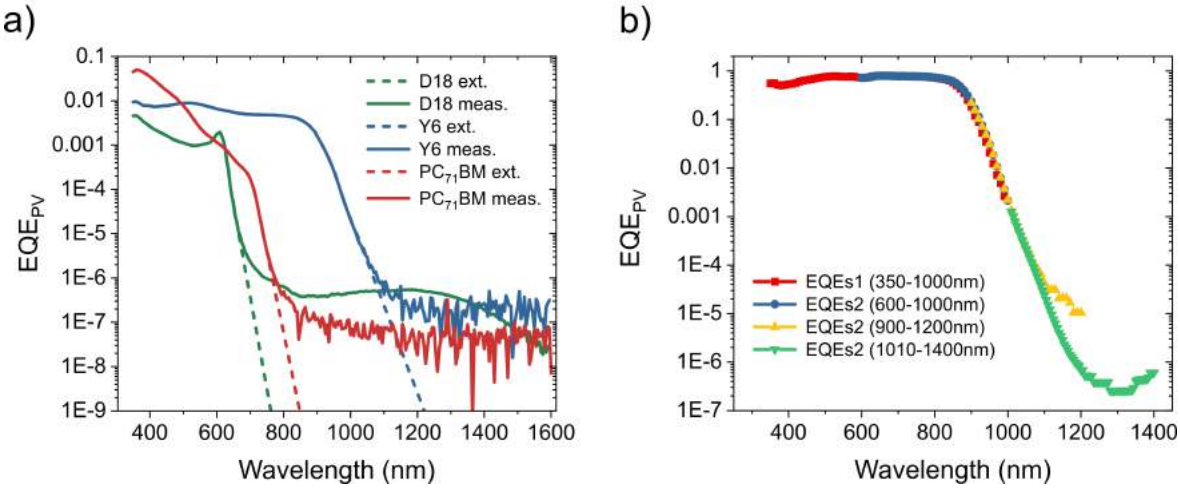

Figure S3.5: EQE_{PV} measurements. a) Measured EQE_{PV} spectra of pristine devices (solid curves) and their respective linearly extended EQE_{PV} spectra (dashed curves). b) Individual EQE_{PV} measurements of a typical D18:Y6 solar cell. The spectra were measured with different setups, spectral regions, and amplification. An excellent overlap of the EQE_{PV} spectra from the individual measurements can be observed.

EL / PL / EM_{EQE} Measurements

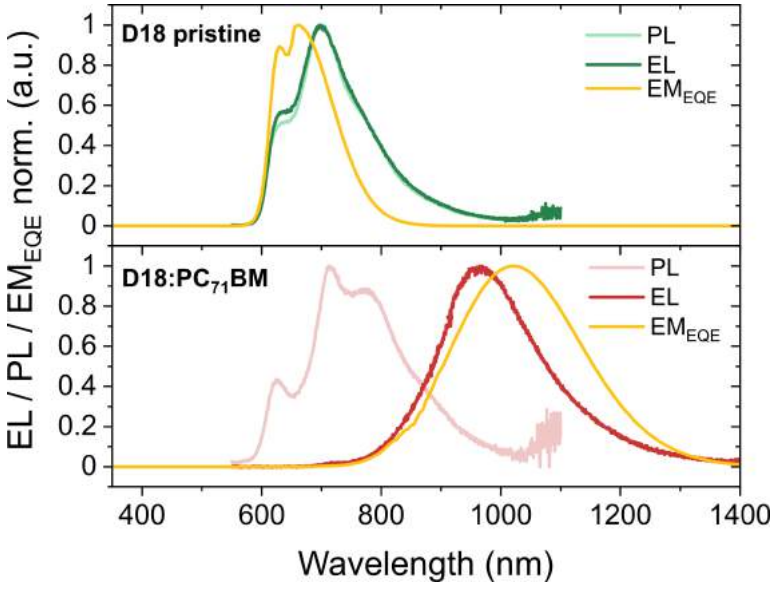

Figure S3.6: Photo- and electroluminescence characterizations. Comparison of PL / EL / EM_{EQE} spectra of pristine D18 and D18:$PC_{71}BM$ devices.

Evaluation of the Optical Bandgap

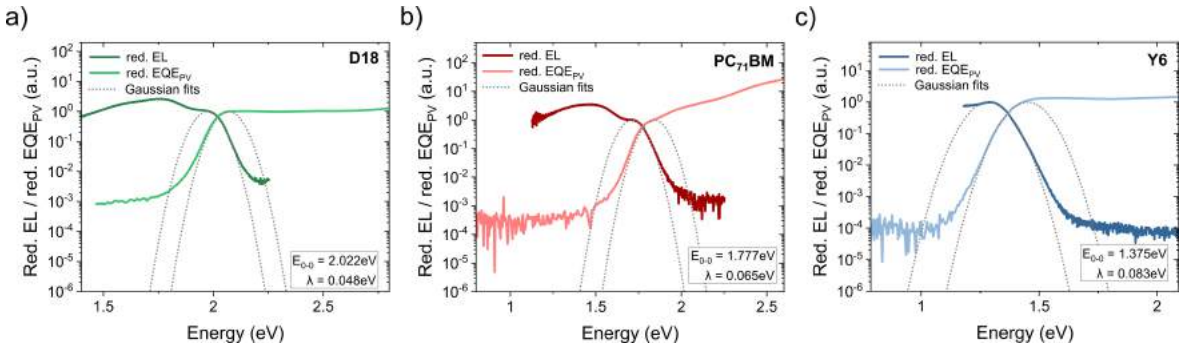

Figure S3.7: EQE_{PV} and EL spectra of D18, Y6, and $PC_{71}BM$. The high-energy EL and low-energy EQE_{PV} peaks were normalized to 1. The crossing point between EQE_{PV} and EL spectra of the pristine materials was used to determine their optical gaps.

Photovoltaic Parameter in the SQ Limit

Table S3.2: Measured photovoltaic parameters of D18:Y6 and D18:$PC_{71}BM$ solar cells in comparison with their respective parameters in the SQ limit.

		V_{OC} (V)	J_{SC} (mA cm^{-2})	FF (%)	PCE (%)
D18:Y6	measured	0.87	24.46	70.5	15.2
	SQ limit	1.09	33.98	89.0	33.2
	% of SQ limit	79.8%	72.0%	79.2%	45.6%
D18:$PC_{71}BM$	measured	0.98	11.26	71.4	8.0
	SQ limit	1.48	20.07	91.3	27.1
	% of SQ limit	66.1%	56.1%	78.2%	29.3%

Chapter 4

Material Screening

This chapter gives an overview of the novel acceptor materials investigated within the scope of the "ALTAFOS" FFG project and rationalizes the selection and in-depth investigation of the PMI-FF-PMI acceptor discussed in Chapter 5. The main goal of the project "ALTAFOS" was to explore the basic properties and the working principles of the new family of non-fullerene acceptor materials and to give an estimation of the efficiency potential of this new generation of organic solar cells. For this purpose, a variety of perylene-based acceptor materials were synthesized by the group of Prof. Trimmel from the Technical University of Graz. In the following, optical and electrochemical measurements were used as screening methods to identify the most promising candidates suited for the application in OSCs.

4.1 ALTAFOS Materials

Perylenediimide (PDI) derivatives are widely used as pigments or vat dyes in the traditional dye industry due to their strong light absorption and emission properties, low synthesis cost, and remarkable thermal and (photo-)chemical stability.[121] Moreover, PDI-based materials typically exhibit high electron affinities and have shown excellent electron transport properties. The combination of their superior optical and electrical properties make them prime candidates for usage in organic (opto-)electronic applications e.g. solar cells, OLEDs, or OFETs.[122–126] The application of perylenes in organic solar cells goes back to 1986 when Tang reported the first heterojunction OSCs with an efficiency of 1 % using a perylene tetracarboxylic derivative and copper phthalocyanine.[23] Since then PDIs have been considered promising candidates for fullerene-free organic solar cells, which led to the development of a wide variety of perylene-based acceptor materials.[127–133] Owing to their rigid and planar conjugated backbones PDIs tend to form large micrometer-sized aggregates in blend films which impedes the desired nanoscale morphology in BHJ blends. Thus, PDI-based acceptor design has been focused on limiting the aggregation effects aiming for sufficiently small PDI

domains, while keeping them large enough to ensure percolating networks for high charge carrier mobilities. The key to reducing the π-stacking of PDIs is to reduce their planarity. In addition to general approaches like side-chain engineering, it has been shown beneficial to link two or several PDI units forming dimeric, trimeric, or tetrameric structures. These linked structures typically lead to twisted subunits, which have been shown to greatly impede the excessive aggregation behavior. For a detailed discussion of PDI design strategies and a compilation of the most successful developed PDI based acceptors the reader is referred to the excellent reviews of Wadsworth *et al.*[128], Hou *et al.*[129], Fujimoto *et al.*[130] or Zhang *et al.*[133]

The developed materials within the scope of the "ALTAFOS" project can be categorized into two main groups. (1) Materials based on the PDI monomers and (2) materials based on a perylene monoimide (PMI) triad structure in the form of PMI-linker-PMI. An illustration of the perylene core and the two main building blocks for the presented acceptors (PDI and PMI) are shown in Figure 4.1. Functional group substitution at the imide nitrogen position offers a great possibility to tune the self-assembly properties due to side-chain engineering as discussed above. It is well known that the imide nitrogen is not conjugated to the aromatic system and thus allows for a modulation of the morphological properties without significantly affecting the frontier molecular orbitals and optoelectronic properties.[128] For all the perylene-based acceptors in this thesis, a bulky 2,6-diisopropylphenyl group attached at the imide nitrogen position was used to reduce the π-stacking and improve the solubility in common chlorinated solvents (see Figure 4.1).

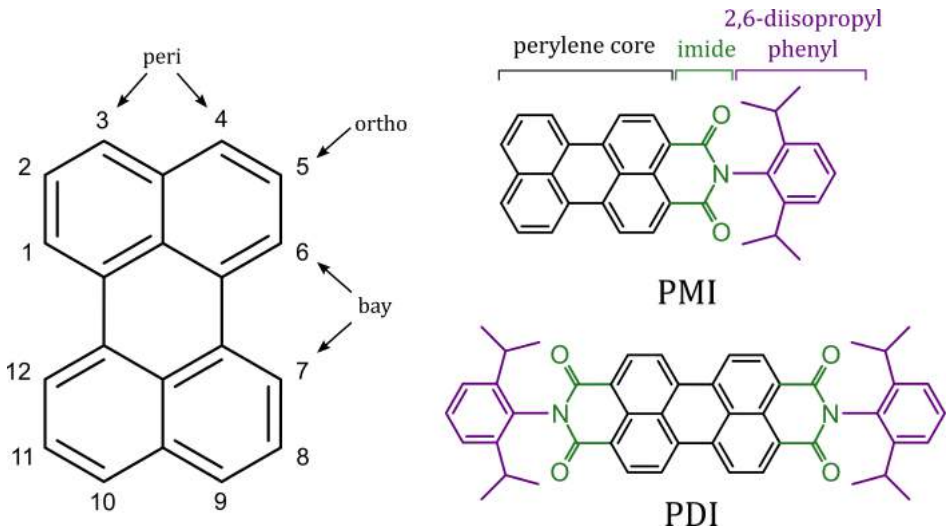

Figure 4.1: Left: Chemical structure of a perylene core. Right: Chemical structure of PMI and PDI units, which served as building blocks for the presented acceptor materials.

4.1.1 PDI Acceptors

A not yet discussed, attractive property of PDI-based acceptors is the great possibility to influence their optoelectronic properties by simple substitution at *ortho* or *bay*-position. Compound **1** in Figure 4.2 shows the unsubstituted PDI molecule, which acts as reference material for its *bay*-substituted analogs (compound **2-4**). Compounds **2** and **3** represent halogenated versions of compound **1** (Br_2-PDI and Cl_4-PDI), while compound **4** incorporates diethylsilane at the *bay* position of the perylene backbone (Et_2Si-PDI).

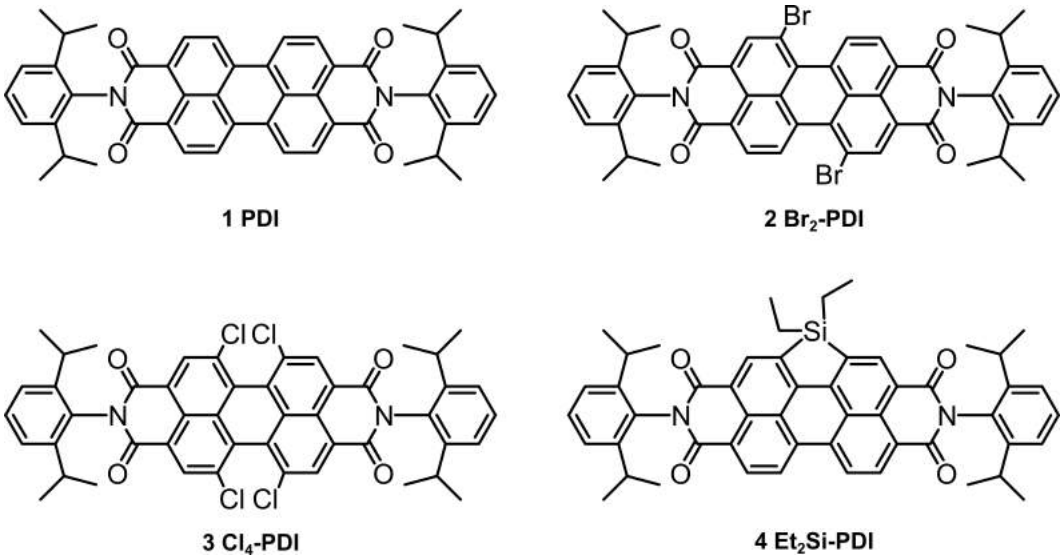

Figure 4.2: Chemical structures of the investigated PDI-based acceptor materials.

4.1.2 PMI-linker-PMI Acceptors

In contrast to the great variety of reported acceptors based on the PDI-monomer, its close structural relative, perylene monoimide (PMI), has attracted significantly less research attention despite possessing comparable optical and electronic properties.[134] As a building block for organic solar cell materials, PMIs offer similar traits as PDIs such as strong absorption, high stability, low synthesis cost, and high electron affinity. Moreover, the asymmetric structure of PMI unlocks additional molecular design concepts based on modifications at the *peri* position. One possible example is the coupling of two PMI units via a π-conjugated linker molecule resulting in a PMI-linker-PMI structure as presented in this thesis. This triad structure can be interpreted as an acceptor-donor-acceptor (A-D-A) like motif, which has been used in a large number of high-performing NFAs.[135] As shown in Figure 4.3, phenylene-, thiophene-, and fluorene-bridged PMI-linker-PMI structures have been realized.

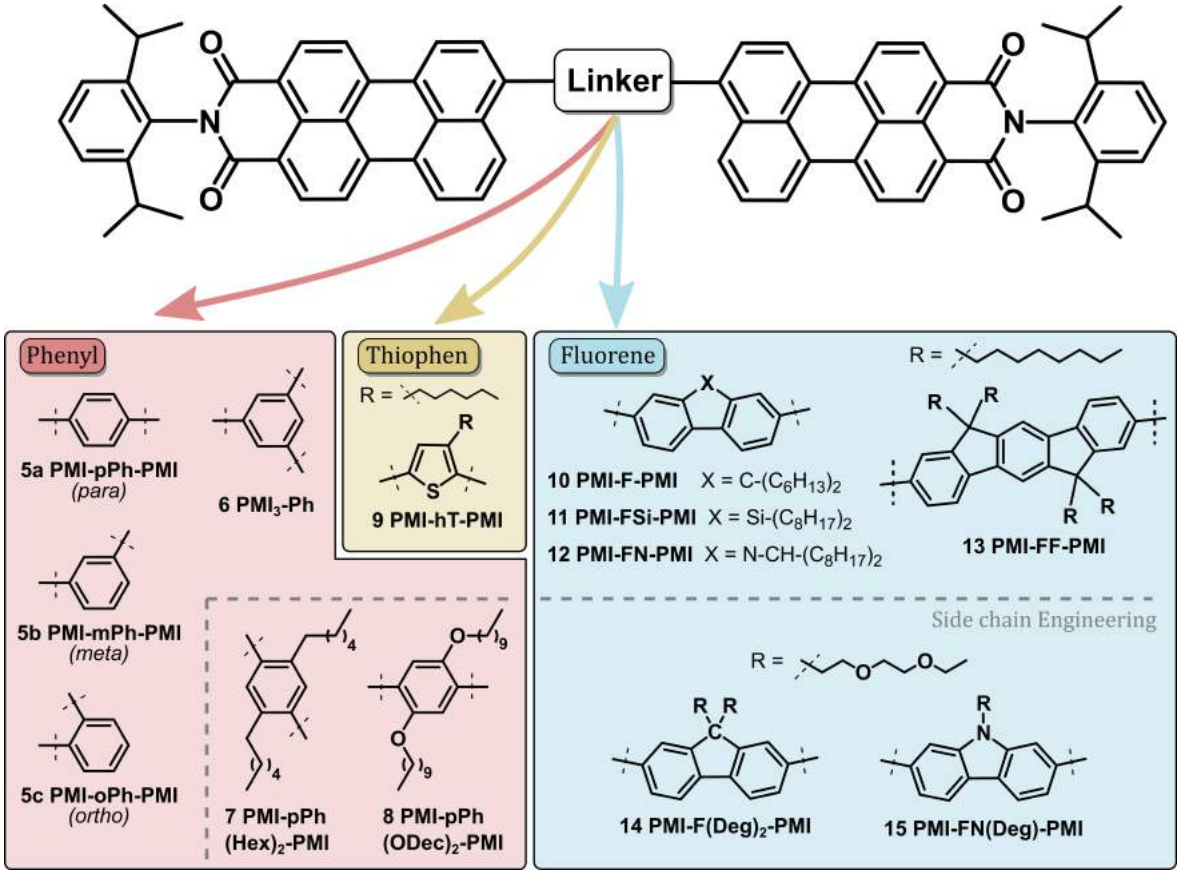

Figure 4.3: Chemical structures of the investigated PMI-linker-PMI-based acceptor materials.

4.1.3 Screening Process

As discussed above, electrochemical and optical measurements have been performed to screen the large number of synthesized materials for the most promising candidates for OSC applications. Figure 4.4 gives an estimation of the HOMO and LUMO energy levels of all investigated materials. Donor polymers are depicted in green, PDI-based acceptors in purple and PMI-linker-PMI acceptors in red (phenylene), yellow (thiophene) and blue (fluorene) depending on the bridging molecule. As described in Section 2.1.1, the "first deviation" and "tangent" methods were used to evaluate the reduction and oxidation onsets from EVS measurements. In Figure 4.4 the results from the "first deviation" method are represented by the box plot, while the onset values determined from the "tangent" method are represented by the whiskers. Barring a few exceptions (Compound **5c** and **14**) the HOMO level could be identified with good accuracy and a small evaluation dependency. Thus, the optical bandgaps E_{opt} were used to calculate the $LUMO_{opt}$ levels (yellow bars) according to Equation 2.2. Due to the large uncertainty of the electrochemically derived LUMO levels, only the $LUMO_{opt}$ levels were considered in the following discussion. For the sake of clarity,

the interpretation of Figure 4.4 is segmented by the three material classes shown in the tabs above the top axis.

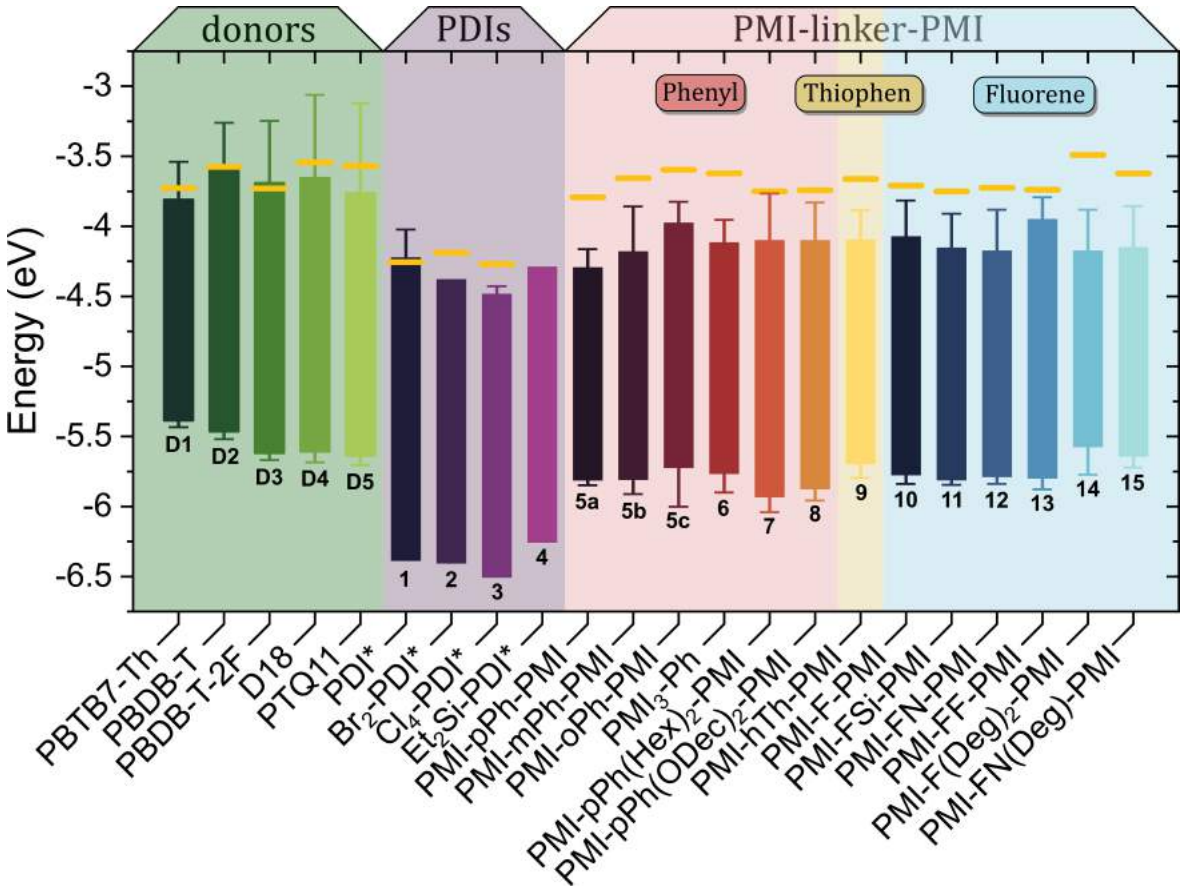

Figure 4.4: Summary of the derived HOMO and LUMO energy levels of all presented materials.

Donor polymers

In general, all EVS measurements of the presented, commercially available donor polymers follow the same characteristics. As shown in Figure 4.4, the oxidation onsets (HOMO levels) could be determined with great accuracy. On the other hand, the reduction onset was difficult to determine due to a non-ideal baseline behavior as depicted in the EVS measurement in Figure 2.3. Ideally, the baseline is constant until the reduction/oxidation onset is reached. At this point the transported charge ΔQ should start to deviate from the baseline, followed by a sharp exponential-like decrease/increase. However, all the reductive EVS measurements of the investigated polymers displayed an additional segment characterized by a slight, linear slope before showing the typical exponential-like decrease. Within this thesis, this behavior is referred to as "delayed reduction" and is the reason for the large deviations between the two evaluation methods shown in Figure 4.4. The measured optical gaps of the donor polymers tend to be in good agreement with the LUMO levels determined from the first deviation

method. Moreover, it should be noted that the subtle effect of the "delayed reduction" is not visible in standard CV measurements (see Figure 2.3), which leads to a significant overestimation of the LUMO of typical donor polymers. As a consequence, their optical and electrochemical gaps reported in literature often deviate by more than 0.5 eV.[43,55,57]

From the five investigated donors, polymer **D1** has the lowest LUMO and highest HOMO level which is in good agreement with its significantly lower optical bandgap. Compounds **D3**-**D5** exhibit deep HOMO levels around -5.6 eV. Interestingly, the studied donors are characterized by similar LUMO levels of either $\sim$ -3.55 eV for **D2**, **D4**, and **D5** or $\sim$ -3.75 eV for **D1** and **D3**.

PDIs

First and foremost, it should be noted that the HOMO/LUMO levels of compounds **1**-**4**, as presented in Figure 4.4, were not derived from EVS measurements. Due to the pronounced stacking properties of PDIs, the drop-casting onto the Pt plate resulted in large crystallites instead of a continuous film. The adhesion of the crystallites on the Pt plate was very weak and once the acetonitrile was added into the cell they got washed away from the surface. In general, acetonitrile is a bad solvent for the PDIs but the solubility was just good enough to perform homogeneous CV measurements, where the material of interest is dissolved in the electrolyte solution. Due to the limited solubility, the reduction and oxidation currents were rather weak and for the most part, the first deviation and tangent method led to similar reduction and oxidation onsets. Figure 4.4 shows that the LUMO levels of PDI-based acceptors are on average around 0.5 eV lower than those of PMI-linker-PMI acceptors. Although it is precarious to compare different electrochemical techniques, the large difference suggests significantly lower LUMO levels of the PDI-based acceptors. The low LUMO levels of the acceptors reduce the maximum achievable V_{OC}, which can be approximated by the difference between the HOMO of the donor and the LUMO of the acceptor. Consequently, first trials using PBDB-T as a donor in combination with the PDI acceptors led to solar cells with low open-circuit voltages between 0.6 - 0.8 V. In addition, the limited solubility and bad film formation properties inhibited the further use of PDI-based acceptors in OSC devices. A non-ideal nano-morphology caused by the strong π-stacking is thought to be responsible for the low J_{SC} values between 3 and 4 mA cm^{-2}. It should be noted that within the PDI family the Si substituted PDI (compound **4**) showed the most promising photovoltaic parameters with J_{SC} values around 6 mA cm^{-2}. However, the moderate current densities in combination with the low maximum achievable V_{OC} values of only 0.8 V minimizes the optimization potential of Et_2Si-PDI and its analogs. A new class of donor materials with significantly lower HOMO and LUMO levels would be necessary to reduce the large voltage loss of solar cells based on compounds **1**-**4**. An alternative area of application for those new low-LUMO acceptors could be the use as interlayers in organic or perovskite solar cells. Corresponding studies

were not the focal point of this thesis and further research would be necessary to evaluate their performance as interlayer materials.

PMI-linker-PMI

In contrast to the excellent agreement of optical and electrochemical gap for the presented donor polymers, the electrochemical measurements of the LUMO of the PMI acceptors tend to be significantly lower than the derived $LUMO_{opt}$ levels. Additionally, the measurements of compounds **5c** and **14** should be considered with special care due to the comparatively large uncertainty in the HOMO evaluation. In general, the LUMO levels of the PMI-linker-PMI acceptors are significantly higher compared to the LUMO levels of the presented PDIs. In fact, some acceptors (compounds **5b**, **6**, **9**) exhibit similar LUMO energy levels to those of donors **D1**-**D5**. Therefore, the driving force for charge transfer could be seriously reduced in some of the D/A blends. As a consequence, blends with low LUMO donors **D1** and **D3** failed to reach J_{SC} values greater than 1.5 mA cm^{-2}. Thus, D/A blends with donors **D2**, **D4** and **D5** were mainly investigated in this thesis.

Based on the first trials of fabricating OSC devices, fluorene-derivative-linked PMI acceptors seemed to outperform their phenylene and thiophene-linked counterparts. Especially compounds **10**-**13** stand out due to their excellent film formation properties and good solubility in common chlorinated solvents. Additional alkyl side chains on the fluorene-derivative linker molecules are thought to be responsible for the enhanced solubility. Moreover, their $LUMO_{opt}$ levels are slightly lower than those of most phenyl and thiophene-linked analogs, which could be beneficial for photocurrent generation.

Despite their slightly worse performance, the phenylene-linked PMI acceptors lend themselves as an ideal model system to thoroughly analyze the structure-properties relationship of acceptors based on the PMI-linker-PMI structure. Benzene, the simplest aromatic linker, gives the possibility to study the effect of different attachment positions and investigate the influence of different side chains on the solubility or film formation properties. A corresponding study has recently been published.[136]

Due to their superior photovoltaic performance, here, the fluorene-linked PMI acceptors were chosen as the most promising candidates to fabricate efficient OSCs. Optimized organic solar cells based on blends of PBDB-T (donor **D2**) with acceptors **10**, **11,** and **12** led to efficiencies beyond 5 %. The solar cells were characterized by high V_{OC}s > 1 V, J_{SC}s between 8-10 mA cm^{-2} and FFs between 44-53 %. For a detailed analysis and characterization of these OSCs, the reader is referred to our recent publication, which investigates the effects of fluorene, silafluorene, and carbazole linkers on the photovoltaic performance of PMI-linker-PMI based acceptors.[137] Based on the presented screening results, the tetraoctyl-indeno[1,2-b]fluorene-linked acceptor PMI-FF-PMI (compound **13**) was chosen as the most

promising material from all the presented novel perylene-based acceptors. In comparison to its close relative PMI-F-PMI, compound **13** is characterized by a larger π-conjugated linker molecule and two additional octyl side chains for enhanced solubility. Within the accuracy of the electrochemical measurements, these structural changes did not significantly alter the HOMO and LUMO energy levels with respect to compound **10**. In a direct comparison of photovoltaic parameters of PMI-F-PMI and PMI-FF-PMI based solar cells (with PBDB-T as donor polymer), the indenofluorene-linked acceptor showed slightly higher V_{OC} and FF values, which was the main motivation to conduct an extensive study on the PMI-FF-PMI acceptor and its use in OSC applications. The corresponding study is discussed in Chapter 5.

For the sake of completeness, it should be mentioned that this section covers only the materials, which were reasonably stable and were delivered in large enough quantities to perform the discussed screening measurements. A full list of all the synthesized acceptors can be found in the soon-to-be-published final report of the "ALTAFOS" project. In addition, it should be mentioned that the effect of diethylene glycol side chains on the photovoltaic performance of fluorene-linked PMI acceptors (compounds **14** and **15**) is currently being investigated and a corresponding manuscript is in preparation.

Chapter 5

Wide-bandgap organic solar cells with a novel perylene-based non-fullerene acceptor enabling open-circuit voltages beyond 1.4 V.

J. Hofinger, S. Weber, F. Mayr, A. Jodlbauer, M. Reinfelds, T. Rath, G. Trimmel and M. C. Scharber

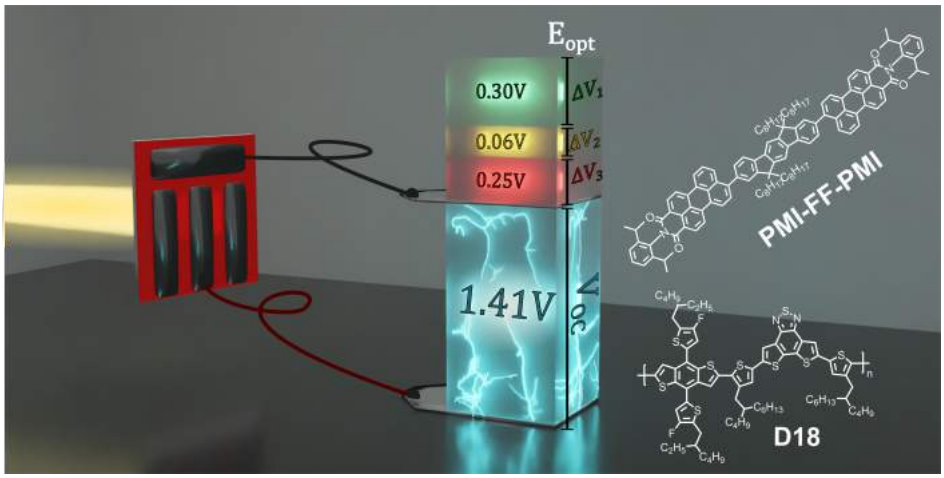

The results of this chapter have been published in:

Journal of Materials Chemistry A, 2022, **10**, 2888-2906
DOI: https://doi.org/10.1039/D1TA09752K

5.1 Abstract

A perylene-based acceptor (PMI-FF-PMI), consisting of two perylene monoimide (PMI) units bridged with a dihydroindeno[1,2 b]fluorene molecule was developed as a potential non-fullerene acceptor (NFA) for organic solar cells (OSCs). The synthesized NFA was combined with the high-performance donor polymer D18 to fabricate efficient OSCs. With an effective bandgap of 2.02 eV, the D18:PMI-FF-PMI blend can be categorized as a wide-bandgap OSC and is an attractive candidate for application as a wide-bandgap sub-cell in all-organic triple-junction solar cell devices. Owing to their large effective bandgap, D18:PMI-FF-PMI solar cells are characterized by an extremely high V_{OC} of 1.41 V, which to the best of our knowledge is the highest reported value for solution-processed OSCs so far. Despite the exceptionally high V_{OC} of this blend, a comparatively large non-radiative voltage loss ($\Delta V_{OC}^{non-rad}$) of 0.25 V was derived from a detailed voltage loss analysis. Measurements of the electroluminescence quantum yield (ELQY) of the solar cell reveal high ELQY values of $\sim$ 0.1 %, which is contradicting the ELQY values derived from the non-radiative voltage loss ($\Delta V_{OC}^{non-rad}$ = 0.25 V, ELQY = 0.0063 %). This work should help to raise awareness that (especially for BHJ blends with small Δ_{HOMO} or Δ_{LUMO} offsets) the measured ELQY cannot be straightforwardly used to calculate the $\Delta V_{OC}^{non-rad}$. To avoid any misinterpretation of the non-radiative voltage losses, the presented ELQY discrepancies for the D18:PMI-FF-PMI system should encourage OPV researchers to primarily rely on the $\Delta V_{OC}^{non-rad}$ values derived from the presented voltage loss analysis based on EQE_{PV} and *J-V* measurements.

5.2 Introduction

During the last decade, the research field of organic photovoltaics (OPV) has witnessed the rise and prevalence of a new class of acceptor materials. The development of non-fullerene acceptors (NFAs) with superior light-harvesting properties and readily adjustable electronic energy levels compared to typical fullerene acceptors has led to a dramatic increase in power conversion efficiencies (PCEs) of bulk heterojunction (BHJ) organics solar cells (OSCs).[135,138] In the last 5 years, PCEs of NFA-based solar cells have almost doubled and efficiencies of over 18 % have been reported.[43,139,140] Despite these rapid improvements, organic solar cell efficiencies still fall short compared to state-of-the-art inorganic or perovskite solar cells. As summarized in Table 5.1, the larger open-circuit voltage loss (ΔV_{OC}^{total}) of OPV devices can be identified as one of the main factors limiting the overall performance of organic solar cells. The total voltage loss of a solar cell is defined as the difference between the optical gap of the absorber (E_{opt}) and the measured open-circuit voltage (V_{OC}) under AM1.5G illumination as given by $\Delta V_{OC}^{total} = (1/q) \times E_{opt} - V_{OC}$. In Chapter 3 the individual loss contributions of high-performance fullerene (D18:$PC_{71}BM$) and non-fullerene (D18:Y6) solar cells were compared following the voltage loss analysis described in Section 2.2.2. The results of the

voltage loss analysis for the two organic solar cells are summarized in Table 5.1, revealing that the high-performance NFA-based solar cell exhibits significantly lower non-radiative voltage losses ($\sim$ 0.2 V) compared to its fullerene-based counterpart ($\sim$ 0.3 V). Nevertheless, the typically observed non-radiative voltage losses of high-performance NFA-based solar cells around 0.2 V are considerably larger than the 0.03 V or 0.06 V observed for top-end GaAs and perovskite solar cells, respectively. The formation of an interfacial CT state at the donor:acceptor (D/A) interface is thought to be responsible for the increased non-radiative voltage losses in OPV devices compared to their inorganic counterparts. Due to the low-dielectric constants of organic semiconductors and the resulting high exciton binding energies, a charge transfer (CT) state is required for the efficient dissociation of photogenerated excitons. Simultaneously, most of the recombination processes in OPV devices proceed via the CT state, underlining its importance for the performance of organic solar cells.

Table 5.1: Comparison of the bandgaps, photovoltaic parameters, and open-circuit voltage losses of selected organic, inorganic, and perovskite solar cells. J_{SC} and FF represent the short-circuit current density and the fill factor, respectively

Material	E_{opt} (eV)	V_{OC} (V)	J_{SC} (mA cm^{-2})	FF (%)	PCE (%)	ΔV_{OC}^{total} (V)	$\Delta V_{OC}^{non\text{-}rad}$ (V)	ELQY (%)	Source
GaAs	1.43	1.12	29.78	86.7	29.1	0.31	0.03	35.7	[48, 49]
Perovskite	1.53	1.19	26.35	81.7	25.6	0.34	0.06	10.1	[50]
D18:Y6	1.38	0.87	25.24	73.6	16.1	0.51	0.20	0.04	[51]
D18:PC$_{71}$BM	1.78	0.98	11.26	71.4	8.0	0.80	0.33	0.0003	[51]

Recently, An *et al.* have reported an OPV device with an impressively low $\Delta V_{OC}^{non-rad}$ of 0.16 V and an excellent electroluminescence quantum yield (ELQY) as high as 0.19 %.[141] The small voltage loss was ascribed to a high-lying CT state energy and a low offset (ΔE_{LE-CT}) between the local exciton (LE) and CT state. It should be noted that for blends of a wide bandgap donor and small bandgap acceptor, the offset between the HOMO levels of donor and acceptor is usually taken as an estimate for the driving force to form a CT state and can be considered as a first approximation of the ΔE_{LE-CT} offset.[142] Thus, the moderate observed EQE_{PV} values of around 40 % reported by An and co-workers can be explained by the reduced driving force for CT state formation due to the small ΔE_{LE-CT} offset in this D/A blend. Amongst others,[74,86] the work by An *et al.* highlights the inverse relationship between CT efficiency and non-radiative voltage loss in organic solar cells. Encouragingly, highly efficient polymer:NFA blends have recently been reported with a minimal energetic offset between the HOMOs of donor and acceptor.[56–58] A better understanding of the high CT efficiencies despite the small energetic offsets in those OPV blends is required to develop new highly efficient D/A blends with minimal non-radiative voltage losses, closing the performance gap to efficient inorganic and perovskite solar cells.

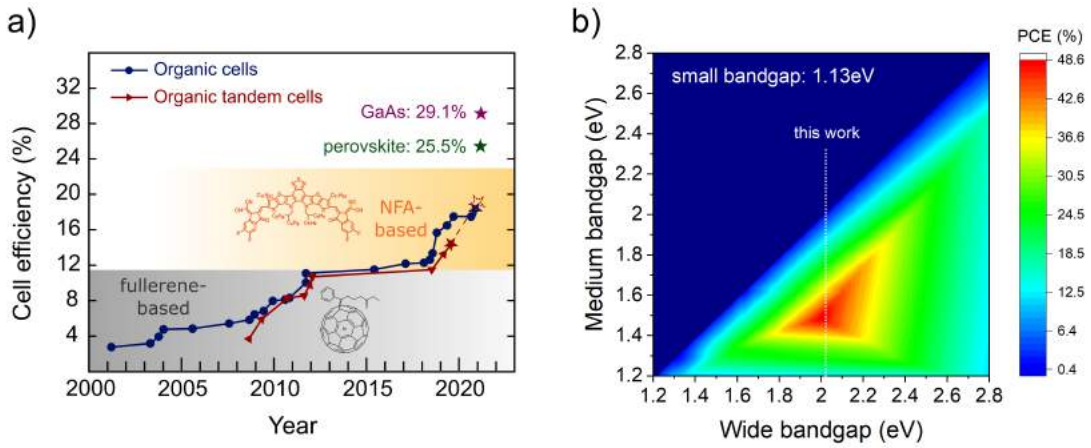

Figure 5.1: History of OSC efficiencies and triple-junction efficiency map. a) Research cell efficiency chart for organic single-junction and tandem cells. Additionally, current record efficiencies for GaAs and perovskite solar cells are presented. The data was taken from the NREL efficiency chart.[12] In addition, the 19.6 % efficient tandem cell reported by Wang *et al.* is added to the NREL data and is depicted as a dashed star symbol.[140] b) 2D-efficiency map for a triple-junction device. The efficiencies were calculated in the SQ limit for a fixed small bandgap absorber of 1.13 eV. The white dotted line represents the effective bandgap of the D18:PMI-FF-PMI blend.

A complementary approach to overcome the performance deficit caused by the large open-circuit voltage losses of OSC devices is to take advantage of the great variety and possibility to readily adjust the optical bandgaps of organic semiconductors. In addition, their solution processability allows easy fabrication of multi-junction devices consisting of stacked OPV blends with different optical bandgaps. According to the SQ theory, only photons with energy larger than the bandgap get absorbed in an ideal single-junction solar cell. At short circuit current (I_{SC}) conditions, the absorption is followed by a rapid thermalization to the bottom of the conduction band, where the exciton is separated into free charges. Photons with energy $E_{h\nu} > E_{opt}$ lose the energy difference $\Delta E = E_{h\nu} - E_{opt}$ in form of heat during the thermalization process. In principle, a multi-junction device allows to significantly reduce thermalization losses due to a more efficient photon to energy conversion, enabling efficiencies well beyond the SQ limit for single-junction devices of approximately 33 %. However, efficiencies of tandem or triple-junction OPV devices based on fullerene acceptors seldomly exceeded those of single-junction devices as shown in Figure 5.1a. In the past, the benefit of reduced thermalization losses in tandem devices was partly negated by the limited NIR absorption properties and the combined open circuit voltage losses of two fullerene-based sub-cells. As argued above state-of-the-art non-fullerene acceptors are primed to overcome both of these shortcomings. According to the NREL efficiency chart, the current record-breaking organic tandem device (PCE=14.2 %) still consists of a wide-bandgap, fullerene-based sub-cell.[12,143] The development of wide-bandgap NFAs for applications in all-NFA-based tandem devices

could reduce the overall voltage losses and significantly boost power conversion efficiencies, eventually fulfilling their promise in surpassing the efficiencies of single-junction devices. This statement has been confirmed by recent studies (not included in the current NREL efficiency chart[12]), claiming PCEs of almost 20 % for OPV tandem cells with NFA-based wide-bandgap sub-cells.[45,140] A study by Eperon *et al.* showed that the theoretical efficiency limit of triple junction devices is exceeding the efficiency limit of tandem devices only if spectral absorption around 1100 nm can be realized.[144] The analysis is based on a simple SQ model assuming a step-like EQE_{PV}. For perovskite triple-junction cells the optimal bandgaps for wide, middle, and small-gap components derived from the simple SQ model were confirmed (only minor shifts in optimal E_{opt} values) by a more realistic model based on a transfer matrix and device modeling approach. The good agreement between the two models highlights the validity of the simple approach in the framework of SQ theory. Recently, an efficient organic solar cell based on a novel non-fullerene acceptor with strong infrared absorption up to 1100 nm (PTB7-Th:COTIC-4F) has been reported by Lee *et al.*[145]. As discussed above, optical absorption up to 1100 nm unlocks the regime, where the theoretical efficiency limit of triple junction devices is significantly increased compared to tandem devices. Moreover, other narrow-bandgap NFAs with absorption beyond 1000 nm have recently been reported such as SiOTIC-4F, CO1-4F, and CO1-4Cl.[145–147] Thus, the recent progress of low bandgap, non-fullerene acceptors strongly suggests developing specialized NFA-based organic solar cells optimized for usage in all-organic triple junction devices. A simple SQ model, as discussed in Reference [144], was developed to identify the optimal bandgaps for an all-organic triple-junction device. Figure 5.1b shows the maximum efficiency map in the detailed balance limit assuming a small bandgap absorber with a fixed bandgap of 1.13 eV (=1100 nm) while varying the bandgaps of medium and wide bandgap absorbers between 1.2 and 2.8 eV. A maximum theoretical efficiency of 48.6 % was derived for a triple-junction device. Furthermore, Figure 5.1b shows that wide and medium bandgap sub-cells with bandgaps in the range of 1.95-2.05 eV and 1.45-1.55 eV are required for optimal performance. A variety of high-efficient OSCs with an optical bandgap between 1.45 and 1.55 eV have already been reported.[148–152] A well-established example is the D/A combination of PBDBT-2F (a.k.a. PM6) and IT-4F with a PCE and EQE_{PV} beyond 13 % and 80 %, respectively.[152] On the contrary, high efficient OPV devices with an extremely low bandgap in the range of 1.1 eV are scarce. The development of novel NFAs like COTIC-4F is a promising start, but the currently only moderate EQE_{PV} values of around 50 % obtained for ultra-small-bandgap OSCs suggest that further optimization is necessary to increase their performance.[145] Similarly, due to the strong research effort of maximizing the absorption range of single-junction OPV blends, highly specialized wide-bandgap solar cells with effective bandgaps around 2 eV, required for triple-junction solar cell applications, are rare.

Herein, we report the synthesis, electrochemical and optical characterization of a wide-bandgap, perylene-based non-fullerene acceptor (PMI-FF-PMI). In combination with the

commercially available, high-performance donor polymer D18, the newly developed acceptor is used to fabricate efficient, wide-bandgap, BHJ solar cells with extremely high V_{OC} values beyond 1.4 V. The photovoltaic parameters of the solar cells were investigated with *J-V*-response and EQE_{PV} measurements. Moreover, a detailed characterization of the electro- (EL) and photoluminescence (PL) properties of the D18:PMI-FF-PMI solar cells was performed. PL quenching experiments and time-correlated single-photon counting measurements (TCSPC) were conducted to analyze the driving force for CT state formation in this D/A blend. As discussed above, the high V_{OC} loss is one of the main limiting factors of OPV device efficiencies and furthering the understanding in this area is one of the main focal points of contemporary OPV research. Therefore, a D/A blend with a record-breaking high V_{OC} beyond 1.4 V is an interesting candidate to thoroughly investigate the individual open circuit voltage loss contributions using the presented voltage loss analysis. To evaluate the performance of the newly synthesized acceptor, the photovoltaic parameters and the determined voltage losses of D18:PMI-FF-PMI cells were compared to those of state-of-the-art fullerene (D18:$PC_{71}BM$) and non-fullerene (D18:Y6) solar cells.[51]

5.3 Experimental Notes

This section provides additional experimental details relevant for this chapter, which have not been discussed in the general experimental section in Chapter 2.

Addendum: Materials and Device Preparation

D18 and Y6 were purchased from 1-materials, while $PC_{71}BM$ was purchased from Solenne BV. Before the solar cell fabrication, pre-patterned ITO glass was first wiped with toluene, followed by subsequent ultrasonication in Hellmanex (2 %v/v solution in deionized water, 50 °C), 2x in deionized water, acetone and isopropanol. Each sonication step was performed for 15 min. Following the cleaning process, the substrates were blow-dried with N_2 followed by an O_2 plasma treatment for 5 min at 100 W. Solar cells in the standard configuration (ITO/PEDOT:PSS/absorber layer/Ca/Al) were prepared spin coating a 0.45 µm filtered PEDOT:PSS solution (Clevios Al4083) onto the clean substrates. A recipe with 3000 rpm for 45 s was used to obtain films thicknesses of 30-40 nm. The PEDOT:PSS films were annealed at 150 °C for 10 min to remove residual water and were then transported into a nitrogen-filled glove box where the active layer was spin-coated. The active layer solution of D18:PMI-FF-PMI was prepared in chlorobenzene with a D/A weight ratio of 1:1 and a total concentration of 13.3 mg/mL. The active layer solution was prepared from master solutions of D18 (10 mg/mL in chlorobenzene) and PMI-FF-PMI (15 mg/mL in chlorobenzene). Before use, the D18 and D18:PMI-FF-PMI solutions were stirred at 90 °C for 30 min in order to fully

dissolve the polymer. The active layer was spin-coated at 60 °C with a two-step recipe of 1500 rpm for 2 s and 4000 rpm for 20 s. The spin-coating recipe resulted in film thicknesses between 70-90 nm. The substrates were transferred to a thermal evaporator under a dry nitrogen atmosphere, where a 10 nm Ca and a 100 nm Al layer were deposited at a pressure $< 10^{-6}$ mbar using a shadow mask. The active area of the cells was around 0.1 cm^2. The exact area of each solar cell was determined with an optical microscope. All cells were encapsulated in the glovebox using a two-component epoxy sealant. The device preparation of D18:PMI-FF-PMI cells in the inverted device structure is summarized in Note S5.7, ESI. The detailed fabrication of the D18:Y6 and D18:$PC_{71}BM$ solar cells is reported elsewhere.[51]

Addendum: EQE_{PV}

Due to their limited NIR absorption, the EQE_{PV} spectra of D18:PMI-FF-PMI solar cells were measured using the EQE setup optimized for measurements between 350 and 1000 nm (EQEs1 setup) as described in Section 2.1.3. The EQE_{PV} measurements presented in this chapter consist of two separate measurements. In addition to the standard EQE_{PV} measurement, a second measurement with a 610 nm long-pass filter and increased preamplification in the range from 630-800 nm is performed to analyze the behavior below the band edge.

Addendum: Electro- and Photoluminescence

For PL measurements the devices were excited with a solid-state laser (Coherent OBIS 488 nm LX150mW) with a wavelength of 488 nm. The optical output power of the laser was adjusted to obtain similar currents as measured under AM1.5G illumination. A 550 nm long-pass filter in front of the monochromator was used to successfully suppress the 488 nm laser light and allowed the acquisition of a PL spectrum without the influence of the excitation light. For EL measurements a Keithley 2401 Source Meter Unit (SMU) was used to apply different potentials to the solar cells. The injection currents were set to match the observed photocurrents under AM1.5G illumination.

5.4 Results

In Figure 5.2a, the chemical structures of the investigated OPV materials are presented. PMI-FF-PMI was synthesized via Suzuki coupling using a perylene pinacol ester and the linker dihydroindeno[1,2 b]fluorene dibromide. The detailed synthesis procedure is presented in Note S5.1 and Figure S5.1, ESI. The structure was verified by ^{1}H and ^{13}C APT NMR spectroscopy as well as MALDI-TOF mass spectrometry (see Figure S5.2-S5.4, ESI). The linker exhibits a larger conjugated π-system in the donor subunit compared to the recently

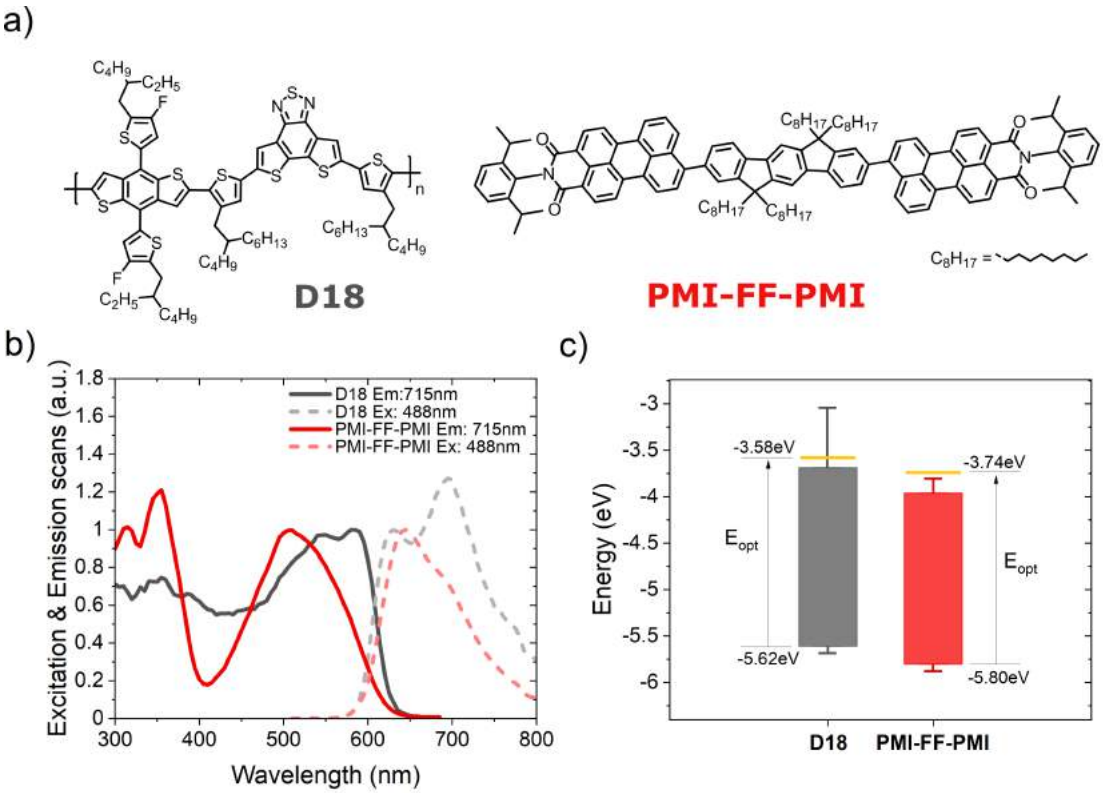

Figure 5.2: Chemical structure, optical and electrochemical characterizations. a) Chemical structure of the D18 polymer and the PMI-FF-PMI small-molecule acceptor. b) Measurements of the excitation and emission spectra of pristine D18 and PMI-FF-PMI. c) HOMO and LUMO level estimations for the donor and acceptor materials obtained from electrochemical voltage spectroscopy measurements. The yellow line represents the theoretical $LUMO_{opt}$ level calculated by adding E_{opt} to the HOMO level. The whiskers represent the maximum evaluation uncertainty of EVS measurements, as discussed in Note S5.2, ESI.

investigated fluorene analog PMI-F-PMI.[137] The newly synthesized acceptor PMI-FF-PMI shows strong optical absorption, good solubility in common chlorinated solvents, and excellent processability and film formation properties, which makes this molecule an interesting candidate to be tested in photovoltaic applications. Here, we investigated the performance of the perylene-based acceptor in combination with the commercially available donor polymer D18. A detailed optical characterization of D18 and PMI-FF-PMI in chlorobenzene solution is presented in Figure S5.5, ESI. The excitation and emission spectra of donor and acceptor thin films on glass are presented in Figure 5.2b. The spectra are normalized to the low energy absorption and high energy emission peak, respectively. The PMI-FF-PMI absorption consists of two prominent peaks at 350 nm and 520 nm. The peak at 520 nm can be ascribed to the absorption of the PMI moieties, while the peak at 350 nm can be identified as the absorption of the dihydroindeno[1,2-b]fluorene linker. Furthermore, Figure 5.2b displays a strong optical overlap of the excitation spectra of donor and acceptor. The crossing point of the excitation and emission spectra was used to estimate the optical bandgap.[89] Both materials exhibit very similar wide optical bandgaps of 2.04 eV and 2.06 eV for D18 and PMI-FF-PMI, respectively.

In addition, the absorption coefficients of D18, PMI-FF-PMI, and D18:PMI-FF-PMI (1:1) thin films are presented in Figure S5.6, ESI. Peak absorption coefficient values beyond 10^5 cm^{-1} highlight the strong absorption properties of both materials. In addition to the optical measurements, the OPV materials were electrochemically characterized using electrochemical voltage spectroscopy (EVS) and cyclic voltammetry (CV). During EVS measurements the system is kept close to its thermodynamic equilibrium. Thus, typical dynamic influences of standard CV measurements (e.g. scan speed) are reduced due to the slow, incremental variation of the applied potential. The HOMO and LUMO energy levels of the molecules presented in Figure 5.2c were derived from EVS measurements of D18 and PMI-FF-PMI drop-casted thin films (see Figure S5.7a, ESI). A comparison between EVS and CV measurements is shown in Figure S5.7b, ESI. Following the evaluation procedure described in Note S5.2, ESI results in HOMO energy levels of 5.62 eV and 5.80 eV and $LUMO_{opt}$ (= HOMO + E_{opt}) energy levels of 3.58 eV and 3.74 eV for D18 and PMI-FF-PMI, respectively. The EVS measurements indicate two large bandgap materials with similar energy levels. The system can be considered a small $HOMO_D - HOMO_A$ (Δ_{HOMO}) and small $LUMO_D - LUMO_A$ (Δ_{LUMO}) offset system with nominal offsets of 0.18 eV and 0.16 eV, respectively. As discussed in Note S5.2, ESI, the presented values should be considered as rough estimates due to the large error margins of electrochemical measurements.[85] However, the measurements were evaluated uniformly and the relative differences between the materials should thus provide a reliable insight into the relevant energy offsets of this D/A combination.

Table 5.2: Summary of the photovoltaic parameters. Equation 2.34 was used to calculate the short circuit current density ($J_{SC,EQE}$) from the measured EQE_{PV} spectrum. Average values and standard deviations were calculated from 14 cells.

Material	V_{OC} (V)	J_{SC} (mA cm^{-2})	$J_{SC,EQE}$ (mA cm^{-2})	FF (%)	PCE (%)
D18:PMI-FF-PMI (ave.)	1.40 ± 0.01	6.11 ± 0.25	-	59.3 ± 1.0	5.12 ± 0.20
D18:PMI-FF-PMI (best)	1.41	6.09	6.04	60.9	5.34

In the next step, the PMI FF PMI acceptor was used in combination with the donor polymer D18 to fabricate BHJ organic solar cells in a standard (ITO/PEDOT:PSS/active layer/Ca/Al), as well as in an inverted (ITO/ZnO/active layer/MoO_3/Ag) device architecture. In the main text, we would like to focus on the devices fabricated in the standard configuration, while the results of the devices fabricated in the inverted configuration can be found in Figure S5.8 and Table S5.1, ESI. A detailed description of the device fabrication process is provided in the Methods section. Figure 5.3a shows the characteristic *J-V*-response of a D18:PMI FF PMI solar cell. The presented measurements were performed under AM1.5G (100 mW cm^{-2}) illumination (dark blue curve) and in the dark (light blue curve) on a solar cell with a D/A ratio of 1:1. The derived photovoltaic parameters (V_{OC}, I_{SC}, FF, and PCE) of the *J-V*-curve are summarized in Figure 5.3a and Table 5.2. Additionally, the averages and standard deviations

of 14 equivalent cells are presented in Table 5.2. As shown, D18:PMI-FF-PMI solar cells consistently exhibit extraordinary high V_{OC} values beyond 1.4 V. With J_{SC} values beyond 6 mA cm^{-2} and FFs of around 60 %, the material combination allows for efficiencies over 5 %.

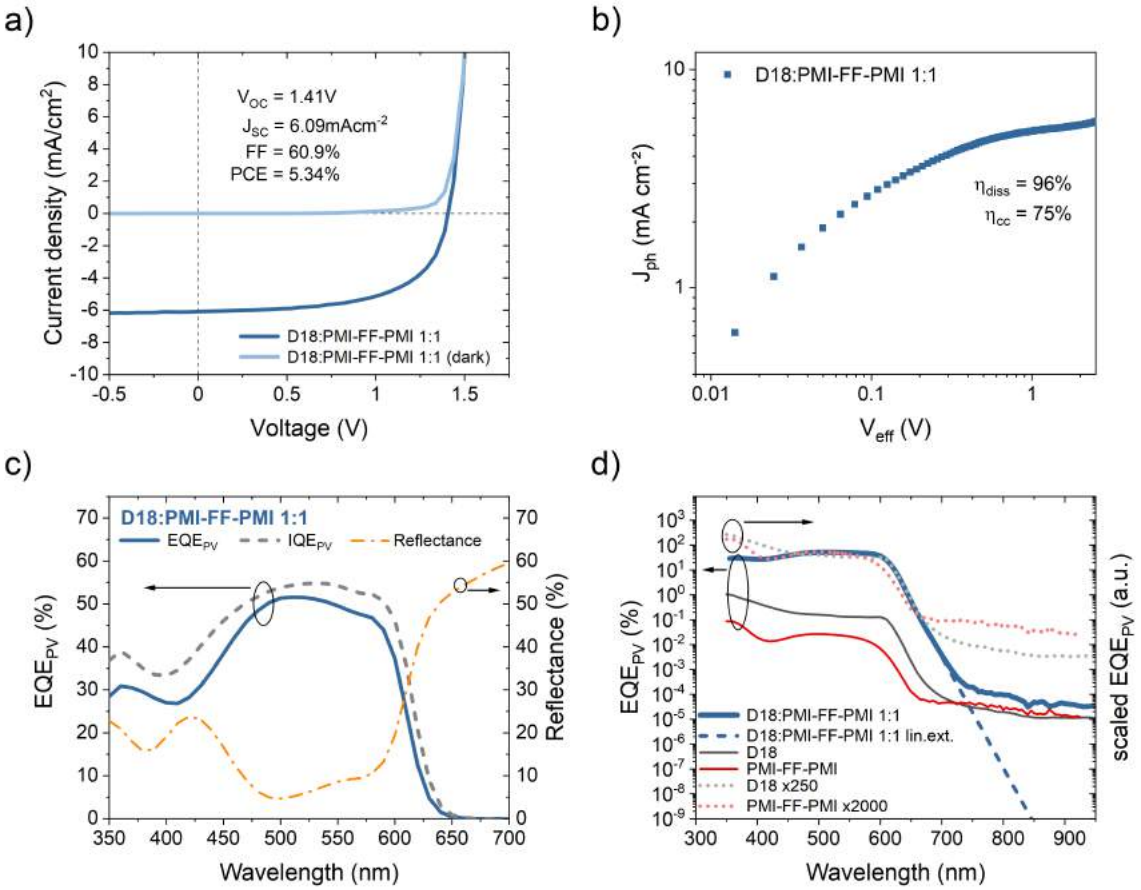

Figure 5.3: Photovoltaic characterization. a) Current density-voltage curves in the dark (light blue) and under AM1.5G illumination (dark blue) of a D18:PMI FF PMI solar cell with a D/A ratio of 1:1. b) Plot of the photogenerated current density (J_{ph}) *vs.* the effective voltage (V_{eff}). c) High-sensitivity EQE_{PV} spectrum of a D18:PMI FF PMI solar cell on a linear scale (dark blue, solid line). Additionally, the reflectance (yellow, dash-dotted line) and the IQE_{PV} of the solar cell (grey, dashed line) are presented. d) High-sensitivity EQE_{PV} spectra of a D18:PMI FF PMI solar cell (dark blue), a pristine D18 (black), and PMI FF PMI (red) diode on a semi-logarithmic scale (left axis). The dashed, dark blue line represents a "linear" fit of the EQE_{PV} in the region below the bandgap in the semi-log plot. The grey and red dotted lines illustrate the EQE_{PV} spectra of the pristine devices, which were scaled to match the EQE_{PV} of the D18:PMI FF PMI solar cell (right axis).

To the best of our knowledge, this D/A pair is the first system, based on organic semiconductors, to enable a V_{OC} beyond 1.4 V in combination with a PCE greater than 5 %. In Figure 5.3b the photogenerated current density (J_{ph}) of the D18:PMI-FF-PMI solar cell is

plotted versus the effective voltage (V_{eff}). J_{ph} is defined as the difference between the current densities under AM1.5G illumination and in the dark (J_{light}- J_{dark}) and V_{eff} can be calculated by subtracting the series resistance corrected applied bias voltage ($V_{corr} = V_{app} - J \times R_s$) from the voltage under $J_{ph} = 0$ conditions. From the ratio of J_{ph} at short circuit conditions and J_{ph} at $V_{eff} = 2\,V$ (= saturation current density J_{sat}), the exciton dissociation efficiency (η_{diss}) can be estimated. Similarly, the ratio of the current density at the maximum power point and the saturation current is used to estimate the charge collection efficiency (η_{cc}).[153,154] The derived values are presented in Figure 5.3b. An exciton dissociation efficiency of 96 % suggests that once a CT state is formed, the dissociation process into free charge carriers is highly efficient. Furthermore, a charge collection efficiency of 75 % was derived. Light intensity-dependent measurements of the *J-V*-response of the D18:PMI-FF-PMI solar cells are presented in Figure S5.9, ESI. The light-intensity dependence of the J_{SC} data is fitted to the power-law $J_{SC} \propto {P_{light}}^{\alpha}$, where P_{light} is the average incident light intensity. An α value of 1 indicates negligible bimolecular recombination at J_{SC} conditions. Moreover, the ideality factor n was extracted from the light-intensity-dependent V_{OC} measurements using $V_{OC} \propto \frac{nk_BT}{q} \times \ln(P_{light})$, where k_B is the Boltzmann constant, T is the temperature and q is the elementary charge.[155] An ideality factor of 1.6 was derived for the D18:PMI-FF-PMI system, which is indicative of Shockley-Read-Hall recombination. Moreover, in order to investigate the electronic transport properties of the novel PMI-FF-PMI acceptor, the electron mobility was determined from transfer characteristic measurements of organic field-effect transistors (OFETs) in a bottom gate, top contact geometry as discussed in Note S5.3, ESI. The measured transfer curves and the derived mobilities ($\mu_e^{sat} = 1.3 \times 10^{-4}\,cm^2V^{-1}s^{-1}$) are presented in Figure S5.10a&b, ESI. The reported hole mobility values of D18 range from $1.2 \times 10^{-3}\,cm^2V^{-1}s^{-1}$ to $1.6 \times 10^{-3}\,cm^2V^{-1}s^{-1}$, and suggest a slightly better hole than electron transport in D18:PMI-FF-PMI solar cells.[43,156] However, the determined exponent α=1 from light-intensity-dependent measurements suggests no severe imbalance of electron and hole mobilities in the optimized D18:PMI-FF-PMI device.[157]

In Figure 5.3c the EQE_{PV} of a D18:PMI FF PMI solar cell is depicted. The EQE_{PV} curve exhibits spectral features of both donor and acceptor absorption and reaches its maximum value of 52 % at 505 nm. As described in the methods section, changing the angle of incidence of the monochromatic radiation in the EQE_{PV} experiment slightly (from 0° to 13°) allows measuring the reflected light intensity using a Si photodiode. From this measurement, the spectral reflectance of the solar cell can be calculated, as shown in Figure 5.3c (yellow, dash-dotted line). At maximum EQE_{PV} (505 nm), the reflectance reaches its minimum value of 4.7%, which mainly corresponds to the reflection at the glass substrate/air interface. Beyond 600 nm, the optical absorption of the active layer is severely reduced and the sharp increase of the reflectance can be related to the reflection at the highly reflective Ca/Al top electrode. Under the assumption that the Ca/Al electrode is a perfect mirror, and that all the non-reflected light gets absorbed by the active layer, it is possible to calculate the IQE_{PV} of the

solar cell. The presented IQE_{PV} curve in Figure 5.3c should be interpreted as a lower estimate of the actual IQE_{PV} spectrum since the underlying assumption neglects scattering, non-ideal reflection at the Ca/Al electrode, or parasitic absorption in the ITO or hole transport layer. In Figure 5.3d the high-sensitivity EQE_{PV} spectrum, presented in Figure 5.3c, is plotted on a semi-logarithmic scale. As depicted, the EQE_{PV} of the solar cell (dark blue curve) is recorded over a range of 6 orders of magnitude. EQE_{PV} values >700 nm are considered limited by the sensitivity of the measurement. As discussed in the introduction, the EQE_{PV} spectrum can be used to calculate the dark saturation current J_0 using Equation 2.35. To avoid distortion of the determined J_0 values by the measurement noise, a "linear" function (linear in the semi-log plot) was fitted to the tail of the EQE_{PV} (dark blue, dashed line), assuming that no physically relevant contributions to the EQE_{PV} spectrum are hidden below the sensitivity limit of the experimental setup. In addition, the EQE_{PV} spectra of the pristine D18 (black, solid line) and PMI FF PMI (red, solid line) devices are shown in Figure 5.3d. The black and red dotted curves represent the EQE_{PV} spectra of the two pristine devices, each scaled with a constant factor to match the EQE_{PV} spectrum of the D18:PMI FF PMI solar cell. Comparing the scaled EQE_{PV} curves with the EQE_{PV} of the solar cell indicates that the sub-bandgap behavior of the solar cell is identical to the one of the pristine D18 device. This observation confirms that in this material blend the D18 donor polymer is the low-bandgap component and thus dictates the sub-bandgap behavior. Furthermore, the sub-bandgap behavior of the solar cell does not show any additional CT state absorption features, as often reported for fullerene-based solar cells.[51,98]

In addition to the photovoltaic characterization, the luminescence properties of the D/A blend and the pristine devices were investigated. The recorded photoluminescence (PL) and electroluminescence (EL) spectra are presented in Figure 5.4a. A solid-state laser with an emission wavelength of 488 nm was used for photoexcitation. As discussed in the Methods section, the injection current during EL and the photocurrent during PL measurements were set to match the recorded I_{SC} under AM1.5G illumination. In the three panels of Figure 5.4a, the normalized EL and PL spectra of the D18, PMI-FF-PMI, and D18:PMI-FF-PMI (1:1) devices are compared. The individual EL and PL spectra of all three devices exhibit similar emission features, which makes it difficult to analyze the spectrum of the D18:PMI-FF-PMI solar cell device. At first glance, the solar cell emission closely resembles the spectrum of the pristine D18 device. However, due to the strong spectral overlap of donor and acceptor emission, EL and PL measurements do not allow to exclude any emission contribution from the acceptor. Moreover, it should be emphasized that the low energy region of the EL spectrum of the D18:PMI-FF-PMI device does not show any sign of an additional CT state emission and closely resembles the EL spectrum of the pristine D18 device.

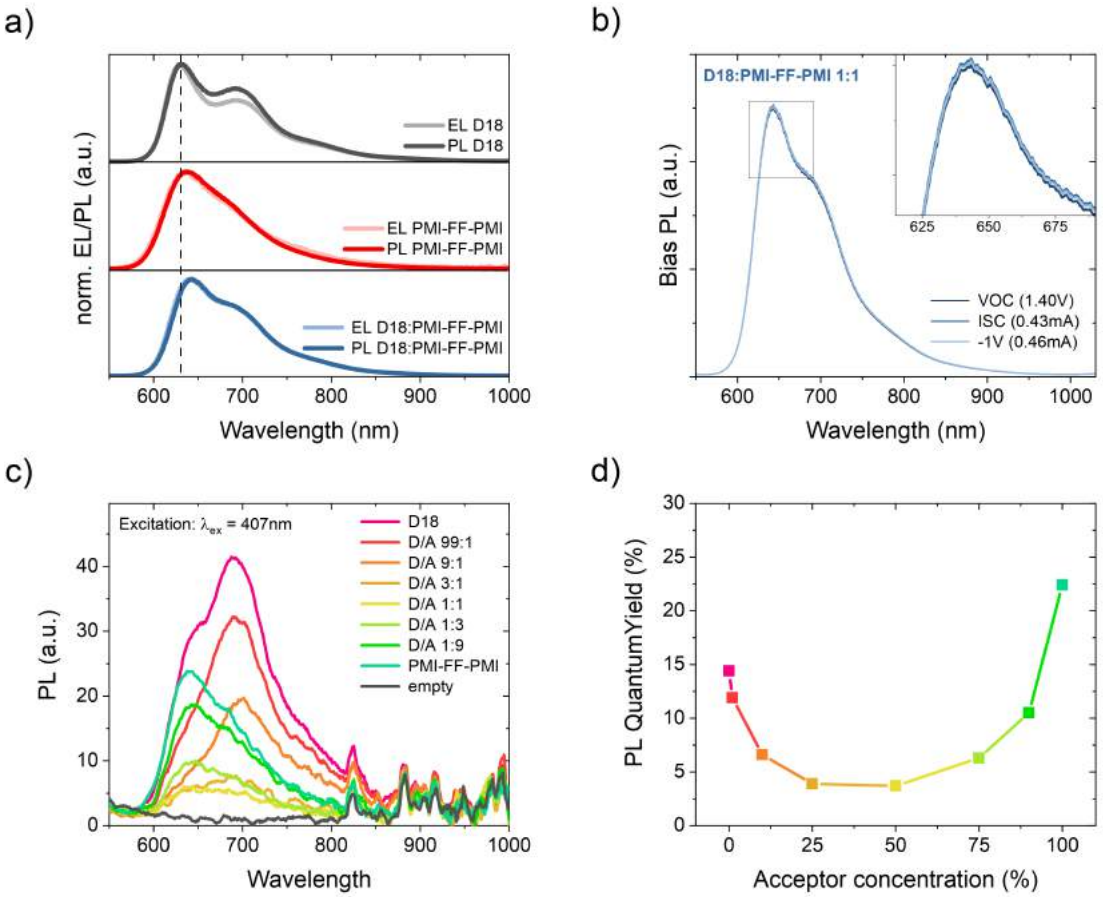

Figure 5.4: Photo- and electroluminescence measurements. a) Normalized PL (excitation at 488 nm) and EL spectra of D18, PMI FF PMI, and the D18:PMI FF PMI blend with a D/A ratio of 1:1. b) Bias-dependent PL spectra of the D18:PMI FF PMI solar cell at V_{OC}, I_{SC}, -1 V. The inset shows an enlarged view of the PL maximum at 643 nm. c) Integrating sphere PL measurements of D18, PMIFFPMI, and D18:PMI-FF-PMI thin films on glass with varying D/A ratios. The black curve represents a blank measurement without a sample inserted into the integrating sphere. An excitation wavelength λ_{ex} of 407 nm was used. d) Absolute PLQY values as a function of acceptor concentration in the blend. The PLQY values were determined from the integrating sphere measurements presented in c).

In Figure 5.4b bias-dependent photoluminescence measurements of a D18:PMI-FF-PMI solar cell are presented. In addition to the standard PL measurements at open-circuit conditions, the PL intensity was recorded under short-circuit (I_{SC}) and reverse bias conditions (1 V). The D18:PMI-FF-PMI solar cell does not show any signal reduction upon bias variation from V_{OC} to I_{SC}. Even at an applied potential of 1 V, the PL signal intensity does not change. The bias-insensitivity of the PL signal suggests that the emission is mainly caused by radiative recombination of excitons, which are not involved in the charge generation and recombination processes in the solar cell and do not contribute to the photocurrent. In order to investigate the quenching efficiency in D18:PMI-FF-PMI blends, the absolute PLQY of D18:PMI-FF-PMI

thin films on glass substrates with D/A ratios of 1:0, 99:1, 9:1, 3:1, 1:1, 1:3, 1:9, and 0:1 were measured with an integrating sphere setup. The individual PL spectra are presented in Figure 5.4c and the extracted PLQY values as a function of acceptor concentration are presented in Figure 5.4d. Measurements of the pristine D18 and PMI-FF-PMI films highlight the excellent emissive properties of both donor and acceptor. PLQY values of around 15% and 22% were observed for neat D18 and PMI-FF-PMI, respectively. Increasing the acceptor concentration to 1%, 10%, and 25% results in a continuous reduction of the PLQY. A further increase of the acceptor concentration to 75% or 90% leads to a rise of PLQY values, resulting in an overall u-shape as depicted in Figure 5.4d. In a typical quenching experiment, the reduction of the PL intensity upon the introduction of a quencher is monitored. It is worth noting that due to the strong emissivity of the quencher (PMI-FF-PMI) and the strong spectral overlap of donor and acceptor emission (see Figure 5.4c), the evaluation of the quenching efficiency is difficult. An increased acceptor concentration on the one hand quenches the polymer emission, but on the other hand, leads to a significant PL emission from the acceptor itself. However, for the D18:PMI-FF-PMI film with an optimized solar cell D/A ratio of 1:1, a mutual PL quenching is expected, where the emission of the donor is efficiently quenched by the presence of the acceptor and *vice versa*. The PLQY of the D18:PMI-FF-PMI 1:1 blend is reduced from 14.4% to 3.8% compared to the pristine D18 film.

In addition to the quenching experiments, time-correlated single-photon counting (TCSPC) measurements were performed to analyze the PL lifetimes of D18:PMI-FF-PMI blends with varying acceptor concentrations. TCSPC measurements of the thin films used in the PLQY quenching experiments (see Figure 5.4c&d) are presented in Figure 5.5a&b. For both measurements, the excitation wavelength was set to 530 nm to ensure a balanced absorption between D18 and PMI-FF-PMI (see Figure S5.6). Based on the PL spectra presented in Figure 5.4c, the detection wavelength was set to 650 nm (PMI-FF-PMI emission peak) and 700 nm (D18 emission peak), respectively. Both TCSPC measurements suggest that an increase of the acceptor concentration shifts the decay behavior from D18 dominated to PMI-FF-PMI dominated. The PL lifetimes of the blend films are found in between the lifetimes of pristine D18 and PMI-FF-PMI. A comparison of Figure 5.5a&b indicates that the measured lifetime can be manipulated by changing the detection wavelength from 650 nm (Figure 5.5a, pronounced PMI-FF-PMI emission) to 700 nm (Figure 5.5b, pronounced D18 emission). The lifetime of the D18:PMI-FF-PMI 1:1 blend (yellow curve) in Figure 5.5a is significantly increased compared to the pristine D18 lifetime, while in Figure 5.5b the lifetimes of the 1:1 blend and the pristine D18 film are almost identical. Figure 5.5c shows the PL decay behavior of a D18:PMI-FF-PMI film with a D/A ratio of 99:1 in comparison to the behavior of analog D18 blends with state-of-the-art fullerene ($PC_{71}BM$) and non-fullerene (Y6) acceptors. For the highly efficient D/A blends D18:Y6 and D18:$PC_{71}BM$ (EQE_{PV} > 80%), even a small amount of acceptor in the polymer film significantly reduces the observed PL lifetime as depicted in Figure 5.5c. On the

contrary, the decay curves of the pristine D18 film (black) and the D18:PMI-FF-PMI 99:1 film (dark blue) are congruent and no lifetime reduction can be observed.

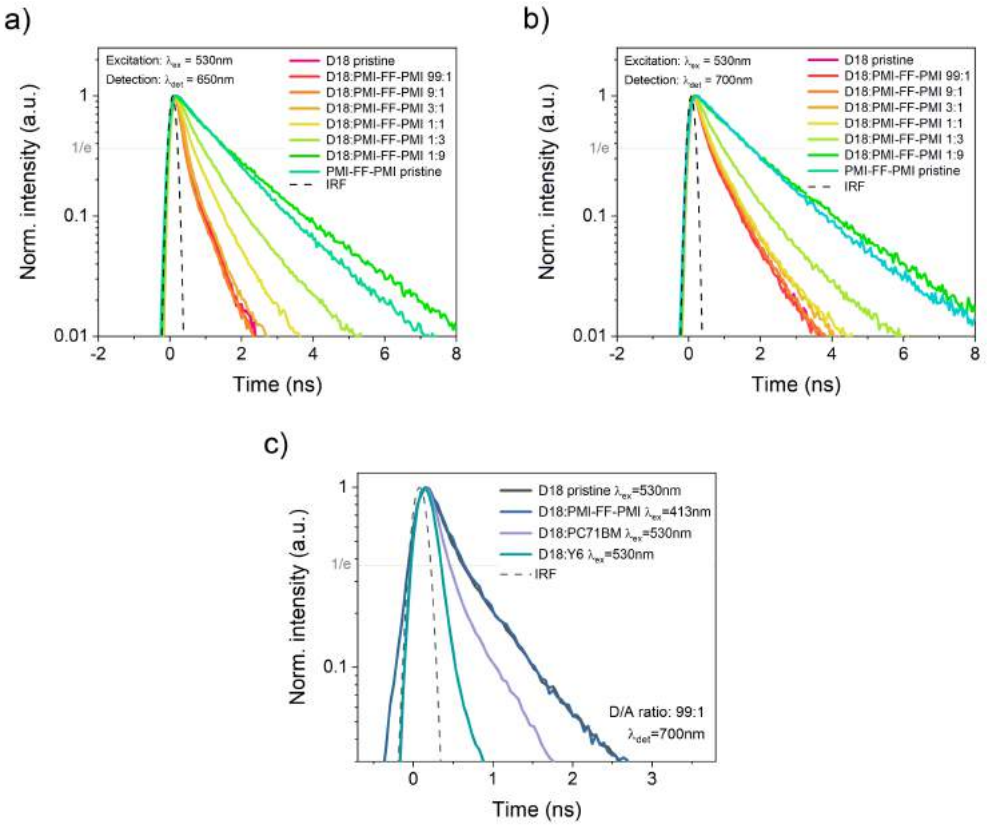

Figure 5.5: Time-correlated single-photon counting measurements. Time-resolved PL measurements of films of D18, PMI-FF-PMI, and D18:PMI-FF-PMI blends with varying D/A ratios. For all films, an excitation wavelength of 530 nm was chosen, while the detection wavelength was set to a) 650 nm and b) 700 nm. c) Comparison of the time-resolved PL decay of pristine D18 versus D18:acceptor films with a D/A ratio of 99:1. The three materials PMI-FF-PMI, Y6, and $PC_{71}BM$ were used as acceptors. The excitation and detection wavelengths were set to 530 nm and 700 nm, respectively, except for the D18:PMI-FF-PMI (99:1) film where an excitation wavelength of 413 nm was used as rationalized in the text. In all three panels the instrument response function (IRF), which indicates the minimum time resolution of the experiment, is displayed as a black dashed curve. Additionally, the value where the normalized intensity is reduced to $1/e$ of its initial value is indicated by the grey dotted line. This value was used to compare the PL lifetimes.

In Figure 5.6a, the energy difference between the relaxed ground and excited state (E_{0-0}) of the D18:PMI-FF-PMI solar cell (2.02 eV) was determined from the crossing point of the reduced EQE_{PV} and the reduced EL spectrum.[89] The orange curve represents the absorption spectrum of the D18:PMI-FF-PMI solar cell determined from its EL spectrum using the reciprocity relation EL/Φ_{bb} , where Φ_{bb} is the black body radiation at 300 K. In Figure 5.6b, the determined voltage loss contributions (see Equation 2.36) of D18:PMI-FF-PMI are

compared to the ones from high-performance D18 solar cells based on Y6 and $PC_{71}BM$ acceptors. The measured ELQY values of D18:PMI-FF-PMI, D18:Y6, D18:$PC_{71}BM$, and pristine D18 devices are summarized in Figure 5.6c. The star symbols highlight the situation where the injection current is equal to the short circuit current under AM1.5G illumination. Figure 5.6d presents the photovoltaic parameters of the individual solar cells, normalized with respect to their maximum parameters in the Schockley-Queisser limit. The photovoltaic parameters in the SQ limit were calculated assuming an ideal step function EQE_{PV}[10] and an optical gap of the small gap component of 1.36 (Y6), 2.02 (D18), and 1.78 eV ($PC_{71}BM$).

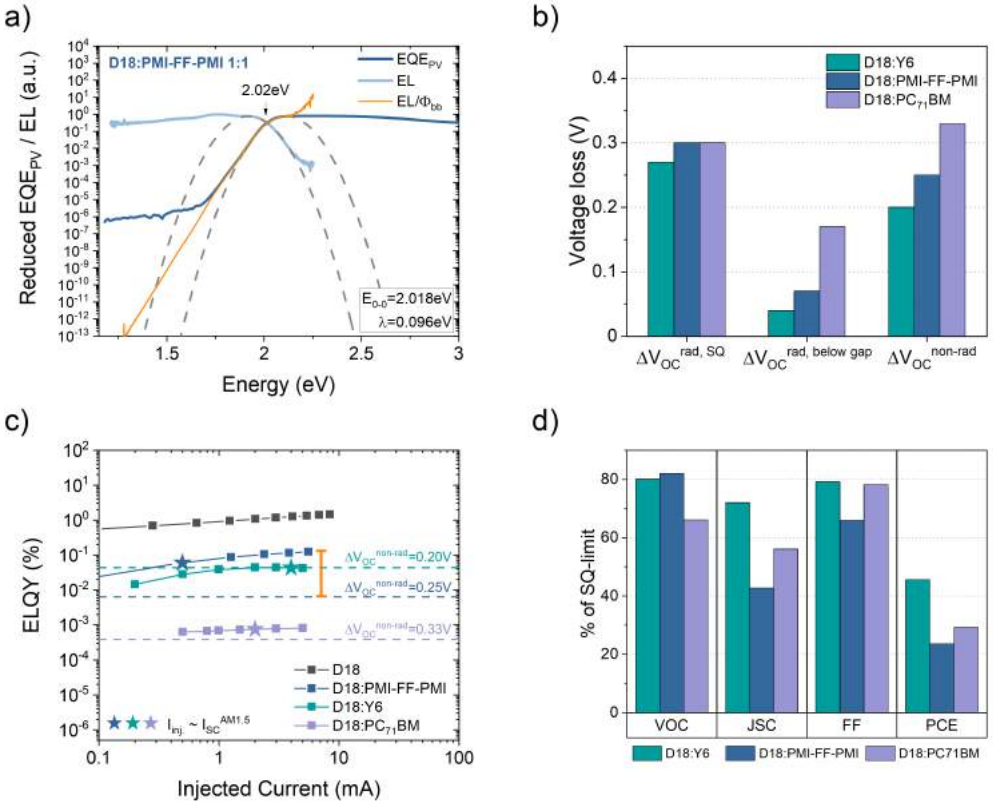

Figure 5.6: Analysis of the CT state energy, V_{OC} losses, ELQY, and photovoltaic parameters. a) Reduced EL (light blue) and reduced EQE_{PV} (dark blue) spectra of the D18:PMI-FF-PMI solar cell. The dashed parabolas were calculated from Equations 2.23 and 2.24 using the derived fit parameters E_{0-0} and λ, which are presented in the small inset. b) Comparison of the voltage losses derived for the D18:PMI-FF-PMI device with the ones reported for highly efficient non-fullerene (D18:Y6) and fullerene-based (D18:$PC_{71}BM$) solar cells.[51] The respective data is presented in Table 5.4. c) ELQY measurements of D18:PMI-FF-PMI, D18:Y6, D18:$PC_{71}BM$, and pristine D18 devices. The dashed lines represent the ELQY values calculated from Equation 2.37 assuming a non-radiative voltage loss of 0.20 V, 0.25 V, and 0.33 V for D18:Y6, D18:PMI-FF-PMI, and D18:$PC_{71}BM$, respectively. The orange bar highlights the large discrepancy between the measured and calculated ELQY for D18:PMI-FF-PMI solar cells. d) Illustration of the relative photovoltaic parameters of D18:Y6, D18:PMI-FF-PMI, and D18:$PC_{71}BM$ in % of their respective values in the SQ limit.

5.5 Discussion

In the following, the photovoltaic parameters of D18:PMI-FF-PMI solar cells (see Figure 5.3a) are compared to highly efficient solar cells based on D18 in combination with a fullerene ($PC_{71}BM$) and non-fullerene acceptor (Y6). The two materials were chosen as examples of state-of-the-art fullerene and non-fullerene acceptors, which provide a good benchmark for the PMI-FF-PMI acceptor. D18:Y6 and D18:$PC_{71}BM$ solar cells are characterized by high EQE_{PV} values beyond 80 %. Thus, optimizing the EQE_{PV} of the D18:PMI-FF-PMI blend ($EQE_{PV} \sim 50$ %) can be identified as one of the main challenges to close the performance gap to state-of-the-art fullerene and non-fullerene-based solar cells. Therefore, in the next section, the presented experimental results are used to investigate the origin of the moderate EQE_{PV} values of D18:PMI-FF-PMI solar cells.

5.5.1 Charge Generation Efficiency in D18:PMI-FF-PMI Blends

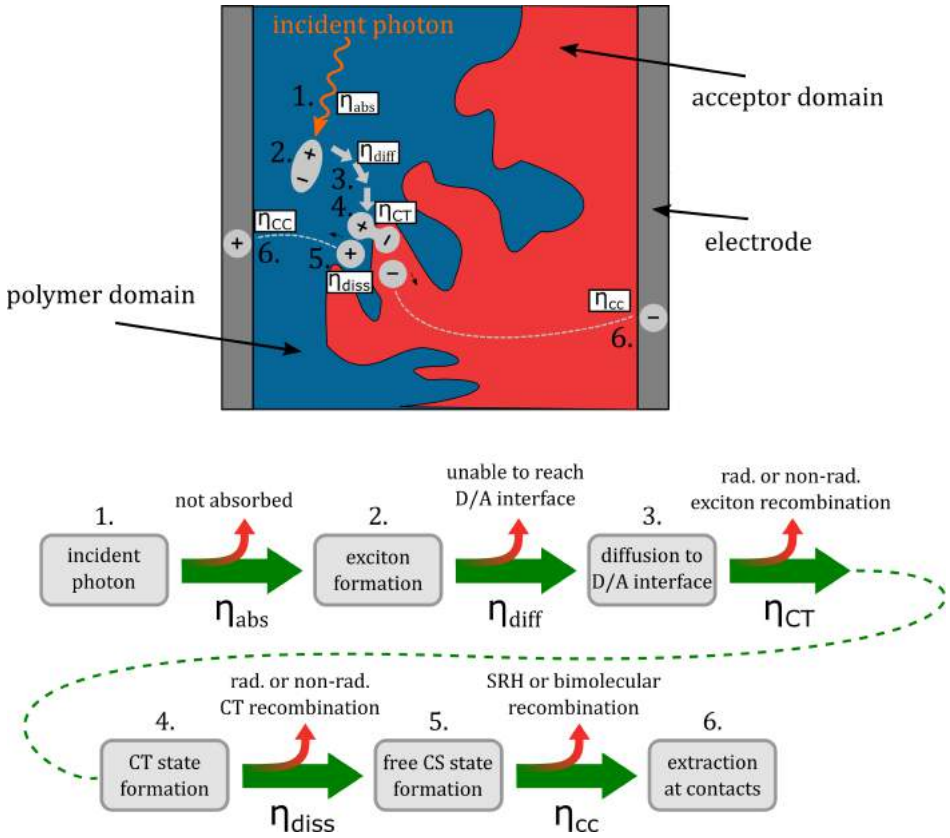

Figure 5.7: Photovoltaic conversion process of OSCs. Graphical and schematic illustration of the five efficiencies determining the EQE_{PV} of OSCs. It should be noted that the charge collection efficiency η_{cc} represents the combined efficiencies of charge transport and charge extraction. Common parasitic processes altering the respective efficiencies are indicated by the small red arrows.

As illustrated in Figure 5.7, the EQE_{PV} of OSCs is determined by the efficiencies of five processes: light absorption (η_{abs}), exciton diffusion to the D/A interface (η_{diff}), CT state formation (η_{CT}), CT dissociation into free charges (η_{diss}), and charge collection (η_{cc}). In principle, a shortcoming in one or more of the five efficiencies can cause the moderate EQE_{PV} values of D18:PMI-FF-PMI solar cells. The IQE_{PV} of the solar cell was estimated (see Figure 5.3c) to exclude adverse effects on the EQE_{PV} due to limited photon absorption. The IQE_{PV} spectrum suggests that in the high absorption region of D18:PMI-FF-PMI, the EQE_{PV} is only slightly reduced due to reflection losses. At the maximum EQE_{PV}, the reflectance of the solar cell is approaching the reflectance of the glass/air interface (4 %), suggesting that almost all the photons are absorbed within the solar cell stack. As shown in Figure 5.3b, the determined dissociation probability suggests that once a CT state is formed at a D18/PMI-FF-PMI interface, it has an extremely high probability of 96 % to dissociate into free charges. With an estimated charge collection efficiency of 75 %, none of the discussed processes is expected to severely limit the maximum EQE_{PV} value. Therefore, either a reduced driving force for CT state formation (low η_{CT}) or a non-ideal blend morphology with D/A domain sizes exceeding the exciton diffusion length (low η_{diff}) is expected to be responsible for the moderate EQE_{PV} values in D18:PMI-FF-PMI solar cells. This hypothesis is in good agreement with the presented bias-dependent PL measurements in Figure 5.4b. For an ideal PV device, the PL intensity is expected to vanish when the applied bias is swept from V_{OC} to I_{SC} conditions. At V_{OC} conditions the photogenerated charge carriers are forced to recombine radiatively within the device, resulting in a PL emission signal. At I_{SC} conditions, ideally, all photogenerated charge carriers are extracted at the contacts and charge carriers do not recombine in the active layer (no PL emission). Experimentally, a similar behavior has been reported for highly efficient perovskite solar cells (EQE_{PV} > 85 %), where the PL intensity is strongly reduced when operated at I_{SC} conditions.[158] With few exceptions, the PL of organic solar cells show very little or no bias-dependence.[159] Typically, the small bias-dependent fraction of the PL signal is buried under a large bias-insensitive PL signal stemming from singlet emission of the pristine donor or acceptor components. It should be noted that we recently have investigated the high-performance D/A system D18:Y6 (EQE_{PV} >80 %), which showed a moderate PL reduction of almost 10 % when measured at I_{SC} conditions.[51] Bias-dependent PL measurements of an efficient D18:Y6 solar cell are presented in Figure S5.11, ESI. Even the emission of this high-efficiency D/A blend primarily consists of a bias-insensitive component, which accounts for the majority (>90 %) of the observed PL signal. However, the fact that there is a noticeable difference between I_{SC} and V_{OC} conditions is separating this system from most other D/A combinations and highlights its exceptional performance. In OPV blends the singlet emission can be caused by photovoltaically inactive, isolated pure donor or acceptor domains which can be a result of a non-ideal morphology. When the size of these domains exceeds the exciton diffusion length, the photogenerated excitons cannot diffuse to the D/A interface and are forced to recombine in the pure material. Even in the case of an ideal BHJ morphology with domain sizes smaller than the exciton

diffusion length, the PL emission can be dominated by singlet exciton recombination if the driving force to form a CT state is weak. Thus, there is a direct competition between radiative and non-radiative exciton decay into the ground state and the formation of a CT state, if the rate for charge transfer is not significantly faster than the rate of singlet exciton recombination. Due to the typically high oscillator strength of singlet transitions in pristine donor or acceptor molecules, even a small fraction of recombining singlet excitons can overpower the weak emission from radiative CT state recombination. Therefore, the bias-insensitivity of the PL signal of D18:PMI-FF-PMI solar cells (see Figure 5.4b) suggests that the recorded emission is dominated by radiative recombination of excitons, which do not contribute to the photocurrent. As discussed above, the photovoltaically inactive excitons are either caused by the presence of large domains of pristine material (non-ideal morphology) or a low charge transfer state efficiency. Various attempts to change the D/A morphology by common processing techniques like (post-) annealing, solvent additives, solvent mixing, varying D/A ratios, or the processing temperature did not lead to a significant increase in the observed EQE_{PV} or J_{SC} values as summarized in Figure S5.12, ESI. Although non-ideal domain sizes cannot be excluded from the presented optimization trials, the inability to significantly improve the J_{SC} of the solar cells strongly suggests investigating the driving force of CT state formation. Especially, as electrochemical measurements of D18 and PMI-FF-PMI (see Figure 5.2c) hint at small energetic offsets between the individual HOMO and LUMO levels of donor and acceptor. Atomic force microscopy (AFM) measurements did not allow to distinguish between donor and acceptor domains and could not be used to quantify the domain sizes. A common way to investigate the charge generation efficiency in a D/A blend is to perform a PL quenching experiment.[74] As shown in Figure 5.4c&d, PLQY measurements were used to study the quenching of the PL intensity of D18 polymer thin films with increasing acceptor concentrations. The PLQY can be defined as the ratio of the radiative recombination rate (k_r) to the sum of the rates of radiative (k_r) and non-radiative (k_{nr}) and the quenching rate (k_q), as shown in Equation 5.1.[160]

$$\mathrm{PLQY_{blend}} = \frac{k_r}{k_r + k_{nr} + k_q} \tag{5.1}$$

$$\mathrm{PLQY_{pristine}} = \frac{k_r}{k_r + k_{nr}} \tag{5.2}$$

$$\mathrm{QE} = 1 - \frac{\mathrm{PLQY_{blend}}}{\mathrm{PLQY_{pristine}}} \tag{5.3}$$

The quenching rate depends on the efficiency of the deactivation process of the excited state. In OPV blends quenching occurs when photogenerated excitons in a pristine domain can diffuse to a D/A interface and form a CT state. The radiative recombination rate of the CT state is typically several orders of magnitude lower compared to the one of the pristine materials and is thus assumed negligible. It should be stated that the quenching rate does

not allow to differentiate between the effects of non-ideal morphology (η_{diff}) or CT state formation efficiency (η_{CT}). For pristine materials, the rate k_q is zero, and Equation 5.1 can be reduced to Equation 5.2. The quenching efficiency QE can be calculated according to Equation 5.3. It should be noted that the denominator in Equations 5.1 and 5.2 is dominated by the fastest rate. Fullerene-based solar cells are typically characterized by extremely fast CT rates and exhibit strong PL quenching efficiencies beyond 95 %.[161] In contrast, the quenching efficiency for the D18:PMI-FF-PMI film with a D/A ratio of 1:1 is around 74 %. It has been shown that for a variety of different D/A pairs the quenching efficiency directly correlates with the maximum IQE_{PV} of the solar cell.[74] For D18:PMI-FF-PMI this would lead to a maximum IQE_{PV} which is approximately 20 % below the one from high efficient fullerene blends. This observation is in good agreement with the reduced EQE_{PV} of D18:PMI-FF-PMI solar cells ($\sim$ 50 %) compared to EQE_{PV} values >80 % for D18:Y6 or D18:PC_{71}BM solar cells. It should be noted that D18:PC_{71}BM and D18:Y6 films with a D/A ratio of 99:1 showed a strong PLQY quenching below the detection limit of the integrating sphere setup. Assuming a PLQY detection limit of 1 % allows estimating a lower limit for the quenching efficiency for D18:Y6 and D18:PC_{71}BM thin films. From this estimation, the QEs of D18:Y6 and D18:PC_{71}BM blends are expected to be larger than 93 %. As discussed in Note S5.4, ESI, PLQY and PL lifetime measurements (τ_{meas}) of a pristine D18 film allow the calculation of the radiative (k_r) and non-radiative (k_{nr}) recombination rates in the pure polymer. Assuming that k_r and k_{nr} of the polymer in D/A blends are not affected by the presence of the acceptor allows determining the quenching rate k_q from PLQY measurements of the blends. Table 5.3 shows that a $PLQY_{blend}$ of 11.9 % for the D18:PMI-FF-PMI 99:1 blend yields a quenching rate of $3.4 \times 10^8\,s^{-1}$, which is almost identical to the calculated radiative recombination rate ($k_r = 2.3 \times 10^8\,s^{-1}$). In contrast, the quenching rates of D18:Y6 and D18:PC_{71}BM films with a D/A ratio of 99:1 are estimated to be beyond $2.2 \times 10^{10}\,s^{-1}$, if a $PLQY_{blend}$ <1 % is assumed. The film morphologies of all three 99:1 D/A blends are expected to be similar since the morphology is mainly determined by the D18 polymer. The unbalanced D/A ratio of 99:1 suggests large domains of pristine D18, while the small amount of acceptor is assumed to be evenly distributed in the polymer matrix. In this case, the diffusion of an exciton to the D/A interface (η_{diff}) is assumed equally efficient for all three films. Consequently, the quenching rate k_q is directly related to the efficiency for CT state formation (η_{CT}) and can be used to compare the driving force for charge transfer between the three D/A blends. The comparison between the quenching rates of D18:PMI-FF-PMI ($\sim 2 \times 10^8\,s^{-1}$) and D18:Y6 ($\sim 2 \times 10^{10}\,s^{-1}$) suggests that a reduced driving force for charge transfer can be identified as the main factor limiting the EQE_{PV} of D18:PMI-FF-PMI solar cells.

A similar conclusion can be drawn from TCSPC measurements of the three 99:1 films as shown in Figure 5.5c. The PL lifetime of a pristine D18 film can be identified as the denominator in Equation 5.1 with k_q = 0 (see Equation S5.5, ESI). Consequently, a quenching rate k_q which is in the same order of magnitude or larger than k_r and k_{nr} should lead to a significant

Table 5.3: PLQY and TCSPC lifetimes. PLQY and TCSPC measurements of D18 films with small amounts of PMI FF PMI, Y6, and $PC_{71}BM$. The individual rates are calculated according to Note S5.4, ESI.

D/A blend	D/A ratio	PLQY (%)	τ_{meas} (ns)	k_r^{calc} (s^{-1})	k_{nr}^{calc} (s^{-1})	k_q^{calc} (s^{-1})
Pristine D18	1:0	14.4	0.62	2.3×10^8	1.4×10^9	-
D18:PMI-FF-PMI	99:1	11.9	0.62	2.3×10^8	1.4×10^9	3.4×10^8
D18:Y6	99:1	<1	0.35	2.3×10^8	1.4×10^9	$> 2.2\times10^{10}$
D18:$PC_{71}BM$	99:1	<1	0.45	2.3×10^8	1.4×10^9	$> 2.2\times10^{10}$

reduction of the PL lifetime for D18 films with an acceptor concentration of 1 %. Indeed, the measured PL lifetimes (τ_{meas}) of high-performance D18:Y6 and D18:$PC_{71}BM$ blends are significantly lower (0.35 ns and 0.45 ns, respectively) compared to the lifetime of pristine D18 films (τ_{meas} = 0.62 ns). On the contrary, the lifetime of the D18:PMI-FF-PMI blend does not show any reduction and highlights the low quenching efficiency of this blend compared to efficient D18:Y6 or D18:$PC_{71}BM$ blends. Considering Equation S5.5, ESI, the lack of lifetime reduction upon the introduction of a quencher for the D18:PMI-FF-PMI blends (see Figure 5.5a-c) seems counterintuitive. However, such a behavior can be rationalized by the strong emission contribution of pristine domains as discussed in Note S5.5, ESI.

5.5.2 CT State & Voltage Loss Analysis

In OSC blends the driving force for charge transfer is thought to be strongly related to the energetic offset between the local exciton (LE) state of the low bandgap component and the CT state (ΔE_{LE-CT}). The proposed low driving force for CT state formation in D18:PMI-FF-PMI solar cells is in good agreement with the experimental results of EQE_{PV} and EL measurements. No clear evidence of CT state absorption or emission features can be extracted from the measurements of D18:PMI-FF-PMI solar cells (see Figure 5.3d and Figure 5.4a). To confirm these observations a common method suggested by Vandewal *et al.*[89] was performed to determine the CT state energy (see Section 2.2.1). For solar cells with a prominent CT state absorption and emission, Equations 2.23 and 2.24 can be used to fit the low energy CT absorption and high energy CT emission behavior as shown for D18:$PC_{71}BM$.[51] In this case the crossing point E_{0-0} can be identified as the CT state energy E_{CT}. As shown in Figure 5.6a the reduced emission spectrum of the D18:PMI-FF-PMI device does not show any sign of CT state emission. Therefore, Equation 2.24 was used to fit the high-energy part of the singlet emission peak. A two-parameter fit using a Levenberg-Marquardt iteration algorithm was performed. The final fit parameters E_{0-0} and λ are presented in the inset in Figure 5.6a and were used to construct the reduced absorption and emission curves using Equations 2.23 and 2.24. Figure 5.6a shows that the reduced absorption curve (dashed

parabola) is in excellent agreement with the experimentally observed EQE_{PV} spectrum. Moreover, the reciprocity relation between the electroluminescence and the EQE_{PV} can be used to express the latter as the EL spectrum divided by the blackbody radiation at 300 K. The calculated EQE_{PV} spectrum using the reciprocity relation EL/Φ_{bb} perfectly reproduces the experimentally observed EQE_{PV} behavior as shown in Figure 5.6a. The analysis strongly highlights the importance of the D18 singlet absorption and emission properties, which completely dominate the EL and EQE_{PV} spectrum of D18:PMI-FF-PMI solar cells. In this case, the derived parameter E_{0-0} represents the optical bandgap of D18, and no exact value for the CT state energy can be derived from the performed measurements. The analysis suggests that potential CT state features are buried under the strong D18 singlet emission and absorption. Even if no exact value for the CT state energy could be determined, the lack of additional CT state absorption or emission features indicates that the CT state energy is not significantly lower than the singlet state energy of D18. As discussed in the introduction, a better understanding of the voltage losses in OPV devices is of paramount importance for future device optimization. The extremely high V_{OC} beyond 1.4 V makes the D18:PMI-FF-PMI blend an interesting candidate to closely investigate the individual open circuit voltage loss contributions described in Equation 2.36. The EQE_{PV} measurements of the D18:PMI-FF-PMI device presented in Figure 5.3c&d were used to perform the open-circuit voltage loss analysis as outlined in Equations 2.33 - 2.36. The results are summarized in Table 5.4. Despite the extremely high V_{OC} under AM1.5G illumination, the D18:PMI-FF-PMI solar cell exhibits a relatively high total open circuit voltage loss of 0.61 V. Furthermore, Table 5.4 shows the result of the voltage loss analysis for D18:Y6 and D18:PC_{71}BM solar cells. The individual loss contributions of all three solar cells are summarized in Figure 5.6b. The comparison of the voltage losses of solar cells based on the three different acceptors clearly shows that the PMI-FF-PMI device exhibits higher losses in all three categories compared to the highly efficient Y6-based device. Especially the non-radiative voltage loss of 0.25 V of the D18:PMI-FF-PMI solar cell is considerably higher than the 0.20 V of the D18:Y6 device. Still, the D18:PMI-FF-PMI device shows significantly less $\Delta V_{OC}^{rad,b.g.}$ and $\Delta V_{OC}^{non-rad}$ losses compared to the fullerene-based device. The results confirm the frequently observed trend that NFA-based solar cells suffer from less open circuit voltage losses than their fullerene-based counterparts. As shown in Section 2.2.2, the non-radiative voltage loss can be directly linked to the ELQY of a solar cell device according to Equation 2.37. Therefore, additional measurements of the ELQY of the solar cell can be used to validate the performed voltage loss analysis. As shown in Figure 5.6c, the calculated ELQYs ($ELQY_{calc}$) from non-radiative voltage losses (dashed lines) are in good agreement with the measured ELQY ($ELQY_{meas}$) for D18:Y6 and D18:PC_{71}BM solar cells. As highlighted by the orange bar in Figure 5.6c, the $ELQY_{meas}$ values of the D18:PMI-FF-PMI solar cell are approximately a factor of ten higher than the ELQY calculated from the observed non-radiative voltage loss of 0.25 V. $ELQY_{meas}$ values as high as 0.1 % were recorded for the D18:PMI-FF-PMI device, which would correspond to a non-radiative voltage loss of only 0.18 V. The V_{OC} of such devices should be as high as 1.48 V,

which is contradictory to the experimentally observed V_{OC} values. The large discrepancy between the measured and calculated ELQY is further discussed in the next section.

Table 5.4: Comparison of the voltage losses in D18 solar cells with different acceptor molecules.

Material D18:	E_{opt}/q (V)	$\Delta V_{OC}^{rad,SQ}$ (V)	V_{OC}^{SQ} (V)	$\Delta V_{OC}^{rad,b.g.}$ (V)	V_{OC}^{rad} (V)	$\Delta V_{OC}^{non\text{-}rad}$ (V)	V_{OC} (V)	ΔV_{OC}^{total} (V)	Source
PMI-FF-PMI	2.02	0.30	1.72	0.06	1.66	0.25	1.41	0.61	This work
Y6	1.38	0.27	1.11	0.04	1.07	0.20	0.87	0.51	[51]
$PC_{71}BM$	1.78	0.30	1.48	0.17	1.31	0.33	0.98	0.80	[51]

In addition to the voltage losses, the photovoltaic performance of D18:PMI-FF-PMI, D18:$PC_{71}BM$, and D18:Y6 solar cells was compared. Due to the different effective bandgaps of the three solar cells, the measured photovoltaic parameters were normalized by the respective photovoltaic parameters in the SQ limit. With the knowledge of the effective bandgap of the blends and assuming an ideal step-like EQE_{PV}, J_0^{SQ} and J_{SC}^{SQ} can be calculated using Equations 2.34 and 2.35. The derived values can be used to construct the *J-V*-curve in the SQ limit using the following formula.

$$J(V) = J_0^{SQ}\left(\exp\left(\frac{qV}{k_B T}\right) - 1\right) - J_{SC}^{SQ} \tag{5.4}$$

The photovoltaic parameters in the SQ limit can then be extracted from the obtained *J-V*-curves. The measured photovoltaic parameters and calculated SQ photovoltaic parameters are summarized in Table S5.4, ESI. In addition, the measured photovoltaic parameters of all three solar cells in percent of their respective SQ limit are graphically illustrated in Figure 5.6d. The V_{OC} of the D18:PMI-FF-PMI cell reaches an impressive value of 82 % of its maximum value, which once again highlights the extraordinary high V_{OC} in this D/A blend. Moreover, it can be seen that the overall performance of this blend is limited by the moderate J_{SC} values. Only 42 % of the ideal J_{SC} in the SQ limit is reached, which is significantly lower than the 72 % of the highly efficient D18:Y6 system. Once again, the moderate EQE_{PV} values of the D18:PMI-FF-PMI solar cell can be identified as the main factor limiting the overall photovoltaic performance. In addition, Figure 5.6d shows that the D18:PMI-FF-PMI device reaches only 66 % of its FF^{SQ} compared to approximately 80 % for D18:Y6 and D18:$PC_{71}BM$, indicating another possibility to further optimize the device performance.

5.5.3 ELQY *vs.* Non-Radiative Voltage Loss

To elucidate the large differences between $ELQY_{meas}$ and $ELQY_{calc}$, the non-radiative voltage losses and electroluminescence properties of D18:PMI-FF-PMI solar cells are discussed within

the framework of a three-state-model reported by Chen and co-workers, which specifically incorporates the interaction (hybridization) between LE and CT states.[142] Their model accounts for the thermal population of LE and CT states and can be used to determine the radiative and non-radiative recombination rates of OPV devices. With the extended three-state model they are able to explain the energy gap law dependence found in fullerene-based blends[76], as well as the deviation from the energy gap law in state-of-the-art NFA-based blends. The three-state model highlights the importance of the $\Delta E_{\mathrm{LE-CT}}$ offset and the electronic coupling between LE and CT state ($t_{\mathrm{LE-CT}}$). Moreover, they show that for low $\Delta E_{\mathrm{LE-CT}}$ offset systems the ELQY approaches the ELQY of the pristine low bandgap component, which is ultimately determining the minimum non-radiative voltage loss for any D/A blend. Within the framework of the energy gap law and the three-state model, the D18:PMI-FF-PMI solar cell is expected to exhibit minimal non-radiative voltage losses. As discussed above, the presented experimental data show no clear CT state absorption or emission features and suggest that the CT state is energetically close to the LE state of D18 ($\sim$2 eV). The assumption of a small $\Delta E_{\mathrm{LE-CT}}$ offset system is supported by the low quenching efficiency and the moderate $\mathrm{EQE_{PV}}$ values of D18:PMI-FF-PMI solar cells. According to the energy gap law, the high CT state energy should lead to a reduced wavefunction overlap between the relaxed CT state and higher-order vibrational modes of the ground state. Moreover, as suggested by the three-state model, the D18:PMI-FF-PMI blend should benefit from LE-CT state hybridization due to a low $\Delta E_{\mathrm{LE-CT}}$ offset. Both of these properties hint at a D/A blend with an extremely low non-radiative voltage loss. However, these predictions cannot be confirmed with the presented voltage loss analysis, as a moderate $\Delta V_{\mathrm{OC}}^{\mathrm{non-rad}}$ loss of 0.25 V, corresponding to an $\mathrm{ELQY_{calc}}$ of 6.4×10^{-3} %, was observed. As highlighted in Figure 5.6c, there exists a vast discrepancy between $\mathrm{ELQY_{calc}}$ and the measured ELQY of the solar cell (1.2×10^{-1} %). It should be noted that the ELQY of the D18:PMI-FF-PMI solar cell is indeed approaching the ELQY of the pristine D18 device as predicted by the three-state model. However, the high measured ELQY values do not translate to a reduced non-radiative voltage loss of the solar cell device. In the following, we will argue that the measured ELQY value is overestimating the radiative efficiency of the solar cell. From PLQY quenching and bias-dependent PL experiments we have derived that the PLQY of a D18:PMI-FF-PMI blend with a D/A ratio of 1:1 is approximately 3 %, and we have observed that the emission spectrum of the solar cell is independent of the applied bias. At V_{OC} conditions all the photogenerated free charge carriers are forced to recombine within the active layer, while at I_{SC} conditions the PL intensity should be reduced due to the extraction of these free charge carriers. The minimal detectable change in PL intensity of the experimental setup is assumed to be 1 %. Considering the invariance of the PL intensity upon the applied bias leads to the conclusion that the additional emission from radiative recombination of free charge carriers accounts for less than 1 % of the total emission. Thus, the ELQY of free charge carrier recombination in the D18:PMI-FF-PMI blend has to be lower than 3×10^{-2} %. The derived ELQY value from the voltage loss analysis ($\mathrm{ELQY_{calc}} = 6.4 \times 10^{-3}$ %.) is consistent with the derived upper limit of 3×10^{-2} %. On

the contrary, recombination of injected free charge carriers can be ruled out as an origin of the experimentally measured, large ELQY values ($ELQY_{meas} = 1.2 \times 10^{-1}$ %), since such a large free-carrier contribution would lead to a significant bias-sensitive component in the bias-dependent PL measurement. As clearly shown in Figure 5.4b, a bias dependency of the PL signal is not observed for the D18:PMI-FF-PMI device. However, the source of the additional EL emission contribution, leading to an overestimation of the measured ELQY, remains unclear. A possible explanation for the increased ELQY is the charge injection into pure donor or acceptor domains. Especially for large applied voltages, the electrical energy of injected charge carriers might be high enough to elevate an electron into the LUMO level of the polymer or a hole into the HOMO level of the acceptor, owing to the small energetic offsets between D18 and PMI-FF-PMI. Subsequent recombination of an electron and a hole on the pristine material would be able to explain the boosted ELQY of the solar cell due to the typically larger ELQYs of pristine devices. A schematic sketch of the band diagram of D18:PMI-FF-PMI depicts the electron injection from a metal electrode at different forward bias conditions and highlights the possibility of direct electron injection into the polymer for an OPV blend with small LUMO offsets (see Figure S5.13a, ESI). Moreover, Figure S5.13b, ESI shows that the pristine D18 device already exhibits high ELQY values at applied voltages between 1.4-1.5 V (close to V_{OC} of the solar cell). Thus, even at moderate applied voltages, an efficient electron injection in the D18 device is expected. It should be noted that also the reverse process of injecting a hole into the HOMO of the acceptor molecule cannot be excluded. This process is conceivable for all small Δ_{HOMO} or Δ_{LUMO} offset systems and could in principle affect ELQY measurements of most common wide-bandgap donor, small bandgap acceptor systems (e.g. OSCs based on the Y-acceptor series). In addition to the effect of direct charge injection, the measured ELQY can be strongly affected by the applied bias voltage, charge carrier mobility, and injection barriers. Regardless of these challenges, various reports have shown excellent agreement between $ELQY_{calc}$ and $ELQY_{meas}$, supporting the feasibility of deriving the $\Delta V_{OC}^{non-rad}$ loss of a solar cell from ELQY measurements.[142,162] However, our detailed study of the emission properties of D18:PMI-FF-PMI solar cells indicates that this is not generally true. Our results suggest that there are exceptions, where the measured ELQY is massively overestimating the ELQY derived from the $\Delta V_{OC}^{non-rad}$ losses of the solar cell. Despite being common practice to determine the $\Delta V_{OC}^{non-rad}$ loss from ELQY measurements, our results strongly emphasize that solely relying on this method is precarious and that the derived $\Delta V_{OC}^{non-rad}$ values should always be validated by performing a voltage loss analysis as described earlier.

5.5.4 Application in Triple Junction Devices & Optimization Potential

The recent success of NFA-based tandem devices highlights the great potential of increasing OPV efficiencies by a more efficient photon-to-energy conversion due to reduced thermaliza-

tion losses in multi-junction OPV devices. As discussed in the introduction, the promising development of ultra-low bandgap OPV blends with strong infrared absorption up to 1100 nm unlocks the possibility of efficient triple-junction OPV stacks. With an effective bandgap of around 2.02 eV, the D18:PMI-FF-PMI device can be identified as an ideal candidate for a wide-bandgap sub-cell in all-organic triple-junction devices. The impressive V_{OC} of 1.41 V for the D18:PMI-FF-PMI system suggests triple-junction open-circuit voltages close to 3 V, as theoretically shown in Figure S5.14, ESI. Here, the OPV blends D18:PMI-FF-PMI, PBDBT-2F:IT-4F, and PTB7-Th:COTIC-4F are presented as possible candidates for an all-organic triple-junction device. The simple model described in Note S5.6, ESI predicts that triple junction efficiencies around 15 % and 20 % can be realized if the maximum EQE_{PV} of the wide-bandgap (D18:PMI-FF-PMI) and small-bandgap sub-cell (PTB7-Th:COTIC-4F) can be improved to 70 % and 85 %, respectively. Thus, in order to fabricate efficient triple-junction devices, further device and material optimizations are necessary to improve the EQE_{PV} of D18:PMI-FF-PMI solar cells. The presented experimental results indicate that a slight modification of the PMI-FF-PMI molecule to increase the Δ_{HOMO} or Δ_{LUMO} offset between donor and acceptor could be beneficial for the charge generation efficiency. An often-used approach to slightly reduce the energy levels of NFAs is halogenation (e.g. chlorination or fluorination). Chemical modification of the perylene π-system by functionalization at the *bay* positions[163] could be a feasible strategy to further improve the EQE_{PV} of D18:PMI-FF-PMI solar cells. Alternatively, it could be beneficial to increase the bandgap of the acceptor (ideally without increasing its LUMO). A larger bandgap would lead to strong complementary absorption in the UV – blue region of the solar spectrum in addition to the strong D18 absorption between 450-630 nm. Moreover, a complementary absorption increases the overlap of acceptor emission and donor absorption and enhances the energy transfer from the acceptor to the donor (Förster Resonant Energy Transfer, FRET). In our case, this would leave the Δ_{HOMO} offset of the blend unimportant and could have a positive effect on the charge generation efficiency as discussed in Reference [74]. A possible design strategy to increase the bandgap of the PMI-FF-PMI molecule is to replace the perylene monoimide unit with a smaller conjugated molecule (e.g. naphthalene monoimide). Alternatively, it has been shown that increasing the lateral extension of the perylene core can lead to a stronger UV absorption.[164,165] In addition, the usage of ester rather than imide end groups might present another possibility to increase the bandgap of perylene-based acceptors.[166,167]

5.6 Summary & Conclusion

In summary, the non-fullerene acceptor PMI-FF-PMI based on two perylene monoimide units bridged via a dihydroindeno[1,2-b]fluorene linker exhibits excellent absorption and emission properties in the visible regime and shows good solubility and film formation properties. The PMI-FF-PMI acceptor was used in combination with the commercially available,

high-performance donor polymer D18 to fabricate organic BHJ solar cells. Electrochemical measurements (EVS & CV) were used to determine the energy levels of donor and acceptor molecules. HOMO energy levels of 5.62 eV and 5.80 eV and $LUMO_{opt}$ energy levels of 3.58 eV and 3.74 eV were obtained for D18 and PMI-FF-PMI, respectively. This material combination thus represents a wide bandgap D/A blend with small Δ_{HOMO} and Δ_{LUMO} offsets. *J-V*-response measurements reveal that D18:PMI-FF-PMI solar cells are characterized by an extremely high V_{OC} of 1.41 V, which to the best of our knowledge is the highest V_{OC} value reported for solution-processed, single-junction organic solar cells to date. A maximum EQE_{PV} of 52 % indicates moderately efficient charge generation in this D/A blend. PLQY quenching and PL lifetime measurements were performed to investigate the charge transfer efficiency of D18:PMI-FF-PMI. Both experiments suggest a lower driving force for charge transfer compared to highly efficient D18:Y6 or D18:PC_{71}BM blends. The low driving force was identified as the main factor restricting the maximum EQE_{PV} of D18:PMI-FF-PMI solar cells. Both, highly sensitive EQE_{PV} and EL measurements did not show any additional CT absorption or emission features. Thus, the presented CT state analysis could not be used to determine an exact value for the CT state energy. Nevertheless, the experimental results indicate a small offset between the LE and CT state. Finally, the photovoltaic parameters and the open-circuit voltage losses of D18:PMI-FF-PMI solar cells were analyzed and compared to high-performance D18:Y6 and D18:PC_{71}BM devices, representing state-of-the-art fullerene and non-fullerene based OSCs. Despite its high V_{OC}, the D18:PMI-FF-PMI suffers from significantly higher $\Delta V_{OC}^{non-rad}$ losses (0.25 V) compared to the solar cell based on D18:Y6 (0.20 V). It was found that the ELQY measured for D18:PMI-FF-PMI OSCs is significantly higher than the ELQY values derived from the non-radiative voltage losses. To conclude, the effective bandgap of about 2.02 eV and the extremely high V_{OC} make D18:PMI-FF-PMI solar cells ideal candidates for the application as a wide-bandgap sub-cell in all-organic triple-junction devices. Considering the large potential to optimize the CT driving force of the D18:PMI-FF-PMI blend in combination with the great possibilities to fine-tune optical and electronic properties of the perylene π-system, we hope that our work can help to accelerate the development of future wide-bandgap NFAs. In addition, our experimental results reveal that in exceptional cases the measured ELQY of a solar cell device cannot be used to derive its non-radiative voltage loss. ELQY measurements of D18:PMI-FF-PMI solar cells show that $ELQY_{meas}$ might overestimate the actual radiative efficiency of the solar cell by more than a magnitude. The direct injection of electrons in the LUMO of the donor polymer or holes in the HOMO of the acceptor molecule are presented as possible explanations for the enhanced ELQY values. Regardless, the large discrepancy between $ELQY_{meas}$ and $ELQY_{calc}$ values observed in D18:PMI-FF-PMI solar cells strongly suggests that solely relying on the measured ELQY can lead to severe misinterpretation of the observed $\Delta V_{OC}^{non-rad}$ loss. Therefore, our results should encourage OPV researchers to always validate the $ELQY_{meas}$ values with the $ELQY_{calc}$ values derived from a voltage loss analysis.

5.7 Acknowledgments

Financial support by the Austrian "Climate and Energy Fund" within the program Energy Emission Austria (Project: ALTAFOS, FFG No. 865 072) is gratefully acknowledged. Moreover, J.H. acknowledges the Austrian Academy of Science for the financial support under the Chemical Monthly Fellowship (MOCHEM). M.R. acknowledges the Austrian Science Fund (FWF) via Meitner-Programm grant M 2738.

5.8 Supplementary Information

Synthesis of PMI-FF-PMI

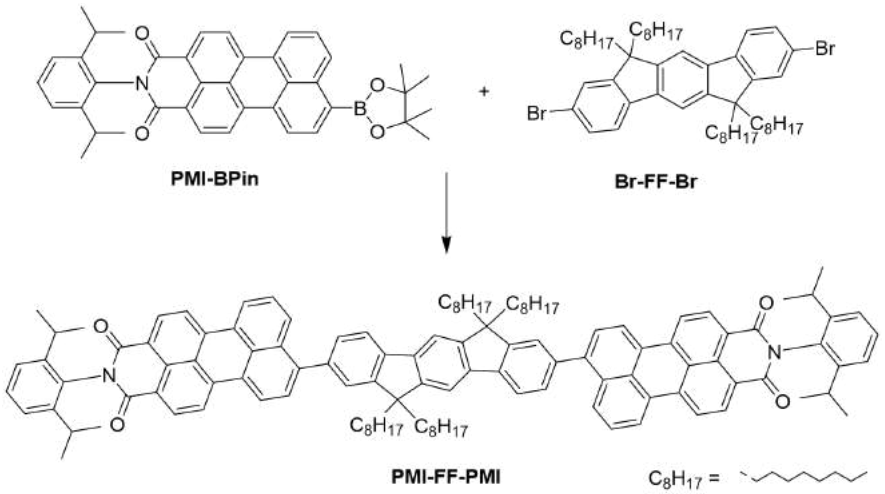

Figure S5.1: Synthesis scheme of PMI-FF-PMI.

Note S5.1.
In a Schlenk tube, operated under nitrogen, 500 mg (0.823 mmol, 2.1 equiv.) of 8-(4,4,5,5-tetramethyl-1,3,2-dioxaborolan-2-yl)-N-(2,6-diisopropylphenyl)-perylene-3,4-dicarboximide (PMI-BPin) and 337 mg (0.392 mmol, 1.0 equiv.) of 2,8-dibromo-6,6,12,12-tetraoctyl-6,12-dihydroindeno[1,2 b]fluorene (Br-FF-Br, CAS Number 264281-45-0) were dissolved in 50 mL toluene followed by the addition of 1 M K_2CO_3 (5 ml) and 1 drop of Aliquat 336. Afterwards, $Pd(PPh_3)_4$ (0.039 mmol, 0.1 equiv.) was added and the reaction mixture was heated at 100 °C for 24 h. Upon completion, the reaction mixture was extracted with H_2O and dried over Na_2SO_4 followed by evaporation of the solvent under reduced pressure. The residue was purified by column chromatography (eluent: CH_2Cl_2/pentane – 10/1) and further recrystallized using CH_2Cl_2/hexane to yield PMI-FF-PMI as a violet solid. Yield: 228 mg (35 %). Rf = 0.39 – 0.52 (CH_2Cl_2) ^{1}H NMR (500 MHz, $CDCl_3$): δ = 8.71 (dd, J

= 7.8 Hz, 4H), 8.60 (d, J = 8.0 Hz, 2H), 8.58-8.52 (m, 6H), 8.11 (d, J = 8.5 Hz, 2H) 7.97 (d, J = 7.7 Hz, 2H) 7.79 (s, 2H), 7.73 (d, J = 7.7 Hz, 2H), 7.62 (t, J = 7.8 Hz 2H), 7.58 (dd, J = 7.7, 1.1 Hz, 2H), 7.56 (s, 2H), 7.49 (t, J = 7.8 Hz, 2H) 7.35 (d, J = 7.8 Hz, 4H), 2.79 (hept, J = 6.9 Hz, 4H), 2.18-2.09 (m, 8H), 1.24-1.10 (m, 64H), 0.90-0.78 (m, 20H) ppm. ^{13}C NMR (75 MHz, $CDCl_3$): δ = 164.2, 151.7, 150.9, 145.9, 144.3, 141.5, 140.6, 138.5, 138.0, 137.8, 133.1, 132.3, 132.3, 131.3, 130.8, 129.7, 129.6, 129.0, 128.7, 128.6, 128.5, 127.2, 127.1, 124.9, 124.2, 124.1, 123.8, 121.2, 121.0, 120.5, 120.2, 119.8, 114.5, 55.2, 40.8, 32.0, 30.2, 29.5, 29.4, 29.3, 24.2, 22.8, 14.3 ppm. HRMS (MALDI-TOF) calc. for $C_{120}H_{128}N_2O_4H$ 1662.9987, found 1662.9929.

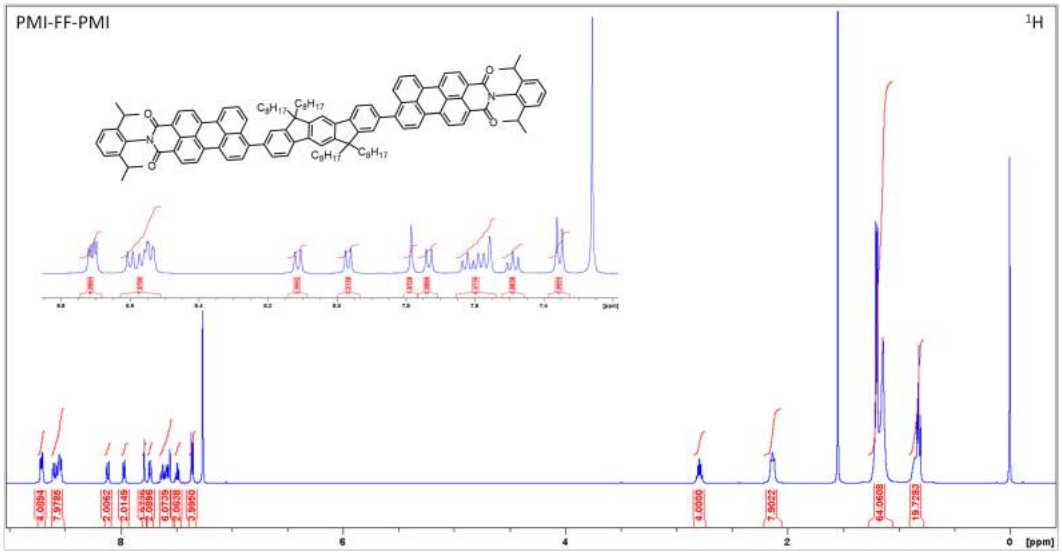

Figure S5.2: ^{1}H NMR (500 MHz, $CDCl_3$) spectrum of PMI-FF-PMI with an inset of the aromatic region, referenced to TMS.

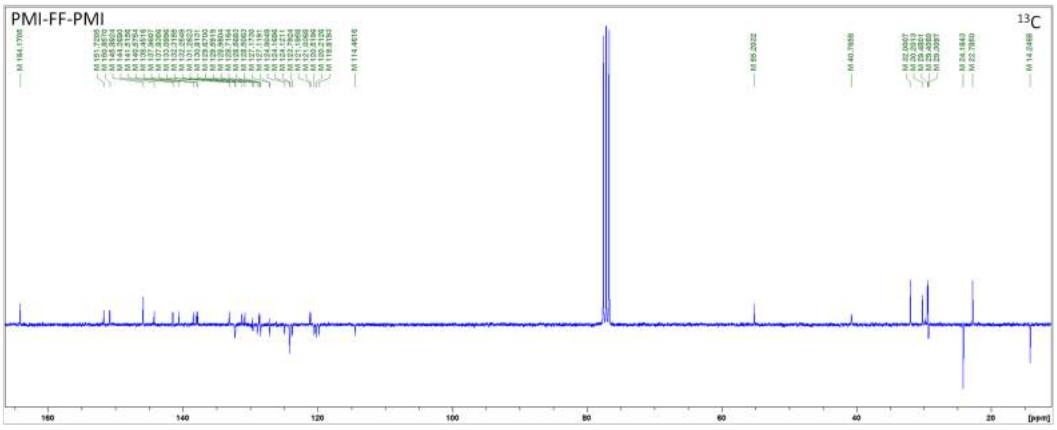

Figure S5.3: ^{13}C APT NMR (75 MHz, $CDCl_3$) spectrum of PMI-FF-PMI, referenced to $CDCl_3$.

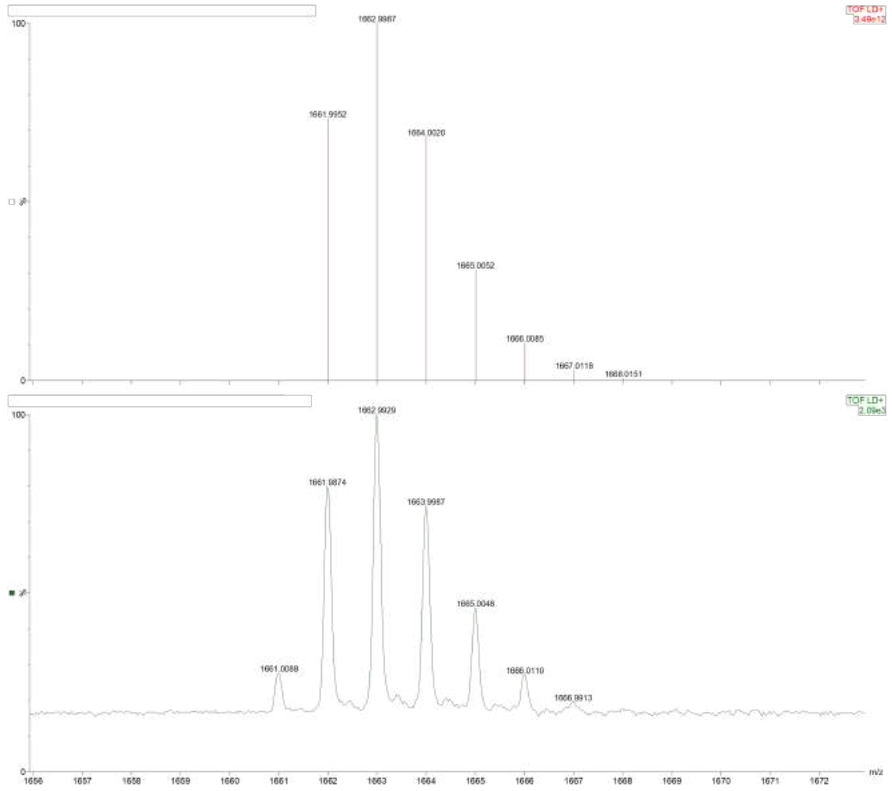

Figure S5.4: HRMS (MALDI-TOF, Dithranol matrix) of PMI-FF-PMI, upper – simulated, lower – found

Additional Optical Characterizations

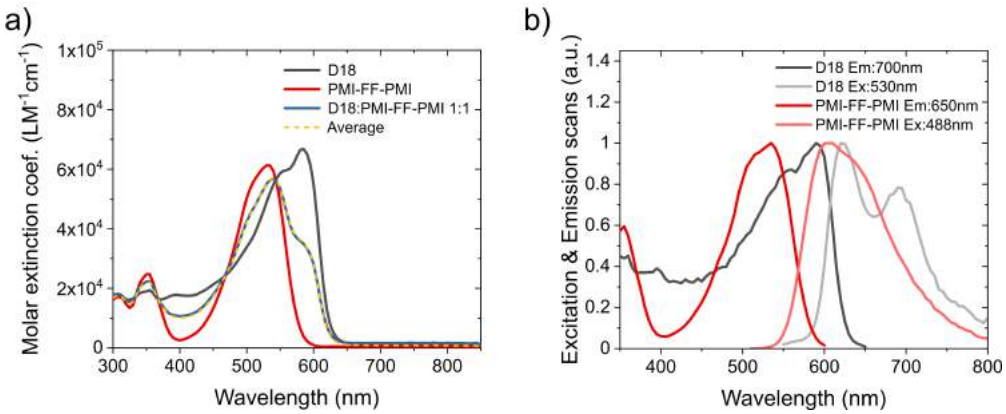

Figure S5.5: Optical characterization of D18 and PMI-FF-PMI solutions dissolved in chlorobenzene. a) Molar extinction coefficient obtained from absorbance measurements. The average spectrum of the two pristine materials (yellow dashed line) coincides with the measured 1:1 mix of D18 and PMI-FF-PMI. b) Excitation and emission scans of D18 and PMI-FF-PMI solutions. Excitation wavelengths during emission, and detection wavelengths during excitation scans are presented in the legend.

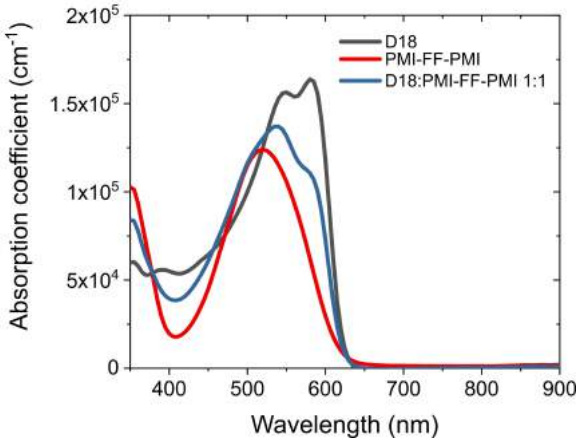

Figure S5.6: Absorption coefficients of D18, PMI-FF-PMI, and D18:PMI-FF-PMI (1:1) calculated from transmission and reflection measurements of thin films on glass substrates.

EVS & CV Measurements

Note S5.2.

a) Evaluation procedure

An exact determination of the energy levels of donor and acceptor is of key importance for OPV performance analysis and future material design. Fine-tuning of the energy levels is necessary to find the optimal balance between small $\Delta V_{OC}^{non-rad}$ losses (low ΔE_{LE-CT} offset) and sufficient driving force for charge generation (large ΔE_{LE-CT} offset). Contradicting reports for HOMO and LUMO levels of organic materials suggest that commonly used techniques such as ultraviolet electron spectroscopy (UPS) or cyclic voltammetry (CV) suffer from large measurement and evaluation errors.[85,86] Depending on the used method, HOMO and LUMO levels may vary significantly, often leading to deviations in the magnitude of several tenths of eV. The difficulty in defining the reduction and oxidation onsets from electrochemical measurements is considered the main contribution to the evaluation error. A so-called tangent evaluation method is commonly used, where a tangent is fitted to the slope of the CV peak and the baseline, respectively. The intersection point is considered as the onset of the electrochemical reaction. Another possibility often used to evaluate EVS data, is to define the first deviation from the baseline as the reduction/oxidation onset. In Figure 5.2c, the results from the "first deviation method" were used to plot the box diagram. The whiskers represent the values obtained from the "tangent evaluation method" and should be considered as a maximum evaluation error, which can still be justified by the measurement data. A detailed illustration of the different evaluation methods is presented in Note S5.2b. Figure 5.2c shows that regardless of the evaluation method the HOMO level of donor and acceptor can be determined with good accuracy. The determination of the LUMO levels on the other hand shows a strong variation between the evaluation

methods. Especially the LUMO of the polymer is hard to identify, which is further discussed in Note S5.2b. Reliable measurements of the HOMO energy levels and difficulties to determine the LUMO energy levels suggest estimating the LUMO level by adding the respective optical bandgap (E_{opt}) to the HOMO energy levels of donor and acceptor ($LUMO_{opt}$).

b) EVS *vs.* CV measurements

Typically, a tangent method, as described in Note S5.2a, is used to determine the reduction and oxidation onsets from CV measurements. As it can be seen from the CV oxidation peaks in Figure S5.7a, determining the tangent is often ambiguous and leaves great scope for interpretation. To reduce evaluation errors, EVS measurements were used as an alternative to estimate the HOMO and LUMO levels of OPV materials. In EVS, the onset of reduction or oxidation is simply defined as the first deviation from the baseline, which significantly reduces the evaluation uncertainty. Furthermore, EVS is used to measure specifically the start of the electrochemical reaction and is thus ideally suited to investigate reduction and oxidation onsets. As shown in Figure S5.7a, the reaction onsets measured in EVS can be associated with the oxidation and reduction peaks in CV experiments. In the following, the CV and EVS measurements were evaluated with both methods. The results from the 1^{st} deviation method should be regarded as a lower limit for the energy levels of donor and acceptor (box), while the tangent method should be considered as an upper limit (whiskers). Figure S5.7b shows the evaluation of the EVS data for D18 and PMI-FF-PMI, respectively. The analysis shows that the HOMO levels of both, donor and acceptor, can be determined with good accuracy regardless of the evaluation method. On the contrary, the determination of the LUMO level of D18 is difficult due to a delayed reduction onset. The delayed onset leads to a large discrepancy between the values obtained from the 1^{st} deviation and the tangent method. To a lesser extent, the same is true for the PMI-FF-PMI acceptor. To avoid this problem the LUMO levels of both materials were calculated by adding the optical bandgaps E_{opt} to the respective HOMO levels. $LUMO_{opt}$ is represented by the yellow bars in Figure S5.7b&c. It is worth noting that the delayed reduction onset for the D18 polymer is not displayed in the CV data and leads to an electrochemical bandgap which is approximately 0.5 eV larger than the optical bandgap. A similar delayed reductive behavior has been observed for all the investigated donor polymers (PTB7, PTB7-Th, PBDB-T, PM6, PTQ11, PTZ1). Our results suggest that CV measurements largely overestimate the LUMO levels of state-of-the-art donor polymers. Figure S5.7c gives a summary of the derived energy levels for D18 and PMI-FF-PMI using both methods and evaluation techniques. A comparison of the HOMO levels suggests that for both donor and acceptor the EVS data exhibits less dependency on the evaluation method and validates the usage of the EVS method over the CV method.

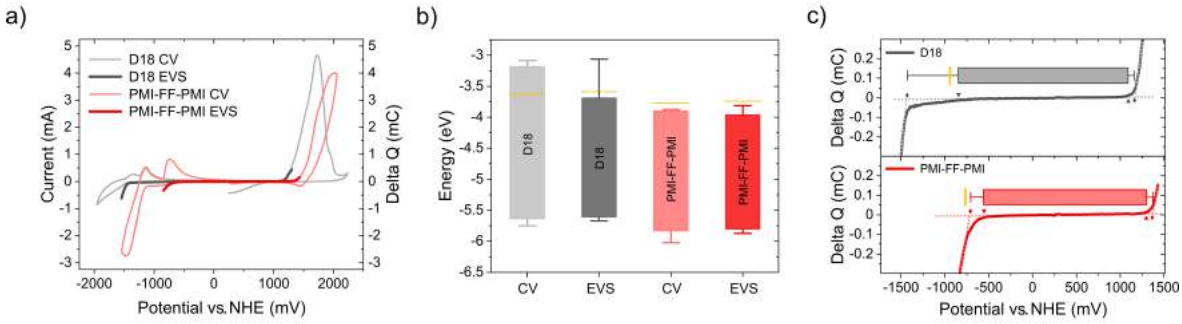

Figure S5.7: Electrochemical characterization of D18 and PMI-FF-PMI films. a) Comparison of EVS and CV measurements of D18 and PMI-FF-PMI. b) Summary of the derived HOMO and LUMO levels from CV and EVS measurements of D18 and PMI-FF-PMI. c) Graphical illustration of the two discussed evaluation methods. The values obtained from the 1st deviation and tangent method are indicated by the red and black triangle and diamond symbols, respectively. The LUMO level, determined from the HOMO level and the optical bandgap, is highlighted in yellow.

D18:PMI-FF-PMI solar cells fabricated in the inverted structure

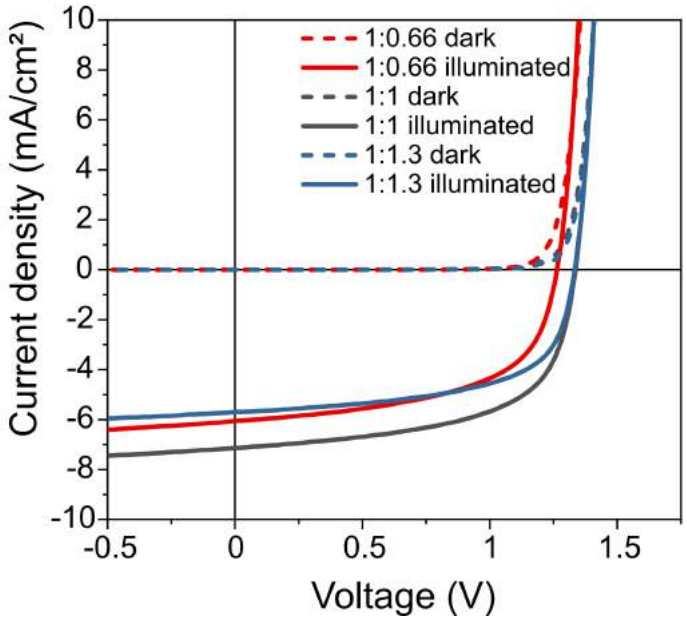

Figure S5.8: *J-V*-characteristics measured in the dark and under 100 mW cm^{-2} AM1.5G illumination of typical D18:PMI-FF-PMI based solar cells prepared in the inverted device architecture and with different D/A ratios (see also Table S5.1).

Table S5.1: Characteristic device parameters of D18:PMI-FF-PMI based solar cells prepared in inverted architecture (ITO/ZnO/D18:PMI-FF-PMI/MoO_3/Ag). The D/A weight ratio was varied from 1:0.66 to 1:1.33.

D:A ratio		V_{OC} (V)	J_{SC} (mA cm^{-2})	FF (%)	PCE (%)
1:0.66	best cell	1.26	6.0	57.1	4.32
	average	1.24 ± 0.01	5.7 ± 0.2	55.8 ± 1.1	3.92 ± 0.21
1:1	best cell	1.34	7.1	60.1	5.69
	average	1.35 ± 0.01	6.4 ± 0.5	59.8 ± 2.2	5.13 ± 0.32
1:1.3	best cell	1.34	5.7	60.9	4.65
	average	1.32 ± 0.03	5.3 ± 0.3	56.8 ± 6.0	4.00 ± 0.51

Light-dependent *J-V* measurements

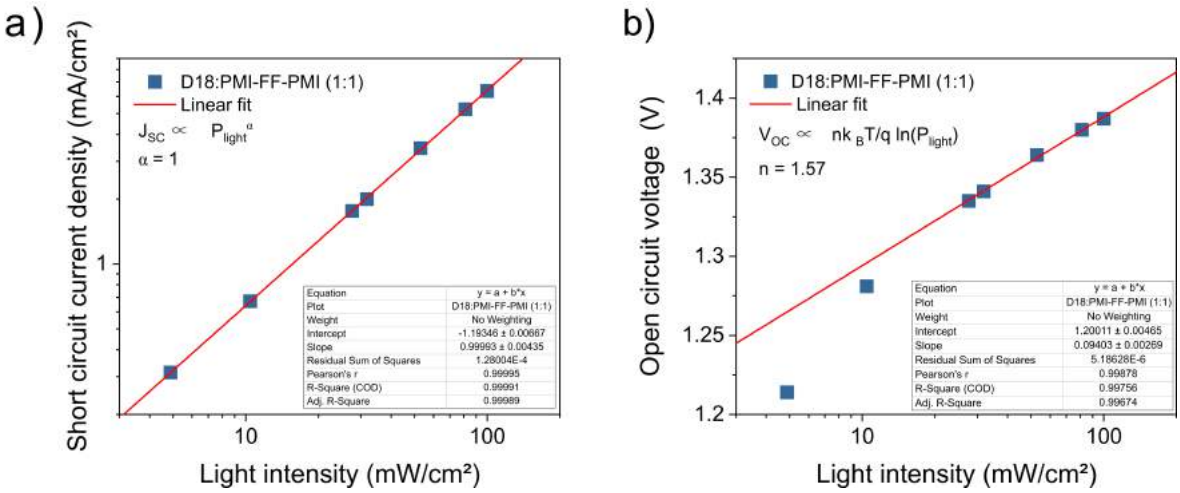

Figure S5.9: Intensity-dependent J_{SC} and V_{OC} measurements.

Mobilities

Note S5.3.

The OFET devices were fabricated in a bottom gate, top contact geometry. The aluminum bottom gate electrode was thermally evaporated onto a glass substrate. A 32 nm aluminum oxide layer (dielectric layer) was obtained by electrochemical anodization. Benzocyclobutene (BCB) was used as a dielectric passivation layer. The PMI-FF-PMI acceptor was spin-coated (33 rps for 30 s) from a 9 mg/mL chloroform solution resulting in typical thicknesses of around 75 nm. Finally, aluminum source and drain top contacts were thermally evaporated resulting in transistors with a channel width W of 2000 µm and a channel length L of 65 µm. The device structure and the detailed fabrication process of the electrodes and dielectric

layers are described elsewhere.[137] In the saturation regime, the drain current I_{drain} can be described with

$$I_{\text{drain}} = \frac{WC_{\text{ox}}}{2L}\mu_{\text{e}}^{\text{sat}}\left(V_{\text{gate}} - V_{\text{Th}}\right)^2, \tag{S5.1}$$

where C_{ox} is the capacitance per unit area, $\mu_{\text{e}}^{\text{sat}}$ is the electron saturation mobility, V_{gate} is the gate and V_{Th} is the threshold voltage. Rearranging Equation S5.1 allows calculating the saturation mobility $\mu_{\text{e}}^{\text{sat}}$ from the slope of the $(V_{\text{gate}} - V_{\text{Th}})$ *vs.* $\sqrt{I_{\text{drain}}}$ plot:

$$\mu_{\text{e}}^{\text{sat}} = \frac{2L}{WC_{\text{ox}}}\left(\frac{\partial\sqrt{I_{\text{drain}}}}{\left(V_{\text{gate}} - V_{\text{Th}}\right)}\right)^2 \tag{S5.2}$$

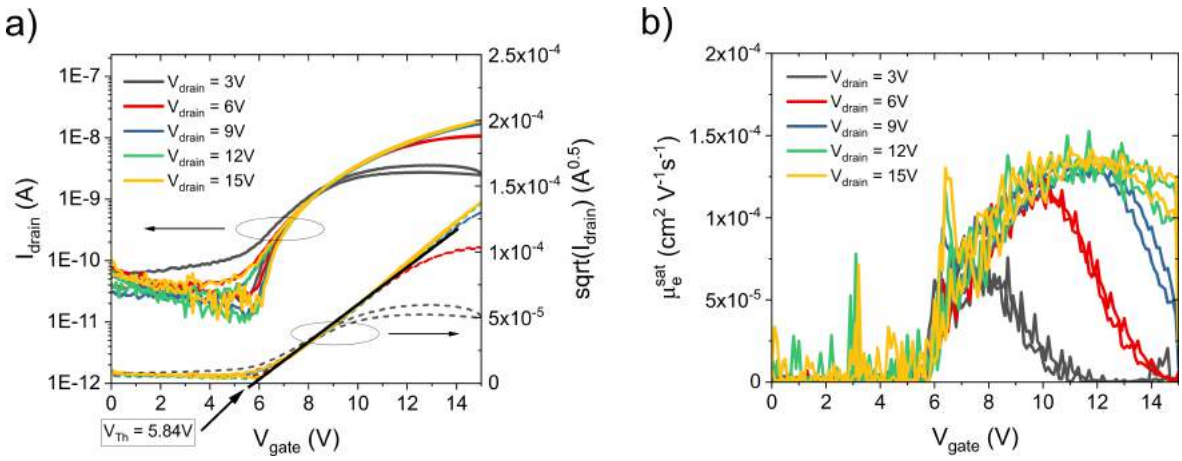

Figure S5.10: OFET transfer characteristic and saturation mobility. a) Transfer characteristic of a PMI-FF-PMI OFET. The devices were measured with an Agilent B1500A semiconductor device parameter analyzer. The OFET transfer curves were measured by sweeping the gate voltage from 0 to 15 V and back to 0 V in 100 mV steps. After each sweep, the drain voltage was increased by 3 V until a final drain voltage of 15 V was reached. The solid curves indicate the drain current on a logarithmic scale (left y-axis), while the dashed curves represent the square root of the drain current on a linear scale (right y-axis). The straight black line indicates the linear fit of $\sqrt{I_{\text{drain}}}$. The intersection of the black line with the x-axis allows to read out the values of the threshold voltage V_{Th}. b) The measurements presented in a) were used to derive the saturation mobility curves following Equation S5.2.

Bias PL reduction of D18:Y6

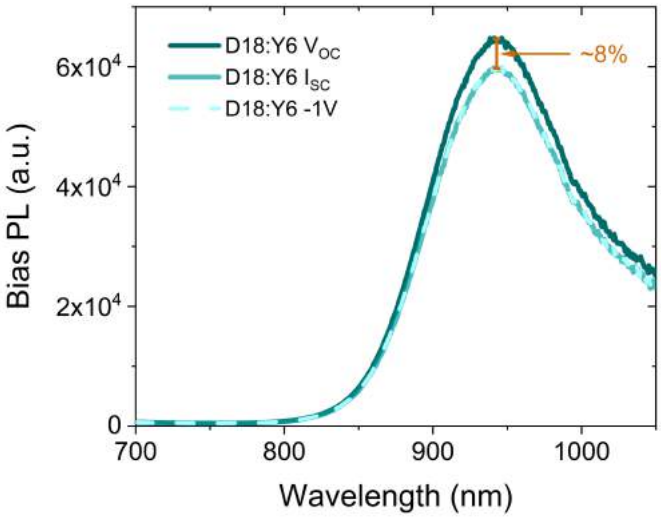

Figure S5.11: Bias dependent Photoluminescence. PL of a high efficient D18:Y6 solar cell with a D/A ratio of 1:1.6. The detailed device fabrication and characterization of the solar cells are reported in Reference [51]. Measured PL signal decreases about 8 % upon changing bias conditions from V_{OC} to I_{SC}. A further increase to reverse bias conditions (-1 V) does not alter the PL signal.

D18:PMI-FF-PMI optimization

As shown in Figure S5.12a, varying the D/A weight ratio of D18:PMI-FF-PMI solar cells only slightly affects the solar cell performance. D/A blends with a ratio of 1:0.6 exhibit the highest J_{SC} values but suffer from a reduced V_{OC} and FF. On the contrary, if the ratio is changed to 1:1.3 the solar cell FF slightly increases compared to the 1:1 blend, but the J_{SC} is continuously reduced. Overall, the optimum performance was found for solar cells with a balanced D/A ratio of 1:1. No further improvements were obtained upon annealing of the D/A blend prior to the evaporation of the top contact. Extraordinary thermal stability of D18:PMI-FF-PMI solar cells was observed showing no significant change up to annealing temperatures of 200 °C. Pre-heating of the substrates prior to the spin coating process resulted in D/A films with an increased thickness and is the reason for the slightly reduced FFs in those solar cells. As seen in Figure S5.12c, the device structure with PEDOT:PSS as hole transport layer (HTL) and Ca as electron transport layer (ETL) resulted in solar cells with the best performance. Inverting the structure and using ZnO as ETL and MoO_3 as HTL slightly increased the current but led to reduced V_{OC} and FF values. Replacing Ca with ETLs like PDIN or PFN-Br significantly reduced the performance. Most probably the high-work function Ca layer is needed to form an ohmic contact with the wide-bandgap (high LUMO) acceptor PMI-FF-PMI.

Various tries to use different solvents, solvent mixtures or solvent additives did not result in an improvement in either V_{OC}, J_{SC}, or FF as depicted in Figure S5.12d-f.

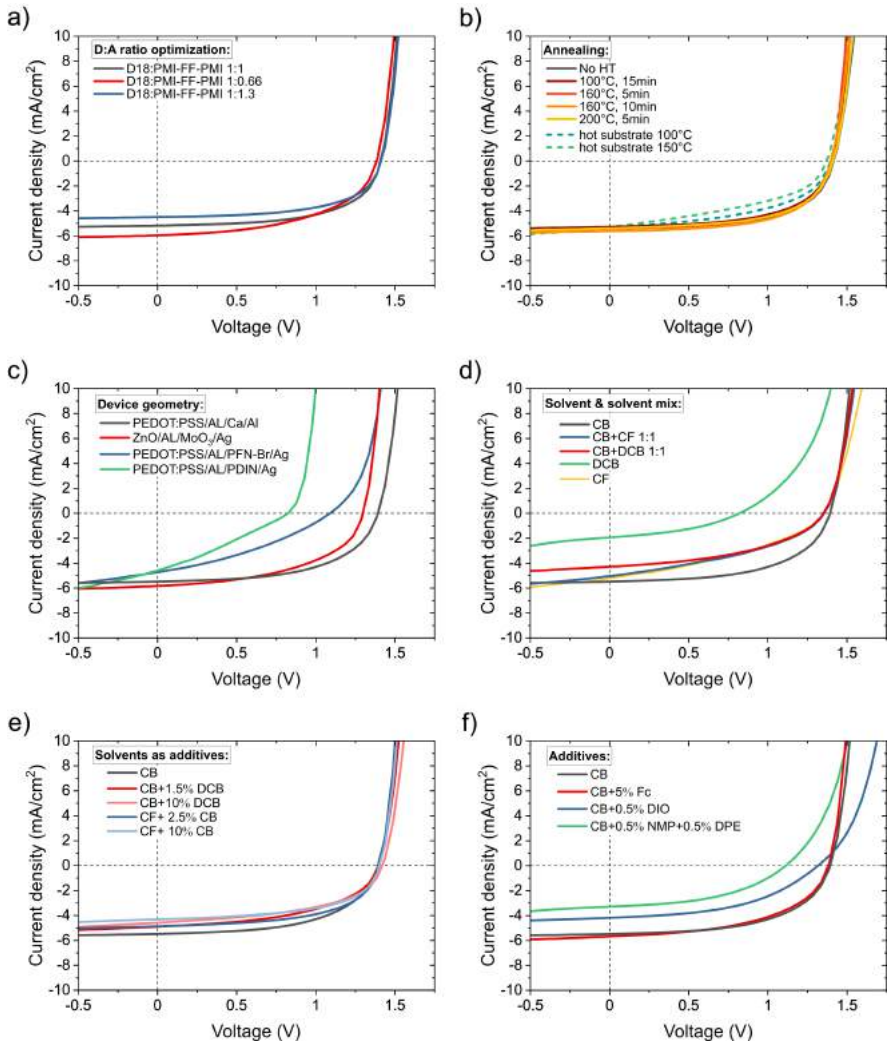

Figure S5.12: D18:PMI-FF-PMI solar cell device optimizations. a) *J-V*-curves of solar cells with varying D/A ratios. b) *J-V*-curves of D18:PMI-FF-PMI 1:1 solar cells upon changing the annealing temperature and time. The dashed lines represent *J-V*-curves where the substrates have been heated prior to the spin-coating process. c) *J-V*-curves of D18:PMI-FF-PMI solar cells with different device geometry. d) *J-V*-curves of D18:PMI-FF-PMI 1:1 solar cells fabricated using different organic solvents and solvent mixtures including chlorobenzene (CB), chloroform (CF), and dichlorobenzene (DCB). e) *J-V*-curves of D18:PMI-FF-PMI 1:1 solar cells using CB and CF as solvents and adding DCB and CB as respective additives. f) *J-V*-curves of D18:PMI-FF-PMI 1:1 solar cells using CB as a solvent and adding solvent additives like ferrocene (Fc), diiodooctane (DIO), and N-methyl pyrrolidone (NMP), and diphenyl ether (DPE). The presented *J-V*-curves are averaged over at least 6 solar cells.

Calculation of radiative, non-radiative, and quenching rates

Note S5.4.
According to Equation 5.2, the PLQY of the pristine D18 film can be used to express the ratio between k_{nr} and k_r as

$$\frac{k_{nr}}{k_r} = \frac{1 - \mathrm{PLQY}_{pristine}}{\mathrm{PLQY}_{pristine}} \tag{S5.3}$$

The denominator in Equation 5.2 can be interpreted as the TCSPC lifetime of the pristine D18 film (see Equation S5.5). Therefore, τ_{meas} of D18 can be used to calculate the absolute values of k_{nr} and k_r. With the knowledge of k_{nr} and k_r the quenching rate k_q can be determined from Equation S5.3 as follows:

$$k_q = \frac{k_r - k_r \times \mathrm{PLQY}_{blend} - k_{nr} \times \mathrm{PLQY}_{blend}}{\mathrm{PLQY}_{blend}} \tag{S5.4}$$

Table S5.2 summarizes the derived values for the D18:PMI-FF-PMI films with varying acceptor concentrations from 1 % to 50 %.

Table S5.2: Calculated radiative, non-radiative, and quenching rates of D18:PMI-FF-PMI films with varying acceptor concentrations. Equation S5.5 was used to calculate τ_{calc}.

D/A ratio	PLQY (%)	k_{nr}/k_r (a.u.)	τ_{meas} (ns)	k_r^{calc} (s^{-1})	k_{nr}^{calc} (s^{-1})	k_q^{calc} (s^{-1})	τ_{calc} (ns)
D18 pristine	14.4	5.9	0.62	2.32×10^8	1.38×10^9	-	0.62
99:1	11.9	-	-	2.32×10^8	1.38×10^9	3.4×10^8	0.51
9:1	6.6	-	-	2.32×10^8	1.38×10^9	1.9×10^9	0.28
3:1	3.9	-	-	2.32×10^8	1.38×10^9	4.3×10^9	0.17
1:1	3.7	-	-	2.32×10^8	1.38×10^9	4.7×10^9	0.16

TCSPC lifetime of D18:PMI-FF-PMI blends

Note S5.5.
In a simple model, the denominator of Equation 5.1 can be identified as the PL lifetime (τ) of a D/A blend:

$$\tau = \frac{1}{\sum_i k_i} = \frac{1}{k_r + k_{nr} + k_q} \tag{S5.5}$$

The calculated lifetime τ_{calc} can be derived from the rate constants derived as described in Note S5.4 and presented in Table 5.3. A comparison of the measured and calculated

lifetimes of the three 99:1 D/A films as shown in S5.3 indicates that the measured lifetime is significantly larger than the calculated one for all the investigated blends. The large discrepancy between the measured and calculated lifetime suggests that Equation S5.5 has to be adapted to describe the measured lifetime in a TCSPC measurement. Strong emission from pristine donor domains is expected for D18 films with a low acceptor concentration of 1 %. The unbalanced D/A ratio of 99:1 gives rise to large D18 domains exceeding the diffusion length of photogenerated excitons. Therefore, we propose that the measured TCSPC lifetime of any D18 film with 1 % acceptor concentration is a weighted average, consisting of two contributions according to

$$\tau_{meas} = w_D \times \tau_D + w_B \times \tau_B = w_D \times \frac{1}{k_r^D + k_{nr}^D} + w_B \times \frac{1}{k_r^D + k_{nr}^D + k_q^D} \tag{S5.6}$$

The weight coefficient w_D represents the emission contribution of excitons created within large domains of D18. With the domain sizes larger than the exciton diffusion length, the excitons are not able to reach a D/A interface ($k_q = 0$) and are forced to recombine into the ground state. The weight coefficient w_B represents the emission contribution of excitons that are created within the diffusion length of a D/A interface and have a chance to form a charge-transfer state with a quenching rate k_q. Accordingly, the TCSPC lifetime of a D18:PMI-FF-PMI blend (99:1) with large domain sizes and a moderate quenching rate is expected to approach the PL lifetime of the pristine D18 film. For films with high quenching rates (D18:Y6 or D18:$PC_{71}BM$), a reduction of the measured lifetime can be realized as depicted in Figure 5.5c. However, even for highly efficient D/A blends the emission of pristine D18 domains affects the measured lifetime, as indicated by the large difference between τ_{meas} and τ_{calc}. With a similar approach, it is possible to explain the TCSPC results presented in Figure 5.5a&b. As discussed in the experimental section, the lifetimes of the D18:PMI-FF-PMI blend films with varying acceptor concentrations are found in between the lifetimes of the pristine donor and acceptor. This can be explained by the fact that the PL of the D18:PMI-FF-PMI solar cell with an optimized BHJ morphology is entirely dominated by singlet emission of pristine donor or acceptor. From the bias PL measurements in Figure 5.4b we know that the PL signal is insensitive to an applied bias (I_{SC} *vs.* V_{OC} conditions). The minimal detectable change in PL intensity of the experimental setup is assumed to be 1 %. Accordingly, the insensitivity of the bias-PL signal of D18:PMI-FF-PMI suggests that more than 99 % of the emission stems from bias-insensitive singlet emission and that the radiative recombination of free charge carriers via the CT-state accounts for less than 1 % of the total emission. Consequently, the measured PL lifetime in TCSPC experiments is expected to be a weighted average of the pristine donor and pristine acceptor lifetimes. In this case, the summation in Equation S5.6 has to be extended with an acceptor term (wD $\times$ τ_A). For blends with a low quenching rate such as D18:PMI-FF-PMI, the third term in Equation S5.6 does not lead to a significant reduction of the lifetime. Thus, the measured lifetime is governed by the weighted average of the pristine lifetimes of donor and acceptor, as confirmed by the

experimental results in Figure 5.5a&b. Moreover, changing the detection wavelength from 650 (PMI-FF-PMI emission peak) to 700 nm (D18 emission peak) allows manipulating the weight coefficients w_D and w_A. Consequently, the lifetime of the D18:PMI-FF-PMI 1:1 blend (yellow curve in Figure 5.5a) is significantly increased compared to the pristine D18 lifetime due to the increased PMI-FF-PMI emission at a detection wavelength of 650 nm. In contrast, at a detection wavelength of 700 nm (enhanced D18 emission), the lifetimes of the 1:1 blend and the pristine D18 film are almost identical as shown in Figure 5.5b.

Table S5.3: Measured and calculated PL lifetime of different D/A blends. Equation S5.5 was used to calculate τ_{calc} from the rates summarized in Table 5.3.

D/A blend	D/A ratio	τ_{meas} (ns)	τ_{calc} (ns)
Pristine D18	1:0	0.62	0.62
D18:PMI-FF-PMI	99:1	0.62	0.51
D18:Y6	99:1	0.35	<0.04
D18:$PC_{71}BM$	99:1	0.45	<0.04

Solar cell performance in % of the SQ limit

Table S5.4: Measured photovoltaic parameters of D18:PMI-FF-PMI, D18:Y6, and D18:$PC_{71}BM$ solar cells in comparison with their respective parameters in the SQ limit.

		V_{OC} (V)	J_{SC} (mA cm^{-2})	FF (%)	PCE (%)
D18:PMI-FF-PMI	measured	1.41	6.09	60.9	5.34
	SQ limit	1.72	14.25	92.3	22.6
	% of SQ limit	82.0%	42.7%	66.0%	23.6%
D18:Y6	measured	0.87	24.46	70.5	15.2
	SQ limit	1.09	33.98	89.0	33.2
	% of SQ limit	79.8%	72.0%	79.2%	45.6%
D18:$PC_{71}BM$	measured	0.98	11.26	71.4	8.0
	SQ limit	1.48	20.07	91.3	27.1
	% of SQ limit	66.1%	56.1%	78.2%	29.3%

Charge injection model

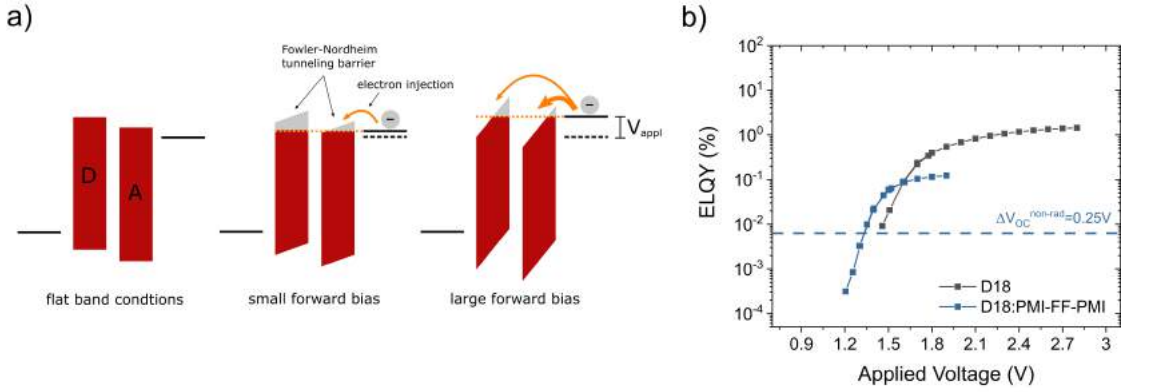

Figure S5.13: Charge carrier injection. a) Schematic sketch of the electron injection into the D/A blend from a high work function metal electrode. Due to the small energetic offset between the LUMO levels of donor and acceptor, the electron injection into the LUMO level of the donor is possible at a large forward bias. b) ELQY measurements of pristine D18 and D18:PMI-FF-PMI 1:1 devices versus the applied voltage.

Triple junction EQE_{PV} optimization potential

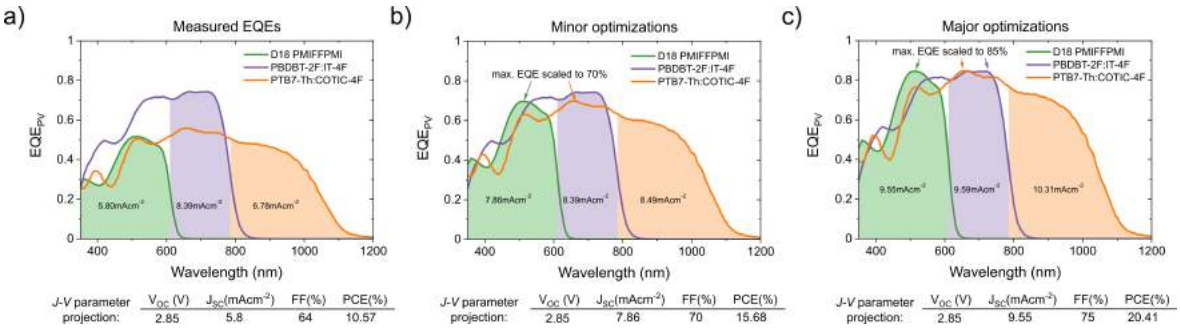

Figure S5.14: Optimization potential of an all-organic triple-junction solar cell. a) The measured EQE_{PV} spectra of D18:PMI-FF-PMI, PBDBT-2F:IT-4F, and PTB7-Th:COTIC-4F solar cells. The EQE_{PV} of the PTB7-Th:COTIC-4F was taken from Reference [142].

Note S5.6.

The single-junction solar cells D18:PMI-FF-PMI, PBDBT-2F:IT-4F, and PTB7-Th:COTIC-4F were chosen as possible candidates for an application in triple junction devices. The photovoltaic parameters of the solar cells are summarized in Table S5.5. As discussed in the introduction, the PTB7-Th:COTIC-4F device shows strong optical absorption until approximately 1100 nm, which makes this solar cell an ideal candidate for the small-bandgap sub-cell of a triple-junction device. The EQE_{PV} of this device was extracted from the data presented in Reference [142]. The EQE_{PV} of D18:PMI-FF-PMI and PBDBT-2F:IT-4F were measured with

the EQE_{PV} setup described in the methods section. The single-junction EQE_{PV} spectra were used to derive a simple model to estimate the efficiency of the triple-junction device. We assume that the V_{OC} of the triple-junction device is the sum of the open-circuit voltages of the sub-cells and that the FF of the triple-junction device is the average of the observed FFs of the individual sub-cells. Furthermore, the current of the triple junction device is limited by the minimum current of the three sub-cells, which highlights the importance of "current matching" of the individual sub-cells. In our simple model, the short circuit currents of the sub-cells are calculated by integrating the product of the EQE_{PV} and the AM1.5G solar spectrum within the spectral boundaries highlighted in Figure S5.14a (shaded area under the curves). Once again it should be emphasized that this model is derived to give a rough estimate of the triple-junction device performance. Optical modeling would be necessary to incorporate interference or layer thickness effects. The model also assumes that all the light within the spectral absorption region of the front and middle sub-cells is absorbed and is not transmitted to the sub-cells below. With these assumptions, a power conversion efficiency of 10.6 % is derived for this specific triple-junction stack. According to our model an impressive V_{OC} around 2.85 V, a J_{SC} around 5.8 mA cm^{-2}, and a FF around 64 % can be expected from the measured single-junction EQE_{PV} spectra. As shown in Figure S5.14a, the currents of the sub-cell are not ideally matched and lead to a serious performance decrease. The large current mismatch could be reduced by increasing the EQE_{PV} of the D18:PMI-FF-PMI and PTB7-Th:COTIC-4F sub-cells. Further improvements of wide and small-bandgap sub-cells can substantially boost the overall performance as shown in Figure S5.14b&c. Assuming a maximum EQE_{PV} of 70 % in combination with an increased average FF of 70 % significantly reduces the current mismatch and allows for PCEs around 15 %. In an optimization scenario, where the EQE_{PV} maximum of all the sub-cells is improved to 85 % and with an increased average FF of 75 %, PCEs beyond 20 % seem feasible. EQE_{PV}s of 85 % and FFs of 75 % have been reported for state-of-the-art single-junction cells and are thus considered as best-case scenarios for D18:PMI-FF-PMI and PTB7-Th:COTIC-4F sub-cell optimization.

Table S5.5: Measured photovoltaic parameters of D18:PMI-FF-PMI, PBDBT-2F:IT-4F, and PTB7-Th:COTIC-4F solar cells. PTB7-Th:COTIC-4F data has been taken from the ESI of Reference [142].

Material	V_{OC} (V)	J_{SC} (mA cm^{-2})	FF (%)	PCE (%)
D18:PMI-FF-PMI	1.41	6.1	61	5.3
PBDBT-2F: IT-4F	0.87	20.1	70	12.2
PTB7-Th:COTIC-4F	0.57	23.1	60	7.8

Device fabrication of solar cells in the inverted structure

Note S5.7.

A zinc oxide precursor solution was prepared by dissolving 0.5 g zinc acetate dihydrate in 5 mL 2 methoxyethanol and 150 µL ethanolamine followed by stirring for at least 12 h. The filtered (PVDF syringe filter, pore size: 0.45 µm) precursor solution was spin-coated onto patterned, cleaned and plasma etched glass/ITO substrates ($15 \times 15 \times 1.1\,mm^3$, $15\,\Omega$/sq, Luminescence Technology Corp.) at 4000 rpm for 30 s and afterward annealed at 150 °C for 15 minutes in air. The donor/acceptor solutions in chlorobenzene were prepared in an N_2 filled glove box with D/A weight ratios of 1/0.66, 1/1, and 1/1.3 by mixing the respective amounts of 10 mg/mL stock solutions of donor and acceptor. Before mixing, the stock solutions were stirred overnight at 70 °C. The spin coating was performed using hot solutions and substrates (85 °C). The solar cell fabrication was completed by thermal evaporation of MoO_3 (10 nm) and Ag (100 nm) layers at a pressure of 1×10^{-5} mbar. *J-V*-characteristics were recorded under a nitrogen atmosphere using a Keithley 2400 SMU and a LabView-based software. Illumination ($100\,mW\,cm^{-2}$) was provided by a Dedolight DLH400 lamp, calibrated using a monocrystalline silicon WPVS reference solar cell (Fraunhofer ISE). The active area of the solar cells was defined by a shadow mask (2.65×2.65 mm) used for the illumination.

Chapter 6

Optimization of D18:PMI-FF-PMI

6.1 Introduction

In the previous chapter, we have analyzed organic solar cells based on the novel NFA PMI-FF-PMI. In combination with the donor polymer D18, the wide bandgap acceptor PMI-FF-PMI enables organic solar cells with extraordinarily high open-circuit voltages of 1.41 V. It was shown that the effective bandgap of about 2.02 eV in combination with the extremely high V_{OC} makes D18:PMI-FF-PMI solar cells ideal candidates for the application in organic triple-junction devices. The limited J_{SC} was identified as the main parameter hampering the device performance of D18:PMI-FF-PMI solar cells. This limitation is even more critical in tandem or triple-junction devices since the total device current is equal to the lowest current of the individual subcells.

As discussed in Section 5.5, optimization efforts trying to increase the EQE_{PV} or J_{SC} of the D18:PMI-FF-PMI solar cells did not lead to a significant improvement. The optimization attempts were mainly focused on improving the D/A morphology by common processing techniques like (post-) annealing, solvent additives, solvent mixing, varying D/A ratios, or the processing temperatures. The low driving force for CT formation was determined as the main factor restricting the maximum EQE_{PV} of D18:PMI-FF-PMI solar cells. While this finding in general remains valid, a direct comparison between D18:PMI-FF-PMI solar cells in the "standard" and "inverted" device architecture indicates the potential to improve the J_{SC}. Figure 6.1 compares the *J-V* measurements of the best cells in the standard (ITO/PEDOT:PSS/D18:PMI-FF-PMI/Ca/Al) and inverted (ITO/ZnO/D18:PMI-FF-PMI/MoO_3/Ag) device architecture initially presented in the previous chapter. In accordance with the findings of Chapter 5, both device geometries exhibit moderate EQE_{PV} values below 60 %. However, the solar cells in the inverted geometry with ZnO as ETL show higher J_{SC} values. At the same time, the V_{OC} of this devices is significantly lower leading to a similar PCE.

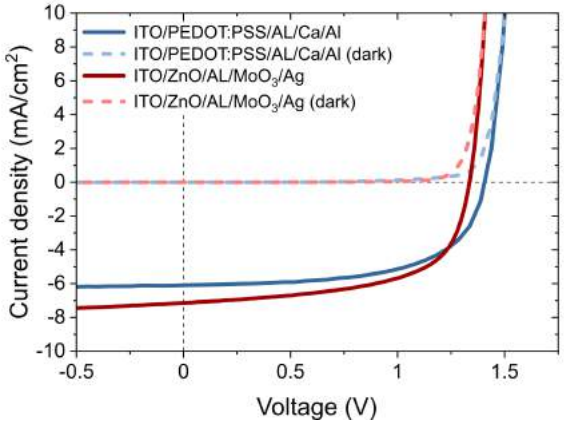

AL: D18:PMI-FF-PMI 1:1

Device geometry	V_{OC} (V)	J_{SC} (mA cm^{-2})	FF (%)	PCE (%)
standard	1.41	6.1	61	5.3
inverted	1.34	7.1	60	5.7

Figure 6.1: Left: Comparison of the *J-V* characteristic of D18:PMI-FF-PMI solar cells in the standard and inverted device geometry. Right: Summary and comparison of the derived photovoltaic parameters.

These findings raise the question of whether an optimum device geometry can be achieved, where J_{SC} and V_{OC} can be maximized at the same time. The exceptionally low work function of Ca (2.9 eV[101]) is thought to be responsible for the enhanced V_{OC} in the standard configuration. An electrode material with an extremely low work function seems to be beneficial to form a "good" (ohmic) contact with the high LUMO level of the wide bandgap acceptor PMI-FF-PMI. The ZnO work function is reported between -4.1 and -4.3 eV[168–170] and is most likely significantly lower than the Ca/Al WF. The WF of the Ca/Al interlayer is expected to lie between the WF of the two pristine metals (between -4.3 and -2.9 eV).[101] An effective work function of 3.7 eV has been reported for a Ca/Al contact, which is comparable to the determined LUMO level of PMI-FF-PMI and could explain the superior V_{OC} in Ca/Al devices.[171] The reported WF levels are graphically summarized in Figure 6.2. In order to replace the J_{SC}-limiting calcium layer, while maintaining the high V_{OC} of D18:PMI-FF-PMI devices, an alternative interlayer has to be developed which is capable of increasing the work function of aluminum to a similar extent. It has been shown that polymers like PEIE or PFN-Br can reduce the work function of ITO or ZnO layers by forming dipole moments on the electrode surface.[80,172,173]

In the course of optimizing the electron injection layer in OLEDs, Ohisa *et al.* have recently demonstrated that a 1:1 blend of PEIE and PFN-Br reduces the WF of ZnO nanoparticles more effectively than using either PEIE or PFN-Br as interlayer.[174] In fact, the work function of unmodified ZnO NPs (4.21 eV) could be reduced to ∼3.7 eV by inserting either a PEIE or PFN-Br interlayer, while the blend of PEIE:PFN-Br surprisingly decreased the WF of the ZnO NPs to values of 3.46 eV. This synergetic WF reduction effect is not fully understood. According to the authors, the enhanced WF reduction of the blend could be explained by the compliment WF reduction effects of both PEIE and ionic functionalities of PFN-Br. Inspired

by this result, the PEIE:PFN-Br blend is investigated as a potential alternative to the calcium ETL of D18:PMI-FF-PMI solar cells in the "standard" device architecture.

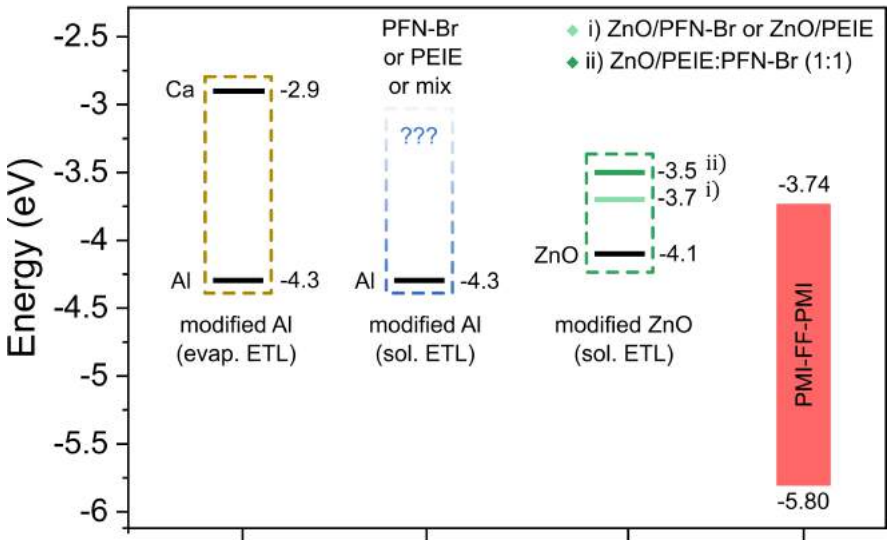

Figure 6.2: Estimated work functions of ETL-modified and pristine contact materials. The WF data for Ca and Al is taken from Reference [101]. The WF data for sol-gel ZnO and ZnO modified (ZnO/PEIE, ZnO/PFN-Br and ZnO/PEIE:PFN-Br(1:1)) electrodes is taken from References [168] and [174]. In addition, the HOMO and LUMO level of D18:PMI-FF-PMI is depicted.

6.2 Experimental Notes

Addendum: Materials & device preparation

The device preparation of the reference D18:PMI-FF-PMI solar cells (ITO/PEDOT:PSS/AL/Ca/Al) was done according to the recipe reported in Section 5.3. The devices with PEIE:PFN-Br electron transport layer were prepared analogously. Before evaporating Al top contacts a 0.9 mg/mL PEIE:PFN-Br solution in methanol (MeOH) was spin-coated on top of the active layer (30 s/2000 rpm/2000 rpm s^{-1}). The PEIE 5 mg/mL Master solution in MeOH described in Section 2.3.2 was mixed with a 0.5 mg/mL solution of PFN-Br in MeOH using a volume ratio of 1:10 in order to obtain a 0.9 mg/mL solution of PEIE:PFN-Br with a mass ratio of 1:1.

6.3 Results & Discussion

6.3.1 Optimization of D18:PMI-FF-PMI Solar Cells

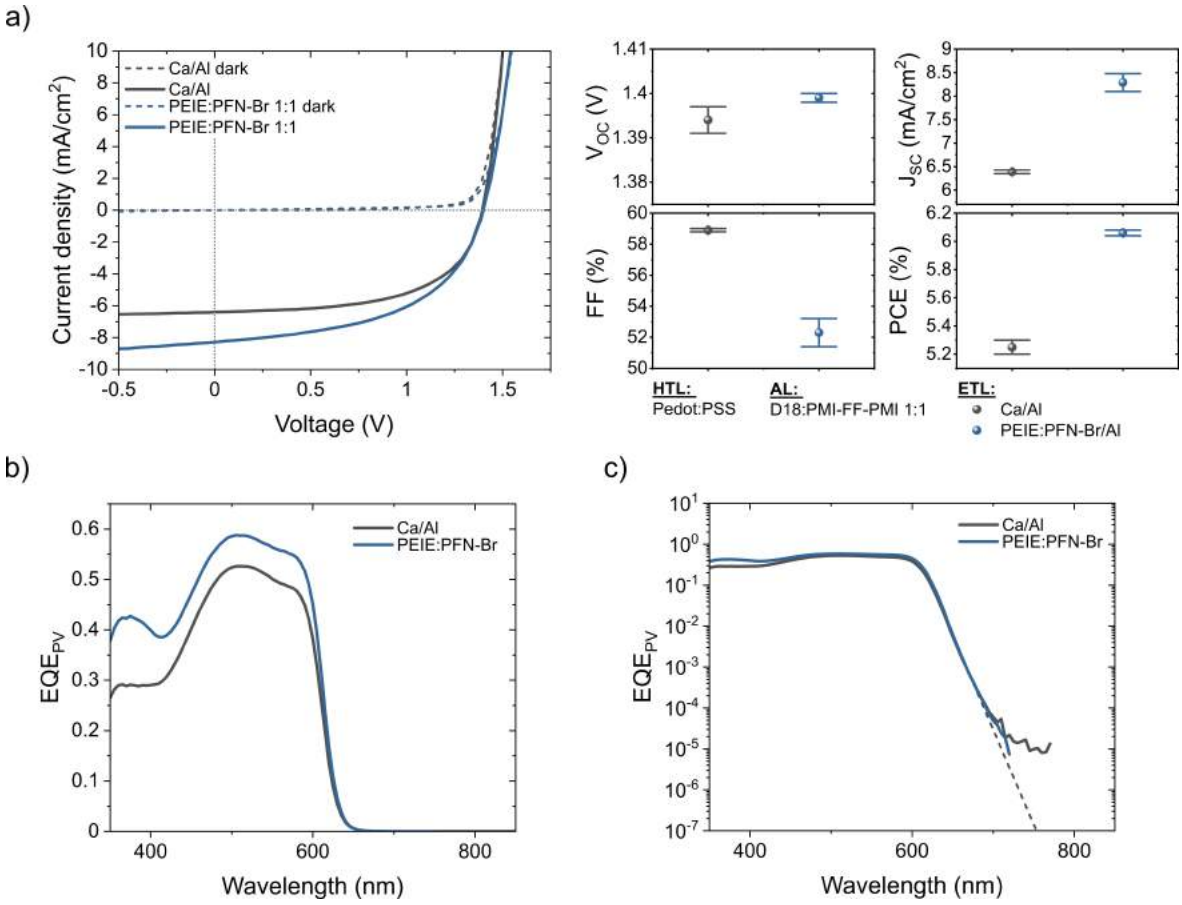

Figure 6.3: Photovoltaic performance of D18:PMI-FF-PMI devices using PEIE:PFN-Br and Ca as ETL.

As indicated by the *J-V* measurements shown in Figure 6.3a, the PEIE:PFN-Br interlayer allows the fabrication of D18:PMI-FF-PMI solar cells with high V_{OC}. In fact, devices with a PEIE:PFN-Br interlayer even showed slightly higher V_{OC} values than the reference devices using Ca as ETL. These results suggest that the PEIE:PFN-Br blend tremendously decreases the work function of Al to extremely low values, which are comparable to those obtained using a thin Ca ETL. Moreover, the implementation of PEIE:PFN-BR significantly increased the J_{SC} of D18:PMI-FF-PMI (1:1) solar cells by almost 2 mA cm^{-2}. The FF of these devices is slightly worse compared to Ca devices. Eventually, this effect could be reduced by further optimization of the novel PEIE:PFN-Br interlayer in terms of e.g. thickness or processing conditions. Nevertheless, the improved J_{SC} already significantly boosts the overall PCE of PEIE:PFN-Br devices above 6 % and could be further improved to around 7 % if the FF of the Ca device can be maintained. EQE_{PV} measurements of PEIE:PFN-Br devices confirm

the observed J_{SC} increase. As shown in Figure 6.3c, the EQE_{PV} is increased over the entire absorption region of the D18:PMI-FF-PMI blend and reaches a maximum value of almost 60 %. The semi-logarithmic plot in Figure 6.3d shows that the sub-bandgap EQE_{PV} behavior of D18:PMI-FF-PMI solar cells is unaffected by the variation of ETL. Similarly, no significant change in the emissive properties (EL, PL) was observed (not shown here).

As depicted in Figure 6.4a, the variation of the PEIE:PFN-Br concentration strongly affects the interlayer thickness and the overall performance of D18:PMI-FF-PMI solar cells. A too thick PEIE:PFN-Br interlayer (1.96 mg/mL) leads to a severe S-shaped *J-V*-curve. This behavior is indicative of a hindered charge extraction and a pile-up of charges at the contact. Here, a severe increase in the serial resistance due to a thick insulating PEIE:PFN-Br film is thought to be responsible for the observed behavior. Reducing the film thickness below 10 nm eliminates the conductivity problem due to an enhanced tunneling probability of electrons and prevents the formation of an S-shaped *J-V*-curve. A concentration of 0.09 mg/mL is thought to result in either no film or too thin films, leading to a similar performance as shown in Figure 6.4b for solar cells with no ETL.

In order to compare the effect of different ETL/metal contacts, additional solar cells with no ETL/Al, PFN-Br/Al, and PEIE:PFN-Br/Ag were prepared and compared to the Ca/Al and PEIE:PFN-Br/Al devices. The direct comparison of the presented solar cells in Figure 6.4b allows us to evaluate the V_{OC} and estimate the WF enhancement effects of the different ETLs. The device with bare Al electrodes suffers from a significantly reduced V_{OC} due to the low WF of Al. Insertion of a PFN-Br interlayer boosts the V_{OC} to values around 1.3 V, which is however still significantly lower than the V_{OC} of Ca or PEIE:PFN-Br devices. The WF of silver is thought to be slightly lower than Al ($\sim$4.6 eV[101]), which could explain the reduced V_{OC} in the PEIE:PFN-Br/Ag solar cells compared to their PEIE:PFN-Br/Al counterparts. Interestingly the synergetic WF enhancement of PEIE:PFN-Br apparently achieves lower WFs with Ag electrodes than pristine PFN-Br in combination with Al.

Since the PEIE:PFN-Br blend was initially developed in combination with ZnO NP we have investigated the incorporation of PEIE:PFN-Br in D18:PMI-FF-PMI solar cells in the inverted device geometry (ITO/ZnO/AL/MoO_3/Ag). Here, PEIE:PFN-Br is used as an additional interlayer on top of the ZnO film. A comparison of the device performance of solar cells with pristine ZnO, ZnO/PFN-Br, and ZnO/PEIE:PFN-Br is presented in Figure 6.4c. Once again the lowering of the contacts WF continuously increases the V_{OC} of the device. Extremely high V_{OC} values of 1.42 V have been found. Moreover, solar cells in this device architecture showed the highest FF (>62 %) of all measured D18:PMI-FF-PMI solar cells.

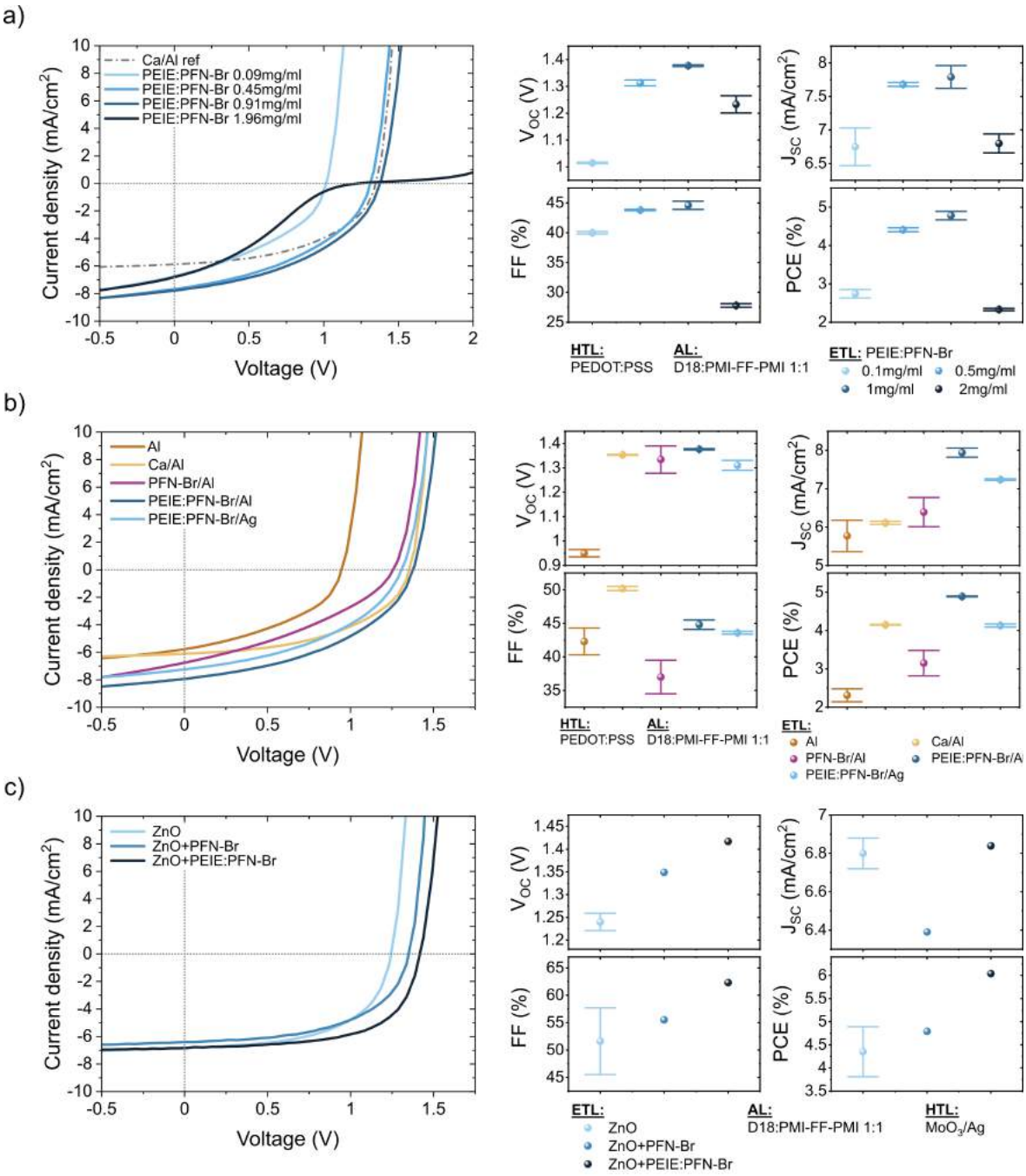

Figure 6.4: *J-V* characteristics of D18:PMI-FF-PMI solar cells with varying PEIE:PFN-Br thickness, varying ETL materials and in the inverted device geometry.

6.3.2 Universality of the PEIE:PFN-Br Interlayer Approach

Having demonstrated the beneficial effect of PEIE:PFN-Br interlayers on the solar cell performance of D18:PMI-FF-PMI leads to the question of the universality of this approach. To that end, Figure 6.5 compares the photovoltaic performance of other D/A systems upon

the incorporation of PEIE:PFN-Br as ETL. D18:$PC_{71}BM$ was chosen as a representative of a high-performance fullerene-based solar cell, while the established D/A combination PTB7-Th:EH-IDTBR was chosen as an alternative NFA-based system.

As shown in Figure 6.5a the D18:$PC_{71}BM$/PEIE:PFN-Br/Al device showed comparable performance to the Ca/Al reference device. The PEIE:PFN-Br ETL had a positive effect on the V_{OC} and J_{SC} but led to a decreased FF. Thus, the overall PCE of both devices is almost identical.

Figure 6.5b shows that the *J-V*-curve of the PTB7-Th:EH-IDTBR/PEIE:PFN-Br/Al device exhibits a slight S-shape giving rise to a very low FF value. Hence, despite increasing its J_{SC} and V_{OC} compared to the Ca/Al reference device, the overall photovoltaic performance of the PEIE:PFN-Br/Al device is lower. Interestingly, if the electrode material is changed from Al to Ag, the S-shape completely vanishes and the measured FF values are even higher than those of the Ca/Al control device. In combination with a significant increase of V_{OC} and J_{SC} the PCE of the PEIE:PFN-Br device increases impressively from around 6 to 9 %.

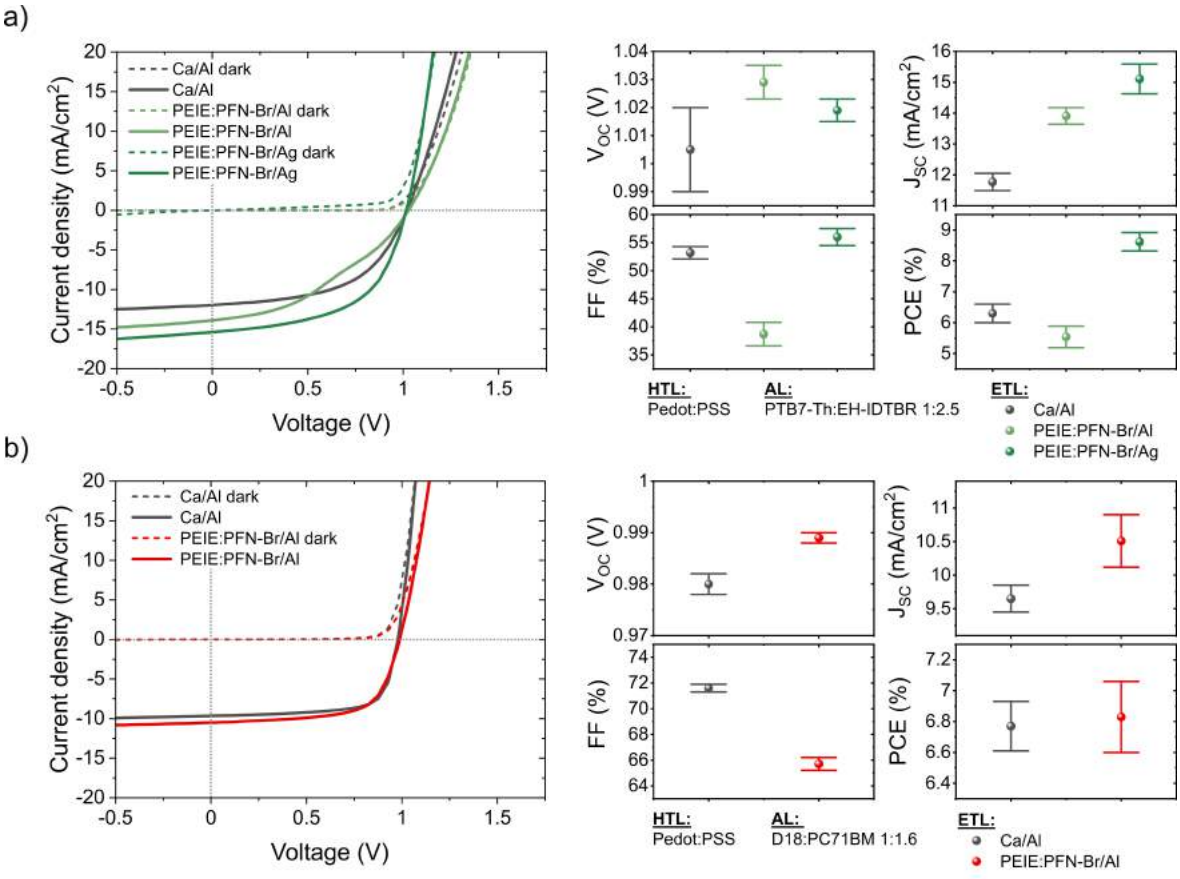

Figure 6.5: *J-V* characteristics of D18:$PC_{71}BM$ and PTB7-Th:EH-IDTBR in combination with the PEIE:PFN-Br electron transport layer.

6.4 Summary & Conclusion

To conclude, we have reported the applicability of the polymer blend PEIE:PFN-Br as a suitable electron transport layer in organic solar cells. The combination of these two well-known surface-modifying interlayers was first studied by Oshia *et al.* as a low-WF electron injecting layer for OLEDs.[174] In addition to the reported capability of modifying the WF of ZnO nanoparticle films, we have shown that PEIE:PFN-Br interlayers can be successfully used to modify the WF of ZnO sol-gel films or metal electrodes (e.g. Al, Ag). The high LUMO level of the PMI-FF-PMI acceptor requires a low WF electrode interface such as calcium to form a good ohmic contact. The sensitivity of the D18:PMI-FF-PMI solar cell's V_{OC} on WF variations could be used to qualitatively estimate the WF lowering effect of different ETLs. The reported synergetic WF reduction effect of the PEIE:PFN-Br blend could be confirmed and was exploited to optimize the photovoltaic performance of D18:PMI-FF-PMI solar cells. Compared to devices with Ca/Al electrodes the EQE_{PV} could be significantly improved, while the exceptionally high V_{OC} of the Ca devices could be maintained. As discussed in Section 5.5, these minor improvements in the EQE_{PV} are of paramount importance for the application of D18:PMI-FF-PMI in organic triple-junction solar cells. Moreover, the benefit of incorporating a PEIE:PFN-Br interlayer instead of the widely used Ca interlayer has been demonstrated for other D/A systems underlining the general validity of this approach. Both, devices based on another donor:NFA combination (PTB7-Th:EH-IDTBR) and a D18:fullerene blend (D18:$PC_{71}BM$) have shown a similar or better performance when using PEIE:PFN-Br as ETL.

Chapter 7

Summary & Outlook

A comparison with state-of-the-art inorganic or perovskite solar cells allows us to identify the enhanced open-circuit voltage loss of organic solar cells as one of the main factors limiting their overall power conversion efficiency. Therefore, in this thesis, special emphasis has been placed on investigating the open-circuit voltage losses of state-of-the-art as well as newly developed OSCs. Particularly, the non-radiative voltage loss of OPV devices has to be reduced in order to close the gap to their inorganic or perovskite counterparts. The loss mechanisms in the D/A blend D18:Y6, which is considered one of the most efficient NFA-based OSCs to date, were investigated and compared to devices based on D18:$PC_{71}BM$ blends. The direct comparison between the two devices based on the same donor polymer highlights the differences in photovoltaic and optical performance between the intensively investigated fullerene acceptor ($PC_{71}BM$) and a representative of the new class of efficient NFAs based on the Y-series (Y6). Besides the apparent increase of the spectral absorption range due to the NIR absorption of the Y6 acceptor, the excellent luminescence properties of this new family of acceptors seem to separate them from their fullerene-based counterparts. Moreover, the ability to fine-tune the energy level alignment in polymer:NFA blends allows reducing the HOMO-HOMO offset in these systems. In accordance with the so-called three-state model a strong electronic coupling and a decreased energy offset result in a hybridization of localized exciton and charge transfer states which is thought to significantly improve the radiative efficiency. Thus, the reduced non-radiative voltage loss is caused by the improved electroluminescence quantum yield according to the respective reciprocity relation. In addition, the three-state model predicts that the maximum radiative efficiency of the solar cell is ultimately limited by the radiative efficiency of the low-bandgap component, which suggests to focus novel NFA design strategies on improving their luminescence properties. The validity and conclusions drawn from the three-state model are still under debate. It should be noted that the results of the high-performance blend D18:Y6 presented in this thesis are in good agreement with the predictions of the three-state model and support its validity.

In general, it has been observed that a stepwise reduction of the energetic offsets to increase the radiative efficiency will at some point result in a decrease in the J_{SC} as the driving force for CT formation and dissociation is thought to scale with the energy offsets. Therefore, the critical question arises on how these new D/A blends are capable of efficiently forming and separating CT states despite minimal energetic offsets. Although several studies suggest the important role of intermolecular electrostatic fields and/or enhanced exciton diffusion due to an efficient energy transfer from donor to acceptor, the secret behind the success of current acceptors based on the Y-series remains ambiguous. However, the current extensive research effort of analyzing the prototypical NFA Y6 may lead to the elucidation of the relevant mechanisms, which can subsequently be transferred to other classes of NFAs.

A unique selling point of OPV is the broad variety and tunability of organic materials. Especially the possibility to tune the bandgap of organic semiconductors allows developing solar cells with tailor-made spectral absorption properties. These properties in combination with the simple, solution-based fabrication process make organic solar cells prime candidates to be employed in tandem and multi-junction devices. The great advantage of multi-junction devices with different optical bandgaps is the reduction of the fundamental thermalization loss compared to single-junction devices. Therefore, the development of multi-junction OSCs can be considered as a complementary approach aiming to minimize the V_{OC} deficit of OSCs compared to other inorganic or perovskite PV technolgies. With an effective bandgap around 2 eV and an extremely high $V_{OC,}$ the novel D/A blend D18:PMI-FF-PMI constitutes an ideal candidate for the application as a wide-bandgap sub-cell in all-organic triple-junction applications. However, a detailed photovoltaic and spectroscopic analysis of the D18:PMI-FF-PMI system suggests that the charge generation in this D/A blend is limited by a low driving force for charge transfer state formation. The limited J_{SC}/EQE_{PV} was thus identified as the main parameter hampering the device performance of D18:PMI-FF-PMI solar cells. This limitation is even more critical in tandem or triple-junction devices where the total device current is equal to the lowest current of the individual subcells. Encouragingly, by optimizing the device geometry the EQE_{PV} of D18:PMI-FF-PMI solar cells could be enhanced by about 10 %. At the current development stage, organic triple-junction devices incorporating D18:PMI-FF-PMI subcells are expected to reach efficiencies of about 15 % with V_{OC} values of almost 3 V. Improvements in the field of NIR absorbing OSCs as well as further development of the D18:PMI-FF-PMI are needed to significantly boost the triple-junction performance beyond 20 %.

Based on the gained knowledge from the high-performance material combination D18:Y6 and findings from the detailed analysis of D18:PMI-FF-PMI solar cells, the following design strategies to improve the performance of future wide-bandgap PMI-linker-PMI based acceptors can be formulated:

- Halogenation (e.g. PMI *bay*-positions) of the PMI-FF-PMI acceptor could improve the driving force for CT state formation and improve the EQE_{PV}. Furthermore, halogenation could reduce the LUMO level of the PMI-FF-PMI acceptor and might help to improve the air stability of the D18:PMI-FF-PMI solar cell.
- Reducing the steric hindrance by replacing the 2,6-diisopropylphenyl group with less bulky side chains could improve the π-π-overlap and increase the electron mobility and FF of the solar cell. However, one should be aware that this approach could negatively impact the solubility and film formation properties due to a pronounced stacking behavior.
- It could be beneficial to increase the bandgap of the acceptor to realize complementary absorption. In addition to increasing the absorption in the UV-blue region of the spectrum, the complementary absorption should improve the FRET efficiency, which has been shown beneficial for Y6 based solar cells. A straightforward approach could be to replace the PMI units with smaller naphthalene imide units.
- The high-performance Y6 acceptor employs an A-D-A'-D-A structure in contrast to the A-D-A structure of PMI-FF-PMI. In addition to testing a variety of new donor-type linker molecules, one could try to incorporate linkers with a D-A'-D structure mirroring the successful structure of Y6.

To conclude the discussion of the novel PMI-FF-PMI acceptor it should be emphasized that D18:PMI-FF-PMI solar cells match extremely well with common 2700 K LED light sources and could be an intriguing candidate for indoor-PV applications. However, within the scope of this PhD work, no tests under these light conditions have been performed. Therefore, evaluating the potential of D18:PMI-FF-PMI solar cells under indoor illumination could be an interesting subject of future studies.

To sum up the current state of OPV from a bigger perspective, the demonstration of high-performance devices with PCEs >20 % is only the first step towards the commercialization of organic solar cells. The gained knowledge from developing and characterizing these high-performance devices has to be applied to reduce the synthetic complexity (*i.e.* cost) of current OPV materials in combination with improving the device stability. Only when the three requirements of efficiency, cost, and lifetime can be fulfilled satisfactorily, broad commercialization of the OPV technology seems feasible. Therefore, with the impressive boost in device efficiency in recent years, the focus of future research efforts should be primarily shifted on device stability and evaluation of the scale-up potential of high-performance OPV materials.

Bibliography

[1] bp global, *Statistical Review of World Energy | Energy economics | Home*, 10.04.2021, https://www.bp.com/en/global/corporate/energy-economics/statistical-review-of-world-energy.html.

[2] U.S. Energy Information Administration, *EIA projects nearly 50% increase in world energy usage by 2050, led by growth in Asia - Today in Energy*, 10.04.2021, https://www.eia.gov/todayinenergy/detail.php?id=41433.

[3] R. E. Smalley, "Future Global Energy Prosperity: The Terawatt Challenge", *MRS Bulletin*, 2005, **30**, 412–417, DOI: 10.1557/mrs2005.124.

[4] S. Kurtz, A. M. Leilaeioun, R. R. King, I. M. Peters, M. J. Heben, W. K. Metzger and N. M. Haegel, "Revisiting the Terawatt Challenge", *MRS Bulletin*, 2020, **45**, 159–164, DOI: 10.1557/mrs.2020.73.

[5] UNFCCC, *The Paris Agreement*, 10.04.2021, https://unfccc.int/process-and-meetings/the-paris-agreement/the-paris-agreement.

[6] World Health Organization, *Air pollution*, 10.04.2021, https://www.who.int/health-topics/air-pollution#tab=tab_1.

[7] International Energy Agency, *Data & Statistics*, 10.04.2021, https://www.iea.org/data-and-statistics?country=WORLD&fuel=Energy%20supply&indicator=TPESbySource.

[8] R. Perez and M. Perez, "A fundamental look at energy reserves for the planet.", *The International Energy Agency SHC Programme Solar Update*, 2015, **62**, 4–6.

[9] P. Würfel, *Physics of Solar Cells: From Basic Principles to Advanced Concepts*, Wiley-VCH, Weinheim Germany, 3rd edn., 2016.

[10] W. Shockley and H. J. Queisser, "Detailed Balance Limit of Efficiency of p–n Junction Solar Cells", *Journal of Applied Physics*, 1961, **32**, 510–519, DOI: 10.1063/1.1736034.

[11] A. DeVos, *Thermodynamics of solar energy conversion*, Wiley-VCH, Weinheim, 2008.

[12] National Renewable Energy Laboratory, *Best Research-Cell Efficiency Chart*, https://www.nrel.gov/pv/cell-efficiency.html.

[13] A. E. Becquerel, "Recherches sur les effets de la radiation chimique de la lumiere solaire au moyen des courants electriques", *C. R. Acad. Sci.*, 1839, **9**, 145–149.

[14] C. E. Fritts, "On a new form of selenium cell, and some electrical discoveries made by its use", *American Journal of Science*, 1883, **156**, 465–472, DOI: 10.2475/ajs.s3-26.156.465.

[15] D. M. Chapin, C. S. Fuller and G. L. Pearson, "A New Silicon p–n Junction Photocell for Converting Solar Radiation into Electrical Power", *Journal of Applied Physics*, 1954, **25**, 676–677, DOI: 10.1063/1.1721711.

[16] M. Riede, D. Spoltore and K. Leo, "Organic Solar Cells—The Path to Commercial Success", *Advanced Energy Materials*, 2021, **11**, 2002653, DOI: 10.1002/aenm.202002653.

[17] N. M. Haegel, H. Atwater, T. Barnes, C. Breyer, A. Burrell, Y.-M. Chiang, S. de Wolf, B. Dimmler, D. Feldman, S. Glunz, J. C. Goldschmidt, D. Hochschild, R. Inzunza, I. Kaizuka, B. Kroposki, S. Kurtz, S. Leu, R. Margolis, K. Matsubara, A. Metz, W. K. Metzger, M. Morjaria, S. Niki, S. Nowak, I. M. Peters, S. Philipps, T. Reindl, A. Richter, D. Rose, K. Sakurai, R. Schlatmann, M. Shikano, W. Sinke, R. Sinton, B. J. Stanbery, M. Topic, W. Tumas, Y. Ueda, J. van de Lagemaat, P. Verlinden, M. Vetter, E. Warren, M. Werner, M. Yamaguchi and A. W. Bett, "Terawatt-scale photovoltaics: Transform global energy", *Science*, 2019, **364**, 836–838, DOI: 10.1126/science.aaw1845.

[18] S. Philipps and W. Warmuth, *Photovoltaics Report*, ed. Frauenhofer ISE, https://www.ise.fraunhofer.de/en/publications/studies/photovoltaics-report.html.

[19] O. O. Ogbomo, E. H. Amalu, N. N. Ekere and P. O. Olagbegi, "A review of photovoltaic module technologies for increased performance in tropical climate", *Renewable and Sustainable Energy Reviews*, 2017, **75**, 1225–1238, DOI: 10.1016/j.rser.2016.11.109.

[20] K. A. Mazzio and C. K. Luscombe, "The future of organic photovoltaics", *Chemical Society reviews*, 2015, **44**, 78–90, DOI: 10.1039/c4cs00227j.

[21] *Semiconducting Polymers: Chemistry, Physics and Engineering*, ed. G. Hadziioannou and G. G. Malliaras, Wiley-VCH, Weinheim, 2nd edn., 2006.

[22] G. A. Chamberlain, "Organic solar cells: A review", *Solar Cells*, 1983, **8**, 47–83, DOI: 10.1016/0379-6787(83)90039-X.

[23] C. W. Tang, "Two–layer organic photovoltaic cell", *Applied Physics Letters*, 1986, **48**, 183–185, DOI: 10.1063/1.96937.

[24] N. S. Sariciftci, L. Smilowitz, A. J. Heeger and F. Wudl, "Photoinduced electron transfer from a conducting polymer to buckminsterfullerene", *Science*, 1992, **258**, 1474–1476, DOI: 10.1126/science.258.5087.1474.

[25] N. S. Sariciftci, D. Braun, C. Zhang, V. I. Srdanov, A. J. Heeger, G. Stucky and F. Wudl, "Semiconducting polymer–buckminsterfullerene heterojunctions: Diodes, photodiodes, and photovoltaic cells", *Applied Physics Letters*, 1993, **62**, 585–587, DOI: 10.1063/1.108863.

[26] G. Yu and A. J. Heeger, "Charge separation and photovoltaic conversion in polymer composites with internal donor/acceptor heterojunctions", *Journal of Applied Physics*, 1995, **78**, 4510–4515, DOI: 10.1063/1.359792.

[27] S. Morita, A. A. Zakhidov and K. Yoshino, "Doping effect of buckminsterfullerene in conducting polymer: Change of absorption spectrum and quenching of luminescene", *Solid State Communications*, 1992, **82**, 249–252, DOI: 10.1016/0038-1098(92)90636-N.

[28] J. Zhao, Y. Li, G. Yang, K. Jiang, H. Lin, H. Ade, W. Ma and H. Yan, "Efficient organic solar cells processed from hydrocarbon solvents", *Nature Energy*, 2016, **1**, 15027, DOI: 10.1038/nenergy.2015.27.

[29] M. C. Scharber, "On the Efficiency Limit of Conjugated Polymer:Fullerene-Based Bulk Heterojunction Solar Cells", *Advanced Materials*, 2016, **28**, 1994–2001, DOI: 10.1002/adma.201504914.

[30] S. Holliday, R. S. Ashraf, C. B. Nielsen, M. Kirkus, J. A. Röhr, C.-H. Tan, E. Collado-Fregoso, A.-C. Knall, J. R. Durrant, J. Nelson and I. McCulloch, "A Rhodanine Flanked Nonfullerene Acceptor for Solution-Processed Organic Photovoltaics", *Journal of the American Chemical Society*, 2015, **137**, 898–904, DOI: 10.1021/ja5110602.

[31] J. Liu, S. Chen, D. Qian, B. Gautam, G. Yang, J. Zhao, J. Bergqvist, F. Zhang, W. Ma, H. Ade, O. Inganäs, K. Gundogdu, F. Gao and H. Yan, "Fast charge separation in a non-fullerene organic solar cell with a small driving force", *Nature Energy*, 2016, **1**, 16089, DOI: 10.1038/nenergy.2016.89.

[32] D. Meng, H. Fu, C. Xiao, X. Meng, T. Winands, W. Ma, W. Wei, B. Fan, L. Huo, N. L. Doltsinis, Y. Li, Y. Sun and Z. Wang, "Three-Bladed Rylene Propellers with Three-Dimensional Network Assembly for Organic Electronics", *Journal of the American Chemical Society*, 2016, **138**, 10184–10190, DOI: 10.1021/jacs.6b04368.

[33] Y. Lin, J. Wang, Z.-G. Zhang, H. Bai, Y. Li, D. Zhu and X. Zhan, "An electron acceptor challenging fullerenes for efficient polymer solar cells", *Advanced Materials*, 2015, **27**, 1170–1174, DOI: 10.1002/adma.201404317.

[34] H. Bin, L. Gao, Z.-G. Zhang, Y. Yang, Y. Zhang, C. Zhang, S. Chen, L. Xue, C. Yang, M. Xiao and Y. Li, "11.4% Efficiency non-fullerene polymer solar cells with trialkylsilyl substituted 2D-conjugated polymer as donor", *Nature communications*, 2016, **7**, 13651, DOI: 10.1038/ncomms13651.

[35] Y. Cui, H. Yao, L. Hong, T. Zhang, Y. Tang, B. Lin, K. Xian, B. Gao, C. An, P. Bi, W. Ma and J. Hou, "17% efficiency organic photovoltaic cell with superior processability", *National Science Review*, 2020, **7**, 1239–1246.

[36] S. Liu, J. Yuan, W. Deng, M. Luo, Y. Xie, Q. Liang, Y. Zou, Z. He, H. Wu and Y. Cao, "High-efficiency organic solar cells with low non-radiative recombination loss and low energetic disorder", *Nature Photonics*, 2020, **14**, 300–305, DOI: 10.1038/s41566-019-0573-5.

[37] B. Fan, D. Zhang, M. Li, W. Zhong, Z. Zeng, L. Ying, F. Huang and Y. Cao, "Achieving over 16% efficiency for single-junction organic solar cells", *Science China Chemistry*, 2019, **62**, 746–752, DOI: 10.1007/s11426-019-9457-5.

[38] T. Wang, J. Qin, Z. Xiao, X. Meng, C. Zuo, B. Yang, H. Tan, J. Yang, S. Yang, K. Sun, S. Xie and L. Ding, "A 2.16 eV bandgap polymer donor gives 16% power conversion efficiency", *Science Bulletin*, 2020, **65**, 179–181, DOI: 10.1016/j.scib.2019.11.030.

[39] Y. Wu, Y. Zheng, H. Yang, C. Sun, Y. Dong, C. Cui, H. Yan and Y. Li, "Rationally pairing photoactive materials for high-performance polymer solar cells with efficiency of 16.53%", *Science China Chemistry*, 2020, **63**, 265–271, DOI: 10.1007/s11426-019-9599-1.

[40] J. Xiong, K. Jin, Y. Jiang, J. Qin, T. Wang, J. Liu, Q. Liu, H. Peng, X. Li, A. Sun, X. Meng, L. Zhang, L. Liu, W. Li, Z. Fang, X. Jia, Z. Xiao, Y. Feng, X. Zhang, K. Sun, S. Yang, S. Shi and L. Ding, "Thiolactone copolymer donor gifts organic solar cells a 16.72% efficiency", *Science Bulletin*, 2019, **64**, 1573–1576, DOI: 10.1016/j.scib.2019.10.002.

[41] J. Yuan, Y. Zhang, L. Zhou, G. Zhang, H.-L. Yip, T.-K. Lau, X. Lu, C. Zhu, H. Peng, P. A. Johnson, M. Leclerc, Y. Cao, J. Ulanski, Y. Li and Y. Zou, "Single-Junction Organic Solar Cell with over 15% Efficiency Using Fused-Ring Acceptor with Electron-Deficient Core", *Joule*, 2019, **3**, 1140–1151, DOI: 10.1016/j.joule.2019.01.004.

[42] K. Jin, Z. Xiao and L. Ding, "D18, an eximious solar polymer!", *Journal of Semiconductors*, 2021, **42**, 010502, DOI: 10.1088/1674-4926/42/1/010502.

[43] Q. Liu, Y. Jiang, K. Jin, J. Qin, J. Xu, W. Li, J. Xiong, J. Liu, Z. Xiao, K. Sun, S. Yang, X. Zhang and L. Ding, "18% Efficiency organic solar cells", *Science Bulletin*, 2020, **65**, 272–275, DOI: 10.1016/j.scib.2020.01.001.

[44] M. Kaltenbrunner, G. Adam, E. D. Głowacki, M. Drack, R. Schwödiauer, L. Leonat, D. H. Apaydin, H. Groiss, M. C. Scharber, M. S. White, N. S. Sariciftci and S. Bauer, "Flexible high power-per-weight perovskite solar cells with chromium oxide-metal contacts for improved stability in air", *Nature materials*, 2015, **14**, 1032–1039, DOI: 10.1038/nmat4388.

[45] L. Meng, Y. Zhang, X. Wan, C. Li, X. Zhang, Y. Wang, X. Ke, Z. Xiao, L. Ding, R. Xia, H.-L. Yip, Y. Cao and Y. Chen, "Organic and solution-processed tandem solar cells with 17.3% efficiency", *Science*, 2018, **361**, 1094–1098, DOI: 10.1126/science.aat2612.

[46] M. Moser, A. Wadsworth, N. Gasparini and I. McCulloch, "Challenges to the Success of Commercial Organic Photovoltaic Products", *Advanced Energy Materials*, 2021, **11**, 2100056, DOI: 10.1002/aenm.202100056.

[47] A. Polman, M. Knight, E. C. Garnett, B. Ehrler and W. C. Sinke, "Photovoltaic materials: Present efficiencies and future challenges", *Science (New York, N.Y.)*, 2016, **352**, aad4424, DOI: 10.1126/science.aad4424.

[48] M. A. Green, E. D. Dunlop, J. Hohl–Ebinger, M. Yoshita, N. Kopidakis and X. Hao, "Solar cell efficiency tables (Version 58)", *Progress in Photovoltaics: Research and Applications*, 2021, **29**, 657–667, DOI: 10.1002/pip.3444.

[49] M. A. Green and A. W. Y. Ho-Baillie, "Pushing to the Limit: Radiative Efficiencies of Recent Mainstream and Emerging Solar Cells", *ACS Energy Letters*, 2019, **4**, 1639–1644, DOI: 10.1021/acsenergylett.9b01128.

[50] J. Jeong, M. Kim, J. Seo, H. Lu, P. Ahlawat, A. Mishra, Y. Yang, M. A. Hope, F. T. Eickemeyer, M. Kim, Y. J. Yoon, I. W. Choi, B. P. Darwich, S. J. Choi, Y. Jo, J. H. Lee, B. Walker, S. M. Zakeeruddin, L. Emsley, U. Rothlisberger, A. Hagfeldt, D. S. Kim, M. Grätzel and J. Y. Kim, "Pseudo-halide anion engineering for α-FAPbI3 perovskite solar cells", *Nature*, 2021, **592**, 381–385, DOI: 10.1038/s41586-021-03406-5.

[51] J. Hofinger, C. Putz, F. Mayr, K. Gugujonovic, D. Wielend and M. C. Scharber, "Understanding the low voltage losses in high-performance non-fullerene acceptor-based organic solar cells", *Materials Advances*, 2021, **2**, 4291–4302, DOI: 10.1039/D1MA00293G.

[52] O. V. Mikhnenko, P. W. M. Blom and T.-Q. Nguyen, "Exciton diffusion in organic semiconductors", *Energy Environ. Sci.*, 2015, **8**, 1867–1888, DOI: 10.1039/C5EE00925A.

[53] W. Tress, *Organic Solar Cells: Theory, Experiment, and Device Simulation*, Springer International Publishing, Cham, 2014, vol. 208, DOI: 10.1007/978-3-319-10097-5.

[54] M. C. Scharber, D. Mühlbacher, M. Koppe, P. Denk, C. Waldauf, A. J. Heeger and C. J. Brabec, "Design Rules for Donors in Bulk-Heterojunction Solar Cells—Towards 10 % Energy-Conversion Efficiency", *Advanced Materials*, 2006, **18**, 789–794, DOI: 10.1002/adma.200501717.

[55] C. Sun, S. Qin, R. Wang, S. Chen, F. Pan, B. Qiu, Z. Shang, L. Meng, C. Zhang, M. Xiao, C. Yang and Y. Li, "High Efficiency Polymer Solar Cells with Efficient Hole Transfer at Zero Highest Occupied Molecular Orbital Offset between Methylated Polymer Donor and Brominated Acceptor", *Journal of the American Chemical Society*, 2020, **142**, 1465–1474, DOI: 10.1021/jacs.9b09939.

[56] J. Zhang, W. Liu, G. Zhou, Y. Yi, S. Xu, F. Liu, H. Zhu and X. Zhu, "Accurate Determination of the Minimum HOMO Offset for Efficient Charge Generation using Organic Semiconducting Alloys", *Advanced Energy Materials*, 2020, **10**, 1903298, DOI: 10.1002/aenm.201903298.

[57] Y. Zou, Y. Dong, C. Sun, Y. Wu, H. Yang, C. Cui and Y. Li, "High-Performance Polymer Solar Cells with Minimal Energy Loss Enabled by a Main-Chain-Twisted Nonfullerene Acceptor", *Chemistry of Materials*, 2019, **31**, 4222–4227, DOI: 10.1021/acs.chemmater.9b01175.

[58] S. Li, L. Zhan, C. Sun, H. Zhu, G. Zhou, W. Yang, M. Shi, C.-Z. Li, J. Hou, Y. Li and H. Chen, "Highly Efficient Fullerene-Free Organic Solar Cells Operate at Near Zero Highest Occupied Molecular Orbital Offsets", *Journal of the American Chemical Society*, 2019, **141**, 3073–3082, DOI: 10.1021/jacs.8b12126.

[59] M. A. Faist, T. Kirchartz, W. Gong, R. S. Ashraf, I. McCulloch, J. C. de Mello, N. J. Ekins-Daukes, D. D. C. Bradley and J. Nelson, "Competition between the charge transfer state and the singlet states of donor or acceptor limiting the efficiency in polymer:fullerene solar cells", *Journal of the American Chemical Society*, 2012, **134**, 685–692, DOI: 10.1021/ja210029w.

[60] D. Veldman, S. C. J. Meskers and R. A. J. Janssen, "The Energy of Charge–Transfer States in Electron Donor–Acceptor Blends: Insight into the Energy Losses in Organic Solar Cells", *Advanced Functional Materials*, 2009, **19**, 1939–1948, DOI: 10.1002/adfm.200900090.

[61] A. A. Bakulin, A. Rao, V. G. Pavelyev, P. H. M. van Loosdrecht, M. S. Pshenichnikov, D. Niedzialek, J. Cornil, D. Beljonne and R. H. Friend, "The role of driving energy and delocalized States for charge separation in organic semiconductors", *Science (New York, N.Y.)*, 2012, **335**, 1340–1344, DOI: 10.1126/science.1217745.

[62] D. Amarasinghe Vithanage, A. Devižis, V. Abramavičius, Y. Infahsaeng, D. Abramavičius, R. C. I. MacKenzie, P. E. Keivanidis, A. Yartsev, D. Hertel, J. Nelson, V. Sundström and V. Gulbinas, "Visualizing charge separation in bulk heterojunction organic solar cells", *Nature communications*, 2013, **4**, 2334, DOI: 10.1038/ncomms3334.

[63] B. Bernardo, D. Cheyns, B. Verreet, R. D. Schaller, B. P. Rand and N. C. Giebink, "Delocalization and dielectric screening of charge transfer states in organic photovoltaic cells", *Nature communications*, 2014, **5**, 3245, DOI: 10.1038/ncomms4245.

[64] F. C. Jamieson, E. B. Domingo, T. McCarthy-Ward, M. Heeney, N. Stingelin and J. R. Durrant, "Fullerenecrystallisation as a key driver of charge separation in polymer/fullerene bulk heterojunction solar cells", *Chem. Sci.*, 2012, **3**, 485–492, DOI: 10.1039/C1SC00674F.

[65] A. J. Ward, A. Ruseckas, M. M. Kareem, B. Ebenhoch, L. A. Serrano, M. Al-Eid, B. Fitzpatrick, V. M. Rotello, G. Cooke and I. D. W. Samuel, "The impact of driving force on electron transfer rates in photovoltaic donor-acceptor blends", *Advanced materials*, 2015, **27**, 2496–2500, DOI: 10.1002/adma.201405623.

[66] S. Albrecht, W. Schindler, J. Kurpiers, J. Kniepert, J. C. Blakesley, I. Dumsch, S. Allard, K. Fostiropoulos, U. Scherf and D. Neher, "On the Field Dependence of Free Charge Carrier Generation and Recombination in Blends of PCPDTBT/PC70BM: Influence of Solvent Additives", *The journal of physical chemistry letters*, 2012, **3**, 640–645, DOI: 10.1021/jz3000849.

[67] G. F. A. Dibb, F. C. Jamieson, A. Maurano, J. Nelson and J. R. Durrant, "Limits on the Fill Factor in Organic Photovoltaics: Distinguishing Nongeminate and Geminate Recombination Mechanisms", *The journal of physical chemistry letters*, 2013, **4**, 803–808, DOI: 10.1021/jz400140p.

[68] P. K. Nayak, K. L. Narasimhan and D. Cahen, "Separating Charges at Organic Interfaces: Effects of Disorder, Hot States, and Electric Field", *The journal of physical chemistry letters*, 2013, **4**, 1707–1717, DOI: 10.1021/jz4002339.

[69] J. A. Bartelt, Z. M. Beiley, E. T. Hoke, W. R. Mateker, J. D. Douglas, B. A. Collins, J. R. Tumbleston, K. R. Graham, A. Amassian, H. Ade, J. M. J. Fréchet, M. F. Toney and M. D. McGehee, "The Importance of Fullerene Percolation in the Mixed Regions of Polymer-Fullerene Bulk Heterojunction Solar Cells", *Advanced Energy Materials*, 2013, **3**, 364–374, DOI: 10.1002/aenm.201200637.

[70] F. Gao and O. Inganäs, "Charge generation in polymer-fullerene bulk-heterojunction solar cells", *Physical chemistry chemical physics*, 2014, **16**, 20291–20304, DOI: 10.1039/c4cp01814a.

[71] N. R. Monahan, K. W. Williams, B. Kumar, C. Nuckolls and X.-Y. Zhu, "Direct Observation of Entropy-Driven Electron-Hole Pair Separation at an Organic Semiconductor Interface", *Physical review letters*, 2015, **114**, 247003, DOI: 10.1103/PhysRevLett.114.247003.

[72] H. Yao, D. Qian, H. Zhang, Y. Qin, B. Xu, Y. Cui, R. Yu, F. Gao and J. Hou, "Critical Role of Molecular Electrostatic Potential on Charge Generation in Organic Solar Cells", *Chinese Journal of Chemistry*, 2018, **36**, 491–494, DOI: 10.1002/cjoc.201800015.

[73] J. Wang, H. Yao, Y. Xu, L. Ma and J. Hou, "Recent progress in reducing voltage loss in organic photovoltaic cells", *Materials Chemistry Frontiers*, 2021, **5**, 709–722, DOI: 10.1039/D0QM00581A.

[74] S. Karuthedath, J. Gorenflot, Y. Firdaus, N. Chaturvedi, C. S. P. de Castro, G. T. Harrison, J. I. Khan, A. Markina, A. H. Balawi, T. A. D. Peña, W. Liu, R.-Z. Liang, A. Sharma, S. H. K. Paleti, W. Zhang, Y. Lin, E. Alarousu, D. H. Anjum, P. M. Beaujuge, S. de Wolf, I. McCulloch, T. D. Anthopoulos, D. Baran, D. Andrienko and F. Laquai, "Intrinsic efficiency limits in low-bandgap non-fullerene acceptor organic solar cells", *Nature materials*, 2020, **20**, 378–384, DOI: 10.1038/s41563-020-00835-x.

[75] U. Rau, "Reciprocity relation between photovoltaic quantum efficiency and electroluminescent emission of solar cells", *Physical Review B*, 2007, **76**, 085303, DOI: 10.1103/PhysRevB.76.085303.

[76] J. Benduhn, K. Tvingstedt, F. Piersimoni, S. Ullbrich, Y. Fan, M. Tropiano, K. A. McGarry, O. Zeika, M. K. Riede, C. J. Douglas, S. Barlow, S. R. Marder, D. Neher, D. Spoltore and K. Vandewal, "Intrinsic non-radiative voltage losses in fullerene-based organic solar cells", *Nature Energy*, 2017, **2**, 17053, DOI: 10.1038/nenergy.2017.53.

[77] X.-K. Chen, V. Coropceanu and J.-L. Brédas, "Assessing the nature of the charge-transfer electronic states in organic solar cells", *Nature communications*, 2018, **9**, 5295, DOI: 10.1038/s41467-018-07707-8.

[78] M. Rahman, A. Asiri, T. Tabbakh and A. Khan, *Post-Transition Metals*, IntechOpen, 2021.

[79] D. W. deQuilettes, M. Laitz, R. Brenes, B. Dou, B. T. Motes, S. D. Stranks, H. J. Snaith, V. Bulović and D. S. Ginger, "Maximizing the external radiative efficiency of hybrid perovskite solar cells", *Pure and Applied Chemistry*, 2020, **92**, 697–706, DOI: doi:10.1515/pac-2019-0505.

[80] R. Sorrentino, E. Kozma, S. Luzzati and R. Po, "Interlayers for non-fullerene based polymer solar cells: distinctive features and challenges", *Energy & Environmental Science*, 2021, **14**, 180–223, DOI: 10.1039/D0EE02503H.

[81] J. Yao, B. Qiu, Z.-G. Zhang, L. Xue, R. Wang, C. Zhang, S. Chen, Q. Zhou, C. Sun, C. Yang, M. Xiao, L. Meng and Y. Li, "Cathode engineering with perylene-diimide interlayer enabling over 17% efficiency single-junction organic solar cells", *Nature communications*, 2020, **11**, 2726, DOI: 10.1038/s41467-020-16509-w.

[82] H. Xu, F. Yuan, D. Zhou, X. Liao, L. Chen and Y. Chen, "Hole transport layers for organic solar cells: recent progress and prospects", *Journal of Materials Chemistry A*, 2020, **8**, 11478–11492, DOI: 10.1039/D0TA03511D.

[83] T. Nishinaga, *Organic Redox Systems: Synthesis, Properties, and Applications*, John Wiley & Sons, Inc., Hoboken, New Jersey, 2016.

[84] D. Baran, A. Balan, S. Celebi, B. Meana Esteban, H. Neugebauer, N. S. Sariciftci and L. Toppare, "Processable Multipurpose Conjugated Polymer for Electrochromic and Photovoltaic Applications", *Chemistry of Materials*, 2010, **22**, 2978–2987, DOI: 10.1021/cm100372t.

[85] C. M. Cardona, W. Li, A. E. Kaifer, D. Stockdale and G. C. Bazan, "Electrochemical considerations for determining absolute frontier orbital energy levels of conjugated polymers for solar cell applications", *Advanced Materials*, 2011, **23**, 2367–2371, DOI: 10.1002/adma.201004554.

[86] Y. Xie, W. Wang, W. Huang, F. Lin, T. Li, S. Liu, X. Zhan, Y. Liang, C. Gao, H. Wu and Y. Cao, "Assessing the energy offset at the electron donor/acceptor interface in organic solar cells through radiative efficiency measurements", *Energy & Environmental Science*, 2019, **12**, 3556–3566, DOI: 10.1039/C9EE02939G.

[87] D. O. Faulkner, J. J. McDowell, A. J. Price, D. D. Perovic, N. P. Kherani and G. A. Ozin, "Measurement of absolute photoluminescence quantum yields using integrating spheres - Which way to go?", *Laser & Photonics Reviews*, 2012, **6**, 802–806, DOI: 10.1002/lpor.201200077.

[88] Y. Wang, D. Qian, Y. Cui, H. Zhang, J. Hou, K. Vandewal, T. Kirchartz and F. Gao, "Optical Gaps of Organic Solar Cells as a Reference for Comparing Voltage Losses", *Advanced Energy Materials*, 2018, **8**, 1801352, DOI: 10.1002/aenm.201801352.

[89] K. Vandewal, J. Benduhn and V. C. Nikolis, "How to determine optical gaps and voltage losses in organic photovoltaic materials", *Sustainable Energy & Fuels*, 2018, **2**, 538–544, DOI: 10.1039/C7SE00601B.

[90] K. Vandewal, S. Albrecht, E. T. Hoke, K. R. Graham, J. Widmer, J. D. Douglas, M. Schubert, W. R. Mateker, J. T. Bloking, G. F. Burkhard, A. Sellinger, J. M. J. Fréchet, A. Amassian, M. K. Riede, M. D. McGehee, D. Neher and A. Salleo, "Efficient charge generation by relaxed charge-transfer states at organic interfaces", *Nature materials*, 2014, **13**, 63–68, DOI: 10.1038/nmat3807.

[91] L. C. Hirst and N. J. Ekins-Daukes, "Fundamental losses in solar cells", *Progress in Photovoltaics: Research and Applications*, 2011, **19**, 286–293, DOI: 10.1002/pip.1024.

[92] J. Yao, T. Kirchartz, M. S. Vezie, M. A. Faist, W. Gong, Z. He, H. Wu, J. Troughton, T. Watson, D. Bryant and J. Nelson, "Quantifying Losses in Open-Circuit Voltage in Solution-Processable Solar Cells", *Physical Review Applied*, 2015, **4**, 014020, DOI: 10.1103/PhysRevApplied.4.014020.

[93] U. Rau, B. Blank, T. C. M. Müller and T. Kirchartz, "Efficiency Potential of Photovoltaic Materials and Devices Unveiled by Detailed-Balance Analysis", *Physical Review Applied*, 2017, **7**, 044016, DOI: 10.1103/PhysRevApplied.7.044016.

[94] F. A. Lindholm, J. G. Fossum and E. L. Burgess, "Application of the superposition principle to solar-cell analysis", *IEEE Transactions on Electron Devices*, 1979, **26**, 165–171, DOI: 10.1109/T-ED.1979.19400.

[95] T. Kirchartz, J. Nelson and U. Rau, "Reciprocity between Charge Injection and Extraction and Its Influence on the Interpretation of Electroluminescence Spectra in Organic Solar Cells", *Physical Review Applied*, 2016, **5**, 054003, DOI: 10.1103/PhysRevApplied.5.054003.

[96] C. Donolato, "A reciprocity theorem for charge collection", *Applied Physics Letters*, 1985, **46**, 270–272, DOI: 10.1063/1.95654.

[97] M. A. Green, "Radiative efficiency of state-of-the-art photovoltaic cells", *Progress in Photovoltaics: Research and Applications*, 2012, **20**, 472–476, DOI: 10.1002/pip.1147.

[98] K. Vandewal, K. Tvingstedt, A. Gadisa, O. Inganäs and J. V. Manca, "On the origin of the open-circuit voltage of polymer-fullerene solar cells", *Nature materials*, 2009, 904–909, DOI: 10.1038/nmat2548.

[99] L. Perdigón-Toro, Q. Le Phuong, S. Zeiske, K. Vandewal, A. Armin, S. Shoaee and D. Neher, "Excitons Dominate the Emission from PM6:Y6 Solar Cells, but This Does Not Help the Open-Circuit Voltage of the Device", *ACS Energy Letters*, 2021, **6**, 557–564, DOI: 10.1021/acsenergylett.0c02572.

[100] X. Wang and M. S. Lundstrom, "On the Use of Rau's Reciprocity to Deduce External Radiative Efficiency in Solar Cells", *IEEE Journal of Photovoltaics*, 2013, **3**, 1348–1353, DOI: 10.1109/JPHOTOV.2013.2278658.

[101] *CRC Handbook of chemistry and physics*, ed. W. M. Haynes, CRC Press, Boca Raton, London and New York, 97th edition, 2017, http://gbv.eblib.com/patron/FullRecord.aspx?p=4711508.

[102] P. Morvillo, R. Diana, A. Mucci, E. Bobeico, R. Ricciardi and C. Minarini, "Influence of annealing treatments on solution-processed ZnO film deposited on ITO substrate as electron transport layer for inverted polymer solar cells", *Solar Energy Materials and Solar Cells*, 2015, **141**, 210–217, DOI: 10.1016/j.solmat.2015.05.038.

[103] L. Znaidi, "Sol–gel-deposited ZnO thin films: A review", *Materials Science and Engineering: B*, 2010, **174**, 18–30, DOI: 10.1016/j.mseb.2010.07.001.

[104] R. Lin, M. Miwa, M. Wright and A. Uddin, "Optimisation of the sol–gel derived ZnO buffer layer for inverted structure bulk heterojunction organic solar cells using a low band gap polymer", *Thin Solid Films*, 2014, **566**, 99–107, DOI: 10.1016/j.tsf.2014.07.026.

[105] J. C. Hummelen, B. W. Knight, F. LePeq, F. Wudl, J. Yao and Wilkins, Charles, L., "Preparation and Characterization of Fulleroid and Methanofullerene Derivatives", *The Journal of Organic Chemistry*, 1995, **60**, 532–538, DOI: 10.1021/jo00108a012.

[106] H. Kim, S. Nam, J. Jeong, S. Lee, J. Seo, H. Han and Y. Kim, "Organic solar cells based on conjugated polymers : History and recent advances", *Korean Journal of Chemical Engineering*, 2014, **31**, 1095–1104, DOI: 10.1007/s11814-014-0154-8.

[107] R. Ganesamoorthy, G. Sathiyan and P. Sakthivel, "Review: Fullerene based acceptors for efficient bulk heterojunction organic solar cell applications", *Solar Energy Materials and Solar Cells*, 2017, **161**, 102–148, DOI: 10.1016/j.solmat.2016.11.024.

[108] S. Holliday, R. S. Ashraf, A. Wadsworth, D. Baran, S. A. Yousaf, C. B. Nielsen, C.-H. Tan, S. D. Dimitrov, Z. Shang, N. Gasparini, M. Alamoudi, F. Laquai, C. J. Brabec, A. Salleo, J. R. Durrant and I. McCulloch, "High-efficiency and air-stable P3HT-based polymer solar cells with a new non-fullerene acceptor", *Nature communications*, 2016, **7**, 11585, DOI: 10.1038/ncomms11585.

[109] Y. Liang, Z. Xu, J. Xia, S.-T. Tsai, Y. Wu, G. Li, C. Ray and L. Yu, "For the bright future-bulk heterojunction polymer solar cells with power conversion efficiency of 7.4%", *Advanced materials*, 2010, **22**, E135–E138, DOI: 10.1002/adma.200903528.

[110] S.-H. Liao, H.-J. Jhuo, Y.-S. Cheng and S.-A. Chen, "Fullerene derivative-doped zinc oxide nanofilm as the cathode of inverted polymer solar cells with low-bandgap polymer (PTB7-Th) for high performance", *Advanced materials*, 2013, **25**, 4766–4771, DOI: 10.1002/adma.201301476.

[111] D. Qian, L. Ye, M. Zhang, Y. Liang, L. Li, Y. Huang, X. Guo, S. Zhang, Z. Tan and J. Hou, "Design, Application, and Morphology Study of a New Photovoltaic Polymer with Strong Aggregation in Solution State", *Macromolecules*, 2012, **45**, 9611–9617, DOI: 10.1021/ma301900h.

[112] S. Zhang, Y. Qin, J. Zhu and J. Hou, "Over 14% Efficiency in Polymer Solar Cells Enabled by a Chlorinated Polymer Donor", *Advanced materials*, 2018, **30**, 1800868, DOI: 10.1002/adma.201800868.

[113] *Organic Photovoltaics and Related Electronics - From Excitons to Devices*, ed. Cambridge University Press, Materials Research Society Symposium Proceedings Vol 1270, 2010.

[114] A. J. Heeger, N. S. Sariciftci and E. B. Namdas, *Semiconducting and Metallic Polymers*, Oxford University Press, 2010.

[115] M. C. Scharber and N. S. Sariciftci, "Low Band Gap Conjugated Semiconducting Polymers", *Advanced Materials Technologies*, 2021, 2000857, DOI: 10.1002/admt.202000857.

[116] W.-y. Zhou, S.-s. Xie, S.-f. Qian, G. Wang and L.-x. Qian, "Photothermal deflection spectra of solid C60", *J.Phys.: Condens. Matter*, 1996, **8**, 5793–5800.

[117] T. E. Saraswati, U. H. Setiawan, M. R. Ihsan, I. Isnaeni and Y. Herbani, "The Study of the Optical Properties of C60 Fullerene in Different Organic Solvents", *Open Chemistry*, 2019, **17**, 1198–1212, DOI: 10.1515/chem-2019-0117.

[118] T. Kirchartz, U. Rau, M. Kurth, J. Mattheis and J. H. Werner, "Comparative study of electroluminescence from Cu(In,Ga)Se2 and Si solar cells", *Thin Solid Films*, 2007, **515**, 6238–6242, DOI: 10.1016/j.tsf.2006.12.105.

[119] D. Qian, Z. Zheng, H. Yao, W. Tress, T. R. Hopper, S. Chen, S. Li, J. Liu, S. Chen, J. Zhang, X.-K. Liu, B. Gao, L. Ouyang, Y. Jin, G. Pozina, I. A. Buyanova, W. M. Chen, O. Inganäs, V. Coropceanu, J.-L. Bredas, H. Yan, J. Hou, F. Zhang, A. A. Bakulin, F. Gao, Shula Chen, Sunsun Li, Jing Liu, Shangshang Chen, Jiangbin Zhang, Xiao-Ke Liu, Bowei Gao, Liangqi Ouyang, Yingzhi Jin, Galia Pozina, Irina A. Buyanova, Weimin M. Chen, Olle Inganäs, Veaceslav Coropceanu, Jean-Luc Bredas, He Yan, Jianhui Hou, Fengling Zhang, Artem A. Bakulin and Feng Gao, "Design rules for minimizing voltage losses in high-efficiency organic solar cells", *Nature materials*, 2018, **17**, 703–709, DOI: 10.1038/s41563-018-0128-z.

[120] J. Sworakowski, "How accurate are energies of HOMO and LUMO levels in small-molecule organic semiconductors determined from cyclic voltammetry or optical spectroscopy?", *Synthetic Metals*, 2018, **235**, 125–130, DOI: 10.1016/j.synthmet.2017.11.013.

[121] H. M. Smith, *High performance pigments*, Wiley-VCH, Weinheim, 2nd, 2009.

[122] K. Hidehiro, O. Ayanori, T. Toshiaki, N. Masafumi, H. Tetsuya, N. Takao and O. Osamu, "A Structural Study for Highly Efficient Electroluminescence Cells Using Perylene-Doped Organic Materials", *J. Electrochem. Soc.*, 1997, **144**, 3628–3633, DOI: 10.1149/1.1838060.

[123] C. Keum, D. Becker, E. Archer, H. Bock, H. Kitzerow, M. C. Gather and C. Murawski, "Organic Light–Emitting Diodes Based on a Columnar Liquid–Crystalline Perylene Emitter", *Advanced Optical Materials*, 2020, **8**, 2000414, DOI: 10.1002/adom.202000414.

[124] N. Liang, Y. K. Zhao, Y. Z. Wu, C. R. Zhang and M. Shao, "Highly efficient non-doped blue OLED based on perylene", *Applied Physics Letters*, 2021, **119**, 053301, DOI: 10.1063/5.0044609.

[125] S. V. Dayneko, E. Cieplechowicz, S. S. Bhojgude, J. F. van Humbeck, M. Pahlevani and G. C. Welch, "Improved performance of solution processed OLEDs using N -annulated perylene diimide emitters with bulky side-chains", *Materials Advances*, 2021, **2**, 933–936, DOI: 10.1039/D0MA00827C.

[126] C. Wang, H. Dong, W. Hu, Y. Liu and D. Zhu, "Semiconducting π-conjugated systems in field-effect transistors: a material odyssey of organic electronics", *Chemical reviews*, 2012, **112**, 2208–2267, DOI: 10.1021/cr100380z.

[127] Y. Zou, Z. Zhang, J. Yuan and Q. Wei, "Small-Molecule Electron Acceptors for Efficient Non-fullerene Organic Solar Cells", *Frontiers in chemistry*, 2018, **6**, 414, DOI: 10.3389/fchem.2018.00414.

[128] A. Wadsworth, M. Moser, A. Marks, M. S. Little, N. Gasparini, C. J. Brabec, D. Baran and I. McCulloch, "Critical review of the molecular design progress in non-fullerene electron acceptors towards commercially viable organic solar cells", *Chemical Society reviews*, 2019, **48**, 1596–1625, DOI: 10.1039/c7cs00892a.

[129] J. Hou, O. Inganäs, R. H. Friend and F. Gao, "Organic solar cells based on non-fullerene acceptors", *Nature materials*, 2018, **17**, 119–128, DOI: 10.1038/nmat5063.

[130] K. Fujimoto, M. Takahashi, S. Izawa and M. Hiramoto, "Development of Perylene-Based Non-Fullerene Acceptors through Bay-Functionalization Strategy", *Materials*, 2020, **13**, 2148, DOI: 10.3390/ma13092148.

[131] C. Li and H. Wonneberger, "Perylene imides for organic photovoltaics: yesterday, today, and tomorrow", *Advanced materials*, 2012, **24**, 613–636, DOI: 10.1002/adma.201104447.

[132] N. Zink-Lorre, E. Font-Sanchis, Á. Sastre-Santos and F. Fernández-Lázaro, "Perylenediimides as more than just non-fullerene acceptors: versatile components in organic, hybrid and perovskite solar cells", *Chemical communications*, 2020, **56**, 3824–3838, DOI: 10.1039/d0cc00337a.

[133] G. Zhang, J. Zhao, P. C. Y. Chow, K. Jiang, J. Zhang, Z. Zhu, J. Zhang, F. Huang and H. Yan, "Nonfullerene Acceptor Molecules for Bulk Heterojunction Organic Solar Cells", *Chemical reviews*, 2018, **118**, 3447–3507, DOI: 10.1021/acs.chemrev.7b00535.

[134] R. Roy, A. Khan, O. Chatterjee, S. Bhunia and A. L. Koner, "Perylene Monoimide as a Versatile Fluoroprobe: The Past, Present, and Future", *Organic Materials*, 2021, **3**, 417–454, DOI: 10.1055/a-1551-6930.

[135] B. Schweda, M. Reinfelds, P. Hofstadler, G. Trimmel and T. Rath, "Recent Progress in the Design of Fused-Ring Non-Fullerene Acceptors—Relations between Molecular Structure and Optical, Electronic, and Photovoltaic Properties", *ACS Applied Energy Materials*, 2021, DOI: 10.1021/acsaem.1c01737.

[136] B. Schweda, M. Reinfelds, J. Hofinger, G. Bäumel, T. Rath, P. Kaschnitz, R. C. Fischer, M. Flock, H. Amenitsch, M. C. Scharber and G. Trimmel, "Phenylene-Bridged Perylene Monoimides as Acceptors for Organic Solar Cells – A Study on the Structure-Properties Relationship", *Chemistry – A European Journal*, 2022, DOI: https://doi.org/10.1002/chem.202200276.

[137] S. Weber, J. Hofinger, T. Rath, M. Reinfelds, D. Pfeifer, S. M. Borisov, P. Fürk, H. Amenitsch, M. C. Scharber and G. Trimmel, "Comparison of fluorene, silafluorene and carbazole as linkers in perylene monoimide based non-fullerene acceptors", *Materials Advances*, 2020, **1**, 2095–2106, DOI: 10.1039/D0MA00470G.

[138] A. Armin, W. Li, O. J. Sandberg, Z. Xiao, L. Ding, J. Nelson, D. Neher, K. Vandewal, S. Shoaee, T. Wang, H. Ade, T. Heumüller, C. Brabec and P. Meredith, "A History and Perspective of Non–Fullerene Electron Acceptors for Organic Solar Cells", *Advanced Energy Materials*, 2021, **11**, 2003570, DOI: 10.1002/aenm.202003570.

[139] M. Zhang, L. Zhu, G. Zhou, T. Hao, C. Qiu, Z. Zhao, Q. Hu, B. W. Larson, H. Zhu, Z. Ma, Z. Tang, W. Feng, Y. Zhang, T. P. Russell and F. Liu, "Single-layered organic photovoltaics with double cascading charge transport pathways: 18% efficiencies", *Nature communications*, 2021, **12**, 309, DOI: 10.1038/s41467-020-20580-8.

[140] J. Wang, Z. Zheng, Y. Zu, Y. Wang, X. Liu, S. Zhang, M. Zhang and J. Hou, "A Tandem Organic Photovoltaic Cell with 19.6% Efficiency Enabled by Light Distribution Control", *Advanced Materials*, 2021, **33**, 2102787, DOI: 10.1002/adma.202102787.

[141] N. An, Y. Cai, H. Wu, A. Tang, K. Zhang, X. Hao, Z. Ma, Q. Guo, H. S. Ryu, H. Y. Woo, Y. Sun and E. Zhou, "Solution-Processed Organic Solar Cells with High Open-Circuit Voltage of 1.3 V and Low Non-Radiative Voltage Loss of 0.16 V", *Advanced Materials*, 2020, **32**, 2002122, DOI: 10.1002/adma.202002122.

[142] X.-K. Chen, D. Qian, Y. Wang, T. Kirchartz, W. Tress, H. Yao, J. Yuan, M. Hülsbeck, M. Zhang, Y. Zou, Y. Sun, Y. Li, J. Hou, O. Inganäs, V. Coropceanu, J.-L. Bredas and F. Gao, "A unified description of non-radiative voltage losses in organic solar cells", *Nature Energy*, 2021, **6**, 799–806, DOI: 10.1038/s41560-021-00843-4.

[143] B. Guo, W. Li, G. Luo, X. Guo, H. Yao, M. Zhang, J. Hou, Y. Li and W.-Y. Wong, "Exceeding 14% Efficiency for Solution-Processed Tandem Organic Solar Cells Combining Fullerene- and Nonfullerene-Based Subcells with Complementary Absorption", *ACS Energy Letters*, 2018, **3**, 2566–2572, DOI: 10.1021/acsenergylett.8b01448.

[144] G. E. Eperon, M. T. Hörantner and H. J. Snaith, "Metal halide perovskite tandem and multiple-junction photovoltaics", *Nature Reviews Chemistry*, 2017, **1**, 0095, DOI: 10.1038/s41570-017-0095.

[145] J. Lee, S.-.-J. Ko, M. Seifrid, H. Lee, B. R. Luginbuhl, A. Karki, M. Ford, K. Rosenthal, K. Cho, T.-.-Q. Nguyen and G. C. Bazan, "Bandgap Narrowing in Non–Fullerene Acceptors: Single Atom Substitution Leads to High Optoelectronic Response Beyond 1000 nm", *Advanced Energy Materials*, 2018, **8**, 1801212, DOI: 10.1002/aenm.201801212.

[146] J. Lee, S.-J. Ko, H. Lee, J. Huang, Z. Zhu, M. Seifrid, J. Vollbrecht, V. V. Brus, A. Karki, H. Wang, K. Cho, T.-Q. Nguyen and G. C. Bazan, "Side-Chain Engineering of Nonfullerene Acceptors for Near-Infrared Organic Photodetectors and Photovoltaics", *ACS Energy Letters*, 2019, **4**, 1401–1409, DOI: 10.1021/acsenergylett.9b00721.

[147] J. Huang, J. Lee, J. Vollbrecht, V. V. Brus, A. L. Dixon, D. X. Cao, Z. Zhu, Z. Du, H. Wang, K. Cho, G. C. Bazan and T.-Q. Nguyen, "A High-Performance Solution-Processed Organic Photodetector for Near-Infrared Sensing", *Advanced materials*, 2020, **32**, 1906027, DOI: 10.1002/adma.201906027.

[148] L. Ye, S. Zhang, W. Zhao, H. Yao and J. Hou, "Highly Efficient 2D-Conjugated Benzodithiophene-Based Photovoltaic Polymer with Linear Alkylthio Side Chain", *Chemistry of Materials*, 2014, **26**, 3603–3605, DOI: 10.1021/cm501513n.

[149] S. Li, L. Ye, W. Zhao, S. Zhang, S. Mukherjee, H. Ade and J. Hou, "Energy-Level Modulation of Small-Molecule Electron Acceptors to Achieve over 12% Efficiency in Polymer Solar Cells", *Advanced Materials*, 2016, **28**, 9423–9429, DOI: 10.1002/adma.201602776.

[150] D. Baran, N. Gasparini, A. Wadsworth, C. H. Tan, N. Wehbe, X. Song, Z. Hamid, W. Zhang, M. Neophytou, T. Kirchartz, C. J. Brabec, J. R. Durrant and I. McCulloch, "Robust nonfullerene solar cells approaching unity external quantum efficiency enabled by suppression of geminate recombination", *Nature communications*, 2018, **9**, 2059, DOI: 10.1038/s41467-018-04502-3.

[151] C. Yan, S. Barlow, Z. Wang, H. Yan, A. K.-Y. Jen, S. R. Marder and X. Zhan, "Non-fullerene acceptors for organic solar cells", *Nature Reviews Materials*, 2018, **3**, 18003, DOI: 10.1038/natrevmats.2018.3.

[152] Q. Fan, W. Su, Y. Wang, B. Guo, Y. Jiang, X. Guo, F. Liu, T. P. Russell, M. Zhang and Y. Li, "Synergistic effect of fluorination on both donor and acceptor materials for high performance non-fullerene polymer solar cells with 13.5% efficiency", *Science China Chemistry*, 2018, **61**, 531–537, DOI: 10.1007/s11426-017-9199-1.

[153] C. Xu, K. Jin, Z. Xiao, Z. Zhao, X. Ma, X. Wang, J. Li, W. Xu, S. Zhang, L. Ding and F. Zhang, "Wide Bandgap Polymer with Narrow Photon Harvesting in Visible Light Range Enables Efficient Semitransparent Organic Photovoltaics", *Advanced Functional Materials*, 2021, 2107934, DOI: 10.1002/adfm.202107934.

[154] Z. Hu, L. Yang, W. Gao, J. Gao, C. Xu, X. Zhang, Z. Wang, W. Tang, C. Yang and F. Zhang, "Over 15.7% Efficiency of Ternary Organic Solar Cells by Employing Two Compatible Acceptors with Similar LUMO Levels", *Small*, 2020, **16**, 2000441, DOI: 10.1002/smll.202000441.

[155] L. J. A. Koster, v. d. Mihailetchi, R. Ramaker and P. W. M. Blom, "Light intensity dependence of open-circuit voltage of polymer:fullerene solar cells", *Applied Physics Letters*, 2005, **86**, 123509, DOI: 10.1063/1.1889240.

[156] H. Huang, L. Jiang, J. Peng, Y. Qi, S. Bai and Q. Lin, "High-Performance Organic Phototransistors Based on D18, a High-Mobility and Unipolar Polymer", *Chemistry of Materials*, 2021, **33**, 8089–8096, DOI: 10.1021/acs.chemmater.1c02839.

[157] L. J. A. Koster, v. d. Mihailetchi, H. Xie and P. W. M. Blom, "Origin of the light intensity dependence of the short-circuit current of polymer/fullerene solar cells", *Applied Physics Letters*, 2005, **87**, 203502, DOI: 10.1063/1.2130396.

[158] B. Hailegnaw, S. Paek, K. T. Cho, Y. Lee, F. Ongül, M. K. Nazeeruddin and M. C. Scharber, "Optoelectronic Properties of Layered Perovskite Solar Cells", *Solar RRL*, 2019, **3**, 1900126, DOI: 10.1002/solr.201900126.

[159] J. Kurpiers, T. Ferron, S. Roland, M. Jakoby, T. Thiede, F. Jaiser, S. Albrecht, S. Janietz, B. A. Collins, I. A. Howard and D. Neher, "Probing the pathways of free charge generation in organic bulk heterojunction solar cells", *Nature communications*, 2018, **9**, 2038, DOI: 10.1038/s41467-018-04386-3.

[160] S. Narra, S. Tsai, K. Awasthi, S. Rana, E. W.-.-G. Diau and N. Ohta, "Photoluminescence of P3HT : PCBM bulk heterojunction thin films and effect of external electric field", *Journal of the Chinese Chemical Society*, 2022, **69**, 140–151, DOI: 10.1002/jccs.202100267.

[161] C. Wang, W. Zhang, X. Meng, J. Bergqvist, X. Liu, Z. Genene, X. Xu, A. Yartsev, O. Inganäs, W. Ma, E. Wang and M. Fahlman, "Ternary Organic Solar Cells with Minimum Voltage Losses", *Advanced Energy Materials*, 2017, **7**, 1700390, DOI: 10.1002/aenm.201700390.

[162] Q. Liu, S. Smeets, S. Mertens, Y. Xia, A. Valencia, J. D'Haen, W. Maes and K. Vandewal, "Narrow electroluminescence linewidths for reduced nonradiative recombination in organic solar cells and near-infrared light-emitting diodes", *Joule*, 2021, **5**, 2365–2379, DOI: 10.1016/j.joule.2021.06.010.

[163] K. Fujimoto, M. Takahashi, S. Izawa and M. Hiramoto, "Development of Perylene-Based Non-Fullerene Acceptors through Bay-Functionalization Strategy", *Materials*, 2020, **13**, 2148, DOI: 10.3390/ma13092148.

[164] J. Kelber, M.-F. Achard, F. Durola and H. Bock, "Distorted arene core allows room-temperature columnar liquid-crystal glass with minimal side chains", *Angewandte Chemie (International ed. in English)*, 2012, **51**, 5200–5203, DOI: 10.1002/anie.201108886.

[165] J. Vollbrecht, C. Wiebeler, A. Neuba, H. Bock, S. Schumacher and H. Kitzerow, "Bay-Extended, Distorted Perylene Esters Showing Visible Luminescence after Ultraviolet Excitation: Photophysical and Electrochemical Analysis", *The Journal of Physical Chemistry C*, 2016, **120**, 7839–7848, DOI: 10.1021/acs.jpcc.6b00954.

[166] J. Kelber, M.-F. Achard, B. Garreau-de Bonneval and H. Bock, "Columnar benzoperylene-hexa- and tetracarboxylic imides and esters: synthesis, mesophase stabilisation and observation of charge-transfer interactions between electron-donating esters and electron-accepting imides", *Chem. Eur. J.*, 2011, **17**, 8145–8155, DOI: 10.1002/chem.201100939.

[167] J. Kelber, H. Bock, O. Thiebaut, E. Grelet and H. Langhals, "Room-Temperature Columnar Liquid-Crystalline Perylene Imido-Diesters by a Homogeneous One-Pot Imidification-Esterification of Perylene-3,4,9,10-tetracarboxylic Dianhydride", *European Journal of Organic Chemistry*, 2011, **4**, 707–712, DOI: 10.1002/ejoc.201001346.

[168] Y.-J. Noh, S.-I. Na and S.-S. Kim, "Inverted polymer solar cells including ZnO electron transport layer fabricated by facile spray pyrolysis", *Solar Energy Materials and Solar Cells*, 2013, **117**, 139–144, DOI: 10.1016/j.solmat.2013.05.062.

[169] A. Soultati, A. Verykios, T. Speliotis, M. Fakis, I. Sakellis, H. Jaouani, D. Davazoglou, P. Argitis and M. Vasilopoulou, "Organic solar cells of enhanced efficiency and stability using zinc oxide:zinc tungstate nanocomposite as electron extraction layer", *Organic Electronics*, 2019, **71**, 227–237, DOI: 10.1016/j.orgel.2019.05.023.

[170] M. B. Upama, N. K. Elumalai, M. A. Mahmud, C. Xu, D. Wang, M. Wright and A. Uddin, "Enhanced electron transport enables over 12% efficiency by interface engineering of non-fullerene organic solar cells", *Solar Energy Materials and Solar Cells*, 2018, **187**, 273–282, DOI: 10.1016/j.solmat.2018.08.010.

[171] C.-W. Liang, W.-F. Su and L. Wang, "Enhancing the photocurrent in poly(3-hexylthiophene)/[6,6]-phenyl C61 butyric acid methyl ester bulk heterojunction solar cells by using poly(3-hexylthiophene) as a buffer layer", *Applied Physics Letters*, 2009, **95**, 133303, DOI: 10.1063/1.3242006.

[172] J. H. Seo, R. Yang, J. Z. Brzezinski, B. Walker, G. C. Bazan and T.-Q. Nguyen, "Electronic Properties at Gold/Conjugated-Polyelectrolyte Interfaces", *Advanced Materials*, 2009, **21**, 1006–1011, DOI: 10.1002/adma.200802420.

[173] Y. Zhou, C. Fuentes-Hernandez, J. Shim, J. Meyer, A. J. Giordano, H. Li, P. Winget, T. Papadopoulos, H. Cheun, J. Kim, M. Fenoll, A. Dindar, W. Haske, E. Najafabadi, T. M. Khan, H. Sojoudi, S. Barlow, S. Graham, J.-L. Brédas, S. R. Marder, A. Kahn and B. Kippelen, "A universal method to produce low-work function electrodes for organic electronics", *Science*, 2012, **336**, 327–332, DOI: 10.1126/science.1218829.

[174] S. Ohisa, T. Kato, T. Takahashi, M. Suzuki, Y. Hayashi, T. Koganezawa, C. R. McNeill, T. Chiba, Y.-J. Pu and J. Kido, "Conjugated Polyelectrolyte Blend with Polyethyleneimine Ethoxylated for Thickness-Insensitive Electron Injection Layers in Organic Light-Emitting Devices", *ACS applied materials & interfaces*, 2018, **10**, 17318–17326, DOI: 10.1021/acsami.8b00752.

Nomenclature

Technical Abbreviations

AFM	atomic force microscopy
AM1.5G	air mass 1.5 global spectrum
APT NMR	attached proton test nuclear magnetic resonance
BHJ	bulk heterojunction
CE	counter electrode
CT	charge transfer
CV	cyclic voltametry
D/A	donor:acceptor
EL	electroluminescence
ELQY	electroluminescence quantum yield
EQE_{PV}	photovoltaic external quantum efficiency
ERE	external radiative efficiency
ESP	electrostatic potential
ETL	electron transport layer
EVS	electrochemical voltage spectroscopy
FA	fullerene acceptor
FF	electrical fill factor
FRET	Förster resonant energy transfer
GS	ground state
HOMO	highest occupied molecular orbital
HTL	hole transport layer
I_{SC}	short-circuit current

IoT	internet of things
IQE_{PV}	photovoltaic internal quantum efficiency
IRF	instrument response function
ITO	indium tin oxide
J_{SC}	short-circuit current density
LE	local exciton
LED	light emitting diode
LP	long-pass
LUMO	lowest unoccupied molecular orbital
MALDI-TOF	matrix-assisted laser desorption/ionization-time of flight
NFA	non-fullerene acceptor
NHE	normal hydrogen electrode
NP	nanoparticles
NREL	National Renewable Energy Laboratory
OFET	organic field effect transistor
OPV	organic photovoltaics
OSC	organic solar cell
PCE	power conversion efficiency
PDI	perylene diimide
PL	photoluminescence
PLQY	photoluminescence quantum yield
PMI	perylene monoimide
PV	photovoltaics
QE	quenching efficiency
RE	reference electrode
SMU	Source Meter Unit (Keithley 2401)
SQ	Shockley and Queisser
TCSPC	time-correlated single-photon counting
UPS	ultraviolet photoelectron spectroscopy
UV-vis-NIR	ultraviolet-visible-near infrared
V_{OC}	open-circuit voltage
WE	working electrode
WF	work function